A Comparison of Discrete and Continuum Models of Cardiac Electrophysiology

Douglas A. W. Bruce

Oriel College

University of Oxford

A thesis submitted for the degree of

Doctor of Philosophy

Trinity Term 2014

Acknowledgements

I am indebted to my supervisors, Dr. Jon Whiteley and Dr. Pras Pathmanathan, for their help over the duration of my degree. Their combined knowledge, experience, time, and attention to detail have been invaluable.

I would also like to thank the Life Sciences Interface Doctoral Training Centre, and all involved within, for providing such a strong platform on which to develop as a young researcher.

Finally, to Hannah, who has served as a constant source of motivation: thank you.

Abstract

When modelling tissue-level cardiac electrophysiology, a continuum approximation to the discrete cell-level equations, known as the bidomain equations, is often used to maintain computational tractability. The bidomain equations are derived from the discrete equations using a mathematical technique known as homogenisation. As part of this derivation conductivity tensors are specified for use in the continuum model. Analysing the derivation of the bidomain equations allows us to investigate how microstructure, in particular gap junctions that electrically connect cells, affect tissue-level conductivity properties and model solutions.

We perform two distinct but related strands of investigation in this thesis. In the first, we consider the effect of including gap junctions on the results of both discrete and continuum simulations, and identify when the continuum model fails to be a good approximation to the discrete model. Secondly, we perform a comprehensive study into how cell-level microstructure properties, such as cell shape, impact the homogenised conductivities to be used in a tissue-level continuum model. This will allow us to predict how the onset of a disease or a change in cellular microstructure will affect the propagation of action potentials.

To do this, we first derive a modified version of the bidomain equations that explicitly takes gap junctions into account. We then derive analytic solutions for the homogenised conductivity tensors on a simplified two-dimensional geometry and find that diseased gap junctions have a large impact on the results of homogenisation. On this same geometry we compare the results of discrete and continuum simulations and find a significant discrepancy between model conduction velocities when we introduce gap junctions with lower coupling strength, or when we consider elongated cells. From this, we conclude that the bidomain equations are less likely to give an accurate representation of the underlying discrete system when modelling diseased states whose symptoms include reduced gap junction coupling or an increase in myocyte length.

We then use a more realistic two-dimensional geometry and numerically approximate the homogenised conductivity tensors on this geometry. We discover that the packing of cells has a substantial effect on conduction, with a brick-wall geometry particularly beneficial for fast propagation, and that gap junctions also have a large effect on conduction. Finally, we consider a three-dimensional cellular geometry and show that the effect of changing gap junction properties is different when compared to two dimensions, and discover that the anisotropy ratios of the tissue are highly sensitive to changes in gap junction parameters.

Overall, we conclude that gap junctions and cell structure have a large effect on discrete and continuum model results, and on homogenised conductivity calculations in tissue-level cardiac electrophysiology.

Contents

Chapter 1

Introduction

Cardiac diseases, malfunctions and illnesses represent one of the leading causes of death both nationally (see 'Deaths Registered in England and Wales, 2013' at `http://www.ons.gov.uk/ons/index.html`) and globally (as reported by the World Health Organisation at `http://www.who.int/mediacentre/factsheets/fs310/en/index.html`). An estimate of the resulting cost to the nation for coronary heart disease alone was put at £8.5 billion in 2004 [84], which equates to around £300 per individual taxpayer.

As a result, substantial funding and effort has been invested to conduct research into understanding and treating these conditions. Some overall aims of the research are: to find drug compounds that have a corrective effect on the function of the heart; to prevent the onset of heart diseases; to understand and improve treatment methods for these conditions (*e.g.* defibrillation); and to better diagnose conditions (*e.g.* through the interpretation of electrocardiograms). The ability to predict the effect of a drug or a defibrillatory shock on cardiac function is clearly paramount to these goals, and so mathematical or computational models that allow us to investigate the underlying mechanisms serve as a very useful tool.

Such models have been created for over 50 years for a variety of purposes. The simplest goal, in some sense, is to account for experimentally observed phenomena. These phenomena range from the shape of the electrocardiogram, to the histology of the heart from sub-cellular level to tissue- and organ levels, to the inter-species differences between hearts and

the observed alterations to normal cardiac function in disease. A set of models that can not only recreate the results of clinical or experimental trials, but also give some biological or physiological interpretation to the observations, are an extremely powerful tool in aiding the understanding of cardiac structure and function.

On that note, over the past fifty or so years a large body of work has been done to accurately predict the form of the temporal action potential within a single cell. This began with the work of Hodgkin and Huxley [63] that considered the squid giant axon, progressed onto the Purkinje fibres of the heart via the work of Denis Noble [104], and has touched upon a wide variety of cardiac cell types and phenomena under study, with perhaps the most notable recent example being the ventricular model of ten Tusscher *et al.* [146]. Concurrently, there has been progress in modelling the coupling of cardiac cells with one another, examples of which include the early work of Weidmann [161] that confirmed the existence of gap junctions connecting cells, that of Spach *et al.* [141] that looked at the discontinuous nature of cardiac propagation, and the experiments of Hoyt, Cohen and Saffitz [65] on determining the precise microstructure of cardiac tissue. There is also considerable interest in modelling large slabs of cardiac tissue, reaching towards the goal of whole-organ systems. The most popular formulation of such a model is represented by the bidomain equations, a system created by Tung [155] and formally derived by Neu and Krassowska [102] and Keener and Panfilov [72].

A more lofty goal of a mathematical or computational heart model is that of predictive power — in certain cases models have been used to propose mechanisms for the onset of disease, or to predict the effect of a drug action or of a defibrillatory shock on cardiac rhythm, prominent examples being the work of Keener and Panfilov [72], Moreno *et al.* [97], and Mirams *et al.* [95]. These use-cases are perhaps more exciting, and the idea of screening a drug for suitability using a computer simulation is very appealing. Finally, a model of the human heart is necessary for the wider ambition of creating a virtual physiological human, and in that sense the model will become an important player in a much larger scale system. Given the body of work discussed above and the advances made over the past decades, mathematical models of cardiac behaviour are a worthwhile and important field of study.

In addition, sufficiently detailed and accurate computational simulations of the processes under consideration may aid the initial diagnosis and characterisation of cardiac diseases. To this end, researchers are working towards real-time, patient-specific models of cardiac behaviour. This task, which is far from complete, requires integration of modelling techniques and experimental data at various anatomical levels: from the sub-cellular level of gene expression and chemical pathways to the whole-organ level of the mechanically contracting heart. Connecting these vastly different systems is electrophysiology — it is the biochemical reactions caused by the electrical signal that generate tension in cardiac fibres, which determine when and how these muscle fibres contract. Furthermore, it is the electrical signal that is altered under many common cardiac diseases such as ischaemia, fibrillation and arrhythmia.

Consequently, most cardiac models are underpinned by a description of an electrophysiological system upon which other details can be layered. The first such system emerged in the 1960s [104] and considered the temporal electrical behaviour of a single cell in response to chemical changes. Models were extended to consider small spatial scales shortly afterwards [54] and to the whole-organ level following the recent increase in computational power available [154]. An associated challenge has become the integration of separate scales into one complete system — to model sub-cellular processes precisely in a four-billion cell virtual organ remains intractable, yet these microscale processes have a profound effect on the behaviour of the system at the whole-organ level. The multi-scale models that aim to do this integration are at the crux of large research projects in the field (`http://www.euheart.eu/index.php?id=43`).

Our research focuses on the interface between modelling small regions of tissue and the whole organ, with particular consideration to the propagation of the electrical signal in the models. Impulse propagation is determined on the cellular level by the fine structure of cardiac cells, and in particular *gap junctions*, which are small channels that directly connect cells to one another by allowing ions to freely pass through them. Resistance to electrical flow at this scale is modified under certain disease conditions, and has an impact on the potential failure of propagation. At the organ level it is impractical to model these changes

at the level of individual cells, and the effect of resistive changes due to sub-cellular processes is often neglected or included only in an average sense. To give a specific example, the electrical connection between cardiac cells through gap junctions is weakened when certain diseased states occur, including ischaemia, arrhythmia, fibrillation, and hypertrophy. This is a direct cause of failure in signal conduction, and incorporating these changes in resistance by their average behaviour over the whole system may not sufficiently capture the true characteristics.

To address this, we present in this thesis a novel tissue-level continuum model of cardiac electrophysiology, represented by the bidomain equations, that allows the systematic inclusion of local geometrical and resistive effects into a larger-scale system. We compare the results of simulations between this model and the discrete model from which it was derived in order to determine how gap junctions, both healthy and diseased, affect the behaviour of the two models. We also determine the effect that microstructure properties, such as cell shape, cell structure, and gap junction properties, have on the resultant continuum system, specifically on the conductivity tensors and conduction velocity. We do so for a simplified two-dimensional cell, a more complex two-dimensional geometry, and a three-dimensional geometry. The aim of this is to determine how the changes in cell properties that can occur in common clinical conditions such as ischaemia, fibrillation, and hypertrophy, will affect the conduction of an electrical signal through the diseased tissue.

In the next section, we provide a summary of each subsequent chapter of this thesis and outline our findings.

1.1 Thesis Outline

We begin in Chapter 2 by providing an overview of the biological background relating to the electrical activity of the heart. We detail the structure and function of the heart, consider the response of a single cell to an electrical stimulus, and describe the means by which cells are electrically connected to their neighbours. We include a history of the mathematical modelling of single cardiac cells, and finally go into greater depth on connections between

cells, with a specific focus on gap junctions: we outline how gap junctions are crucial to the propagation of an electric signal in cardiac tissue; detail their structure, distribution and expression levels; and describe how these features are modified during many common diseases along with the resulting effect this has on electrical propagation.

Then, in Chapter 3 we describe existing discrete and continuum models of cardiac tissue and give an overview of how gap junctions have previously been included in these models. We discuss the derivation of continuum models from their discrete counterparts, giving an introduction to homogenisation (the mathematical technique used to create the models) and outline the assumptions made in converting a discrete system to a continuum model. We then summarise the current state of the field with regard to including gap junctions in cardiac tissue models, and describe the limitations concerning the derivation of the continuum model, before identifying potential gaps in the current literature. Finally, we state the research questions that arise from analysing these gaps in the literature, and give an outline of how this thesis will attempt to answer them along with a summary of our findings.

We then begin to answer these research questions. First, in Chapter 4 we derive a modified form of the bidomain equations that explicitly takes gap junctions into account, and perform a mathematical analysis of the derivation in order to study the form of the homogenised conductivity tensors. Using a simplified two-dimensional cell we derive analytic solutions for the continuum conductivity tensors and demonstrate that adding in gap junctions at healthy coupling levels significantly reduces the conduction velocity of the system, while modelling gap junctions with diseased parameters further reduces the conduction velocity. This shows the importance of explicitly including gap junctions, and of incorporating the changes to gap junctions that occur with disease, to the process of creating a continuum model. We also observe an anomaly with homogenising in two dimensions that means we cannot obtain nonzero conductivity values for both tensors in both spatial directions, and so we cannot calculate anisotropy ratios for the domains.

In Chapter 5, we investigate the validity of the bidomain equations by performing computational simulations and compare the results obtained using both discrete and continuum models, and find that the underlying conduction velocity of the propagating action po-

tential ceases to match up between the two models when gap junctions are introduced at physiologically realistic coupling levels. We show that this effect is significantly magnified by modelling gap junctions with reduced conductivity, or by increasing myocyte length. From this we conclude that the conduction velocity arising from the bidomain equations may not be an accurate representation of the underlying discrete system. In particular, the derivation of the bidomain equations is unlikely to be valid when modelling certain diseased states whose underlying electrophysiological changes include a reduction in gap junction coupling strength or an increase in myocyte length.

In Chapter 6 we use a two-dimensional geometry consisting of more complex and realistic cell shapes to determine how cell-level microstructure properties such as cell shape, gap junction shape, cell packing, and microscale conductivities affect the homogenised conductivity tensors. We discover that, for a geometry where cells are aligned with their neighbours, gap junction parameters have a much larger effect than other model parameters on the conductivity tensors and associated predicted conduction velocity. When cells are tightly packed together, the height of the cell also has a major effect on conduction velocity. We then find that, by using a geometry in which cells are offset from each other in a brick-wall packing structure, conduction velocity is substantially increased compared to the case of aligned cells and is much less sensitive to the height of the cells, showing that this cell structure is particularly beneficial for conduction. Lastly, we incorporate cell-to-cell connections between successive fibres of cells and see that these off-fibre gap junctions increase the magnitude of intracellular conductivity in both spatial directions, and also play a major role in determining the anisotropy of the intracellular space. We conclude from this chapter that gap junction properties, off-fibre cell connections and the brick-wall packing of cells are important determinants of conduction when using a more complex and realistic cell membrane shape and packing structure.

Finally, in Chapter 7 we extend the geometry to three spatial dimensions, and find that the effect of gap junctions on the results of conductivity calculations differs depending on whether we consider a two- or three-dimensional cell. We also observe that the conduction velocity change calculated due to modelling diseased gap junctions with reduced conduc-

tivity is similar to that calculated previously for two-dimensional cells. When considering anisotropic cells, we find that conduction velocity is sensitive to changes that represent the effects of gap junction remodelling seen in a number of common clinical conditions, and so we expect that action potential propagation will be greatly affected in these situations. We find that modelling long, thin cells does not in itself give physiologically normal values for either the intracellular or extracellular anisotropy ratio, but that combining this with a reduction in off-fibre gap junction conductivity produces realistic intracellular values. As a consequence of the above, we also find that the difference in anisotropy ratios between intracellular and extracellular spaces, a condition that plays a big part in certain propagation phenomena in cardiac tissue, is highly sensitive to gap junction parameters, which presents an additional method by which changes in gap junctions in disease may affect propagation of electrical signals in cardiac tissue.

We end the thesis in Chapter 8 by writing down the conclusions drawn from our simulations and calculations, and by outlining some suggested ways in which the work in this thesis can be extended in the future.

Chapter 2

Biological Background

Contents

This chapter provides a high-level overview of the biological background behind the electrical activity of the heart, with an emphasis both on the response of a single cell to an electrical stimulus, and on the electrical connections between neighbouring cells.

In Section 2.1 we present a short summary of the structure and function of the heart. We continue in Section 2.2 by considering the electrical properties of a single cardiac cell, and we then discuss the electrical coupling of cells, both in terms of how an electrical signal propagates through the entire heart and in terms of the specifics of the communication

between neighbouring cells, in Section 2.3. In this section we also provide further details of the spatial distribution of gap junctions, how this distribution changes under certain common diseased conditions, and how the cardiac action potential is modified under these conditions.

2.1 Structure and Function of the Heart

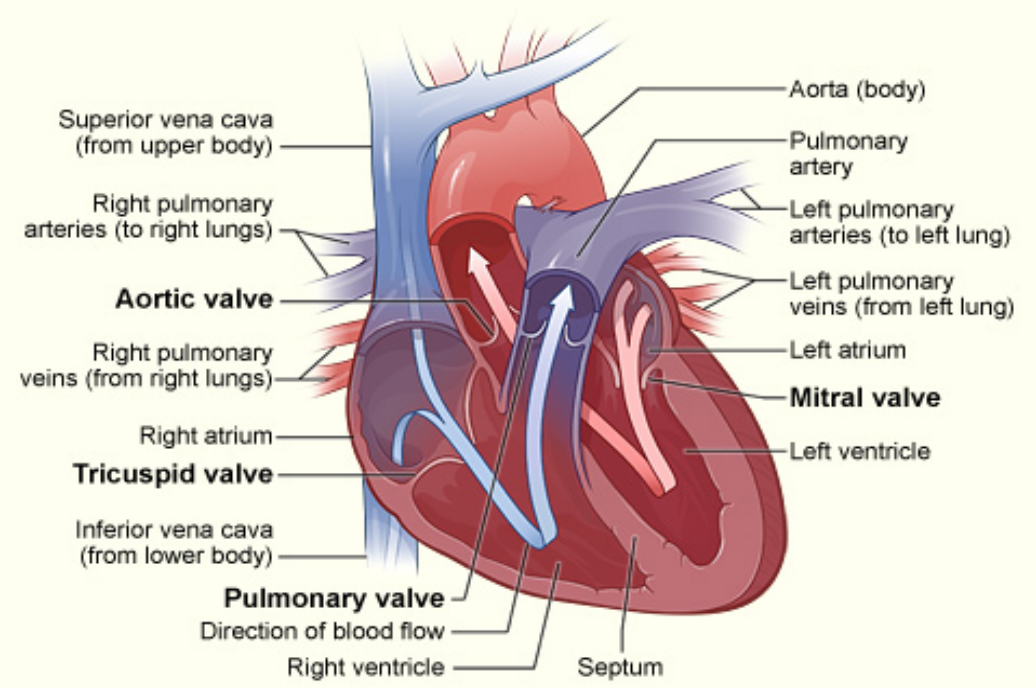

Figure 2.1: *The structure of the human heart. The image is taken from* `http://www.hearthealthywomen.org/cardiovascular-disease/featured/heart-valve-disease.html`.

In this section we briefly outline the key points relating to the structure and function of the heart. To see a more detailed explanation of the physiology of the human heart, refer to [47] for an in-depth medical account or to [75] for a mathematically driven summary.

The human heart is a four-chambered pump, the structure of which is caricatured in Figure 2.1. Its primary role is to pump blood to the rest of the body, which it does by contracting in a rhythmic and repeated fashion. A heart has two halves, each of which has a different function. The right heart drives blood to the lungs, where it is oxygenated (and where

carbon dioxide is excreted), and sent back to the left heart. The left heart then drives this oxygenated blood to the rest of the body. Each side of the heart is further divided into an atrium and a ventricle. The atria are responsible for receiving blood and are relatively small with thin walls, whilst the ventricles propel the blood out of the heart and so are larger and more muscular.

To facilitate this pumping, the three-layered outer wall of the heart contains a middle layer composed of contractile muscle fibres (the myocardium). The cells within, known as myocytes, are excitable — that is, a small stimulus current can instigate a series of biochemical reactions that cause a rise and fall in the transmembrane potential of the cell, known as an action potential. It is these biochemical reactions that generate tension in the cardiac fibres, providing the mechanism for contraction. In addition, cells are electrically coupled to one another via an intercalated disc at the cell terminus that allows an electrical signal to pass from one cell to the next through channels known as gap junctions. This enables the propagation of an action potential through the excitation of neighbouring cells, causing the contraction of the entire collection of cells, which in turn allows blood to be pumped through the system.

2.1.1 The Cardiac Electrical Conduction System

Cardiac function relies on the propagation of electrical signals through heart muscle. This follows a very specific pathway that is formed by the cells of the heart being arranged as a branching syncytium where electrical signals pass from one cell to next via gap junctions. Certain types of cardiac muscle cell are specialised for conduction, in that they contain few of the myofibrils that are the contractile units of the cell, but instead they allow a wave of deploarization to spread through the heart. In a healthy individual, this spread is rapid, rhythmic and coordinated to ensure ordered and regular contraction.

Initiation of cardiac conduction begins at the sinoatrial node, a collection of cells located at the apex of the right atrium that have the ability to self-excite; that is, they can produce an action potential without receiving external stimulation. These cells are not optimised for

contraction but instead spontaneously depolarise in a rhythmic manner, triggering action potentials that are then conducted to the surrounding areas. The frequency of sinoatrial node deploarisation determines the overall frequency of cardiac conduction in the absence of any arrhythmic condition.

The signal from the sinoatrial node stimulates the atria to contract, as the action potentials propagate either to the left atrium via Bachmann's bundle, a band of muscle that connects the right atrium to the left atrium, or via the atrial cells to the atrioventricular node, which itself can generate action potentials in the case that the sinoatrial node fails to do so.

As the atria are are almost fully insulated from the ventricles, electrical impulses can only pass between them through the atrioventricular node, which is another collection of cells that are specialised for conduction and are located within the atrial septum. They dramatically slow conduction down, which not only allows for the atria to contract before the ventricles (so that they can eject their blood into the ventricles before they themselves contract), but also ensures a more regular contraction of the ventricles and protects them from excessively high stimulation rates caused by arrhythmic conditions such as atrial fibrillation.

Following this delay as the action potential passes through the atrioventricular node, it proceeds through the bundle of His to the right and left bundle branches, and then to the Purkinje fibre system that surrounds the ventricles, before being transmitted to the ventricular myocardium.

As the signal travels from the bottom to the top of the left and right ventricles, it spreads from the inside to the outside of the ventricular wall. As a result, ventricular tissue contracts in a manner that expels blood out of the ventricles, whilst blood is prevented from being expelled back to the atria by the unidirectional heart valves shown in Figure 2.1.

2.2 Single-Cell Electrophysiological Modelling

2.2.1 Cardiac Cells

An individual cardiac myocyte is a long (60–225 μm), thin (15–50 μm) [42] structure that contains myofibrils, which are chains of sarcomeres that are the contractile units of the cell. A cardiac myocyte is also abundant in mitochondria, the elements that are responsible for the high energy of the cell, and contains only one or two nuclei. Each cell is surrounded by a cell membrane, which is a phospholipid bilayer separating the cell from the extracellular matrix that makes up the majority of the remainder of the tissue. This bilayer gives rise to the transmembrane potential, which is defined as the difference in electrical potential across the cell membrane. Whilst the membrane itself is highly impermeable to the passage of ions, it contains a number of structures that facilitate transport, the two main types of which are ion pumps and ion channels. Ion pumps use the energy within the cell to pump ions against their concentration gradient, and the most relevant example when considering the cardiac cycle is the sodium-potassium (Na^+/K^+) pump. This transports three sodium ions out of the cell and two potassium ions in, thus keeping the electrical potential higher in the extracellular matrix than in the cell, as well as causing extracellular matrix/cell imbalances in both Na^+ and K^+ concentrations. Ion channels are pore-forming proteins that selectively allow individual ions to pass through them in what is called passive flow. Each cell has lots of channels that are independently open or closed, and the state of each channel is voltage-dependent, in a process known as gating.

To model the electrical potential in a single cardiac cell, we therefore need to find suitable time-dependent equations for the transmembrane potential. As the membrane separates charge between the cell and the extracellular matrix, it can be viewed as a resistor-capacitor circuit consisting of a capacitor (the phospholipid bilayer) and a resistor (the combined effect of the ion channels and pumps) in series. Using Kirchhoff's current law [108] we obtain the equation

$$c_m \frac{\mathrm{d}V}{\mathrm{d}t} + I_{ion} = 0, \tag{2.1}$$

where c_m is the capacitance of the membrane, V is the transmembrane potential and I_{ion} represents the sum of all ionic currents. To model each type of ion channel individually, it is commonly assumed (for instance, in all the single-cell models detailed in Section 2.2.2) that the instantaneous current-voltage curve for a single channel is approximately linear, such that for an ion X the current flow $I_X = g_X(V - V_X)$, where g_X is the time-dependent conductance of the channels and V_X is the Nernst or equilibrium potential of the ion. It is in the nonlinear function g_X that the process of gating is taken into account — the function is often represented as the product of a number of gating variables that describe the proportion of channels open at a given time, and a constant scalar conductance that gives the experimentally observed conductance when all channels are open. The gating variables satisfy first-order ordinary differential equations in which the coefficients are functions of the transmembrane potential V that are empirically determined to match experimentally observed behaviour.

2.2.1.1 The Action Potential

The general form of the cardiac action potential consists of five phases: depolarisation (known as the upstroke); initial repolarisation; plateau; rapid repolarisation; and rest. These are caricatured in Figure 2.2. The majority of cells stay in the rest phase until they receive a sufficiently strong electrical signal from an adjacent cell, but the 'pacemaker' cells found in the sinoatrial or atrioventricular nodes undergo a slow depolarisation during this period, which ultimately causes them to self-activate when they reach what is known as their threshold voltage. The rapid depolarisation phase, also called the upstroke, is caused by the vast majority of Na^+ channels opening as an electrical signal is received, which leads to a large influx of Na^+ ions and therefore a sharp rise in transmembrane potential. The eventual inactivation of these channels after the voltage reaches a certain level, combined with the activation of an outward K^+ current, gives rise to a short reduction in potential

sometimes known as the 'notch'. At this stage, the outward K^+ current becomes slow and balances with the inward movement of calcium from L-type Ca^{2+} channels, and so we see a gently sloping plateau in potential. As the L-type Ca^{2+} channels close, the small net outward current that remains stimulates more K^+ channels to open which causes the cell to rapidly repolarise and return to its resting state.

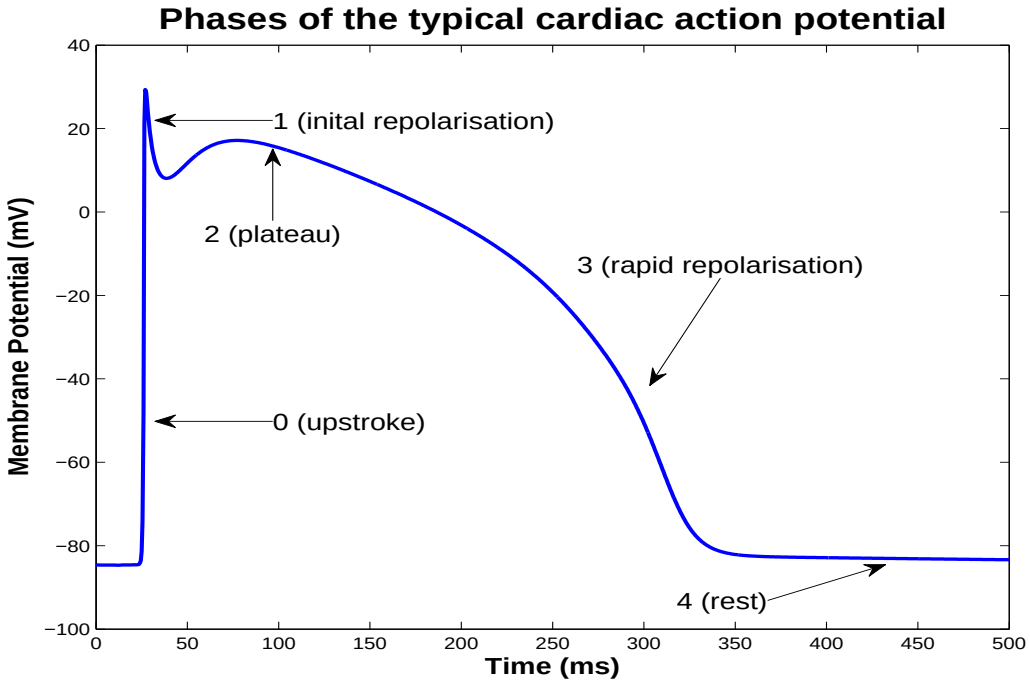

Figure 2.2: *A typical cardiac action potential.*

Whilst this is a simplification of the complex mechanisms occurring within the cardiac myocyte during the course of an action potential, it can be used to write down a basic mathematical model that approximates the ionic current contribution to the behaviour of the transmembrane potential in the form outlined in Equation (2.1). If we model the flux of Na^+, K^+ and Ca^{2+} separately, we arrive at

$$I_{ion} = g_{Na}(V - V_{Na}) + g_K(V - V_K) + g_{Ca}(V - V_{Ca}) + I_{app}, \tag{2.2}$$

where I_{app} is the applied current (*i.e.* any signal received from an adjacent cell or from an external source). The specific Nernst potentials (given by V_{Na}, V_K and V_{Ca}) will impact at what stage the currents come into play as well as whether they are positive or negative

— for the inward Na^+ current the value V_{Na} is positive, whilst for the outward K^+ current the value V_K is negative. The conductances can be modelled in various ways as complex nonlinear functions of both time and voltage, and in general are matched to experimental data to obtain as accurate a form as possible.

Having discussed the key features of a cardiac cell with regard to action potential generation, we next present a brief history of systems that have been created to model the temporal form of the action potential — that is, variations of Equation (2.2). Such models consider the electrical behaviour of a single cardiac cell in isolation.

2.2.2 The Birth of Single-Cell Models

As previously mentioned, one of the main features of cardiac cells is that they are both contractile and excitable. This excitability, which allows for an electrical signal to conduct through cardiac tissue, owes its existence and precise nature to the ion channels embedded in the plasma membrane of the cell, and consequently the logical place to start when formulating a mathematical model of electrical signalling in cells is to consider the ionic currents generated.

Until the advent of the space-clamp technique in the 1940s [88] for direct measurement of the transmembrane current, little was known about the membrane potential of cells. Following the work of Kenneth Cole and others [15–20, 23, 44], Alan Lloyd Hodgkin and Andrew Huxley developed these techniques and applied them to study the ionic fluxes in the squid giant axon over a range of physiological voltages [63]. They hypothesised the initial inward current to be carried by Na^+ and the subsequent outward current to be primarily carried by K^+, with all other currents considered small in comparison and grouped together to form what was designated the 'leakage' current. Using the previously discussed model for the time-dependence of the voltage (Equations (2.1) and (2.2)) and by formulating the conductances of the model to match their experimental data, they arrived at the celebrated Hodgkin-Huxley model [59–62].

The simplicity of the Hodgkin-Huxley model, combined with its ability to quantitatively

predict experimental findings, led others to adapt their formulation to other forms of cells, including cardiac cells. The first application to the heart, specifically to the Purkinje fibres, came in the early 1960s when Denis Noble modified the Hodgkin-Huxley system [104]. Driven by the discovery of an inward K^+ current, the model was constructed to see if combining this new current with a vastly reduced, delayed outward K^+ current and a Hodgkin-Huxley type Na^+ current could reconstruct the experimental results of Weidmann [160] concerning the temporal form of the cardiac action potential. Whilst the model was successful in this respect, explaining the phenomenon of all-or-nothing repolarisation and exhibiting the long plateau phase of the cardiac action potential, Ca^{2+} currents were yet to be discovered and so the model only contained the one voltage-gated inward current (Na^+).

Following the discovery of the Ca^{2+} current and the multiple components of the K^+ current, the McAllister-Noble-Tsien (MNT) model [89] was created in 1975. It reconstructed a wider range of experimental results, including the effect of small current pulses on the pacemaker depolarisation of Purkinje fibres. However, it introduced a slow outward K^+ current to explain the slow conductance changes near resting potential, whereas it is now known that this is due to an inward current. This was a major flaw and as such the model was quickly updated and replaced.

At roughly the same time, Beeler and Reuter [5] were formulating a model for the action potential of ventricular muscle cells, the first of its kind (as opposed to previous work that considered the Purkinje network). They used Hodgkin-Huxley type equations with two inward currents, one driven by Na^+ and a primarily Ca^{2+} 'slow' current, and two outward currents, one due to K^+ and the other a voltage-gated time-dependent current named 'X_1'. One of the main drawbacks of the model is that the maximum upstroke velocity is low (115 V/s) when compared to what has been observed in single cells (up to 400 V/s). Nonetheless, this model has been used extensively for simulations of multi-cellular tissue and has provided a framework for later ventricular muscle models.

Subsequently, more accurate and highly complex models have been developed that account for many dozens of small currents and other dynamic cellular processes, most notably the models of Luo and Rudy [86, 87] and of ten Tusscher *et al.* [146, 147], both of which

are used widely in current work to study a variety of topics. These topics include early afterdepolarisation [157], the formation and breakup of spiral waves [105], arrhythmogenesis [95, 96] and action potential heterogeneity [28] to name just a few.

However, whilst these models seem able to replicate the minutiae of the temporal action potential, we are unsure of the accuracy and homogeneity of the experimental data used to determine the increasing number of model parameters. It was elucidated in [103] that modern models of the temporal cardiac action potential derive their parameters from a huge variety of species (human, dog, frog, mouse, rabbit, *etc.*) and experimental temperatures (ranging from 12°C to 38°C), as well as being derived from a mixture of modelling and experimental studies. This suggests that we must be careful when choosing an appropriate single-cell model of cardiac electrophysiology — for example, we may be looking at a situation where a specific ionic current has a large effect on our system, using a model where certain ion channel properties were derived from measurements on a rabbit heart at room temperature, and attempting to draw a parallel to the human heart at body temperature. In addition, the variations in parameters both in a single subject and across a population are well-documented [13, 38], and therefore a one-size-fits-all model of the temporal action potential is unlikely to be correct.

At the opposite end of the spectrum, in recent years the potential for macroscale whole-organ modelling has led researchers to strive towards a single-cell model that provides sufficient physiological detail for the least possible complexity in order to enhance or preserve computational tractability of their system. A classic example of this was the model developed by Fitzhugh and Nagumo [37, 100], which is an abstract model of excitation. The model tries to retain the qualitative features of an excitable system (specifically the Hodgkin-Huxley model) by considering abstract features such as 'fast' and 'slow' components. This allows not only for more detailed mathematical analysis of the system but for a good approximation to the overall system behaviour by fitting experimental data to the abstract system parameters — for example, in the Fitzhugh-Nagumo model we may specify the threshold value above which the external stimulus will cause the system to excite, and we may specify the relationship between the membrane potential and a recovery variable that determines

how the system returns to rest. The simplicity of the model gives great benefit when considering a large, three-dimensional spatial region, and as such it has been used to study action potential propagation in cardiac tissue. For example, the work of Aliev and Panfilov [2] modified the Fitzhugh-Nagumo equations to create a model that was efficient when used in computer simulations and accurately represented the shape of an action potential.

Further examples of where this type of model has been applied to cardiac electrophysiology are the modified Beeler-Reuter model [110], the reduced model developed by Bueno-Orovio *et al.* [9] and the discrete reaction-diffusion-mechanics model of Weise, Nash and Panfilov [163], all three of which are increasingly being used in simulations. This modelling philosophy, that we may combine abstract variables such as 'excitation', 'recovery' and 'contraction' into one simplified system, represents a shift away from the general trend over the last 50 years of increasing the complexity and physiological realism of cardiac cell models.

2.2.3 Summary

A multitude of single-cell models of cardiac electrophysiology have been developed over the last 50 years — the electrophysiology repository at `http://www.cellml.org` contains over 100 models. Collectively, these models have considered a number of cell types and incorporated widely varying levels of detail with regard to the specific mechanisms occurring inside a cardiac cell. As well as describing the behaviour of a single cell in response to an electrical stimulus, these models can be used in conjunction with a model that electrically couples cells into cardiac tissue. This combination allows us to study the conduction of an electrical signal through the heart, which is the subject of the next section.

2.3 Electrical Connections Between Cardiac Cells

Considering the basic tissue structure of cardiac cells, we know that the long axes of the individual cells are approximately aligned with one another along what is known as the fibre

direction, and side-to-side coupling causes the cells to form what are called sheets. These sheets are several cells thick and wrap around the ventricles and atria. In the formative days of cardiac electrophysiology modelling, it was assumed that cardiac tissue behaved as a syncytial mass with no source of resistance to electrical propagation between connected cells, *i.e.* that there were no gap junctions connecting neighbouring cells. The resulting behaviour could then be modelled using the cable equations that had already been applied to a nerve fibre [64]. With the popularisation of the electron microscope came the revelation that end-to-end coupling of cells was facilitated by a protein structure known as an intercalated disc [156], which is an agglomeration of three types of adhering junction — fascia adherens which help to transmit contractile forces, macula adherens which prevent separation, and gap junctions which permit ions to pass between cells, thus allowing an action potential to propagate. Further investigation revealed the existence of similar structures connecting cells in a side-to-side manner.

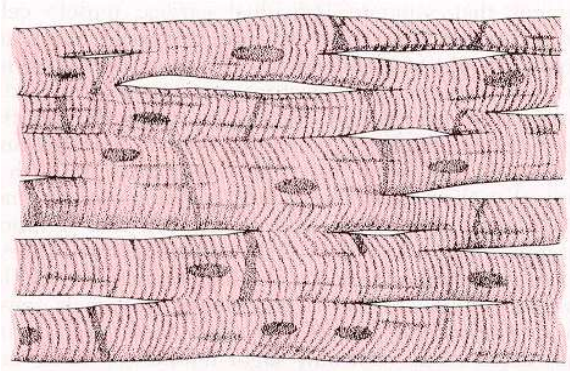

Figure 2.3: *Cardiac cell structure: Guyton and Hall, 1996, Fig. 9-2, p.108.*

Whilst the structure and function of gap junctions is incredibly complex and fascinating, a full explanation goes beyond the scope of this thesis — for such details, see the books by Peracchia [109] or Dhein [30]. However, we will outline the features of gap junctions that are relevant to our research, beginning with an overview of gap junctions in cardiac cells in Section 2.3.1 before going into more detail about the distribution of gap junctions and the levels of expression of their constituent proteins, along with how these change during diseased conditions. Finally, we will discuss how gap junctions affect action potential propagation under diseased conditions in Section 2.3.2.

2.3.1 Gap Junctions in Cardiac Cells

Considering the caricature of the structure of cardiac tissue in Figure 2.3, we see that end-to-end gap junctions within the intercalated disc (represented as dark bands) are present throughout the tissue and may connect more than just two individual cells. In addition, they are of non-trivial width when compared to that of an individual cell. To put numbers on these statements, Hoyt, Cohen and Saffitz [65] estimated that due to overlapping at cell ends — such that cardiac cells form what is commonly referred to as the 'brick-wall' structure shown in Figure 2.4 — myocytes were connected on average to 9.1 $\pm$ 2.2 other myocytes. They found that 80% of junctions were found at end-to-end locations, and that these junctions had a width of up to 8 μm, which is between 5% and 10% of the overall cell length using values for typical myocyte length taken from [42].

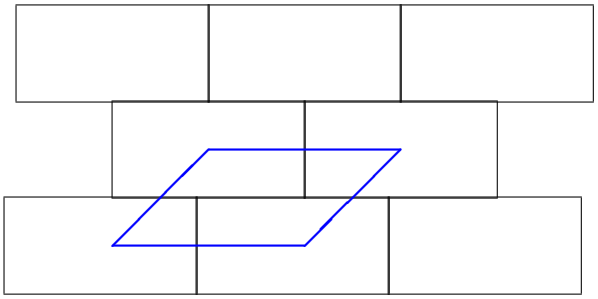

Figure 2.4: *A two-dimensional caricature of the brick-wall structure of cardiac cells. The parallelogram outlined in blue shows an example of a subunit from which we may create a periodic domain using this geometry.*

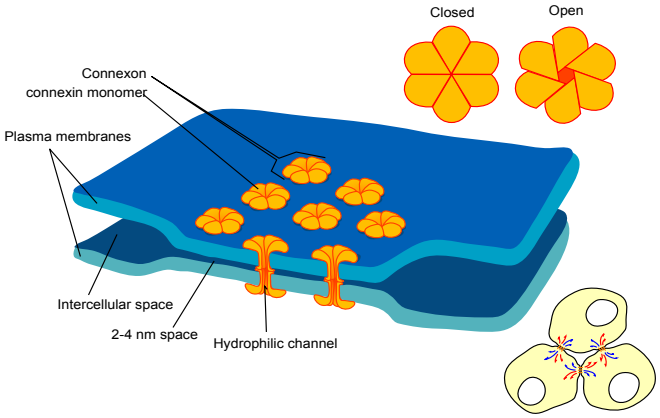

Figure 2.5: *A representation of gap junctions, Mariana Ruiz, 2006.*

In Figure 2.5 we show the basic structure of the gap junctions in an intercalated disc, and see that an individual gap junction is composed of two hexagonal hemichannels, each made up of six identical proteins known as connexins. These hemichannels are known as connexons, and can be open or closed depending on factors such as voltage and Ca^{2+} concentration [53]. There are various estimates for the resistance or resistivity of both the intercalated disc and the gap junctions themselves. In 1966 Weidmann [161] measured the resistance of the intercalated disc at 3 Ω for 1 cm^2 of disc. Since then, values ranging from 10–300 pS have been placed on the individual conductance of a single channel [53], with whole-disc coupling recently measured at around 0.5 μS [166]. Using the value for the gap junctional surface area per intercalated disc of 10-40 μm^2 given in [70], this gives a resistance of 5 Ω for 1 cm^2 of disc, which is very similar to the original measurement of Weidmann. Using the above figures the resistivity for the whole intercalated disc is approximately 500 Ω cm, which is comparatively large when compared to the value of cytoplasmic resistivity of 288 Ω cm measured in [10], especially given that the intercalated disc is relatively short when compared to the length of a myocyte.

The role of gap junctions in the propagation of the cardiac action potential is clear in the sense that these junctions are the means of electrical communication between cells. Whilst the transfer of excitation between cardiac cells can be done both mechanically and chemically, the most important mechanism is through electricity. In cardiac muscle cells, it is gap junctions that provide a comparatively low-resistance pathway to conduction when compared to the rest of the cell membrane — they are large and non-selective which allows ions and other small molecules to diffuse between cells relatively freely (again when compared to the cell membrane).

Based on the above explanation of the structure and function of gap junctions, it seems as though there are two major ways by which they might affect conduction in the heart. Firstly, junctional membranes can be distributed in various fashions in the tissue. Secondly, the connexins making up the channels may be expressed in different numbers. Separately, the geometry of the tissue will have its own effect on conduction in conjunction with these gap junction properties. We will now go into further detail on these topics.

2.3.1.1 Distribution of Gap Junctions

In healthy adult cardiac tissue, gap junctions are located preferentially at the cell ends — that is, in the intercalated disc. Whilst this was known qualitatively following the work of Weidmann and others in the 1950s and 1960s [161], a detailed quantitative analysis of the distribution of gap junctions in the healthy myocardium only appeared in 1989. The work of Hoyt, Cohen and Saffitz [65] consisted of a morphometric analysis of five canine hearts, finding that around 80% of the total gap junctional membrane area was located at the cell ends, with the remaining 20% connecting cells in transverse directions. Previously, it had been observed that this uneven distribution leads to an anisotropy in conduction velocity on the macroscale of a bundle of fibres [14]. The authors found that differences in resistance between transverse and longitudinal directions led to a ratio between the conduction velocities of three to one for longitudinal to transverse conduction.

On the microscale of individual cells, Chapman and Fry [10] measured the individual resistances of both the cytoplasm (282 Ω cm) and the total intracellular pathway (588 Ω cm), thus providing (assuming that these can be treated as resistors in series) a value for the resistance of the intercalated disc (306 Ω cm). This means that gap junctions, previously thought of as 'low-resistance pathways' of electrical communication between cells, actually contribute to the overall resistance to propagation in roughly equal quantity to that of the cytoplasm, despite being significantly narrower.

Combining these two observations suggests that gap junctions may be a source of slow or discontinuous propagation on a local scale — conduction is primarily in the fibre direction and will encounter resistances of significantly larger magnitude than the cytoplasm when it happens upon an intercalated disc. To clarify, the term 'discontinuous propagation' is used to signify propagation that happens with a non-uniform speed, whereby conduction is delayed as it passes through a gap junction.

The first to hypothesise this were Spach *et al.* in 1981 [141], and Fast and Kleber verified this over a decade later in 1993 [35]. The authors of [35] measured conduction delays between opposite ends of an individual cell, as well as between two similar points in neighbouring

cells. They found an overall delay of 118 μs vs. a cytoplasmic delay of 38 μs for a single chain of cells, giving a junctional delay of 80 μs, or more than half of the total conduction time. This agrees with the resistive data published by Chapman and Fry [10], and suggests that a propagating wave spends just over half of its time passing through gap junctions. Given the relative spatial scales of the cytoplasm and the gap junctions, with gap junctions being 5–10% of the length of a cell, this means that the conduction is highly discontinuous.

However, Fast and Kleber also observed that such delays were reduced when considering a multi-fibre cell preparation as opposed to a single myocyte strand — gap junctional delay was reduced so that it accounted for 22% of the total conduction time, which is still a significant amount but not as marked as the values found using a single strand. As such, we expect that the more localised the junctions are to the cell ends (*i.e.* the cells are more like a strand than a bundle), the more discontinuous the propagation will be and thus the higher likelihood of conduction block or a re-entrant arrhythmia.

With regard to the spatial distribution of gap junctions, following the initial results in [65] a more thorough investigation was performed by Spach and colleagues [142, 143]. They used previous observations regarding the distribution and number of gap junctions under certain conditions (including normal growth hypertrophy after birth) in conjunction with the electrical observations of Spach *et al.* and Fast and Kleber [36] that the form of the action potential and the underlying conduction velocity is different between adult and neonatal preparations of canine cardiac muscle. From this, they aimed to determine whether the observed differences in gap junction distribution and cell size could account for the changes in action potential and conduction velocity in both experimental and modelling situations. Their experimental data showed that gap junctions were distributed nearly uniformly in the neonatal preparations, whereas they were highly localised to the cell ends in adult tissue. In addition, neonatal cells were more regular in shape with a larger surface-area-to-volume ratio than adult cells, and were around one tenth of the volume. On the modelling front, the authors found that the action potential was more sensitive to the change of shape and size of the cells than to gap junction distribution, but that reducing coupling between cells due to fewer gap junctions overall led to an increase in discontinuous conduction.

2.3.1.2 Changes in Gap Junction Distribution in Disease

In healthy tissue, gap junctions contribute to safe propagation of the action potential. That they are preferentially located at the intercalated discs means that conduction occurs at a greater speed along the long axis of the cells, and the lateral connections help in reducing conduction delays between cells by allowing the signal to propagate in the off-fibre directions.

However, under diseased conditions the distribution of gap junctions may be altered — either such that the junctions are more evenly distributed around the cell boundary, or such that they are more localised at the cell ends. For example, in healed infarction zones the lateral connections are reduced by 75% whilst the end-to-end coupling is only reduced by 22% [85]. This was shown to increase the anisotropy of propagation that in turn leaves the tissue more susceptible to re-entrant arrhythmias. In acute ischaemia, junctions are lateralised to the cell sides [135], as is the case in the border zone of infarct tissue [7]. This situation is likely to stabilise conduction whilst simultaneously slowing it. In atrial fibrillation, both cases have been reported [101]. These changes are likely to affect the anisotropy of the tissue (that is, the ratio of conductivity between the fibre- and off-fibre directions), and as the anisotropy of cardiac tissue is an important determinant of conduction (for example, a change in anisotropy can alter the preferential direction of conduction block and re-entry from longitudinal to transverse [27, 77]), we expect that this gap junction remodelling will have a large effect on the propagation of an action potential through cardiac tissue.

As can be seen from the variety in the results above, the distribution of gap junctions in cardiac tissue is susceptible to many forms of change, leading to different outcomes. We therefore believe that gaining a quantitative insight into how these changes affect conduction will be important to fully understand the mechanism behind action potential propagation, and doing so using a rigorous mathematical technique may allow us to predict the outcome of previously unstudied junction configurations.

To complicate matters, the remodelling of gap junctions discussed above is often accompanied by a change in the expression of the main connexins that form gap junctions. These expression changes can also occur independently of remodelling, and *vice versa* — that is,

remodelling can involve either the creation of new connexins, or the relocation of existing connexins to different points around the cell membrane, or connexin expression may be reduced uniformly throughout the cell [134]. Given this, we now summarise how connexin expression levels change under various diseased states.

2.3.1.3 Connexin Expression

In cardiac myocytes, there exist three main connexin types, named for their molecular weight: Cx43, Cx40 and Cx45. The predominant of these is typically Cx43, but normal levels of expression for each connexin vary greatly from location to location within the heart, and a more thorough explanation of this can be found in [135]. In diseased conditions, connexin expression is typically downregulated. In atrial fibrillation and ventricular hypertrophy, Cx43 levels are reduced by around 50% [132]. This is also the case in ventricular arrhythmia, but here expression levels are reduced in a heterogeneous manner in the tissue, which contributes heavily to abnormal propagation [46]. In ventricular remodelling, Cx43 levels are reduced by 30%, with accompanying fibrosis [26]. In ischaemia and infarction, all connexin levels are reduced [30] by up to 50%.

Therefore, we can say that downregulation of connexin expression is a fairly general feature of cardiac disease. Combined with remodelling of gap junctions, they can be both pro- and anti-arrhythmic. It has also been observed that there is a linear relationship between connexin expression and overall intercellular gap junction conductivity [30, 90]. This suggests that we can model changes in connexin expression by appropriately modifying an overall gap junction conductivity, which will reduce the complexity of the system as we do not need to consider individual connexins, but rather the percentage of connexins expressed as a proportion of some baseline value representing a physiologically healthy subject. For a comprehensive review of both gap junction remodelling and connexin expression in diseased myocardium, see [134].

As well as gap junction number and distribution, the geometry of the tissue itself is equally important in determining how the action potential propagates through cardiac muscle, and

we will now discuss the important geometric features that contribute to conduction.

2.3.1.4 Tissue Geometry

Cardiac tissue is a complex structure, and the geometrical properties can be considered on various spatial scales. For our purposes, we look at the changes at the level of small regions of tissue (ignoring, for example, varying fibre orientation over larger length scales or the individual forms of tissue comprising the extracellular space), and identify three key ways in which the tissue geometry is important in determining action potential propagation.

The first major feature of tissue geometry that affects conduction is the shape and size of the cells. In many studies, gap junctions were assumed to be of zero length and thus their impact was not considered. The previously mentioned work of Spach *et al.* [143] found that cell size was more important in determining conduction velocities than the distribution of gap junctions, with conduction velocity increasing for longer cells. The work of Ghaly *et al.* [43] came to a similar conclusion, with a reduction in cell length from 100 μm to 80 μm causing a 10% drop in conduction velocity. In addition, McIntyre *et al.* [91] found a correlation between cell diameter and conduction velocity. These effects must surely be combined with those of junction remodelling and connexin expression in certain conditions, most notably hypertrophy, to accurately model diseased cardiac tissue.

Secondly, the brick-wall structure of the cells when stacked in three dimensions has a marked effect on propagation. As found in [35], the delay in conduction between cells is dependent on the number of adjacent cells that are connected to any given myocyte, and this number will be location-dependent. In the Purkinje fibres, for example, the tissue geometry is more cable-like which leads to fast propagation, but increases susceptibility to conduction block [24]. In healed infarcted tissue, cells are connected to only six others on average compared to nine or more in healthy tissue [85], which reduces conduction velocity, especially in transverse directions.

Lastly, the extracellular material surrounding the myocytes is thought to influence conduction. This phenomenon, known as ephaptic coupling, hypothesises that the narrow

extracellular cleft between cells permits drastic changes in ionic concentrations that vary the electrical potential rapidly enough to conduct an electrical signal from one cell to the next [144, 167]. As the extracellular space can change (for example, volume changes, increase in fibroblasts, shape remodelling) under conditions such as ischaemia [92] and heart failure [33], it should be considered in a model of propagation.

We have seen that there are various factors likely to influence conduction of an action potential in cardiac tissue, and how they may change during disease. We wish to be able to relate this to the observed changes in conduction, to attempt to understand how changes in tissue geometry and gap junction structure, location, or function drive changes in action potential propagation. As such, we will now outline how action potential propagation is affected by those diseased conditions for which we have some knowledge of associated changes in gap junction properties.

2.3.2 Action Potential Propagation in Common Clinical Conditions

We have seen that for a given cardiac disease there are a number of changes in tissue geometry, gap junction distribution, and connexin expression that can affect action potential propagation. Whilst we can theorise as to the contribution of a single effect (for example, a uniform reduction in connexin expression should lead to reduced propagation) the combined effects are trickier to unravel. In order to attempt to do this, we must review how conduction of the action potential is affected under such diseased conditions, and then relate this to the combination of changes in gap junction location, connexin expression, and tissue geometry that are simultaneously observed.

In healthy canine tissue, there are observed differences in conduction velocity between adult cells with more localised gap junctions (50 cm/s for longitudinal propagation and 17 cm/s for transverse propagation) and neonatal cells with a more uniform spread (33 cm/s during longitudinal propagation and 12 cm/s during transverse propagation) [143]. Considering acute ischaemia, longitudinal propagation conduction velocities of 25 cm/s were observed along with micro-re-entry in 105 of 139 cases considered in the study by de Bakker *et*

al. [25]. In regions where transverse connections were vastly reduced, values as high as 120 cm/s for longitudinal propagation were found with accompanying low values of 10 cm/s for transverse propagation [142]. When gap junctions were blocked and cells thus uncoupled, transverse block occurred after 28 minutes and longitudinal block after 44 min [29], showing that conduction block preferentially occurred in the off-fibre direction. However, conduction velocity was reduced to very low levels (0.26 cm/s) before block occurred in a different study [122], and this ultra-slow conduction is known to be a key ingredient in arrhythmogenesis. On this front, it has been found that simply reducing the expression levels of Cx43 can have a significant effect on conduction velocity [148] or no effect at all [98], which confirms the notion that it is a combination of factors driving the conduction block and the reduction in conduction velocity seen in disease. Looking at atrial fibrillation, longitudinal propagation speeds were unchanged from healthy tissue and transverse propagation speeds of 30 cm/s were observed [132], showing a marked increase in lateral propagation.

At this point, it is worth distinguishing between atrial and ventricular fibrillation, and discussing the importance of their study. Ventricular fibrillation is an uncoordinated contraction of the ventricular muscle cells. It is the most common arrhythmia found in those patients with cardiac arrests, and if it persists for more than a few seconds it will likely lead to asystole and sudden cardiac death [159]. Treatment is usually provided in the form of a defibrillatory shock [8]. As such, both the mechanism that promotes and sustains ventricular fibrillation, and that which causes a defibrillatory shock to reverse the arrhythmia, are important topics in cardiac research. A large body of work that focuses on various aspects of this from a mathematical perspective has emerged in the last two decades, for example the paper of Keener showing how an excitable cable can be directly activated or defibrillated [74], that of Trayanova reviewing the state of knowledge in the area as of 2005 [153], and that of ten Tusscher *et al.* [145] that combined both simulations and experimental findings to investigate the organisation of ventricular fibrillation.

Somewhat conversely, atrial fibrillation typically presents with moderate symptoms such as tachycardia, or is asymptomatic from the perspective of the patient [45]. A primary reason for this is that the slow conduction velocity within the atrioventricular node reduces and

stabilises the rate at which the fast and disjointed electrical signals coming from the atria reach the ventricular tissue — without this feature, atrial fibrillation would lead directly to ventricular tachycardia and potentially to ventricular fibrillation [76]. Atrial fibrillation is the most common chronic arrhythmia, affecting somewhere between 8–14 % of those over eighty [168], and is often diagnosed using an electrocardiogram. It is treated either using drugs that anticoagulate or that control the rate and rhythm of the heart, or by cardioversion [45]. Given this, a major focus when modelling atrial fibrillation is the effect of drug action on the resulting simulated electrocardiogram [68]. A number of components are required for this, beginning with a single-cell model appropriate for atrial cells such as that of Courtemanche *et al.* [22], a tissue model that accurately captures the complex anatomy found in the atria [52], and an understanding of how to model specific diseased states [11]. As can be seen from the cited works and associated references within, steady progress continues to be made towards a better understanding of the onset and treatment of atrial fibrillation from a mathematical perspective.

Overall, a variety of modifications occur in conduction speed and conduction block properties during disease, and these may be due to changes in gap junction expression or distribution.

2.3.3 Conclusion

The variety of methods by which conduction is altered in disease drives researchers to create a model that explains the observed behaviour. We have discussed the key role that gap junctions play in conduction, and how changes in the distribution and number of gap junctions under diseased conditions can contribute to conduction problems. We have also discussed how tissue geometry affects conduction properties. *As such, we believe that a model of diseased cardiac cells should include gap junctions and a realistic cell geometry.*

On a more general level there are a number of open questions that arise when considering the mathematical modelling of cardiac action potential propagation under diseased conditions, such as: how should the effect of gap junctions be included in a model; how can we include

the effects of cell geometry; and can we predict the response of the system to the onset of a diseased state?

To investigate these questions, we have created a multi-cell model of cardiac electrophysiology in which we can rigorously take into account changes in gap junction properties and cell geometry. In the following chapter, we will describe the mathematical modelling of cell- and tissue-level cardiac electrophysiology in order to give a background understanding of the concepts that underpin the creation of some common models of cardiac electrophysiology. This will allow us to go into more detail regarding the specifics of our model in later chapters. We will conclude Chapter 3 with a description of our research questions and a brief overview of how this thesis attempts to answer those questions.

Chapter 3

Review of Tissue-Level Models and Research Aims

Contents

In this chapter we present an overview of discrete and continuum models of tissue-level cardiac electrophysiology, as well as the mathematical techniques used in the process of deriving the models used in this thesis. We then identify some key gaps in the current literature relating to tissue-level cardiac electrophysiological modelling and finally pose research questions that attempt to address these gaps.

In Section 3.1 we give a brief introduction to tissue-level modelling of cardiac cells and outline a short history of how gap junctions have been included in cardiac electrophysiology models. We follow that in Section 3.2 by discussing the creation of continuum models, paying closer attention to the mathematical technique of homogenisation used to derive the models in Section 3.3. In Section 3.4 we outline the key assumptions made in the continuum model derivation, along with possible limitations of the approach. We then summarise how gap junctions have been included in continuum cardiac electrophysiology models, and present a number of research questions that we wish to answer in Section 3.5, along with an outline of how we propose to answer these questions.

3.1 Tissue-Level Modelling of Cardiac Electrophysiology Using Discrete Cells

Whilst single-cell models are able to predict the temporal form of an action potential, they are insufficient to describe its propagation from one cell to another and, more importantly, how an action potential propagates through cardiac tissue. To study this phenomenon it is necessary to simultaneously model a large number of cells and to include a mechanism that electrically connects them. We will now discuss how the physiology behind this has been interpreted to create multi-cell models of cardiac electrophysiology.

3.1.1 The Cable Equation

The origins of multi-cell modelling lie with the core conductor (or cable) model of Herman, developed in 1879. Classically, the electrical properties of a single active nerve fibre in an infinite medium were described using these equations, for example by Cole and Hodgkin in the 1930s [20]. This model assumes that a fibre is separated from an infinite external medium by a membrane. The fibre and external medium have individual resistances associated with them, as does the membrane. Considering the associated change in potential difference ΔV over a distance Δx from an injected current using Ohm's law [75] gives us

$$\Delta V = -ir\Delta x,$$

where i is the current applied and r is the resistance per unit area of the fibre. The current escaping through the membrane per unit area, i_m, is related to the change in current within the fibre by

$$\Delta i = -i_m \Delta x,$$

and can be calculated from Kirchhoff's law by treating the cell membrane as a resistor-capacitor, giving

$$i_m = c_m \frac{\partial V}{\partial t} + \frac{V}{r_m},$$

where c_m and r_m are the capacitance and resistance of the membrane respectively. Combining the first two equations and taking the limit as $\Delta x \to 0$, the final 'cable equation' is

$$\frac{1}{r}\frac{\partial^2 V}{\partial x^2} = c_m \frac{\partial V}{\partial t} + \frac{V}{r_m}. \tag{3.1}$$

However, the equation above cannot capture the active properties of a cell membrane of a

cardiac cell — driven by the complex network of ion channels and gates discussed in Section 2.2. The introduction of the Hodgkin-Huxley model [63] provided a potential framework for describing the membrane more accurately than the simple resistor form outlined above, and indeed this was done for a single nerve fibre by Clark and Plonsey in 1966 [12], who modelled electrical flow in a single fibre that was situated in an external medium, with the two domains separated by an active membrane with Hodgkin-Huxley nonlinear components. This formulation was adapted to model a Purkinje strand by Hellam and Studt in 1974 [54] and provides a basis for modelling cell coupling either through gap junctions or by other means. Since that time, cell-to-cell coupling via gap junctions has been included in numerous cardiac electrophysiology models, and we will now give a history of these models.

3.1.2 Coupling Cells via Gap Junctions

One of the first papers to include the effect of gap junctions in a model of cardiac cells was that of Diaz *et al.* in 1983 [31]. They used a simple one-dimensional cable model with an active membrane dictated by Beeler-Reuter kinetics and modelled gap junctions as resistors of zero length between individual cells (see Figure 3.1). They noted that changing the gap junction resistance had a much larger effect on the calculated conduction velocity than one would expect from a classic inverse square root relationship (see Figure 3.2), suggesting that gap junctions play a significant role in determining the conduction velocity of the action potential, one that is greater than just reducing conduction velocity by the amount predicted owing to their reduced conductivity. Specifically, they noticed that propagation inside the cell is ten times faster than propagation inside the gap junction even for normal values of gap junction resistance. However, they mention that such starkly discontinuous propagation is likely to be overestimated by their model and will be smoothed when considering a multi-fibre preparation of cells, owing to the brick-wall structure of cardiac cell sheets and the accompanying side-to-side gap junction connections.

In the subsequent years, a number of papers also looked at the effect of gap junctions on propagation in a cable-like model. In 1986, Plonsey and Barr [115, 116] used a passive version of the above model (in the sense that the cell membrane is represented as a resistor of

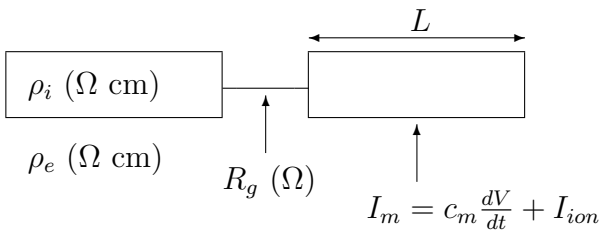

Figure 3.1: *A simple method to model gap junctions connecting one cell to another, as used in [31]. The junction is represented as a resistor of zero length and resistance R_g, and cells of length L and resistivity ρ_i are connected into a fibre by junctional units. The extracellular space is modelled as infinite and of resistivity ρ_e, with the two spaces connected by cell membrane kinetics (I_m).*

constant resistance) to look at the effects of changing gap junction resistance on conduction velocity. They computed the numerical solution for the model taking zero, normal and high values for this resistance. When they used zero resistivity the model showed the behaviour expected of a continuous cable; when a physiologically normal value of resistivity was used there were perceptible fluctuations in potential within each cell; and when a high value of resistivity was used the change in voltage was primarily from intra-cell fluctuations caused by gap junction resistivity and not the overall continuous behaviour. This showed that the behaviour of the system was dominated by changes in gap junction resistance. The 1987 work by Henriquez and Plonsey [55] returned to using an active membrane, and compared the conduction velocity calculated in both discrete and continuum variations of the system, where the continuum model was obtained by computing an effective axial resistance that was the sum of the individual contributions from the cytoplasm and gap junction (in an analogy of the homogenisation process for the heat equations to be described in Section 3.3). They found that the delay in propagation across the gap junction was significant, with overall propagation slower in the discrete case than in the continuum case. This matches the observation in Diaz *et al.* [31] that changes in gap junction resistance gave a larger effect on conduction velocity than an inverse square relationship — the continuum model of Henriquez and Plonsey [55] essentially assumes this property of the gap junction in its calculation of the effective resistance. In addition, the authors found that this discrepancy between conduction velocities was greater when faster membrane kinetics (as a result of simulating using a higher temperature) were used, hinting at a possible relationship between

the steepness of the upstroke of the action potential and the applicability of a continuum model. This is something that we will consider in this thesis.

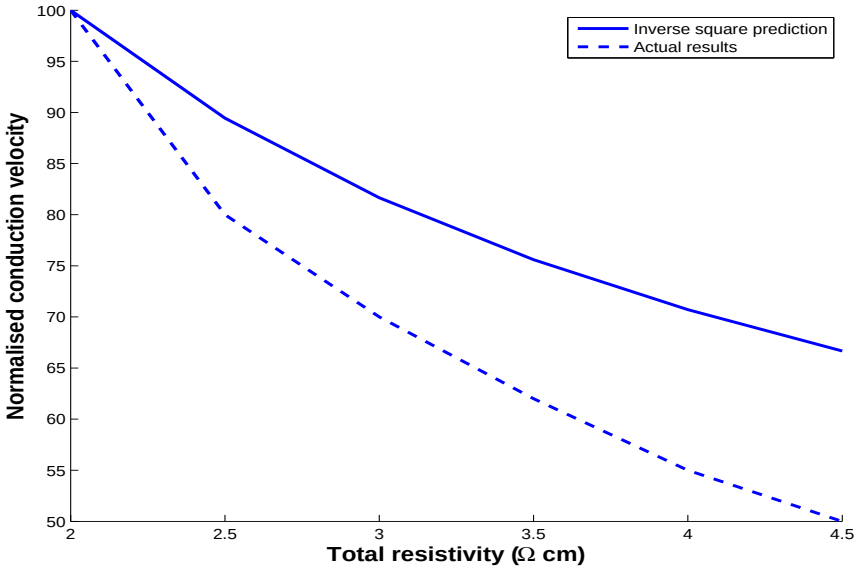

Figure 3.2: *A reproduction of Figure 3 in Diaz* et al. *[31]. The dotted line represents the conduction velocity observed by increasing gap junction resistivity whilst keeping cytoplasmic resistivity constant. The solid line represents the expected outcome of reducing total resistivity by the same amount using an inverse square root relationship.*

Further work along this strand was carried out in 1997 by Shaw and Rudy [136], who considered continuum and discrete formulations of the one-dimensional cable model to study the effect of both gap junction resistance changes and Na^+ and Ca^{2+} current changes on propagation. They noted that conduction velocity decreased monotonically with increasing gap junction resistance, and also qualitatively showed the increased delay in cell-to-cell propagation in such a situation. In addition, they found a relationship between the maximum upstroke velocity of the action potential and gap junction resistance, which in their words served to 'establish the necessity of using a discontinuous fibre model for simulating propagation in multi-cellular myocardial tissue'. A more detailed model of gap junctions appeared in the work of Spach *et al.* in 2000 [143]. They considered a two-dimensional system in which no extracellular space was present — cells were connected to one another through gap junctions across their membrane which were distributed in either 'adult' (concentrated in end-to-end connections) or 'neonatal' (uniformly spread) configurations. They also varied the size of cells to take either typical adult or typical neonatal values, and found that

an increase in cell size on its own brought an increase in the discontinuity of propagation, as did reducing gap junction conductivity.

More recently, the work of Spach *et al.* has been extended to consider how gap junctions affect propagation in an idealised situation in which the extracellular space is not modelled and is assumed to have infinite conductivity. The paper of Hubbard *et al.* [67] looked at how four factors affected propagation: the brick-wall structure of cells; jutting at cell ends; gap junction distribution; and structural discontinuities. The major result concerning gap junctions was that the dramatic reduction of conduction velocity and eventual conduction block (*i.e.* failure of the electrical signal to propagate through some part of the tissue) seen in a uniform model of cells was much smaller when using a brick-wall model with cell jutting, suggesting that these histological features of cardiac cells are required in order to accurately study propagation under conditions of low gap junction expression, and may play important roles when considering conditions of low gap junction coupling strength as they are beneficial to conduction.

3.1.3 Summary

From the biological research mentioned in Chapter 2 and the review of mathematical models in this section, it seems likely that the effect of gap junctions must be included in a model of cardiac electrophysiology, whether explicitly or otherwise. Even under normal physiological conditions they have a profound effect on the form of the spatially propagating action potential, and their impact is magnified when the coupling strength of the gap junctions is reduced, such as is observed under diseased conditions such as ischaemia and atrial fibrillation when the resistance of gap junctions is higher.

Given this, the strength of using a discrete model for simulations of action potential propagation in cardiac tissue is that one can explicitly include gap junctions, and more generally the details of the microstructure of the tissue, into the model. This gives more accurate results and allows us to see how changing these properties affects conduction, which we may then relate to what is observed under diseased conditions. However, discrete modelling is

computationally intractable even when considering small regions of tissue and using modern computers due to the complexity of the system. As such, many have modelled cardiac tissue as a continuum, which results in a more tractable system that has no detail of the cell microstructure and indeed no concept of an individual cell, but instead consists of a piece of tissue with certain properties. We will now give details of some of these continuum systems and of studies performed using them.

3.2 Continuum Models of Cardiac Electrophysiology: the Bidomain and Monodomain Equations

One of the first attempts at creating a continuum model was presented by Leslie Tung in 1978 [155]. He considered an intertwined network of homogeneous and isotropic domains, representing at once both cells and extracellular material, coupled by a passive, resistive membrane. The result was the initial formulation of the bidomain equations, which is the continuum model of cardiac tissue most commonly used today. However, Tung's macroscopic formulation was not connected to the microscopic properties of the cells such as their shape, size or individual conductivity. This relationship had to wait until the advent of formal homogenisation methods, to which we will present an introduction in Section 3.3.

A full derivation of the bidomain equations using a homogenisation technique will be presented in Chapter 4, but we will now state the equations for reference. For a region of cardiac tissue, the bidomain equations govern the intracellular and extracellular potentials ϕ_i and ϕ_e, or equivalently ϕ_e and the transmembrane potential $V = \phi_i - \phi_e$ as follows:

$$\chi c_m \frac{\partial V}{\partial t} = \nabla_{\mathbf{x}} \cdot (\Sigma_i \nabla_{\mathbf{x}} (V + \phi_e)) - \chi I_{ion}, \tag{3.2a}$$

$$\nabla_{\mathbf{x}} \cdot ((\Sigma_i + \Sigma_e) \nabla_{\mathbf{x}} \phi_e + \Sigma_i \nabla_{\mathbf{x}} V) = 0, \tag{3.2b}$$

where Σ_i and Σ_e are the intracellular and extracellular homogenised conductivity tensors, χ is the surface-area-to-volume ratio, c_m is the membrane capacitance per unit area and I_{ion} is the ionic current per unit surface area. Appropriate boundary conditions representing

zero flux across the tissue surface are

$$-(\Sigma_i \nabla_{\mathbf{x}}(V + \phi_e)) \cdot \mathbf{n} = 0,$$
$$(\Sigma_e \nabla_{\mathbf{x}} \phi_e) \cdot \mathbf{n} = 0,$$

where $\mathbf{n}$ is the outward pointing normal vector to the tissue. A commonly-used reduction of the bidomain model is the monodomain model, which is of reduced complexity and has, amongst other things, a conduction velocity that can be analytically derived from the conductivity of the system. The monodomain formulation of the bidomain equations arises from assuming that both intracellular and extracellular domains have equal anisotropy ratios, which are defined as the ratio between fibre direction and off-fibre direction conductivities. This assumption is equivalent to taking $\Sigma_i \propto \Sigma_e$. In many cases, the two models can give very similar predictions [118], but in others the monodomain model is not suitable [21]. Using the same terminology as for the bidomain equations, the monodomain equation is

$$\nabla_{\mathbf{x}} \cdot (\Sigma \nabla_{\mathbf{x}} V) = \chi \left(c_m \frac{\partial V}{\partial t} + I_{\text{ion}} \right), \tag{3.3}$$

where Σ is the system's bulk conductivity tensor and is given by $\Sigma_i(\Sigma_i + \Sigma_e)^{-1}\Sigma_e$.

In the following section we will give an overview of the studies performed both using the bidomain equations to study clinical phenomena and in terms of enhancements to the numerical implementations of the equations.

3.2.1 Examples of Studies Using the Bidomain Equations

The bidomain equations have been used to study a wide range of phenomena within cardiac electrophysiology. In the years following the initial formulation of the equations the focus was purely on computing the potential distribution and current flow in a slab of cardiac tissue [56–58], and modelling the effects of anisotropy [114,133]. These studies demonstrated the viability of using the bidomain equations to study propagation through cardiac tissue.

In the 1990s the model was used to study defibrillation, and estimates for the direct stimulus threshold and defibrillatory threshold were obtained that closely agreed with experimental findings [72, 74, 119].

More recently, the bidomain equations have been used to study more detailed experimental phenomena. The work of Plank *et al.* [113] studied re-entry patterns in a three-dimensional bidomain slab, finding that defibrillation of the tissue depended on both the degree of organisation of the re-entry (with higher levels of disorganisation requiring a larger strength of shock to defibrillate), and on the level of small-scale conductivity fluctuations (with more fluctuation leading to a smaller shock strength required). Lastly, there is a large body of work that considers the onset, diagnosis and treatment of arrhythmias using the bidomain equations — for a review in this area, see [68]. Other areas studied using the bidomain equations include ischaemia [32], ion channel block [94] and conduction block [66].

Concurrently, a great deal of work has been done on the numerical techniques used to solve the bidomain equations. For example, a number of studies [39–41, 71] used asymptotic analysis techniques to approximate the bidomain equations by the eikonal equations [131], which are another class of equations used to represent the solution to wave propagation problems. These equations were deemed suitable for studying phenomena such as the effect of fibre rotation on propagation spread, but did not incorporate an ionic model of action potential spread and as such were of limited use in a broader context of cardiac phenomena. Spectral techniques were also used [150–152] to create an approximation to the solution of the bidomain equations in one dimension, allowing the authors to investigate the effect of anisotropy on membrane potential. In more recent years the focus has shifted towards the computational techniques used to approximate the solution to the bidomain equations, with a number of research groups creating large software packages to solve the bidomain equations on increasingly complex and realistic geometries using increasingly detailed single-cell models. One example of such software is the Cardiac Arrhythmia Research Package (CARP), which uses a finite element method [120] to solve the bidomain equations as well as other physiological problems. Another example is the Cancer, Heart and Soft Tissue Environment (Chaste) [93] which, as well as incorporating the solution methods mentioned

previously, put an emphasis on contemporary software development practices such as Agile and Test-Driven Development [111,112]. Members of the research group have also provided methods to increase the efficiency of the numerical solution of the bidomain equations by calculating certain aspects of the solution on a coarser mesh where applicable [164,165], and have considered the accuracy of the resulting solution when comparing different methods for integrating the ionic current equations [107].

The combined effect of the research above is that we are able to approximate the solution to the bidomain equations using efficient computational techniques and accurate numerical methods on generalised geometries with any single-cell model we wish. Whilst the speed of solution is still too slow to consider real-time modelling, a great deal of valuable research has been done using the bidomain equations.

In order to derive this continuum model of cardiac electrophysiology from an underlying geometry consisting of discrete cells, approximations must be made and mathematical techniques employed. For this we rely on homogenisation, a multiple-scales method used to derive the 'average' behaviour of a discrete system. We will now present an overview of homogenisation and its application to cardiac electrophysiology.

3.3 The Link Between Discrete and Continuum Models: Homogenisation

A limitation of early tissue-level models of cardiac electrophysiology was the lack of computational tractability of the numerical approximation to the solution of the governing equations. The coupling of many cells together, however simply, caused the number of simultaneous equations required to be solved to increase beyond the computing power of the time. For example, in the simple one-dimensional cable model of Plonsey and Barr [115], each gap junction was modelled individually and this resulted in a much larger number of governing equations than could be solved were the model to be extended into two or three spatial dimensions. Additionally, modelling the active properties of the cell membrane gen-

erally means that an analytic solution is not achievable, as does modelling the cell geometry using realistic or even most idealised cell shapes.

To overcome these difficulties, as well as provide more analytic tractability and simplification to the model, we employed a rigorous mathematical technique known as homogenisation. The method, introduced by Bensoussan [6] amongst others, allows large-scale trends to be extrapolated from predominately periodic smaller scale behaviour. It relies on the problem in question being naturally defined on two scales — the macroscale and the microscale — and makes the key assumption that these two scales can be treated as independent. The variations in the solution on the microscale are taken to be small when compared to the macroscale behaviour, with the fine structural details of the microscale 'averaged' and incorporated into a problem governing the macroscale behaviour. For a review of homogenisation from a mathematical perspective, see [34].

3.3.1 An Introduction to Homogenisation

Homogenisation has been used in a large variety of fields outside cardiac electrophysiology, including astronomy [117], nonlinear wave theory [124], cell dynamics [99] and blood flow in the vasculature [138] and is recognised as a versatile and useful tool for multiscale problems. In this section we present a simple example of homogenisation, and will provide the full homogenisation procedure as applied to cardiac electrophysiology in Section 4.1.

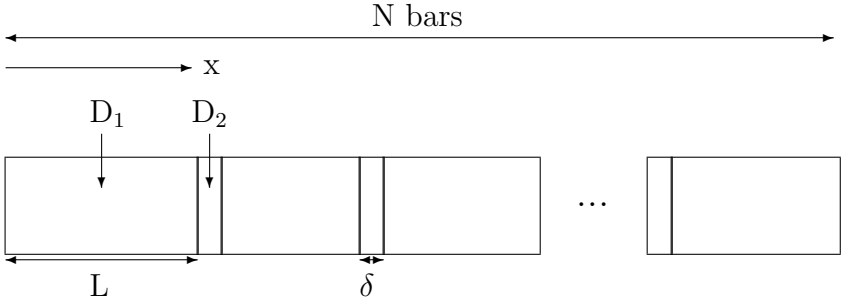

Figure 3.3: *A series of metal bars connected by thin sections of glue. The conductivities (D_1, D_2) of the two media are different, and the bars are arranged periodically, which allows us to perform an asymptotic analysis of the governing equation for heat transfer.*

The example of homogenisation outlined here considers heat transfer in one dimension

through material consisting of two media: one well conducting (*e.g.* a metal bar); and the other poorly conducting (*e.g.* glue). These are arranged periodically as shown in Figure 3.3. Each bar has length L and conductivity D_1, and each glue section is of length δ with conductivity D_2, where we set $L + \delta = 1$ for simplicity. Assuming the transfer of heat T is in only one spatial dimension, it is governed by the heat equation [75]

$$\frac{\partial T}{\partial t} = \frac{\partial}{\partial x}\left(D(x)\frac{\partial T}{\partial x}\right),$$

where $D(x)$ takes the value D_1 or D_2 depending on whether x is in the bar or the glue. Natural interface conditions at points where the conductivity is discontinuous are that the temperature T and flux of heat $-D(x)\frac{\partial T}{\partial x}$ are continuous across the interfaces. The bars are held at temperatures T_0 and T_1 at either end of the domain. We then assume that the temperature varies over lengthscales much greater than that of an individual bar-and-glue unit, with only small variations over the lengthscale of a single unit. Mathematically, we do this by introducing another variable

$$z = \frac{x}{\epsilon},$$

where x is the microscale coordinate, z is the macroscale coordinate and $\epsilon = (L + \delta)/L_{sol}$ is the ratio between the length of our individual subunit and the lengthscale of the solution to the governing equation, L_{sol}. We then treat these two variables as independent, which is equivalent to assuming that $\epsilon \ll 1$. Applying the chain rule, so that the derivative $\frac{\partial}{\partial x}$ changes to $\frac{\partial}{\partial x} + \frac{1}{\epsilon}\frac{\partial}{\partial z}$, the governing equation becomes

$$\frac{\partial T}{\partial t} = \frac{\partial}{\partial x}\left(D(z)\left(\frac{\partial T}{\partial x} + \frac{1}{\epsilon}\frac{\partial T}{\partial z}\right)\right) + \frac{1}{\epsilon}\frac{\partial}{\partial z}\left(D(z)\left(\frac{\partial T}{\partial x} + \frac{1}{\epsilon}\frac{\partial T}{\partial z}\right)\right). \tag{3.4}$$

We then seek an asymptotic solution to Equation (3.4) of the form

$$T = T_0(x,t) + \epsilon T_1(x,z,t) + \epsilon^2 T_2(x,z,t) + \ldots, \tag{3.5}$$

where T_1, T_2, *etc.* are periodic in z with zero mean. Note that, as the diffusion coefficient is periodic of order one, we have that $D(x,z) \simeq D(z)$. We then substitute Equation (3.5) into Equation (3.4) and collect like powers of ϵ. At the order of ϵ^{-1} we have

$$\frac{\partial}{\partial z}\left(D(z)\left(\frac{\partial T_0}{\partial x}+\frac{\partial T_1}{\partial z}\right)\right)=0, \tag{3.6}$$

which can be solved by writing

$$T_1 = -W(z)\frac{\partial T_0}{\partial x}+c, \tag{3.7}$$

where c is a constant that can be set to zero without loss of generality. The periodic function $W(z)$, which determines the small-scale structure of the true solution and will be interpreted from a physiological perspective in Chapter 4, is known as a *weight function*. If we substitute the above form of T_1 into Equation (3.6) and use the fact that W has zero mean in z, we see that the weight function satisfies

$$\frac{\mathrm{d}W}{\mathrm{d}z}=\frac{\bar{D}}{D(z)}-1, \tag{3.8}$$

where $\bar{D}=1/\int_0^1(1/D(z))\,\mathrm{d}z$. At the next order, ϵ^0, we have

$$\frac{\partial T_0}{\partial t}=\frac{\partial}{\partial x}\left(D(z)\left(\frac{\partial T_0}{\partial x}+\frac{\partial T_1}{\partial z}\right)\right)+\frac{\partial}{\partial z}\left(D(z)\left(\frac{\partial T_1}{\partial x}+\frac{\partial T_2}{\partial z}\right)\right). \tag{3.9}$$

Integrating Equation (3.9) with respect to z, which runs between 0 and 1 over a single unit by definition, and using the zero mean property of both T_1 and T_2 gives

$$\begin{aligned}\frac{\partial T_0}{\partial t} &= \int_0^1 \frac{\partial}{\partial x}\left(D(z)\left(\frac{\partial T_1}{\partial z}+\frac{\partial T_0}{\partial x}\right)\right)\mathrm{d}z \\ &= \bar{D}\frac{\partial^2 T_0}{\partial x^2}.\end{aligned}$$

This shows us that, to leading order in ϵ, the heat transfer satisfies a homogenised heat equation where the homogenised conductivity is given by $\bar{D}$. A similar approach can be applied to cardiac electrophysiology, and we will now briefly outline this. It relies on the same assumption as in the simple case described above, that the parameter ϵ, which for cardiac tissue will be the ratio of the length of a cardiac cell to the length of the typical solution to the governing equations, is small. This assumption is not necessarily true in all circumstances, as we will later explain.

3.3.2 Homogenisation Applied to Cardiac Electrophysiology

To the best of our knowledge, the first use of homogenisation in a model of cardiac electrophysiology came in the work of Krassowska *et al.* [81], who considered a one-dimensional cable model of an infinite cardiac fibre. In this model, each cell was coupled to the next by a junctional element of specified resistivity that was assumed to be part of the intracellular domain. As such, the intracellular resistivity was given by a periodic function of length along the fibre. The cell membrane was treated as passive, with capacitive properties ignored. Whilst we refer the reader to the paper in question for a detailed explanation of the model, it is worth noting that the derived macroscale equation for intracellular potential was a cable equation governed by a homogenised conductivity tensor obtained using the same equations presented in detail in Chapter 4 for a three-dimensional, active model of cardiac tissue. This tensor takes into account the microstructure of the domain — initially the authors only incorporated the form of gap junctions, but in future work they included the shape of the cell boundary [78, 80].

Following this, the authors extended their simple one-dimensional model to a three-dimensional

model [79] in which cardiac cells were treated as hexagonally packed cylinders, connected both end-to-end and side-to-side by thin gap junctions. The model considered the steady-state solution, with the whole domain consisting of one medium of periodically varying conductivity (*i.e.* the intracellular space, extracellular space, cell membrane and gap junctions each have their own conductivity). The representation of the problem after homogenisation is equivalent to a monodomain model — a major limitation of which being its restriction to passive, sub-threshold phenomena as opposed to accurately simulating active membrane kinetics.

However, the paper still presented some novel applications of homogenisation to cardiac tissue. The asymptotic analysis demonstrated that the macroscale equations were modified only such that the conductivity moved from a periodic spatial function to a homogenised tensor. This tensor took account of the conductivity profiles of all four subsets of the medium, including their specific geometry. In addition, they related the first-order microscale behaviour of the transmembrane potential to both the derivative of the macroscale problem, and the weight functions that were used to determine the homogenised conductivity tensors. These weight functions will be explored in more detail in Chapter 4.

The first attempt at deriving a continuum model of cardiac electrophysiology that allowed for active membrane processes had to wait until 1993, when Neu and Krassowska [102] modified the microscopic, or discrete, formulation of the problem. They treated potentials inside and outside the cell separately, each governed by Laplace's equation, with the active electrical properties of the membrane represented by the boundary conditions between the two regions. The homogenisation process derived what are known today as the bidomain equations, of which the previous incarnation represents the degenerate case of autonomous processes. However, the calculation of the weight functions (and thus the homogenised conductivity tensors) assumed the cytoplasm to be a homogeneous medium, thus eliminating the presence of gap junctions as distinct objects in the model. In addition, a number of restrictions were placed upon the validity of the derivation — most relevant to our work is that studies must occur on a lengthscale of around 30 individual cardiac cells as this was calculated to be the minimum (or liminal) length of the medium under consideration in

order to accurately represent the initiation of wave propagation. This is greater than the lengthscale over which a typical action potential upstroke passes even when not modelling gap junctions (see Figure 3.4). As we have seen from Diaz *et al.* [31] and other work, propagation is significantly slower inside the gap junction than in the cytoplasm. As such, the lengthscale over which the solution varies will be correspondingly reduced inside the gap junction, which puts further pressure on the lengthscale assumption made by Neu and Krassowska.

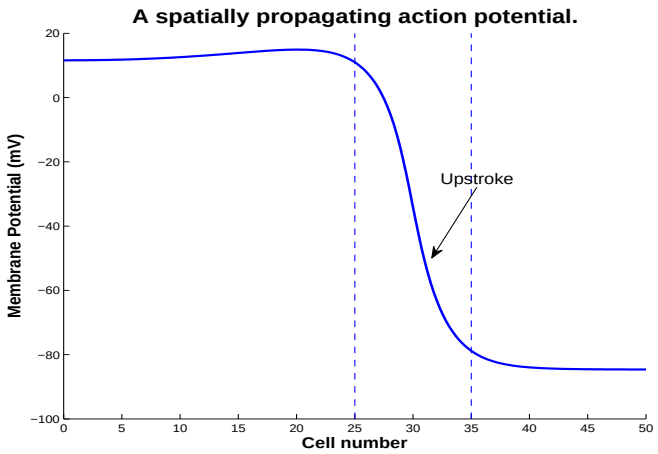

Figure 3.4: *A spatially propagating action potential using a Beeler-Reuter model for membrane kinetics [5] and a discrete geometry. Conductivities are taken from [10] and gap junctions are not modelled. We can see from the figure that the vast majority of the change in potential occurs over a lengthscale of* $\simeq$ *10 cells.*

Keener and Panfilov made a modification of the derivation given in Neu and Krassowska in 1996 [72]. Their method takes into account the microstructure of cardiac tissue in a more rigorous manner. The premise of the paper was to study defibrillation of cardiac tissue, noting that a one-dimensional homogeneous bidomain cannot be directly defibrillated by a single local stimulus as the transmembrane potential dies off exponentially from the stimulus site and thus no transmembrane current is generated in the interior. The authors presented their view as to why this phenomenon was observed in simulations, surmising that inhomogeneities of resistance within the tissue, for example gap junctions, must be included in a continuum model to allow for defibrillation. The specific incorporation of the microstructure came into effect in the form of the ionic current that the authors adapted to include a rotation matrix representing the local orientation of each cell and incorporating

the previously mentioned weight functions. As in Neu and Krassowska [102], the calculation of these weight functions assumes a homogeneous cytoplasm and thus does not explicitly take into account the presence of gap junctions. However, the change from the previous model corrected an error in the derivation of the bidomain equations given by Neu and Krassowska that played a significant role during defibrillation, and the authors were able to defibrillate both two- and three-dimensional domains using a simplification of their derived model that incorporated gap junctions as resistive units.

More recently, a paper by Richardson and Chapman [121] re-derived the bidomain equations from first principles, systematically taking into account changing cell orientation — both in terms of overall fibre direction and in terms of the deformations to a cell during a heartbeat. This was partly to correct a minor error found in the work of Keener and Panfilov concerning the co-ordinate transformation used. In the final governing equations, the weight functions and homogenised conductivity tensors depend on the deformation matrix of this co-ordinate transformation. However, once more the weight functions ignored the presence of intracellular resistive inhomogeneities.

Following a slightly different path, two recent papers by Hand *et al.* [50,51] provide an alternative formulation for the homogenised conductivity tensors. Whilst they use a specification of the bidomain equations that does not take into account the cellular microstructure in the ionic current formulation, they introduce the effect of gap junctions into the model by treating them as resistive units and calculating the steady-state potential of the discrete model. From this, the homogenised conductivity tensors can be derived, which in turn are related to the weight functions (which themselves are modified to incorporate gap junctions as resistors). However, all this was done for a uniform periodic structure with brick-shaped cells either aligned with one another or arranged in a brick-wall structure: that is, without considering the geometry of either the intracellular space or the gap junctions. The second of the two papers includes narrow extracellular clefts into a one-dimensional version of the previous model and examines their effect on the homogenised conductivity. The authors found that the homogenised model was able to capture the behaviour of the full system under normal gap junction coupling levels, but that as coupling was reduced, the two systems

disagreed. This may be due to the simple inclusion of gap junctions as resistive units into the model, or simply because we cannot use a continuum system of any form under low gap junction expression conditions due to the assumptions underlying the derivation of the continuum model ceasing to hold.

Having discussed how the homogenisation process has been applied to cardiac electrophysiology, we will now detail the assumptions made in the creation of continuum systems.

3.4 Assumptions Made in the Derivation of the Bidomain Equations

We begin by looking back at the caricature of the arrangement of cardiac cells shown in Figure 2.3. The long axes of the cells are roughly cylindrical in shape and are packed together in a locally aligned three-dimensional pattern. The cells are oriented in a particular direction, known as the fibre direction, with the majority of electrical connections in the form of gap junctions being located along this direction, coupling cells in an end-to-end fashion. These junctions are of non-negligible width when compared to that of an individual cell (up to 8% according to the imaging data in [65]). Side-to-side junctions are also present but are much less frequent and smaller.

As demonstrated by Figure 3.5 we can use these histological observations to approximate the true geometry of the myocardium by a fully periodic collection of cells, with each cell contained in a 'box' that is stacked in all three spatial dimensions to create the solution domain. Thus, the first assumption in the derivation of our model is that the domain can be broken down into repeatable and identical periodic subunits, though we note that the derivation allows for a slowly varying fibre direction, as shown in Keener and Panfilov [72].

Following this simplification of the underlying geometry it is then assumed that the problem is naturally defined on two scales — the microscale of individual cells and the macroscale of the whole tissue. As we discussed in Section 3.3, the model parameter ϵ is defined as

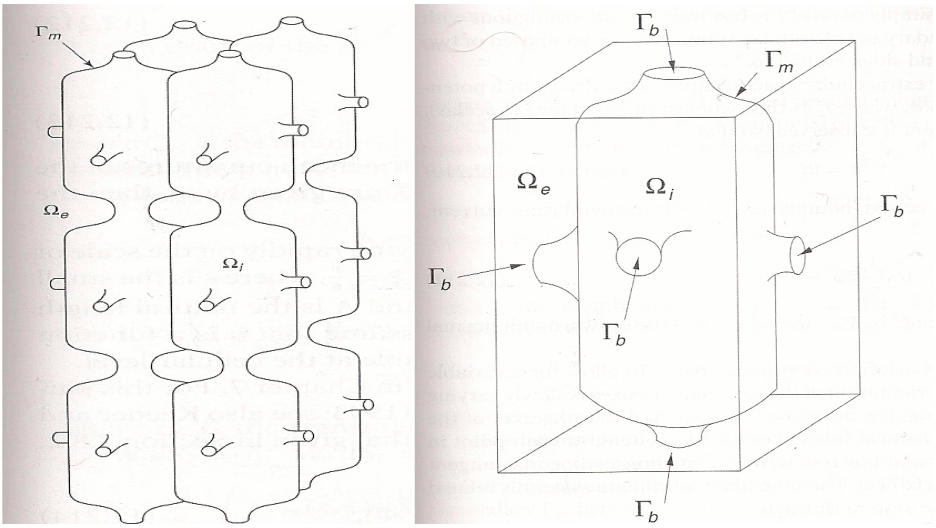

(a) Periodic cell structure (b) An idealised single cell

Figure 3.5: *A representation of cardiac cells. The intracellular domain is labelled* Ω_i*, and the extracellular domain* Ω_e*.* Γ_m *is the membrane separating the two regions, and in the right hand figure* Γ_b *represents the end-to-end coupling of cells via gap junctions. Figures: Keener and Sneyd, 1996, p.619.*

$$\epsilon = \frac{\text{length of a single cell}}{\text{lengthscale of the solution}}. \tag{3.10}$$

In the derivation of the bidomain equations this is assumed to be small. More precisely, it is assumed sufficiently small so that co-ordinate systems that differ by a factor of ϵ are deemed independent and so the contribution to the asymptotic solution to the governing equation from terms of order ϵ and higher is neglected.

Different studies have defined this parameter using different terminology, but the commonality within the literature gives the definition of ϵ as the ratio between the microscale and the macroscale. However, within this definition there is still ambiguity, and there are alternate methods for calculating the solution lengthscale. Two examples of this are in the papers of Neu and Krassowska [102] and Richardson and Chapman [121]. In [102] they estimate the length from fundamental material constants, giving an approximate length of 3.5 mm, while the authors of [121] multiply the typical speed of the propagating wavefront by the time taken to pass a certain point, with an estimate supplied at 25 mm for the sharp front (*i.e.* the upstroke phase) of the action potential. That these estimates differ by nearly

a whole order of magnitude also hints that making a key assumption based on the value of ϵ may not always be correct.

We believe that by conducting simulations using the discrete model from which the continuum model is derived and looking at the spatial form of the resulting solution we are able to find a more precise and model-specific estimate — this estimate needs only to give us a rough indication of the lengthscale of the solution, but by using the underlying discrete model from which we will derive the continuum system to calculate the solution lengthscale, we can be confident that it is of the correct order. Figure 3.4 shows the results of a simulation using a discrete model consisting of isotropic cells without gap junctions, and provides us with an initial estimate of a lengthscale of around ten cells for the sharp front of the action potential. This gives a value of ϵ of around 0.1, which is consistent with values found in the literature (both in the papers outlined above and in [72]). As such, it seems that the contribution to the solution of the governing equations from terms of order ϵ are likely to be relatively modest. When considering the macroscale behaviour of the system it therefore seems plausible to neglect these terms in respect of the computational tractability gained from doing so.

However in the previous studies and calculation methods, the effect of gap junctions on the solution lengthscale has not been accounted for. As we previously mentioned in Sections 2.3 and 3.4.2, it has been observed both in simulations [31] and experiments [166] that propagation speed through gap junctions is around ten times slower than in the cytoplasm, owing to an overall conductivity of the intercalated disc that is 0.01 times that of the cytoplasmic conductivity. As the parameter ϵ scales with the inverse square root of the conductivity [102] or alternatively with the propagation speed [121], we expect that inside the gap junction it will be ten times higher than in the cell and thus we will have $\epsilon \simeq \mathrm{O}(1)$ using our initial estimate of $\epsilon = 0.1$ in the cytoplasm. In this situation, it may not be appropriate to neglect the contribution to the solution from term of order ϵ or higher, and *the assumption that the micro- and macroscale co-ordinates are independent may no longer be valid.*

This notion has been explored recently [48, 49] with a focus on creating a hybrid model

combining elements from both continuum and discrete systems in a one-dimensional framework, using the premise that we cannot use a continuum model around the steep upstroke of the action potential due to the shorter solution lengthscale. Additionally, the effect of gap junctions on propagation in cardiac tissue has been researched (see Section 3.1.2), but not with regard to implementation in both discrete and continuum models.

3.4.1 Possible Limitations of the Bidomain Approach

The derivation of a continuum model of tissue-level cardiac electrophysiology relies on making a number of key assumptions, and it is currently not clear whether these assumptions are valid when considering either physiologically normal or disease-altered states. Nonetheless, the bidomain equations presented previously (Equation (3.2)) may be used without explicitly performing the derivation from a discrete system or considering the validity of the assumptions made, simply by using experimentally measured values for the macroscale conductivities.

Indeed, this is the method by which the vast majority of research has been conducted when using a bidomain formulation. However, such an approach bypasses the rigorous homogenisation technique employed to arrive at the continuum representation, and with it the specific effect of cell size, cell shape and gap junction coupling strength on the continuum model. The impact of all these features manifests in the macroscale conductivities Σ_i and Σ_e, and it is not clear how these tensors should be altered to take into account the factors mentioned above unless we homogenise the actual discrete geometry. When considering situations of reduced gap junction expression or coupling, therefore, such models are likely to be of limited use as they do not have a rigorous and accurate method of incorporating such microscale changes. Gap junctions have been included in continuum models of cardiac electrophysiology, however, and this will be discussed in Section 3.4.2.

Furthermore, it is worth noting that there are certain observed effects that are solely due to the discrete nature of cardiac cells and are thus tricky to model in a continuum setting. The first of these is conduction block — in cardiac tissue, a reduction in membrane excitability

or gap junction coupling strength will reduce conduction velocity up to a point, after which the wave will fail to propagate, as shown by Spach *et al.* [141]. This phenomenon occurs for a nonzero gap junction coupling strength, and has been effectively reproduced using a discrete model [136]. However, in a continuum model conduction will occur for any nonzero value of bulk conductivity, albeit at a vastly reduced pace, and so it cannot replicate this experimental observation. Secondly, it has been surmised that cell-to-cell conduction may take place via the mechanism of ephaptic coupling [83]. As this allows conduction to occur when gap junctions are fully inactive, it is not reproducible using the standard bidomain model in which no gap junction coupling leads to no conduction. The above demonstrates that there are situations in which modelling the same phenomenon using discrete and continuum systems will have a markedly different result.

Despite these concerns, the bidomain equations have been a success and have advanced the state of knowledge in the field, as well as allowing attempts at modelling on the whole-organ level. This is because the equations apply on a homogeneous domain that has no notion of a 'cell', it is simply made up of material with certain conductive and capacitive properties, which allows for a much coarser and less detailed approximation to the tissue geometry of cardiac tissue to be used, therefore increasing the computational tractability of the system.

3.4.2 Continuum Systems Adapted to Include Gap Junctions

In the 1990s, a number of studies were conducted that considered a continuum model of cardiac tissue and incorporated the effect of gap junctions into such a model by treating them as a discontinuity. The 1991 paper by Keener [73] introduced a one-dimensional 'discontinuous cable' model with a simple model of membrane kinetics, where gap junctions were fed into the model as jumps in the transmembrane potential that were proportional to the relative conductivities of the gap junction and cytoplasm. Later, a series of papers by Natalia Trayanova explored the concept of a 'periodic bidomain' representation of cardiac tissue. The initial paper [151] presented a one-dimensional passive bidomain model in which the intracellular conductivity was taken to be a periodic function of space, so that a gap junction was modelled as a region of nonzero length and reduced conductiv-

ity compared to that of the cytoplasm. The simplicity of the model allowed for a Fourier analysis to be carried out to obtain a general solution to the governing equations, and the resulting transmembrane potential showed the 'sawtooth' characteristic caused by gap junctions (see Figure 3.6). The model was extended to two dimensions in [149], however membrane kinetics were not included which limits the use of the model for studying action potential propagation. A similar undertaking can be found in a 1996 paper of Keener [74], which formulates a one-dimensional bidomain model in which the intracellular resistance is a periodically discontinuous function, representing gap junctions as zero length resistive units.

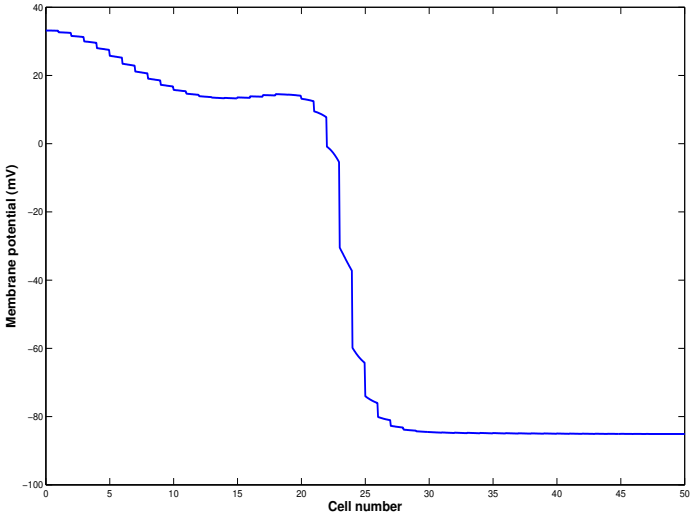

Figure 3.6: *An example of the 'sawtooth' potential observed as a propagating wavefront passes through gap junctions. Due to the low conductivity of the junction with respect to the cytoplasm, the wavefront slows down dramatically and thus causes a jump in potential across the gap junction.*

Whilst these papers present some interesting results and mathematical analysis of continuum models of cardiac electrophysiology, and also describe how gap junctions can be modelled more accurately as units of nonzero length with their own associated conductivity, the notion of a continuum model having structural variations on a microscopic spatial scale is in direct contradiction with the principles underlying the initial formulation of the model; that is, it considers the macroscale behaviour of a system and averages microscale variations.

Now that we have discussed two distinct forms of multi-cell cardiac electrophysiology models

— discrete models where intracellular and extracellular compartments are distinct and are connected by the cell membrane, and continuum models in which the two domains are intertwined to form one medium — we find that neither system is fully appropriate for studying tissue-level cardiac electrophysiology over a range of physiological behaviours. The discrete system lacks computational tractability even on modern computers, whilst the continuum system omits vital details regarding the electrical coupling of cells, as well as being built on potentially invalid assumptions. This drives us to further investigate these continuum assumptions, in order to find out if they are indeed valid, and determine if modelling certain physiological states or geometries affects this validity.

3.5 Research Questions and Contributions of this Thesis

The preceding two chapters have presented a review of the biological background and mathematical modelling principles of tissue-level cardiac electrophysiology. We now outline some research questions that are yet to be answered in the field, followed by a summary of how this thesis aims to answer these questions.

Our work focuses on the effect of microstructural properties such as cell arrangement, cell shape, and gap junctions that electrically connect cells in one or more directions, on discrete and continuum models of cardiac electrophysiology. We are foremost concerned with comparing the impact of changes between models: if we change a particular property in the underlying discrete cellular geometry, then what is the effect on the discrete system, what is the effect on the corresponding continuum system, and do these differences reflect one another?

We can group our work into two distinct but related streams. The first considers the results of simulations of discrete and continuum models of cardiac electrophysiology. When converting to a continuum system certain key assumptions are made, and we ask if these assumptions hold when considering gap junctions. If not, then we determine the factors that affect the extent to which the assumptions cease to hold. The results of our investigation are in Chapter 5, and examples of specific areas of focus are:

- The method of incorporating gap junctions: does how we treat the gap junction affect our results?
- Modelling healthy versus modelling diseased gap junctions: do the properties of diseased gap junctions affect the validity of the continuum approximation, and how does this compare to modelling healthy gap junctions or modelling no gap junctions?
- The effect of the discrete geometry chosen: do changes in cell length and distribution affect the validity of the continuum approximation?

Secondly, the conductivity tensors used in the continuum model can be specified by rigorously homogenising the discrete system, and will depend on various properties of that discrete system. These conductivity tensors can be used to write down the theoretical conduction velocity of the system, and so our results can be used to predict how changes in cellular microstructure affect conduction of an action potential. This is of particular interest when considering the major changes in cell and gap junction properties seen in common conditions such as ischaemia, fibrillation, and hypertrophy, that we outlined in Chapter 2.

The results of the homogenised conductivity tensor calculations are given in Chapters 4, 6 and 7. We will either analytically calculate or numerically approximate these tensors from the underlying geometry, and wish to know:

- How does introducing gap junctions in the fibre direction affect the results of homogenisation?
- How does the geometry of discrete cells affect the results, specifically the properties of the gap junctions?
- What effect do off-fibre direction connections and the arrangement of cells have on the conductivity tensors?
- Does it make a difference whether we use a two-dimensional or a three-dimensional geometry? That is, are the results of conductivity, conduction velocity and anisotropy calculations similar when we change microstructure properties in each of a two- and a three-dimensional framework?

The remainder of this thesis aims to answer these questions, and we now give a summary of the overall aim of each upcoming research chapter in that context, along with a bullet point list of the findings that represent the contribution of this thesis to the field.

Chapter 4: The Effect of Gap Junctions and Cell Arrangement on the Homogenised Conductivity Tensors

To begin our research, we considered the effect of gap junctions and cell arrangement on the results of homogenisation for a simplified geometry consisting of two-dimensional rectangles. We asked both what difference do these factors make when analytically calculating the conductivities and conduction velocity, and also what specific aspects were most important and should always be considered in a model in order to capture the behaviour of the discrete system — a question that we built upon in subsequent chapters for more complex cell shapes in both two and three dimensions. We found the following:

- On this specific geometry, the homogenised conductivity tensors may be written down analytically, and we can use a monodomain approximation to quantify conduction velocity changes.
- The effect of including gap junctions into a single fibre of cells is that of 'resistors in series', in that the cells and gap junctions behave as resistors with their own given resistivities.
- Modelling gap junctions with healthy parameters leads to a reduction in overall domain conduction velocity of more than 50% compared to not including gap junctions, and thus the effect of gap junctions on the results of homogenisation is substantial.
- Halving gap junction conductivity in order to model junctions in diseased tissue (for example, as seen during atrial fibrillation) further reduces conduction velocity by upwards of 20%.

Overall we concluded that gap junction inclusion is important to the homogenisation result, most notably in terms of predicting the effect of the onset of a diseased state on conduction velocity and conductivity.

Chapter 5: Comparing Simplified Discrete and Continuum Models of Cardiac Electrophysiology

In this chapter we performed a computational study to investigate the validity of the bidomain equations. We explicitly added gap junctions into a discrete model, and asked if their impact is picked up in the associated continuum system by performing full numerical simulations using each model and considering the resulting conduction velocity and action potential shape. If the effect of introducing gap junctions does not match between models, then the assumptions underlying the continuum derivation may not hold and the use of a continuum model is not appropriate when simulating the conduction velocity of a propagating action potential. To answer this, we:

- wrote down a discrete model, and rigorously converted it to a continuum system using the mathematical technique of homogenisation;
- included gap junctions in the model, and derived modified discrete and continuum systems;
- performed simulations using both models with no gap junctions included, and found that the model results were almost identical, as expected;
- modelled gap junctions with physiologically healthy parameters, and repeated the simulations. We noticed a small conduction velocity discrepancy between models, along with a qualitative change in action potential — the discrete potential was 'stepped', with sharp changes in membrane potential as the propagating wave passed through gap junctions, whilst the continuum potential was much more uniform;
- performed simulations with diseased gap junction parameters, and found that reducing gap junction conductivity significantly increased the conduction velocity discrepancy; and
- considered different cell geometries, and saw a substantial increase in conduction velocity discrepancy when increasing cell length (for instance, as happens during hypertrophy).

We concluded that whilst the continuum assumptions probably still hold for healthy parameters (where we saw a moderate 3% conduction velocity discrepancy), they are much less likely to be valid for certain unhealthy parameters (for example, reducing gap junction conductivity elicited a 44% discrepancy in conduction velocity, and increasing cell length gave up to a 24% conduction velocity difference).

Chapter 6: How the Geometry of Cardiac Cells Affects the Homogenised Conductivity Tensors

We then used a geometry that incorporated a more realistic cell shape, the brick-wall structure of cardiac cells, and off-fibre gap junctions, and asked how gap junctions and other geometric properties affected homogenisation results. To do this, we created a parameterised two-dimensional cardiac cell with a curved cell membrane and calculated the associated homogenised conductivity tensors for a variety of model parameters. We discovered that:

- gap junction parameters (height, length, and conductivity) have a large effect on conduction velocity, whist other model parameters (membrane curvature and intracellular conductivity) have a much smaller effect;
- when cells were tightly packed together the cell height had a large effect on the extracellular conductivity, which says that the shape of the extracellular space is important in determining conduction;
- including the brick-wall structure of cells increased conduction velocity, with the shape of the extracellular channel having a smaller effect on conductivity, confirming its importance to the results of homogenisation, and showing that having fibres of cells offset from each other is beneficial for conduction; and
- modelling connections between fibres of cells using off-fibre gap junctions led to an increase in both fibre- and off-fibre direction conductivity. This suggests that there are benefits of connecting fibres of cells that go beyond increasing conduction in the off-fibre direction. We also found that the intracellular anisotropy ratio is highly sensitive to changes in the off-fibre gap junction parameters.

In summary, we determined that we should take the effect of gap junctions, a brick-wall cell structure, and off-fibre connections into account when homogenising cardiac tissue, as all three have a significant effect on the predicted conduction velocity of the continuum system.

Chapter 7: Comparing the Homogenised Conductivity Tensors between a Two- and Three-Dimensional Schema.

Finally, we wished to determine how homogenising with a three-dimensional cell compares with a two-dimensional cell in terms of the conductivity tensors, predicted conduction velocity, and anisotropy values. To that end, we extended our geometry to three spatial dimensions using the same parameter scheme as in Chapter 6, and did the following:

- We compared the effect of changing cell and gap junction parameters using an isotropic cell with results obtained using a two-dimensional cell. We found that variation in certain parameters, most notably gap junction height, had a much greater effect on the predicted conduction velocity in three dimensions.
- From this, we concluded that we must be aware of the homogenisation method (be it using a two- or a three-dimensional cell geometry) when specifying the homogenised conductivity tensors for a continuum model of tissue-level cardiac electrophysiology. For example, care and attention would be needed when homogenising in three dimensions (for example if using diffusion tensor imaging) and then running simulations on a two-dimensional slab (or monolayer) continuum model.
- We also noted that the effect of reducing gap junction conductivity to model common diseased conditions had a similar (and significant) impact on conduction velocity when using a three-dimensional cell.
- Finally, we changed the properties of the off-fibre gap junctions such that the cell was anisotropic with a realistic aspect ratio, and calculated intracellular and extracellular anisotropy ratios for the domain. We saw that whilst intracellular anisotropy was highly sensitive to changes in gap junction parameters, the extracellular anisotropy changed very little.

- We concluded that modelling long, thin cells does not alone explain the intracellular anisotropy ratios typically observed in experiments, but that additionally reducing off-fibre gap junction conductivity gave physiologically realistic values. This modelling method also does not give a mechanism for the extracellular anisotropy ratio to reach normal values, and so we suggested that other factors might need to be included in the geometric framework to obtain such values.
- We also observed that the condition of unequal anisotropy ratios, one that is known to be an important factor in propagation, strongly depended on the existence and properties of off-fibre gap junctions, and that this presents a mechanism by which changes that occur to gap junctions in diseased tissue can affect action potential propagation.

Overall, we found the anisotropy ratios of cardiac tissue to be highly sensitive to off-fibre direction gap junction parameters, and saw that changing gap junction properties had a different effect when considering a three-dimensional cell.

Chapter 4

The Effect of Gap Junctions and Cell Arrangement on the Homogenised Conductivity Tensors

Contents

In this chapter we develop a discrete model of cardiac electrophysiology that includes gap junctions as physical entities and investigate the effect of changes in gap junction properties on the resulting homogenised conductivity tensors in two dimensions.

To begin this investigation, we present a discrete model of cardiac electrophysiology in Section 4.1 and use the process of homogenisation to derive a corresponding continuum model, the bidomain equations. In Section 4.2 we discuss how to develop this model to incorporate the effect of gap junctions into the system, deriving an updated version of the bidomain equations that systematically takes gap junctions into account.

In Section 4.3 we write down an analytic form for the homogenised conductivity tensors when using a simplified geometry in which cells are modelled as two-dimensional rectangles. We derive an analytic form for the tensors in the absence of gap junctions in Section 4.3.1, and in Section 4.3.2 we present some anomalies of homogenising a two-dimensional domain. Following that, in Section 4.3.3 we write down corresponding analytic forms of the tensors for the case where we include gap junctions as regions of reduced conductivity at one end of the cell, and quantify how the change to the intracellular conductivity tensor depends on the length of the junction relative to the length of the cell and on the conductivity of the gap junction relative to the conductivity of the intracellular space. In Section 4.3.4 we evaluate the intracellular tensor using parameter values representing no gap junctions, junctions in healthy tissue, and junctions in diseased tissue, in each case looking at the effect on conduction velocity.

Finally, in Section 4.4 we study the effect of cell arrangement on the intracellular homogenised conductivity tensor by considering the case where we have multiple fibres of cells, each of which has variable height and is composed of individual cells with varying length and gap junction size.

4.1 Derivation of Discrete and Continuum Models

In this section, we write down a discrete model of tissue-level cardiac electrophysiology. We then derive a corresponding continuum model, the widely used bidomain equations, using the mathematical technique of homogenisation, and clearly state the assumptions made as part of the derivation.

4.1.1 The Discrete Model

We consider the global problem defined on the geometry given in Figure 3.5a on Page 50. This consists of the intracellular space, denoted Ω_i, and the extracellular space, denoted Ω_e. The boundary between the two, *i.e.* the cell membrane, is denoted by Γ_m and is assumed to have zero thickness. Each space has an associated scalar conductivity — σ_i for the intracellular space and σ_e for the extracellular space. Both of these conductivities may be functions of space. In the intracellular space, current is given by $\mathbf{i} = -\sigma_i \nabla \phi_i$, where ϕ_i is the intracellular potential. This is a consequence of Ohm's law [75] which states that current is the product of conductivity and potential gradient. Conservation of current in the intracellular space then gives

$$\nabla \cdot (\sigma_i \nabla \phi_i) = 0, \qquad \mathbf{x} \in \Omega_i. \tag{4.1}$$

A boundary condition that models current flux across the membrane is

$$-\sigma_i \nabla \phi_i \cdot \mathbf{n} = I_m(\mathbf{x}), \qquad \mathbf{x} \in \Gamma_m, \tag{4.2}$$

where $\mathbf{n}$ is the outward pointing normal (that is, the normal pointing from the intracellular space into the extracellular space) and I_m is the transmembrane current flowing into the intracellular space from the extracellular space. Similarly, in the extracellular space we have

$$\nabla \cdot (\sigma_e \nabla \phi_e) = 0, \qquad \mathbf{x} \in \Omega_e, \tag{4.3}$$

and as the transmembrane current now flows into the extracellular space from the intracellular space, the sign of the current is reversed, and the analogous boundary condition is

$$-\sigma_e \nabla \phi_e \cdot \mathbf{n} = -I_m(\mathbf{x}), \qquad \mathbf{x} \in \Gamma_m, \tag{4.4}$$

where Γ_m and $\mathbf{n}$ are unchanged from Equation (4.2). From our previous discussion of single-cell models in Section 2.2 we know that the transmembrane current may be modelled by treating the cell membrane as a resistor-capacitor, and so it is of the form

$$I_m = c_m \frac{\partial v}{\partial t} + I_{ion}, \tag{4.5}$$

where $v = \phi_i - \phi_e$ is the transmembrane potential, c_m is the capacitance of the cell membrane and the ionic current I_{ion} represents a variety of ionic fluxes across the cell membrane and is of the form given in Equation (2.2).

4.1.2 Conversion to a Continuum System: the Homogenisation Process

To model cardiac tissue as a continuum, we employ a variation of the homogenisation technique introduced in Section 3.3. As outlined in that section, the assumption in the derivation is that the macroscale solution to the governing equations varies on a lengthscale that is much larger than the length of an individual periodic subunit (which in this case is the single cell shown in Figure 3.5b). This introduces another variable

$$\mathbf{z} = \frac{1}{\epsilon}\mathbf{x},$$

where

$$\epsilon = \frac{\text{length of a single cell}}{\text{lengthscale of the solution}}. \tag{4.6}$$

Here, $\mathbf{x}$ and $\mathbf{z}$ are macroscale and microscale coordinates respectively, which we take to be independent variables. Assuming that $\epsilon \ll 1$, we follow the method of Keener and Sneyd [75] and write the intracellular potential ϕ_i as a function of both variables and seek a regular asymptotic solution by expanding in powers of ϵ, giving

$$\phi_i(\mathbf{x}, \mathbf{z}) = \Phi_i(\mathbf{x}) + \epsilon\phi_{i1}(\mathbf{x}, \mathbf{z}) + \epsilon^2\phi_{i2}(\mathbf{x}, \mathbf{z}) + \ldots, \tag{4.7}$$

where $\phi_{i1}, \phi_{i2}, \ldots$, are periodic in $\mathbf{z}$ with zero mean, and $\Phi_i(\mathbf{x})$ represents the macroscale behaviour of the system. We now substitute Equation (4.7) into Equation (4.1) and note that $\nabla \equiv \nabla_{\mathbf{x}} + (1/\epsilon)\nabla_{\mathbf{z}}$, where $\nabla_{\mathbf{x}}$ and $\nabla_{\mathbf{z}}$ are the gradients with respect to the macroscale and microscale coordinates respectively. Equating powers of ϵ then gives

$$\epsilon^{-1}: \qquad \nabla_{\mathbf{z}} \cdot (\sigma_i(\nabla_{\mathbf{x}}\Phi_i + \nabla_{\mathbf{z}}\phi_{i1})) = 0, \tag{4.8}$$

$$\epsilon^{0}: \qquad \nabla_{\mathbf{x}} \cdot (\sigma_i(\nabla_{\mathbf{x}}\Phi_i + \nabla_{\mathbf{z}}\phi_{i1})) + \nabla_{\mathbf{z}} \cdot (\sigma_i(\nabla_{\mathbf{x}}\phi_{i1} + \nabla_{\mathbf{z}}\phi_{i2})) = 0. \tag{4.9}$$

The boundary of Ω_i partitions into the surface labelled Γ_m in Figure 3.5, on which we have the boundary conditions

$$\epsilon^{0}: \qquad -\sigma_i(\nabla_{\mathbf{x}}\Phi_i + \nabla_{\mathbf{z}}\phi_{i1}) \cdot \mathbf{n} = 0, \tag{4.10}$$

$$\epsilon^{1}: \qquad -\sigma_i(\nabla_{\mathbf{x}}\phi_{i1} + \nabla_{\mathbf{z}}\phi_{i2}) \cdot \mathbf{n} = I_m(\mathbf{x}), \tag{4.11}$$

and the remainder of the boundary labelled Γ_b, on which periodic boundary conditions hold. In order to remove the presence of any large-scale terms in Equation (4.8), we express ϕ_{i1} as

$$\phi_{i1} = \nabla_{\mathbf{x}}\Phi_i\mathbf{W}^i + \mathbf{C}, \tag{4.12}$$

where $\mathbf{C}$ is a vector of additive constants that can each be set to zero without loss of generality, the 'weight functions' $W_j^i,\ j = 1, 2, 3$, (where the superscript 'i' denotes 'intracellular' and is not an index) are to be determined, and Φ_i is treated as being a known quantity. Substituting Equation (4.12) into Equation (4.8) thus gives

$$\nabla_{\mathbf{z}} \cdot (\sigma_i(I + \nabla_{\mathbf{z}}\mathbf{W}^i)) = 0, \qquad \mathbf{z} \in \Omega_i, \tag{4.13}$$

with boundary conditions obtained by substituting Equation (4.12) into Equation (4.10)

$$\mathbf{n} \cdot (I + \nabla_{\mathbf{z}}\mathbf{W}^i) = 0, \qquad \mathbf{z} \in \Gamma_m, \tag{4.14}$$

Therefore the weight functions $\mathbf{W}^i$ satisfy Equation (4.13), the boundary conditions given by Equation (4.14), and are periodic in $\mathbf{z}$ with zero mean due to the underlying periodicity of the domain.

From Equation (4.12) we can glean some physical intuition for the weight functions — they describe the first order variation in intracellular potential within the unit cell that arises from the gradient of the macroscale potential. These potentials are due to electrical sources within a single cell and are generated, for example, by changes in conductivity. As such, we expect the weight functions to abruptly change slope at any conductivity interface. We will provide graphical examples of the solution to the intracellular weight functions for a variety of cell geometries later in this thesis in order to gain further intuition as to their form.

Integrating Equation (4.9) over the intracellular space then gives

$$\int_{\Omega_i} \nabla_{\mathbf{x}} \cdot \left(\sigma_i \left(I + \frac{\partial \mathbf{W}^i}{\partial \mathbf{z}} \right) \nabla_{\mathbf{x}} \Phi_i \right) \mathrm{d}V_{\mathbf{z}} = - \int_{\Omega_i} \nabla_{\mathbf{z}} \cdot (\sigma_i(\nabla_{\mathbf{x}}\phi_{i1} + \nabla_{\mathbf{z}}\phi_{i2}))\, \mathrm{d}V_{\mathbf{z}}. \tag{4.15}$$

We may now use the divergence theorem, along with the boundary condition Equation (4.11) and the periodicity of σ_i, ϕ_{i1} and ϕ_{i2} with respect to $\mathbf{z}$, to write Equation (4.15) as

$$\int_{\Omega_i} \nabla_{\mathbf{x}} \cdot \left(\sigma_i \left(I + \frac{\partial \mathbf{W}^i}{\partial \mathbf{z}} \right) \nabla_{\mathbf{x}} \Phi_i \right) \mathrm{d}V_{\mathbf{z}} = \int_{\Gamma_m} I_m \, \mathrm{d}S_{\mathbf{z}}, \tag{4.16}$$

where we have used the notation that the matrix $\partial \mathbf{W}^i / \partial \mathbf{z}$ has entries

$$\left(\frac{\partial \mathbf{W}^i}{\partial \mathbf{z}} \right)_{jk} = \frac{\partial W^i_j}{\partial z_k}, \qquad j,k = 1,2,3.$$

We now define the intracellular *homogenised conductivity tensor* Σ_i by

$$\Sigma_i = \frac{1}{V_{\text{unit}}} \int_{\Omega_i} \sigma_i \left(I + \frac{\partial \mathbf{W}^i}{\partial \mathbf{z}} \right) \mathrm{d}V_{\mathbf{z}}, \tag{4.17}$$

where V_{unit} is the volume of our periodic subunit — including both intracellular and extracellular space — shown in Figure 3.5b. We can then write Equation (4.16) as

$$\nabla_{\mathbf{x}} \cdot (\Sigma_i \nabla_{\mathbf{x}} \Phi_i) = \frac{1}{V_{\text{unit}}} \int_{\Gamma_m} I_m \, \mathrm{d}S_{\mathbf{z}}. \tag{4.18}$$

The same method, applied this time to the extracellular space (denoted by the subscript or superscript 'e') gives

$$\nabla_{\mathbf{x}} \cdot (\Sigma_e \nabla_{\mathbf{x}} \Phi_e) = -\frac{1}{V_{\text{unit}}} \int_{\Gamma_m} I_m \, \mathrm{d}S_{\mathbf{z}}, \tag{4.19}$$

where analogously

$$\Sigma_e = \frac{1}{V_{\text{unit}}} \int_{\Omega_e} \sigma_e \left(I + \frac{\partial \mathbf{W}^e}{\partial \mathbf{z}} \right) \mathrm{d}V_{\mathbf{z}}, \tag{4.20}$$

and where the extracellular weight functions $\mathbf{W}^e$ satisfy

$$\nabla_{\mathbf{z}} \cdot (\sigma_e(I + \nabla_{\mathbf{z}} W^e)) = 0, \qquad \mathbf{z} \in \Omega_e, \tag{4.21}$$

with boundary conditions

$$\mathbf{n} \cdot (I + \nabla_{\mathbf{z}} W^e) = 0, \qquad \mathbf{z} \in \Gamma_m, \tag{4.22}$$

and are periodic in $\mathbf{z}$ with zero mean. Thus, the tissue-level conductivity tensors Σ_i and Σ_e depend on the domain shapes Ω_i and Ω_e, the cell volume V_{unit}, the microscale conductivities σ_i and σ_e, along with any quantity that will change the functions $\mathbf{W}^{(i,e)}$.

Furthermore, by integrating Equation (4.17) by parts, and using the symmetry of the identity matrix along with the definition of the weight functions given in Equation (4.13), we have been able to demonstrate that the homogenised conductivity tensors Σ_i and Σ_e are symmetric. The proof is given in Appendix C.1.

We also observe, by performing a co-ordinate transformation on the equations governing the homogenised conductivity tensors, that the absolute dimensions of the unit cell do not affect the calculation, and so the dimensions of a cell may be defined in relative form. The derivation of this result can be found in Appendix C.3. This means that we may take the periodic subunit to be the box $[0, 1]^n$, where n is the dimension of the geometry under consideration, and define the geometry appropriately on this box such that were the domain to be scaled to the actual dimensions of a myocyte, the cell looks proportionally as we expect it to.

4.1.2.1 The Bidomain Equations

If we now write the transmembrane potential, v, as a regular power expansion in ϵ, so that

$$v = V(\mathbf{x}) + \epsilon v_1(\mathbf{x}, \mathbf{z}) + \epsilon^2 v_2(\mathbf{x}, \mathbf{z}) + \ldots,$$

where v_1, v_2, ..., are periodic and have zero mean over the boundary Γ_m, we can write

$$\begin{aligned}\nabla_{\mathbf{x}} \cdot (\Sigma_i \nabla_{\mathbf{x}} \Phi_i) = &\ \frac{1}{V_{\text{unit}}} \int_{\Gamma_m} \left(c_m \frac{\partial v}{\partial t} + I_{ion}(v,t) \right) \, \mathrm{d}S_{\mathbf{z}}, \\ = &\ \chi \left(c_m \frac{\partial}{\partial t} (V(\mathbf{x}) + \epsilon v_1(\mathbf{x},\mathbf{z}) + \epsilon^2 v_2(\mathbf{x},\mathbf{z}) + \dots) + \right. \\ &\left. \frac{1}{S_m} \int_{\Gamma_m} I_{ion}(V(\mathbf{x}) + \epsilon v_1(\mathbf{x},\mathbf{z}) + \epsilon^2 v_2(\mathbf{x},\mathbf{z}) + \dots, t) \, \mathrm{d}S_{\mathbf{z}} \right),\end{aligned}$$

where S_m is the membrane surface area, the surface-area-to-volume ratio $\chi = S_m / V_{\text{unit}}$, and the integrals over the cell membrane of v_1, v_2, ..., are zero due to their periodicity and zero mean. If we assume that we may ignore the contribution from ϵ^1 and higher order terms, *i.e.* that

$$\frac{1}{S_m} \int_{\Gamma_m} I_{ion}(V(\mathbf{x}) + \epsilon v_1(\mathbf{x},\mathbf{z}) + \epsilon^2 v_2(\mathbf{x},\mathbf{z}) + \dots, t) \, \mathrm{d}S_{\mathbf{z}} = I_{ion}(V(\mathbf{x}), t),$$

which also physiologically implies that there are sufficiently many ion channels in each cell so that we may model the cell membrane as a continuum, we can write

$$\nabla_{\mathbf{x}} \cdot (\Sigma_i \nabla_{\mathbf{x}} \Phi_i) = \chi \left(c_m \frac{\partial V}{\partial t} + I_{ion}(V,t) \right). \tag{4.23}$$

Similarly, Equation (4.19) becomes

$$\nabla_{\mathbf{x}} \cdot (\Sigma_e \nabla_{\mathbf{x}} \Phi_e) = -\chi \left(c_m \frac{\partial V}{\partial t} + I_{ion}(V,t) \right). \tag{4.24}$$

We now use $V = \Phi_i - \Phi_e$ to eliminate Φ_i and write Equations (4.23) and (4.24) — the bidomain equations — in the more familiar form of

$$\chi c_m \frac{\partial V}{\partial t} = \nabla_{\mathbf{x}} \cdot (\Sigma_i \nabla_{\mathbf{x}} (V + \phi_e)) - \chi I_{ion}, \tag{4.25a}$$

$$\nabla_{\mathbf{x}} \cdot ((\Sigma_i + \Sigma_e) \nabla_{\mathbf{x}} \phi_e + \Sigma_i \nabla_{\mathbf{x}} V) = 0. \tag{4.25b}$$

Appropriate boundary conditions representing zero flux across the tissue surface are

$$-\Sigma_i \nabla (V + \phi_e) \cdot \mathbf{n} = 0, \tag{4.26a}$$

$$\Sigma_e \nabla \phi_e \cdot \mathbf{n} = 0. \tag{4.26b}$$

4.2 Inclusion of Gap Junctions

In this section, we outline a method for including gap junctions in a discrete model of cardiac electrophysiology, and present a modified version of the bidomain equations that rigorously takes these gap junctions into account.

To do this, we adapt our cell geometry to include gap junctions as shown in Figure 4.1 (for a two-dimensional geometry) and Figure 4.2 (for a three-dimensional geometry). We include a thin region of length δ, measured as a proportion of the total myocyte length, at each edge of the intracellular space, in which the conductivity is given by σ_g. From here on, we will refer to δ as 'gap junction length' and understand that it is given as a proportion of the overall myocyte length. We then assume that there is no membrane between gap junction and cell (G.S. Bub and R.A. Burton, private correspondence, 16/10/2013), *i.e.* that the gap junction is a part of the cell with reduced conductivity. The junction can then be treated as part of the intracellular space by noting that continuity of flux is observed across the interface between cell and gap junction, and the interface between extracellular space and gap junction is taken to be of the form of the rest of the cell membrane, *i.e.* as a resistor-capacitor unit. The overall intracellular conductivity is now given by $\sigma = \sigma(\mathbf{x})$, where

$$\sigma(\mathbf{x}) = \begin{cases} \sigma_i, & \mathbf{x} \in \text{cytoplasm}, \\ \sigma_g, & \mathbf{x} \in \text{gap junction}. \end{cases} \tag{4.27}$$

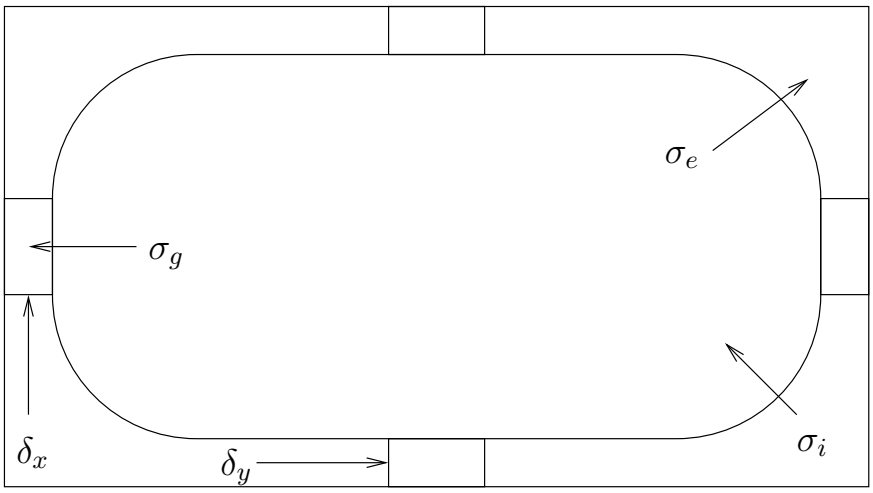

Figure 4.1: *A two-dimensional sketch to show how gap junctions are included in our discrete geometry. They are represented by narrow regions of length δ at each end of the cell unit and have associated conductivity σ_g.*

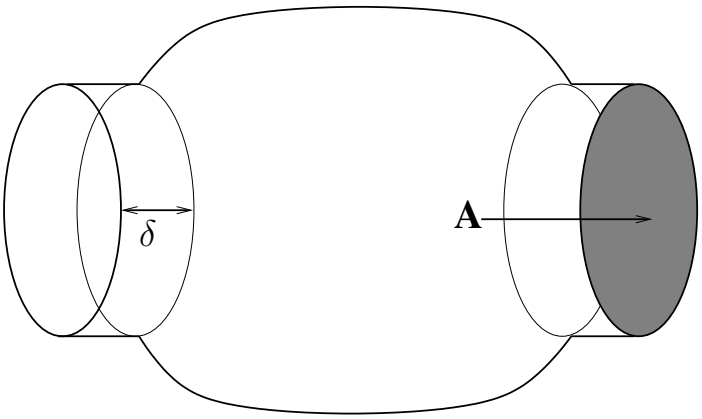

Figure 4.2: *A three-dimensional sketch to show how gap junctions are included in our model with regard to surface area properties. The junctions will be present at all faces of the cell, but here we show them in one direction only for clarity. Each gap junction is represented as a disc of proportional thickness δ and cross-sectional area A. These values will be dimension specific — that is, we will have $\delta_{(x,y,z)}$ and $A_{(x,y,z)}$.*

In addition, we adapt the form of the transmembrane current on the boundary such that

$$I_m = \begin{cases} c_m \frac{\partial v}{\partial t} + I_{ion} & \mathbf{x} \in \text{cytoplasm}, \\ c_g \frac{\partial v}{\partial t} + I_g I_{ion} & \mathbf{x} \in \text{gap junction}, \end{cases} \tag{4.28}$$

where I_g is a Boolean switch that turns ionic flow across the membrane on or off, and c_g is the capacitance of the gap junction membrane, which we are modelling as a continuum. We may then alter the properties of the gap junction membrane by specifying c_g according to one of three cases:

- $c_g = c_m$, treating it as if it were the same material as the cell membrane;
- $c_g \neq c_m$, $c_g > 0$, treating it as a capacitive material with its own properties; or
- $c_g = 0$, treating it as a fully insulative material.

To the best of our knowledge, and having consulted experts in cardiac microstructure imaging on the subject (G.S. Bub and R.A. Burton, private correspondence, 16/10/2013), it is not known which of the above three cases is most physiologically representative, nor is it known what the correct value for I_g is. As such, we will leave both parameters undetermined in the forms stated so that we can explore the effect of changing their values on the results of simulations, which will be done in Chapter 5.

4.2.1 A Modified Formulation of the Bidomain Equations

Returning to Equations (4.18) and (4.19), we now split the right-hand term of the equations, given by

$$\frac{1}{V_{\text{unit}}} \int_{\Gamma_m} I_m \, \mathrm{d}S,$$

into integrals over the cell membrane Γ_i and gap junction membrane Γ_g to give

$$\begin{aligned}\frac{1}{V_{\text{unit}}}\int_{\Gamma_m} I_m \,\mathrm{d}S &= \frac{1}{V_{\text{unit}}}\left[\int_{\Gamma_i} I_m \,\mathrm{d}S + \int_{\Gamma_g} I_m \mathrm{d}S\right] \\ &= \frac{1}{V_{\text{unit}}}\left[c_m S_i \frac{\partial V}{\partial t} + c_g S_g \frac{\partial V}{\partial t} + \int_{\Gamma_i} I_{ion} \,\mathrm{d}S + I_g \int_{\Gamma_g} I_{ion} \,\mathrm{d}S\right] \\ &= (c_m \chi_i + c_g \chi_g)\frac{\partial V}{\partial t} + (\chi_i + I_g \chi_g) I_{ion},\end{aligned}$$

where c_g and c_m are the capacitances of the gap junction membrane and cell membrane, S_g and S_i are the surface areas of Γ_g and Γ_i respectively, $\chi_g = \frac{S_g}{V_{\text{unit}}}$ and $\chi_i = \frac{S_i}{V_{\text{unit}}}$. The final form of the modified bidomain equations is therefore

$$(c_m \chi_i + c_g \chi_g)\frac{\partial V}{\partial t} = \nabla_{\mathbf{x}} \cdot (\Sigma_i \nabla_{\mathbf{x}}(V + \phi_e)) - (\chi_i + I_g \chi_g) I_{ion}, \tag{4.29a}$$

$$\nabla_{\mathbf{x}} \cdot ((\Sigma_i + \Sigma_e)\nabla_{\mathbf{x}} \phi_e + \Sigma_i \nabla_{\mathbf{x}} V) = 0. \tag{4.29b}$$

In the above, the tensor Σ_i is defined through homogenisation of a unit cell that includes gap junctions, and as such it will be different to that calculated in the absence of gap junctions. Note that if the gap junction membrane is taken to have the same properties as that of the cell membrane (with $c_g = c_m$ and $I_g = 1$), the equations reduce to their original form and the effect of gap junctions is restricted solely to the calculation of the intracellular homogenised conductivity tensor.

4.3 The Effect of Gap Junctions on the Intracellular Tensor in Two Dimensions

Having derived discrete and continuum models that account for the presence of gap junctions, we now investigate how gap junctions affect the intracellular conductivity tensor for a geometry consisting of two-dimensional rectangles.

As a reminder, the intracellular homogenised conductivity tensor Σ_i satisfies

$$\Sigma_i = \frac{1}{V_{\text{unit}}} \int_{\Omega_i} \sigma_i \left(I + \frac{\partial \mathbf{W}^i}{\partial \mathbf{z}} \right) \mathrm{d}V_{\mathbf{z}}, \tag{4.30}$$

where V_{unit} is the volume of our periodic subunit. The intracellular weight functions $\mathbf{W}^i$ satisfy

$$\nabla_{\mathbf{z}} \cdot (\sigma_i (I + \nabla_{\mathbf{z}} \mathbf{W}^i)) = 0, \qquad \mathbf{z} \in \Omega_i, \tag{4.31}$$

with boundary conditions

$$\mathbf{n} \cdot (I + \nabla_{\mathbf{z}} \mathbf{W}^i) = 0, \qquad \mathbf{z} \in \Gamma_m, \tag{4.32}$$

and are periodic in $\mathbf{z}$ with zero mean. Similarly the extracellular homogenised conductivity tensor Σ_e satisfies

$$\Sigma_e = \frac{1}{V_{\text{unit}}} \int_{\Omega_e} \sigma_e \left(I + \frac{\partial \mathbf{W}^e}{\partial \mathbf{z}} \right) \mathrm{d}V_{\mathbf{z}}, \tag{4.33}$$

and the extracellular weight functions $\mathbf{W}^e$ satisfy

$$\nabla_{\mathbf{z}} \cdot (\sigma_e (I + \nabla_{\mathbf{z}} W^e)) = 0, \qquad \mathbf{z} \in \Omega_e, \tag{4.34}$$

with boundary conditions

$$\mathbf{n} \cdot (I + \nabla_{\mathbf{z}} W^e) = 0, \qquad \mathbf{z} \in \Gamma_m. \tag{4.35}$$

4.3.1 Solutions for Rectangular Cells in the Absence of Gap Junctions

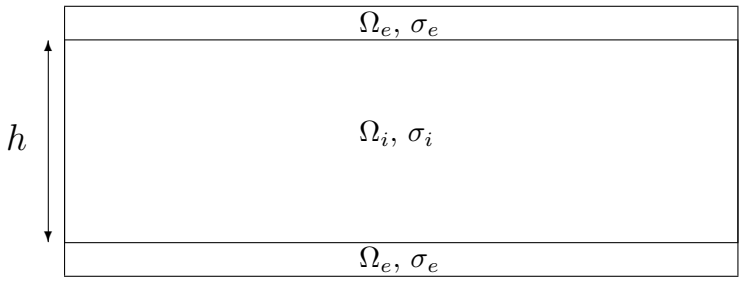

Figure 4.3: *A simple rectangular cell with no gap junctions. The intracellular space Ω_i has conductivity σ_i and height h, and the extracellular space Ω_e has conductivity σ_e.*

We begin by considering the case of uniform, rectangular cells in the absence of gap junctions as shown in Figure 4.3. As stated previously, we will take the periodic subunit to be the box $[0,1] \times [0,1]$ due to the invariance of the homogenised conductivity tensors to simple coordinate transformations, with all other size quantities defined as proportions of the total subunit. In this situation both domains have constant scalar conductivities, and the intracellular portion of the unit cell has height h, where $0 < h < 1$. In the intracellular space, the functions W_j^i given in Equation (4.31) satisfy

$$\nabla^2 W_j^i = 0, \qquad j = 1, 2.$$

The normal is given by $\mathbf{n} = (0,1)^T$ and so the boundary conditions in Equation (4.32) become

$$\frac{\partial W_1^i}{\partial z_2} = 0, \qquad \frac{\partial W_2^i}{\partial z_2} = -1, \qquad \text{on the cell membrane,}$$

the solutions to which are

$$W_1^i = A_1, \qquad W_2^i = -z_2 + A_2,$$

where A_1 and A_2 are constants. The matrix $\frac{\partial \mathbf{W}^i}{\partial \mathbf{z}}$ therefore has entries

$$\frac{\partial \mathbf{W}^i}{\partial \mathbf{z}} = \begin{pmatrix} 0 & 0 \\ 0 & -1 \end{pmatrix}, \tag{4.36}$$

and the tensor Σ_i is of the form

$$\Sigma_i = \begin{pmatrix} h\sigma_i & 0 \\ 0 & 0 \end{pmatrix}. \tag{4.37}$$

By similar logic we have

$$\Sigma_e = \begin{pmatrix} (1-h)\sigma_e & 0 \\ 0 & 0 \end{pmatrix}. \tag{4.38}$$

In this case, we see that both conductivity tensors are zero except in the fibre direction, where the conductivity is equal to the scalar conductivity of the discrete domain scaled by the proportion of the overall geometry taken up by that particular domain.

4.3.2 The Anomalies of Homogenising Two-Dimensional Models

The form of the homogenised conductivity tensors given in Equations (4.37) and (4.38) hint that there may be anomalies in the process of homogenising a two-dimensional geometry. In the above case, where we have a fibre of cells connected only in the fibre direction and extracellular material also only connected in the fibre direction, each homogenised conductivity tensor has one nonzero entry corresponding to conductivity along the fibre. As the extracellular conductivity tensor can be expressed as a scalar multiple of the intracellular conductivity tensor, the resulting continuum system is reduced to a monodomain model (see

Section 3.2) in which propagation can only occur in the fibre direction.

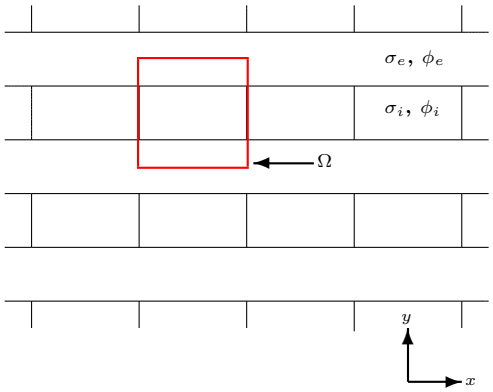

Figure 4.4: *A domain consisting of individual cells as depicted in Figure 4.3 that are joined into fibres. The red box is the periodic subunit that we homogenise and is denoted by* Ω*. It consists of intracellular and extracellular portions which respectively have conductivities* σ_i *and* σ_e *and potentials* ϕ_i *and* ϕ_e*.*

This continuum system does not predict the behaviour of the underlying discrete system in certain circumstances. For example, if we consider the geometry shown in Figure 4.4 and stimulate the extracellular space at the top of the domain, we would expect the stimulus to travel in the off-fibre direction towards the first cell membrane, exciting it if sufficiently strong, which would lead a propagating action potential. However, the continuum model has zero conductivity in the off-fibre direction, and so nothing would happen if we applied this same stimulus to the continuum model.

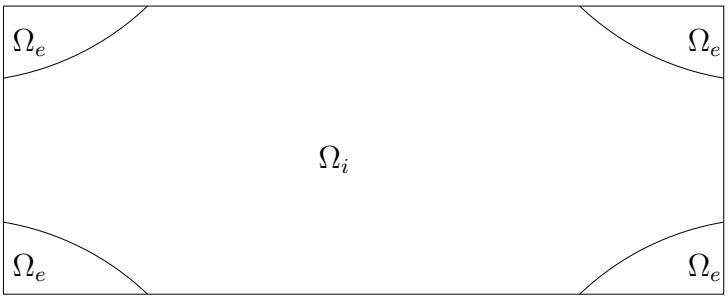

Figure 4.5: *A cell in which the intracellular space* Ω_i *is connected in both directions.*

In an alternative case where we have multiple fibres of cells connected both in the fibre direction and in the off-fibre direction, the periodic subunit for which is depicted in Figure 4.5, there is the possibility of having nonzero intracellular conductivity in both directions. This is because both intracellular weight functions will have a boundary on which periodic

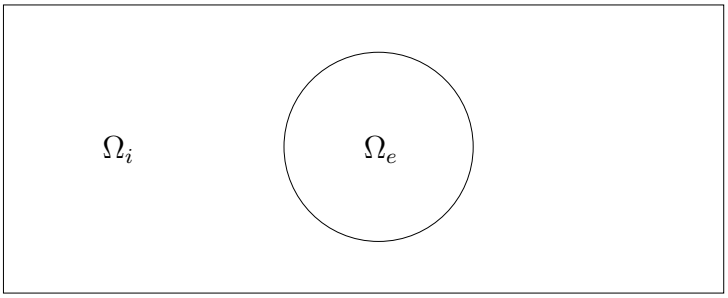

Figure 4.6: *The extracellular space Ω_e as viewed from its centre when the intracellular space Ω_i is connected in both directions (as in Figure 4.5).*

conditions hold, meaning that the previous form

$$W_j^i = -z_j + C, \tag{4.39}$$

does not satisfy all conditions (it is not periodic in $\mathbf{z}$) and so we will not automatically have $\Sigma_{i_{(j,j)}} = 0$ as we do when the above form of W_j^i is valid. The extracellular material will not be connected, as shown in Figure 4.6, and will have zero conductivity. To see this, we note that as the extracellular conductivity is a constant scalar, the weight functions satisfy

$$\nabla^2 W_j^e = 0, \qquad j = 1, 2. \tag{4.40}$$

They are subject to the boundary condition given in Equation (4.35), and a solution is therefore

$$W_1^e = -z_1 + C_1, \qquad W_2^e = -z_2 + C_2. \tag{4.41}$$

As the extracellular space is not connected, it does not have a boundary on which periodicity holds, and so the above solutions are unique up to the addition of the constants C_1 and C_2. Substituting these into the definition of the extracellular conductivity tensor in Equation (4.33) gives an extracellular tensor that is zero in all directions, and as such the continuum system breaks down to a non-spatial model in which no propagation is possible through either domain. Once more, this continuum system does not reflect the behaviour of the

underlying discrete system, as spatial propagation is possible with this discrete geometry.

Despite these anomalies, we can still draw conclusions from the results of homogenisation in two dimensions. If we restrict our attention to propagation in the fibre direction and make any stimulus homogeneous in the off-fibre direction, we can isolate the effect that any parametric or geometric changes have on conductivity and conduction velocity in this direction. If we add intracellular connectivity in the off-fibre direction, we are able to look at the intracellular anisotropy ratio, which is an important determinant of conduction properties in cardiac tissue [77]. Additionally, we will see in Chapter 7 how these anomalies are not present when considering a three-dimensional geometry.

4.3.3 Solutions When Gap Junctions are Modelled

We now solve the equations governing the intracellular homogenised conductivity tensor when we include gap junctions in the discrete geometry initially introduced in Section 4.3.1. We do this in order to see the effect that gap junctions have on the theoretical continuum conductivity obtained by homogenising a discrete geometry in which they are included as physical entities.

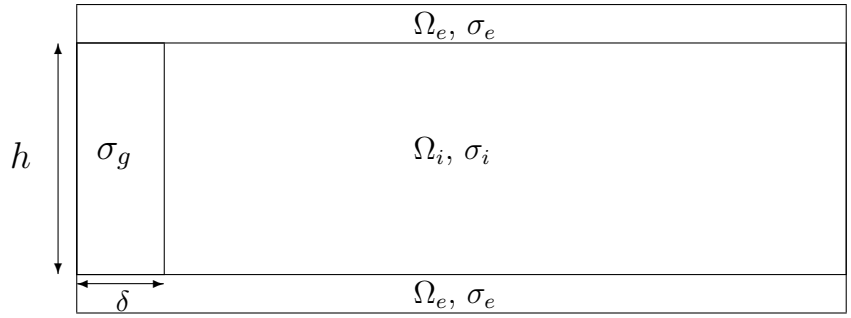

Figure 4.7: *A simple rectangular cell based on that shown in Figure 4.3, with a gap junction of length δ and conductivity σ_g modelled as part of the intracellular space Ω_i.*

As mentioned in Section 4.2, we are incorporating gap junctions as regions of the intracellular space with their own conductivity. This is shown in Figure 4.7, where the gap junction has length δ and conductivity σ_g. Looking at this diagram, we might expect that the cell and gap junction behave like resistors in series, and we will demonstrate this later in this section.

When using this geometry we are able to find an analytic solution by considering the governing equations for the intracellular weight functions (Equation (4.31)) in the cell and the gap junction separately. As each compartment has homogeneous conductivity, W_1^i satisfies Laplace's equation separately in both regions, in addition to satisfying the boundary condition Equation (4.32) on the cell membrane, and so

$$W_1^i = \begin{cases} B_1 z_1 + C_1 & 0 < z_1 < \delta, \\ B_2 z_1 + C_2 & \delta < z_1 < 1, \end{cases} \tag{4.42}$$

where B_1, B_2, C_1 and C_2 are constants. The z_1-derivative of W_1^i thus satisfies

$$\frac{\partial W_1^i}{\partial z_1} = \begin{cases} B_1 & 0 < z_1 < \delta, \\ B_2 & \delta < z_1 < 1. \end{cases} \tag{4.43}$$

We then integrate Equation (4.31) across the boundary between the cell and the gap junction, which is located at $z_1 = \delta$, to give

$$\left[\sigma \frac{\partial W_1^i}{\partial z_1}\right]_{\delta^-}^{\delta^+} = \left[-\sigma\right]_{\delta^-}^{\delta^+},$$

and combine this with Equation (4.43) to obtain the relation between B_1 and B_2

$$\sigma_i B_2 - \sigma_g B_1 = \sigma_g - \sigma_i. \tag{4.44}$$

As W_1^i is periodic in z_1, we have $W_1^i(z_1 = 0) = W_1^i(z_1 = 1)$, and so evaluating Equation (4.42) at $z_1 = 0$ and $z_1 = 1$ gives

$$C_1 = B_2 + C_2. \tag{4.45}$$

As W_1^i is continuous, we have $W_1^i(z_1 = \delta^-) = W_1^i(z_1 = \delta^+)$, and so evaluating Equation

(4.42) at $z_1 = \delta^-$ and $z_1 = \delta^+$ gives

$$B_1\delta + C_1 = B_2\delta + C_2. \tag{4.46}$$

Eliminating C_1 and C_2 between Equations (4.45) and (4.46) gives us

$$B_1\delta + B_2(1-\delta) = 0, \tag{4.47}$$

and we solve Equations (4.44) and (4.47) for B_1 and B_2 so that

$$B_1 = \frac{(\sigma_g - \sigma_i)}{\delta\sigma_i + (1-\delta)\sigma_g} \times (\delta - 1), \qquad B_2 = \frac{(\sigma_g - \sigma_i)}{\delta\sigma_i + (1-\delta)\sigma_g} \times \delta.$$

Substituting the above into Equation (4.30) gives the (1,1) entry of the intracellular conductivity tensor as

$$\Sigma_{i_{(1,1)}} = h\left(\int_0^\delta \sigma_g(1+B_1)\,\mathrm{d}z_1 + \int_\delta^1 \sigma_i(1+B_2)\,\mathrm{d}z_1\right) = \frac{h\sigma_i\sigma_g}{\delta\sigma_i + (1-\delta)\sigma_g}. \tag{4.48}$$

Note that when we set gap junction conductivity to be equal to intracellular conductivity, or gap junction length to be zero (*i.e.* when $\sigma_g = \sigma_i$ or $\delta = 0$), this reduces to the corresponding entry in Equation (4.37) as anticipated. The extracellular tensor is unaffected by the introduction of gap junctions, and is again given by Equation (4.38).

Looking at Equation (4.48), we see that the cell and gap junction behave as resistors in series, as mentioned at the start of this section. To illustrate this we note that a resistor of cross-sectional area A, length L and resistance R has conductivity $\sigma = L/(RA)$. Two resistors R_1 and R_2 of lengths L_1 and L_2 in series thus satisfy, using $R_{total} = R_1 + R_2$,

$$(L_1 + L_2)/\sigma_{total} = L_1/\sigma_1 + L_2/\sigma_2,$$

in the case that their cross-sectional areas are the same. Rearranging gives

$$\sigma_{total} = \frac{(L_1 + L_2)\sigma_1\sigma_2}{L_2\sigma_1 + L_1\sigma_2},$$

which is the same expression as we derived for the conductivity tensor in Equation (4.48) with conductivities σ_i, σ_g and lengths δ, $1-\delta$. We also note that the effect of gap junctions on the intracellular conductivity tensor in this simplified case is parameterised by the length and conductivity of the gap junction, *i.e.* the quantities δ and σ_g.

4.3.4 Quantitative Changes in Conductivity and Conduction Velocity

We now wish to know what the expression in the previous section, Equation (4.48), means on a quantitative level. That is, how do the length and conductivity of a gap junction affect intracellular fibre direction conductivity and overall domain conduction velocity? If we express the conductivity as

$$\Sigma_{i_{(1,1)}} = \frac{h\sigma_i}{\delta(\sigma_i/\sigma_g) + (1-\delta)}, \tag{4.49}$$

then the numerator of the expression, $h\sigma_i$, is equal to the conductivity in the absence of gap junctions (when $\delta = 0$). Using Equation (4.49) we can calculate conductivity relative to this control value as a function of gap junction length δ and the conductivity ratio $\sigma_R = \sigma_i/\sigma_g$. Physiologically we expect δ to be around 0.05 [65] and σ_R to be of the order of 100 [31], and these are the values we will take to represent normal, healthy cells in the remainder of this thesis.

In Table 4.2 we show relative conductivities for parameter values surrounding these healthy values. In Table 4.3 we show relative conduction velocities from a theoretical standpoint, where conduction velocity is proportional to the square root of conductivity, and conductivity is equal to $\Sigma_i(\Sigma_i + \Sigma_e)^{-1}\Sigma_e$ as we have a monodomain reduction here (see Section 3.2). We also present these numbers in graphical form in Figure 4.8 and Figure 4.9. In addition, we also compute the simulated continuum conduction velocities by solving the full bidomain equations using a finite element method (details of which can be found in Appendix A). We

have performed simulations for a subset of values of δ and σ_R, and the results are provided in Table 4.1. In these simulations we use the conductivity tensors corresponding to the given geometry that are calculated in Table 4.2, and all other parameters as specified in Chapter 5.

δ/σ_R	**10**	**100**	**1000**
0.01	96.8	76.1	34.7
0.05	86.4	46.5	16.4
0.10	77.6	34.9	11.7

Table 4.1: *The relative conduction velocities obtained by performing continuum simulations using conductivity tensors from a subset of the parameter values given in Table 4.2, expressed as a percentage of the value obtained in the absence of gap junctions.*

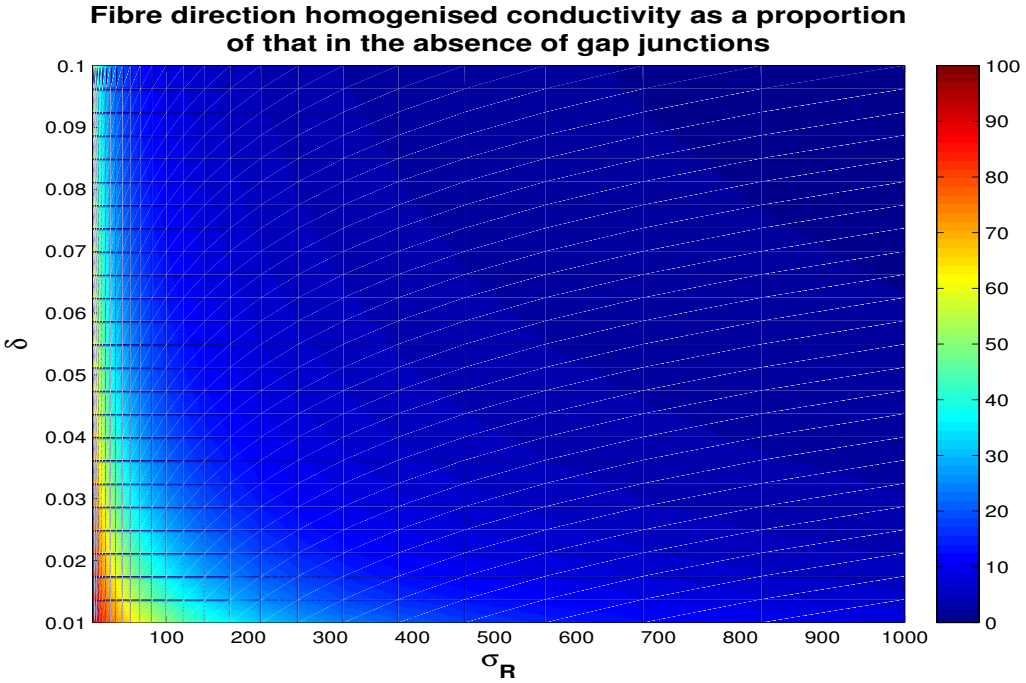

Figure 4.8: *A graphical display of the fibre direction homogenised* ***conductivity*** $\Sigma_{i_{(1,1)}}$ *as a percentage of its value in the absence of gap junctions, where values are mapped to a red/-green/blue colour scheme in which the value 100 represents red and the value zero represents blue.*

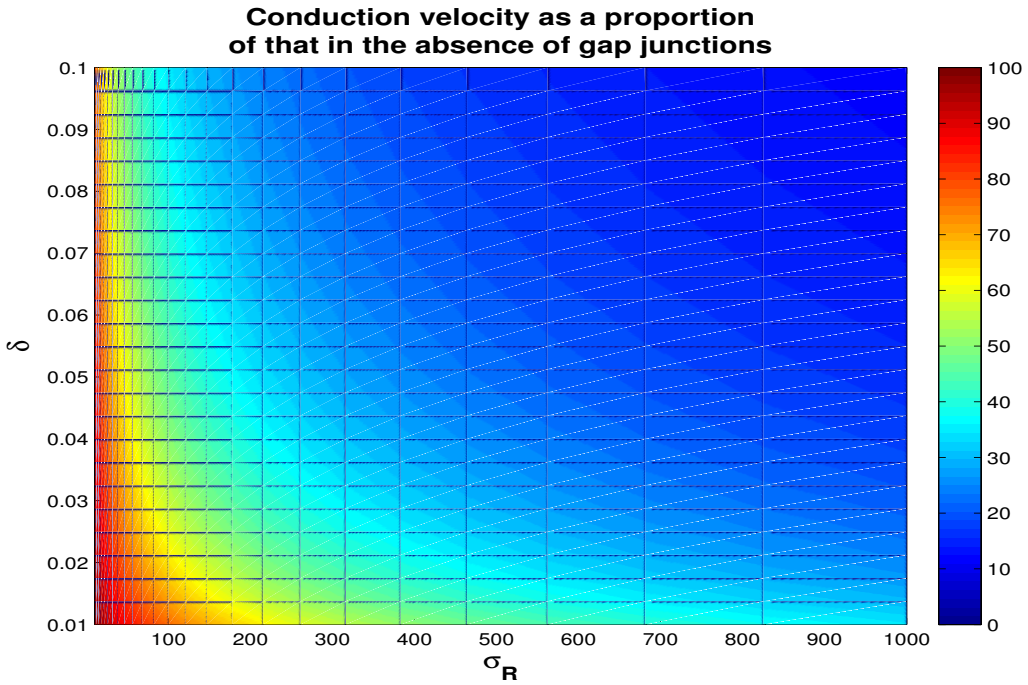

Figure 4.9: *A graphical display of the relative* ***theoretical conduction velocities*** *given by the conductivity values in Table 4.2 as a percentage of that expected in the absence of gap junctions, where values are mapped to a red/green/blue colour scheme in which the value 100 represents red and the value zero represents blue.*

δ/σ_R	**10**	**20**	**50**	**100**	**200**	**500**	**1000**
0.01	91.7	84.0	67.1	50.2	33.4	16.6	9.09
0.02	84.7	72.4	50.5	33.5	20.0	9.11	4.76
0.03	78.7	63.6	40.4	25.1	14.3	6.26	3.22
0.04	73.5	56.8	33.7	20.1	11.1	4.77	2.44
0.05	68.9	51.2	28.9	**16.8**	9.13	3.85	1.96
0.06	64.9	46.7	25.3	14.4	7.72	3.23	1.64
0.07	61.3	42.9	22.5	12.6	6.69	2.78	1.40
0.08	58.1	39.6	20.3	11.2	5.91	2.44	1.23
0.09	55.2	36.9	18.4	10.0	5.28	2.17	1.1
0.10	52.6	34.4	16.9	9.17	4.78	1.96	0.99

Table 4.2: *The fibre direction homogenised* ***conductivity*** $\Sigma_{i_{(1,1)}}$ *as a percentage of its value in the absence of gap junctions for values of* δ*. The result using normal parameters representing healthy cells is shown in bold.*

δ/σ_R	**10**	**20**	**50**	**100**	**200**	**500**	**1000**
0.01	96.8	93.7	85.8	76.2	63.9	46.4	34.7
0.02	94.0	88.5	76.4	64.0	50.6	34.7	25.3
0.03	91.4	84.0	69.5	56.2	43.2	29.0	20.9
0.04	89.0	80.2	64.2	50.7	38.3	25.3	18.2
0.05	86.8	76.9	59.9	**46.6**	34.8	22.8	16.3
0.06	84.7	73.9	56.4	43.3	32.1	20.9	14.9
0.07	82.8	71.2	53.4	40.6	29.9	19.4	13.8
0.08	81.0	68.9	50.9	38.4	28.1	18.2	13.0
0.09	79.3	66.7	48.7	36.5	26.7	17.2	12.2
0.10	77.7	64.7	46.8	34.9	25.4	16.3	11.6

Table 4.3: *The relative* ***theoretical conduction velocities*** *predicted by the conductivity values in Table 4.2 as a percentage of that expected in the absence of gap junctions, with the result using healthy parameters shown in bold.*

Comparing entries of Tables 4.3 and 4.1 for the same values of δ and σ_R, we see that the conduction velocities obtained from continuum simulations are almost identical to the 'theoretical conduction velocities' predicted by the homogenisation process for a wide range of gap junction parameters. As such, for all cases in which we have a monodomain reduction of the bidomain equations we will calculate continuum conduction velocities from the value of the homogenised conductivity tensor given by the solutions to Equations (4.30) and (4.33), as opposed to conducting full continuum simulations, and assume throughout the remainder of this thesis that the value returned is an accurate representation of the conduction velocity that would be observed were we to conduct continuum simulations using the calculated homogenised conductivity tensor. Note that we do not make any claim that the conductivity tensor and resulting conduction velocity is an accurate representation of the underlying discrete system — this comparison will be performed in Chapter 5. Rather, we are saying that for continuum models, the theoretical predictions of conduction velocity from the homogenised conductivity tensors closely match that calculated from the solution of the continuum partial differential equations.

Returning to our calculations of conductivity and conduction velocity, perhaps the most interesting values in Tables 4.2 and 4.3 are those for healthy values of gap junction conductivity and length. For example, when $\sigma_R = 100$ and $\delta = 0.05$, which are representative of a normal physiological state, the intracellular conductivity is 16.8% of that in the absence of gap junctions, with the conduction velocity of the system reduced to 46.6% of the value in the absence of gap junctions. This gives some indication of the magnitude of the effect of including gap junctions on the results of homogenisation of a discrete geometry, and the effect that they have on conduction velocity in cardiac tissue. We can also see that changing the length of gap junctions can significantly change conduction velocity — if we take $\sigma_R = 100$ and $\delta = 0.05$ and then double gap junction length so that $\delta = 0.1$, conduction velocity decreases by 25%.

Using the values in Table 4.3 we are also able to give predicted changes in conduction velocity from experimental observations regarding changes in gap junction coupling strength in diseased conditions. For example, in atrial fibrillation and ventricular hypertrophy, expression levels of the main gap junction connexin, Cx43, are reduced by 50% [132]. This corresponds to halving the value of the conductivity σ_g in our model, and thus doubling σ_R in Table 4.3. If we take δ as a variable, we can then plot the expected change in conduction velocity against gap junction length δ when we double σ_R.

In Figure 4.10 we show such plots when changing σ_R from $10 \to 20$, $50 \to 100$, $100 \to 200$ and $500 \to 1000$, and observe that the percentage reduction in conduction velocity is higher for larger values of cytoplasm/gap junction conductivity ratio. That is, the poorer the gap junction coupling strength is to begin with, the more of an effect that halving the strength has on conduction velocity. We also observe that conduction velocity changes are less sensitive to changes in gap junction length δ as we increase cytoplasm/gap junction conductivity ratio — when this ratio doubles from $10 \to 20$ the conduction velocity change increases almost linearly over the range of gap junction lengths, whereas when the ratio goes from $500 \to 1000$, conduction velocity changes plateau fairly quickly as gap junction length increases.

Considering the case when we begin with physiologically normal values (as previously, we

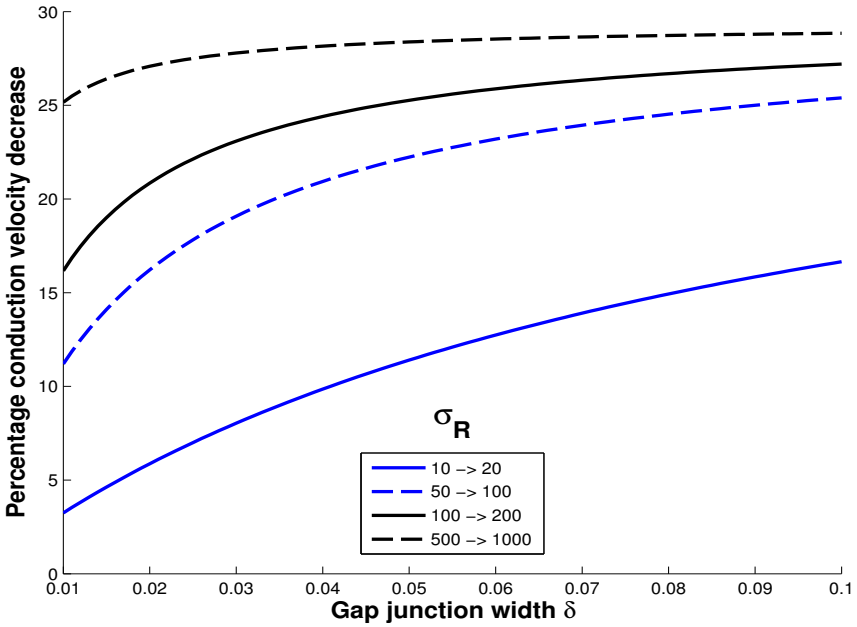

Figure 4.10: *The decreases in predicted conduction velocity when halving gap junction coupling for different values of gap junction length δ (along each line) and cytoplasm/gap junction conductivity ratio (successive lines).*

are using $\sigma_R = 100$ and $\delta = 0.05$) and reduce gap junction conductivity by 50% in order to model diseased states characterised by a reduction in connexin expression (See Section 2.3.1.2), we see that conduction velocity decreases by 25%. This suggests that reducing gap junction connexin expression levels to simulate diseased conditions will significantly reduce the conduction velocity of the system.

4.3.5 Weight functions

In order to get a sense for how the weight functions depend on the width and conductivity of the gap junctions, we have plotted the solution to the fibre direction intracellular weight function (the analytic solution for which is given in Equation (4.42)) in Figure 4.11 and Figure 4.12. We have not shown the extracellular weight function — as outlined previously, it is simply a line of constant gradient throughout the domain.

Overall, we see that the weight function are piecewise linear with a jump in gradient at

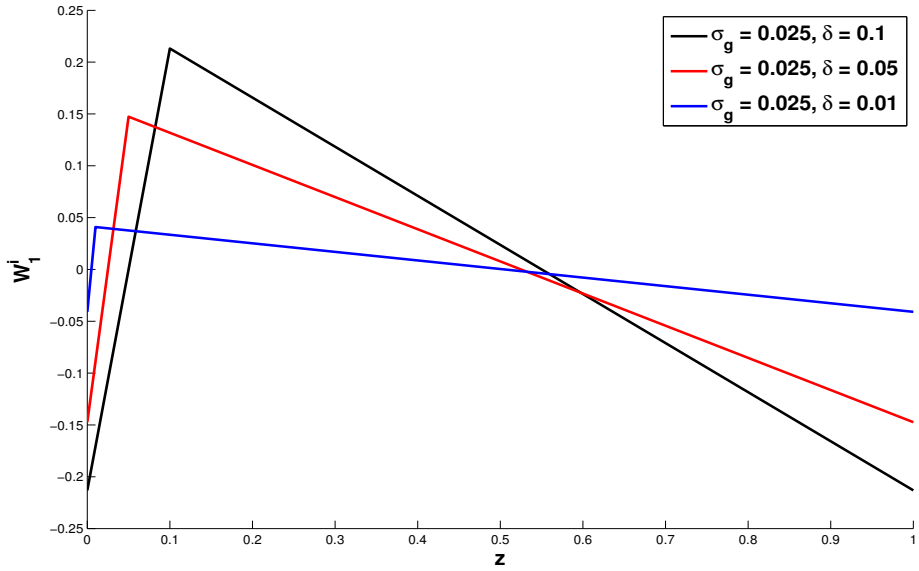

Figure 4.11: *Solutions to the governing equation* (4.31) *for the fibre direction intracellular weight as we change gap junction width* δ.

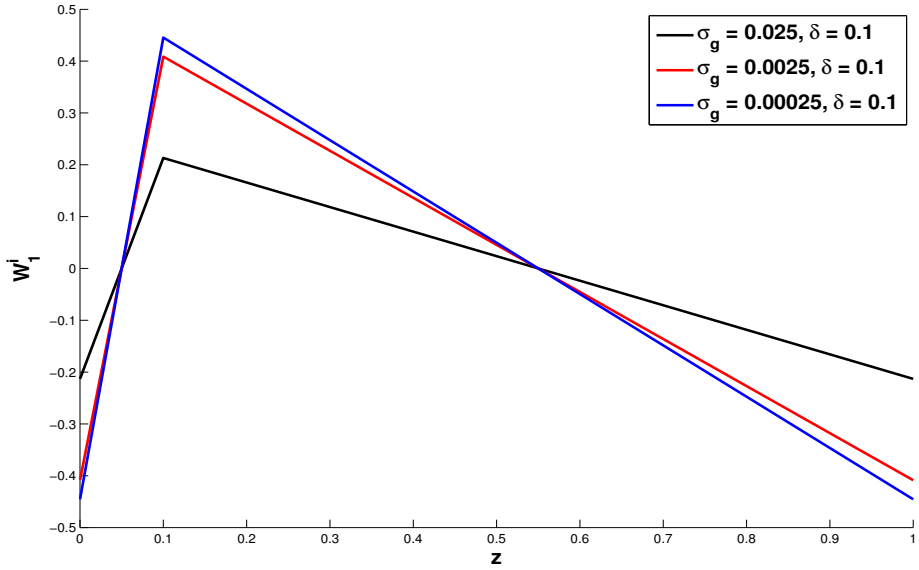

Figure 4.12: *Solutions to the governing equation* (4.31) *for the fibre direction intracellular weight as we change gap junction conductivity* σ_g.

the interface between cell and gap junction that switches the sign of the gradient. The magnitude of this jump is proportional to the change in conductivity at the interface, with sharper changes in gradient resulting from bigger jumps in conductivity (see Figure 4.12). When we decrease gap junction conductivity and thus increase the magnitude of the jump, the gradient of the weight function increases inside the gap junction but decreases in the cell. We see from Figure 4.11 that as gap junction width δ increases, the slope of the weight function decreases, becoming less positive inside the gap junction and more negative in the cell.

As the homogenised conductivity is proportional to the gradient of the weight function (from Equation (4.30)), we have shown graphically that increasing gap junction width and increasing the difference between cell and gap junction conductivity will decrease the homogenised conductivity, which agrees with the analytic results given in Table 4.2.

4.3.6 The Relative Effect on Conduction Velocity of Changes to Intracellular and Extracellular Conductivities

We will now look at how the relative magnitudes of the intracellular and extracellular conductivity affect the sensitivity of conduction velocity to changes in each conductivity. That is, if the intracellular conductivity is changing, how might we expect conduction velocity to behave given the relative size of the intracellular tensor compared to the extracellular tensor. We wish to know this because there is typically a large difference in size between the two, with extracellular conductivity around an order of magnitude larger than intracellular conductivity when including gap junctions in the intracellular conductivity calculations [10,14].

The definition of the homogenised conductivity tensors in Equations (4.30) and (4.33) tells us that they are linear with respect to overall changes in the microscale conductivities σ_i and σ_e, as the weight functions are independent of the microscale conductivities. That is, if we change a microscale conductivity by some constant factor everywhere in its domain of definition, the homogenised tensor will be multiplied by that same factor. As such, when we refer to changing conductivity in this section, we mean changing the microscale values and as such changing the macroscale values by the same amount.

If we consider the case of equal anisotropy ratios where $\Sigma_e = \lambda\Sigma_i$, then we can write down the change in conduction velocity that results from a change in either intracellular or extracellular conductivity. As stated in Section 4.3.4, the conduction velocity (CV) is proportional to

$$CV \propto \sqrt{\frac{\Sigma_i\Sigma_e}{\Sigma_i + \Sigma_e}},$$

which, upon substituting in our expression for Σ_e, becomes

$$CV \propto \sqrt{\frac{\lambda}{\lambda+1}\Sigma_i}.$$

The effect of doubling extracellular conductivity (so that $\Sigma_e = 2\lambda\Sigma_i$) on conduction velocity is thus

$$CV \propto \sqrt{\frac{2\lambda}{2\lambda+1}\,\Sigma_i} = \sqrt{\frac{\lambda}{\lambda+1}\,\Sigma_i} \times \sqrt{1 + \frac{1}{2\lambda+1}}, \tag{4.50}$$

and so the conduction velocity increases by a factor of $\sqrt{1 + \frac{1}{2\lambda+1}}$, which is a *decreasing* function of λ. As such, conduction velocity is less sensitive to changes in extracellular conductivity when the extracellular conductivity is large compared to the intracellular conductivity. Similarly, doubling the intracellular conductivity gives us

$$CV \propto \sqrt{\frac{2\lambda}{\lambda+2}\,\Sigma_i} = \sqrt{\frac{\lambda}{\lambda+1}\,\Sigma_i} \times \sqrt{2\left(1 - \frac{1}{\lambda+2}\right)},$$

and so the conduction velocity increases by a factor of $\sqrt{2\left(1 - \frac{1}{\lambda+2}\right)}$, which is an increasing function of λ. Thus conduction velocity changes are greater when we double the intracellular conductivity if the intracellular conductivity is small compared to the extracellular conductivity. To give some sense of what the above relationships mean on a quantitative level, in Figure 4.13 we plot the relative conduction velocity changes when we double the intracellular conductivity (plot (a)) and extracellular conductivity (plot (b)) for various

values of λ.

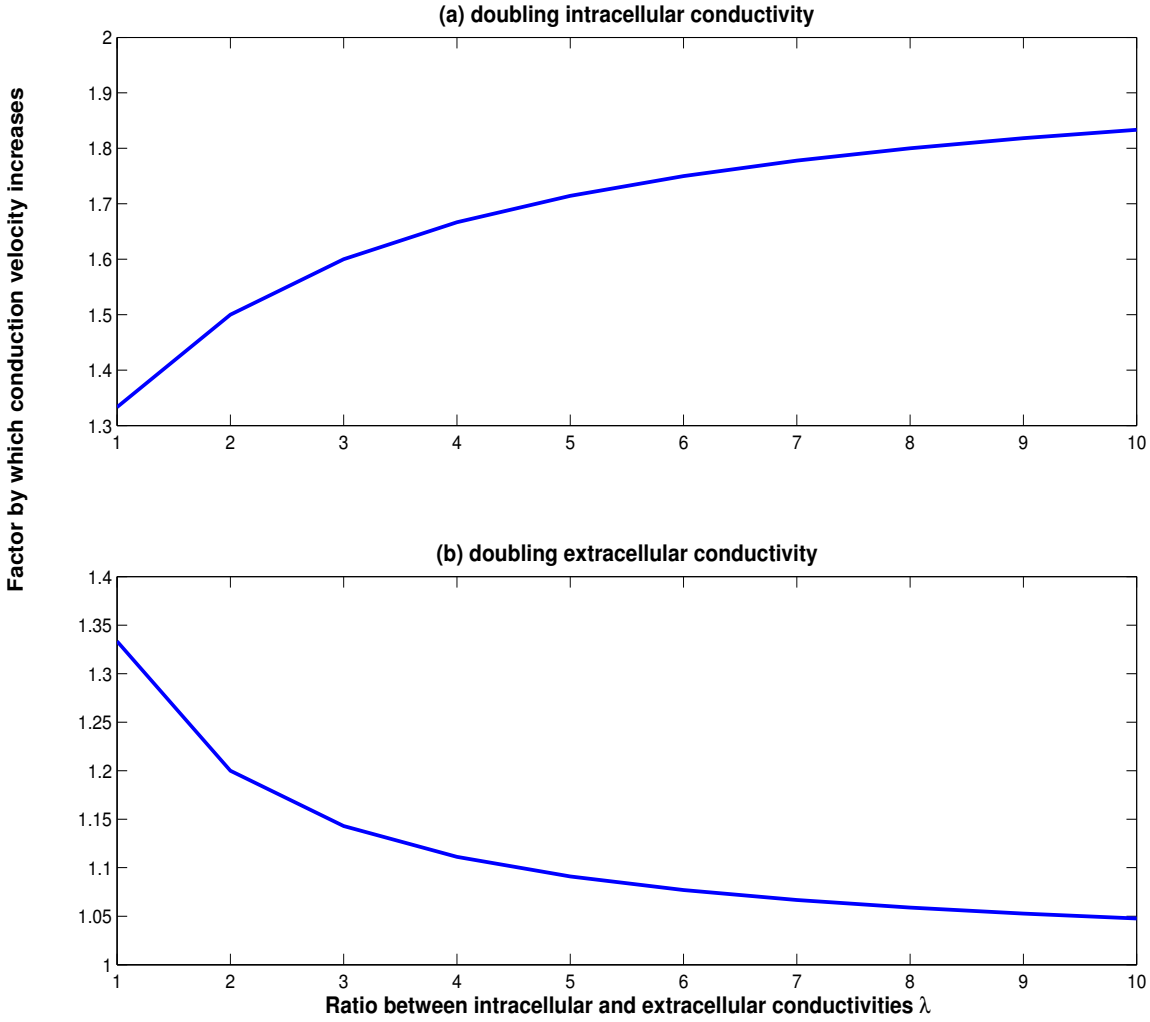

Figure 4.13: *Relative conduction velocity changes when doubling intracellular and extracellular conductivities in the case where we have* $\Sigma_e = \lambda\Sigma_i$*, where we vary the parameter* λ *in the above plots.*

Additionally, we can see how the smaller of the two conductivity tensors dominates the absolute value of conduction velocity when one is much smaller than the other, say by an order of magnitude or more. If we take the intracellular tensor to be small, so that $\Sigma_i \ll \Sigma_e$, then we can approximate $\Sigma_i + \Sigma_e \simeq \Sigma_e$, and so

$$CV \propto \sqrt{\frac{\Sigma_i \Sigma_e}{\Sigma_i + \Sigma_e}} \simeq \sqrt{\Sigma_i},$$

which shows us that the smaller of the two tensors does indeed primarily determine the conduction velocity.

4.3.7 Conclusions

In this section we outlined how gap junctions affect the intracellular conductivity tensor when it is calculated by homogenisation of the underlying discrete geometry. We provided an analytic solution for the tensor in which we found that the conductivity σ_g and length δ of the gap junction determine its effect, and explored this numerically by changing gap junction conductivity and length whilst keeping other parameters the same. We found that the theoretical conduction velocity derived from the conductivity tensors closely matched the conduction velocity obtained by performing full bidomain simulations using the same gap junction parameters.

We also saw that including gap junctions at physiologically healthy coupling strength reduced the conduction velocity of the domain that was predicted by the continuum model by over 50%, and that decreasing coupling strength to diseased levels lowered conduction velocity by a further 20%.

4.4 The Effect of Cell Arrangement on the Intracellular Tensor

In this section, we outline how variation in cell arrangement affects the intracellular conductivity tensor. We consider a single fibre of cells connected by gap junctions in Section 4.4.1, where the length of each individual cell and of each gap junction is variable.

4.4.1 A Single Fibre of Cells

We now look at the homogenised conductivity tensors for the case where we have some variability in cell and gap junction dimensions, once more using idealised rectangular cells.

We consider a chain of connected cells depicted in Figure 4.14, where each cell has its own length and where two adjacent cells are connected by a gap junction that in turn has its own length. If we take the whole chain of cells as our periodic subunit on which to homogenise then we can extend the argument in Section 4.3.3 that was used to calculate the analytic conductivity when introducing gap junctions. That is, Laplace's equation will hold for the intracellular weight functions in each individual isotropic section of the domain, and we integrate across each boundary between two compartments to obtain a jump condition that allows us to evaluate the derivative of the weight functions in each compartment. When aggregated, these derivatives give the conductivity of the domain as that of multiple resistors in series.

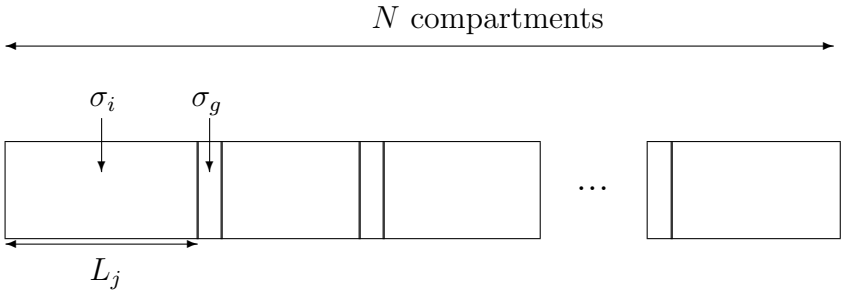

Figure 4.14: *A geometry consisting of rectangular cells connected by gap junctions, each of which has its own length. The unit indexed j has length L_j. We have omitted the extracellular space for the sake of clarity of the image.*

To see this, we consider a series of N domains of variable width L_j and variable conductivity σ_j, where j runs from 1 to N. If we denote the x-coordinate of the junction between domain j and $j+1$ by x_j, then in each domain Laplace's equation holds and we integrate this to give

$$\frac{\partial W_1^i}{\partial x} = B_j, \qquad x_{j-1} < x < x_j, \qquad j = 1, \ldots, N, \tag{4.51}$$

where $x_0 = 0$. We then integrate the governing equation (4.31) across each boundary to give

$$\left[\sigma \frac{\partial W_1^i}{\partial x}\right]_{x_j^-}^{x_j^+} = \left[-\sigma\right]_{x_j^-}^{x_j^+}, \qquad j = 1, \ldots, N-1,$$

which when evaluated and combined with Equation (4.51) gives

$$\sigma_{j+1}B_{j+1} - \sigma_j B_j = \sigma_j - \sigma_{j+1}, \qquad j = 1, \ldots, N-1.$$

The condition that W_1^i has zero mean in x becomes

$$\int_0^{L_D} \frac{\partial W_1^i}{\partial x}\, \mathrm{d}x = \sum_{j=1}^{N} L_j B_j = 0,$$

where the overall domain length $L_D = \sum_{j=1}^{N} L_j$, and solving the above system of equations gives the fibre direction intracellular conductivity as

$$\begin{aligned}
\Sigma_{i_{(1,1)}} &= \frac{1}{V_{\text{unit}}} \int_{\Omega_i} \sigma \left(I + \frac{\partial \mathbf{W}^i}{\partial \mathbf{z}} \right) \mathrm{d}V_{\mathbf{z}} \\
&= \frac{1}{L_D} \sum_{j=1}^{N} L_j \sigma_j (1 + B_j) \\
&= \frac{\sum_{j=1}^{N} L_j}{\sum_{j=1}^{N} L_j / \sigma_j}.
\end{aligned}$$

As we touched upon in Section 4.3.3, this can be thought of as the conductivity of resistors in series in which each compartment is a single resistor. In the case where each cell has conductivity σ_i and each gap junction has conductivity σ_g, the domain conductivity becomes

$$\Sigma_{i_{(1,1)}} = \frac{h\sigma_i\sigma_g}{\delta\sigma_i + (1-\delta)\sigma_g},$$

where δ represents the total proportion of the intracellular domain taken up by gap junctions. This is the same expression as in Equation (4.48), and tells us that if we have a domain that consists of a fibre composed of cells of varying length, the continuum model has a conductivity that represents the mean cell length and gap junction length, disregarding any details of how these quantities might vary within the domain.

4.5 Summary

In this chapter we have created a model of tissue-level cardiac electrophysiology that takes gap junctions into account, and performed analytic calculations to determine the resulting homogenised conductivity tensors used in a continuum model.

In Section 4.1 we presented a discrete model of cardiac electrophysiology and derived the corresponding continuum model using a rigorous mathematical technique, explicitly describing the approximations made. We adapted both models to include gap junctions as a region of reduced conductivity at one end of each cell in Section 4.2.

In Section 4.3 we saw how gap junctions affect the intracellular homogenised conductivity tensor in a two-dimensional geometry consisting of rectangular cells. We derived analytic solutions both with and without gap junctions, and verified that the conduction velocity changes predicted by the homogenised conductivity tensors closely matched those obtained by performing continuum simulations.

We then saw that adding gap junctions into a model at healthy coupling values reduced conduction velocity by over 50%, and that halving gap junction coupling strength to model diseased cells further reduced conduction velocity by 20%.

Finally, in Section 4.4 we saw that when rectangular cells are arranged in series with gap junctions of uniform conductivity, the homogenised conductivity tensor is that of one single cell whose gap junction has the same length as the proportion of total domain size taken up by gap junctions in the case of multiple cells in series.

Having seen how gap junctions and cell arrangement affect the intracellular homogenised conductivity tensor for rectangular cells, we will now study how they affect the results of full discrete and continuum simulations and the validity of the assumptions made in deriving the bidomain equations in Chapter 5.

Chapter 5

Comparing Simplified Discrete and Continuum Models of Cardiac Electrophysiology

Contents

In this chapter we perform a comparison of simulations using both a discrete model and a continuum model rigorously derived from the discrete model, using parameter sets representing healthy and diseased states, in order to see if the assumptions underpinning the derivation of the bidomain equations cease to hold when gap junctions are included in the discrete geometry.

In Section 5.2 we perform simulations using both discrete and continuum models on a simplified geometry consisting of two-dimensional rectangular cells, and compare the form and speed of the resulting action potentials. We begin by conducting simulations without gap junctions in Section 5.2.2 before performing simulations where we model gap junctions with physiologically normal parameters in Section 5.2.3.

We then repeat the simulations in which gap junctions were included, and alter the parameter set to model common diseased conditions by reducing gap junction conductivity in Section 5.2.4, and increasing the upstroke velocity of the action potential in Section 5.2.5. We do this because we expect that, in both of these cases above, the bidomain assumptions will cease to be valid (see Section 3.4).

5.1 Introduction and Motivation

In Chapter 4 we presented a discrete model of tissue-level cardiac electrophysiology and modified it to explicitly include gap junctions. We then rigorously derived a corresponding continuum model from the discrete model. As part of this derivation process, a number of assumptions were made which were more fully outlined in Section 3.4. One of these assumptions is that the ratio parameter ϵ, which is equal to the length of a single cell divided by the lengthscale of the solution to the governing equations, was small. Using this assumption the contributions to the continuum system of terms of order ϵ and higher were neglected.

However, when considering propagation of an action potential through gap junctions, it

has been observed both in simulations and in experiments [31, 166] that the wavefront significantly slows down. As ϵ scales with the inverse of propagation speed [121], we expect it to increase when the propagating wave passes through gap junctions. Furthermore, gap junction conductivity drops under some common clinical conditions such as ischaemia (see Section 2.3) and as such propagation speed drops, so in this situation ϵ will be further increased. It is also the case that when cells are elongated, such as in hypertrophy, ϵ increases.

Given the above, the assumption that ϵ is arbitrarily small and that contributions of order ϵ and above will not significantly contribute to the solution of the continuum model may cease to hold when modelling gap junctions (in particular, when modelling diseased gap junctions with reduced conductivity), when upstroke velocity increases, or when cell length increases, which all occur in common clinical conditions. If this is the case then the derived continuum model is not appropriate to model tissue-level cardiac electrophysiology under these circumstances.

In order to determine if this is the case, we will first perform simulations of both discrete and continuum models in which gap junctions are not included, and confirm that we obtain near-identical results, in particular for the conduction velocity of the propagating action potentials. We will then include gap junctions at healthy coupling levels in the discrete model and repeat the simulations, before performing further simulations where we have gap junctions with reduced conductivity, an ionic current formulation that leads to a steeper upstroke velocity, and a greater myocyte length. If the underlying conduction velocity of the discrete and continuum systems differs significantly, we can say that the continuum approximation made is no longer valid for the specific case under consideration.

5.2 A Comparison of the Results of Simulations on a Simplified Two-Dimensional Geometry

In this section we perform simulations using both discrete and continuum models on a simplified two-dimensional geometry. The specification of the discrete model and derivation of the continuum model can be found in Section 4.1, which contains a formulation of the model both with and without gap junctions included.

We first neglect gap junctions in the simulations in Section 5.2.2 before introducing gap junctions at physiologically realistic coupling levels and repeating our simulations in Section 5.2.3. We then model diseased gap junctions with reduced coupling strength in Section 5.2.4, before increasing the conductance of the fast sodium channel in Section 5.2.5 to increase maximum upstroke velocity.

We do this using a simple geometry consisting of two-dimensional, rectangular cells that are stacked end-to-end to form a fibre. These fibres can then be stacked on top of each other with a layer of extracellular material in between as shown in Figure 5.1a. From this we create our periodic subunit consisting of a single cell as demonstrated in Figure 5.1b. In this simplified model, cells are only coupled to each other in one spatial dimension (the fibre direction), we have no gap junctions connecting cells, and we are considering straight fibres. This allows us to directly compare simulated conduction velocities and action potential propagation for both models.

5.2.1 Description of Simulations

Using the geometry in Figure 5.1, we take cells to be of dimensions 100 μm in length L by 15 μm in height H_i with a periodic subunit of dimensions 100 μm in length by 20 μm in height H, so that the cell occupies 75% of the total domain space. These figures lie within the physiologically realistic ranges outlined in [14] and [140]. The microscale conductivities are taken from [14] and are $\sigma_i = 0.25$ mS/mm, and $\sigma_e = 2.0$ mS/mm.

Using these values, we are able to calculate the homogenised conductivity tensors using the

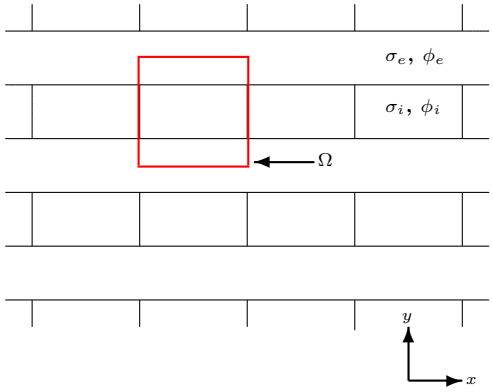

(a) A representation of cardiac cells in two dimensions. σ_i and σ_e are, respectively, the intracellular and extracellular conductivities, with ϕ_i and ϕ_e the potentials. The region Ω represents a periodic subunit containing both intracellular and extracellular space.

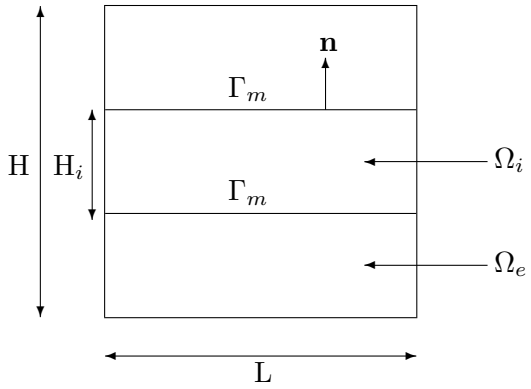

(b) A single periodic subunit of cell and extracellular matrix, as represented by Ω in Figure 5.1a. L represents the length of our subunit, with H its height and H_i the height of the intracellular portion. The intracellular domain is labelled Ω_i, and the extracellular domain Ω_e. The membrane between the two is labelled Γ_m.

Figure 5.1: *A simplified 2D representation of cardiac cells, joined in one direction to form parallel fibres.*

method outlined in Section 4.3. In that section, we showed that a rectangular cell with no gap junctions modelled has tensors given by

$$\Sigma_i = \begin{pmatrix} h\sigma_i & 0 \\ 0 & 0 \end{pmatrix}, \qquad \Sigma_e = \begin{pmatrix} (1-h)\sigma_e & 0 \\ 0 & 0 \end{pmatrix}, \tag{5.1}$$

where here the proportional height of the intracellular space $h = \mathrm{H}/\mathrm{H}_i = 0.75$. This gives us fibre direction conductivity values of $\Sigma_{i_{(1,1)}} = 0.1875$ mS/mm and $\Sigma_{e_{(1,1)}} = 0.5$ mS/mm, and it is worth noting that such values are closely matched to those used in recent bidomain simulations [106].

We simulate 50 ms of electrical activity on a domain of size 50 cells in the fibre direction by 1 cell in the perpendicular direction. The continuum geometry is thus a single block of tissue of dimensions 5 mm in length by 20 μm in height, with conductivity tensors given by Equation (5.1). The cell membrane is taken to be governed by Beeler-Reuter kinetics [5], with a membrane capacitance $c_m = 0.01$ μF/mm^2 and a fast sodium current maximum conductance of $g_{Na} = 0.04$ mS/mm^2, with all other model parameters found in [5]. In

order to induce a propagating action potential we apply a current stimulus of 1.0 μA/mm^2, starting at 5 ms and ending at 10 ms, to the whole cell membrane of the leftmost cell in the discrete case, and apply the same stimulus to the area corresponding to the first cell in the continuum case. Initial conditions are taken to be $\phi_i = V_{eq}$ and $\phi_e = 0$ everywhere in the discrete case, where V_{eq} is the equilibrium potential of the single-cell formulation of the Beeler-Reuter model and can again be found, along with initial values for the gating variables, in [5]. In the continuum case we take $V = V_{eq}$ and $\phi_e = 0$ everywhere as initial conditions.

We solve both the discrete and continuum systems of equations using a finite element method, and details of the derivation and implementation of this method can be found in Appendix A. In both cases the domain is composed of triangles known as elements, which are connected at their vertices by nodes, and in Figure 5.2 we show an example of the mesh used for continuum simulations. The mesh is contiguous, and the conductivities are uniform in each element and given by Equation (5.1) in the case where gap junctions are not modelled. In the discrete case we treat the intracellular and extracellular spaces as two distinct meshes, and we show an example for a single cell in Figure 5.3. The two domains are composed such that the positions of the nodes match up along the interface between the meshes (*i.e.* the cell membrane), which allows us to calculate the transmembrane potential at each node as the difference between the values of the intracellular and extracellular potentials at the node. There is a gap of 10 nm between the two domains, and this represents the width of the cell membrane with a value matching that observed in tissue [1]. In both discrete and continuum cases we define the spacestep in both x and y directions along the boundary of each domain, giving us a set of boundary nodes, and then generate internal nodes and all elements using the software package 'Triangle' [137] to ensure the quality of the resulting mesh.

The space- and timesteps used in each situation are chosen so that computed conduction velocity changes by less than 0.1% when the discretisation is refined either by halving the timestep or the spacestep. We calculate conduction velocity using the time taken for the action potential to travel from $x = 1.25$mm to $x = 3.75$mm in the fibre direction, with

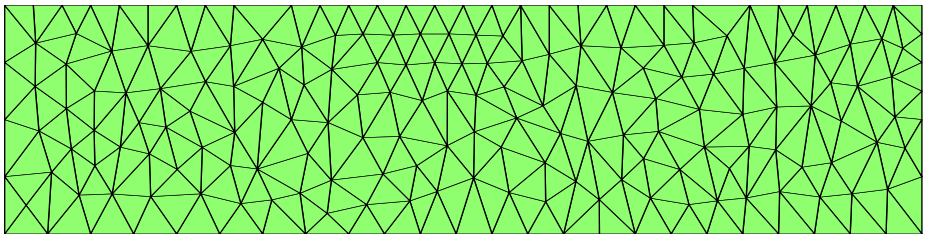

Figure 5.2: *An example of the continuum mesh used for continuum simulations.*

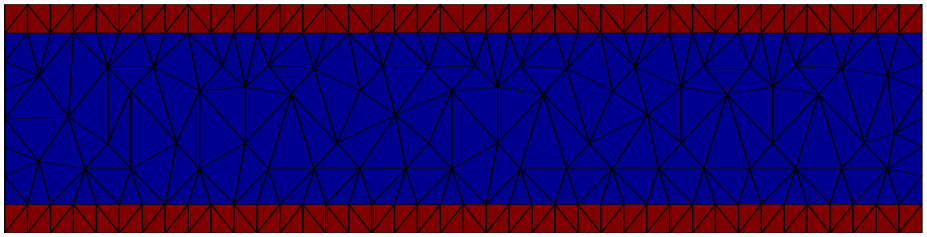

Figure 5.3: *An example of the mesh used for discrete simulations when gap junctions are not modelled. The intracellular space is coloured blue and the extracellular space is coloured red.*

distance measured from the end of the domain at which the electrical stimulus is applied. We quantify the time at which the action potential reaches a certain point along the fibre by the first moment at which the membrane potential becomes positive (so that $V > 0$ in the continuum case or $v > 0$ in the discrete case). This specification of the conduction velocity removes any 'edge effects' caused by the domain boundaries, as a propagating action potential will settle down to a travelling wave with a constant shape when it is not near the edge of a domain. Unless otherwise stated, the parameters above are used in all simulations.

To investigate the effect of gap junctions on the results of simulations, we will now perform the following computations, where the discrete model is given by Equations (4.1) to (4.4) and the continuum model is given by Equations (4.26a) and (4.29):

- run a control in which we do not include gap junctions;
- introduce gap junctions modelling healthy tissue where $\sigma_g = 0.0025$ mS/mm and $\delta = 0.05$ (from [65]). We have chosen $\sigma_g = \sigma_i/100$ based on the observation in Diaz *et al.* [31] that propagation is 10 times faster in the cell than the gap junction. As such (and as we are effectively considering a cable model too) we expect the conductivity

to be different by a factor of 100;

- investigate the membrane properties of the gap junction by varying the parameters I_g and c_g, using the parameter values given in Table 5.1;
- investigate the effect of changes in gap junction conductivity σ_g to model common diseased conditions (see Section 2.3.1.2); and
- increase the sodium conductance of the Beeler-Reuter model such that $g_{Na} = 0.4$ mS/mm^2 to see the influence of a steeper upstroke velocity on conduction.

In all cases we will plot the transmembrane potential as a function of distance along the fibre for a series of times.

5.2.2 Simulations with No Gap Junctions

A snapshot of the results of simulations without gap junctions at 15 ms (solid lines) and 20 ms (dotted lines) can be seen in Figure 5.4. As the graphs of the propagating action potential for both models are almost indistinguishable, the continuum system provides an accurate representation of the discrete problem. In such a situation, the problems concerning the derivation of the continuum model, highlighted in Section 3.4.1 and recapped in Section 5.1, are not applicable — the concept of a cell length does not exist in our geometry in the absence of gap junctions, so there is no separate microscale coordinate in the direction of the fibre (which is the direction of propagation and thus where the solution lengthscale is measured) — and thus the solutions match.

Due to this, we can be confident that the assumptions underlying the derivation of the continuum model hold when gap junctions are not included, and that the continuum system provides an accurate representation of the behaviour of the underlying discrete system. The fact that the continuum and discrete solutions match also provides confidence in the correctness of our numerical implementations of both systems. Using this as a baseline, we will now be able to attribute any discrepancy between the conduction velocities of the underlying systems to an inaccuracy in the continuum approximation introduced by modi-

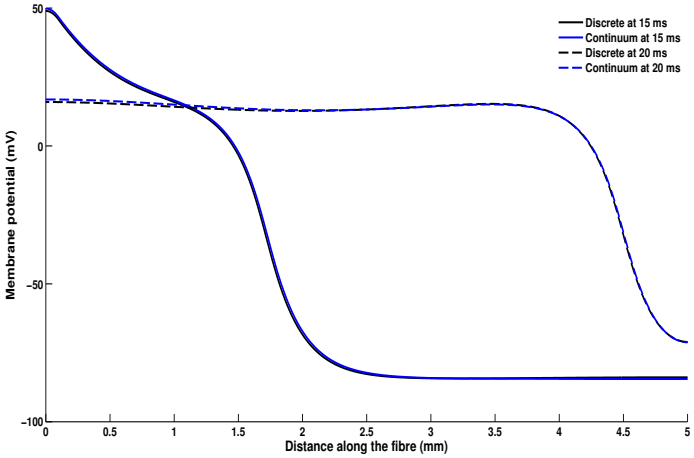

Figure 5.4: *A comparison of discrete and continuum models in which gap junctions are not modelled, denoted 'Base' in Table 5.1.*

fying the discrete system. This will be because the assumptions underlying the conversion to a continuum system cease to hold.

5.2.3 The Effect of Introducing Gap Junctions

To include gap junctions in the model we adapt our discrete geometry as shown in Figure 5.5. The resulting governing systems for both discrete and continuum models are those previously outlined in Section 4.2, and the discrete mesh used for simulations can be seen in Figure 5.6. We perform simulations using the same set of parameters given in the previous subsection and take gap junction length $\delta = 0.05$, with the parameters σ_g, c_g and I_g varied between simulations as shown in Table 5.1. In this case, we set the length and conductivity of gap junctions to model healthy tissue.

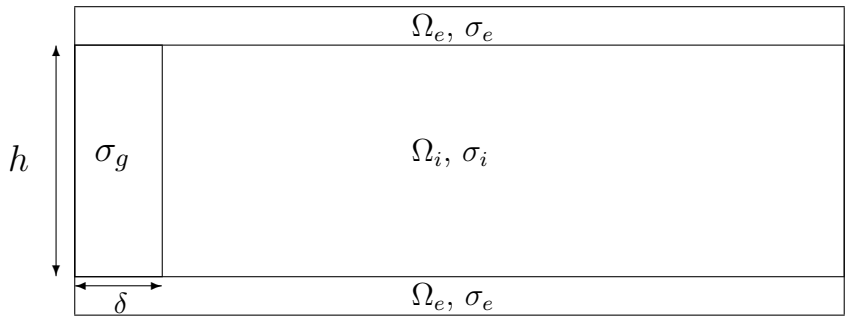

Figure 5.5: *A simple rectangular cell with a gap junction modelled as part of the intracellular space with width δ and conductivity σ_g.*

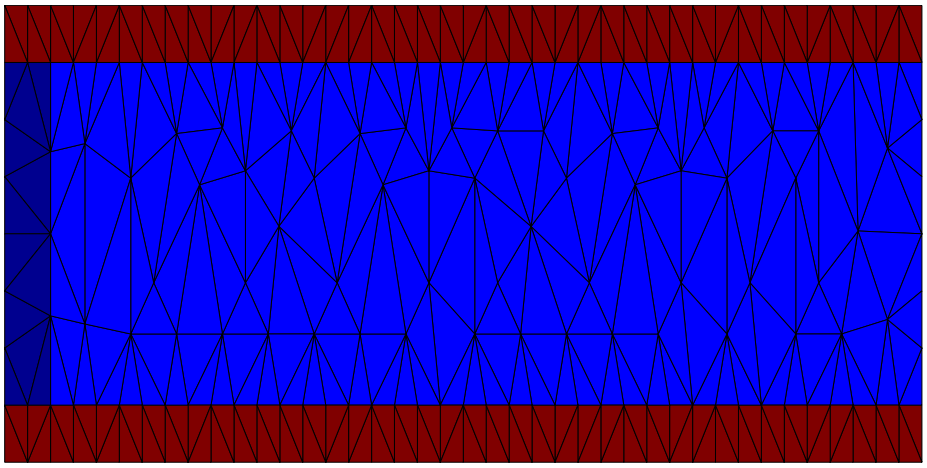

Figure 5.6: *An example of the mesh used in discrete simulations when gap junctions are included. The intracellular space is coloured light blue, the gap junction is coloured dark blue and the extracellular space is coloured red.*

A snapshot of results at 17.5 ms (solid lines) and 27.5 ms (dotted lines) is shown in Figure 5.7, using the membrane parameters given by 'Model 1' in Table 5.1. We see that the propagation speed in the continuum model does not quite match that of the discrete model, and in this case the conduction velocity of the wave for the discrete model is slightly lower than that for the continuum model by 3%. This can be observed by the small discrepancy in the solutions after 17.5 ms and the larger discrepancy after 27.5 ms, and matches previous results of simulations using a cable equation [55], where it was also found that propagation in a discrete model was slower compared to a continuum model when gap junctions were included.

Despite this, the magnitude of the conduction velocity difference is relatively minor in this case. Whilst the models do not completely match, it is likely that the continuum system provides a reasonable representation of the discrete system when modelling gap junctions at physiologically healthy coupling levels. In this situation, the propagating wave does slow as it passes through the gap junctions, but not by enough to completely invalidate the bidomain assumption. However we know that gap junction coupling strength is often reduced in diseased tissue, and so we will subsequently determine how this affects the magnitude of the discrepancy in conduction velocities.

In addition, we also notice that the discrete simulations display the form of 'stepped' action

Parameter values used in simulations						
Model	σ_g (mS/mm)	c_g (μF/mm^2)	I_g	CV (cont.)	CV (disc.)	% CV change
Base	0.25	0.01	1	0.2774	0.2790	0.5
1	0.0025	0.01	1	0.1279	0.1240	3.1
2	0.0025	0.01	0	0.1254	0.1215	3.2
3	0.0025	0.001	1	0.1352	0.1310	3.2
4	0.0025	0.001	0	0.1316	0.1280	2.8
5	0.0025	0	1	0.1355	0.1315	3.0
6	0.0025	0	0	0.1320	0.1285	2.7

Table 5.1: *The various parameter sets used in simulations to test the influence of the membrane capacitance and ionic current of a gap junction with associated computed conduction velocities (CV) measured in units of mm/ms.*

potential that is seen experimentally in [123]. As this did not occur in the absence of gap junctions, we suggest that gap junctions should be included in a model of cardiac electrophysiology at this spatial scale in order to capture this more detailed form of the propagating action potential observed both in experiments and in simulations where gap junctions are modelled [31, 166]. It is worth noting that the continuum model, in fact *any* continuum model, is unable to replicate this behaviour — by its nature it cannot have quantities that vary on the level of single cells, and when modelling gap junctions, intracellular conductivity varies on a sub-cellular level.

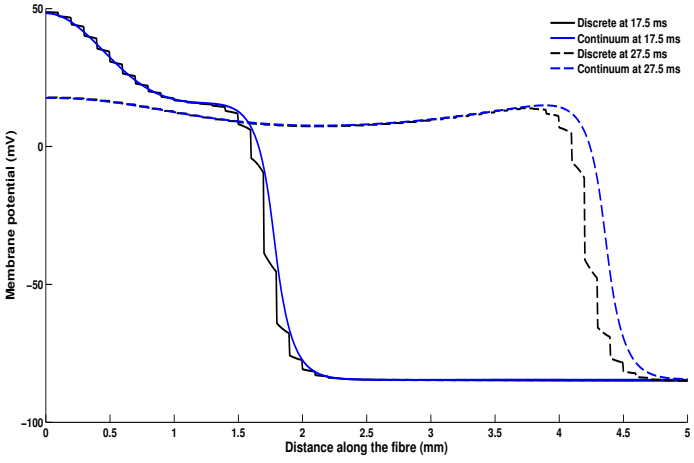

Figure 5.7: *A comparison of discrete and continuum models in which gap junctions are included as a region of reduced conductivity at one end of the cell, denoted 'Model 1' in Table 5.1.*

Having seen that gap junctions change the results of both discrete and continuum simula-

tions of cardiac electrophysiology, ultimately causing the solutions of the two types of model to diverge, we will now investigate whether the precise nature of the implementation of gap junctions further affects the characteristics of solutions. To that end, in Figure 5.8 we plot the results of simulations of both continuum (plot (a)) and discrete (plot (b)) versions of each gap junction membrane model specified in Table 5.1, shown at a time of 22.5 ms.

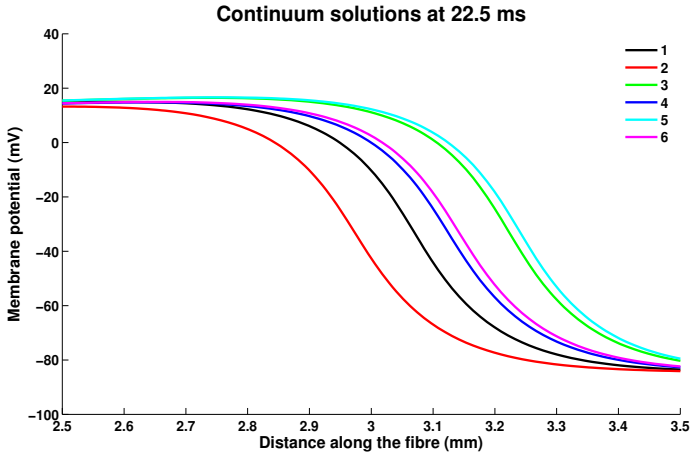

(a)

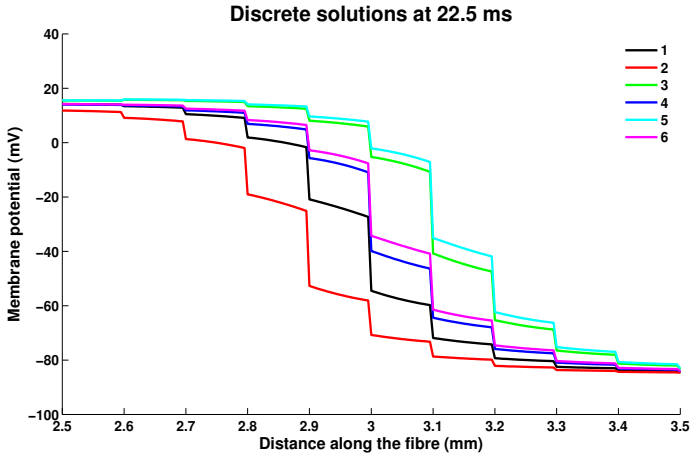

(b)

Figure 5.8: *A magnification of the upstroke of the action potential of the results of simulations using the parameter sets specified in Table 5.1. The numbers in the plot legend refer to the model numbers in the table.*

Whilst we see a difference in the position of the propagating wave and thus the underlying wavespeed between each of the models, this change is almost the same for both continuum and discrete simulations, suggesting that the major cause of the discrepancy between continuum and discrete solutions is the sharp change in conductivity between the cell and the

gap junction, and not the form of the gap junction membrane.

Considering the plots in more detail, we see that setting the ionic current to zero on the gap junction membrane — going from Model 1 to 2, Model 3 to 4 or Model 5 to 6 — slows down the propagated wave as would be expected, but by roughly an equal amount in the continuum and discrete cases. Reducing the capacitance of the gap junction membrane — going from Model 1 to 3 and Model 2 to 4 — again slows down propagation, this time by a larger amount. However, further reducing the capacitance to zero — going from Model 3 to 5 and Model 4 to 6 — has a negligible effect on solutions. Furthermore, we can see that the changes in the results of the discrete model are mirrored in the continuum system, specifically the associated change in propagation speed. As such, in the rest of this thesis we will use the gap junction membrane parameters from Model 1 (that is, $c_g = c_m$ and $I_g = 1$) as the value of these parameters does not seem to significantly affect the discrepancy between discrete and continuum simulations.

5.2.4 The Effect of Changing Gap Junction Conductivity

Under many diseased conditions such as ischaemia and heart failure the coupling strength of gap junctions is reduced, as discussed in Section 2.3.1.2. To model this, we reduce the parameter σ_g by a factor of ten from a normal physiological value so that $\sigma_g = \sigma_i/1000$. Whilst this is an extreme reduction in gap junction conductivity, such values have been observed in diseased tissue, for example in [4] and [69]. In Figure 5.9 we show the results of simulations of both the discrete and continuum models. We see that the underlying conduction velocities between models are markedly different (by 44%, compared to a 3% difference for normal coupling levels) and in addition the discrete solution around the upstroke of the action potential is highly stepped, which we surmise is due to the increased steepness of the upstroke.

We believe that this discrepancy occurs because of the rapid spatial variation in membrane potential in the discrete case as the action potential propagates through a gap junction of reduced conductivity. Here, the solution lengthscale is close to that of an individual cell,

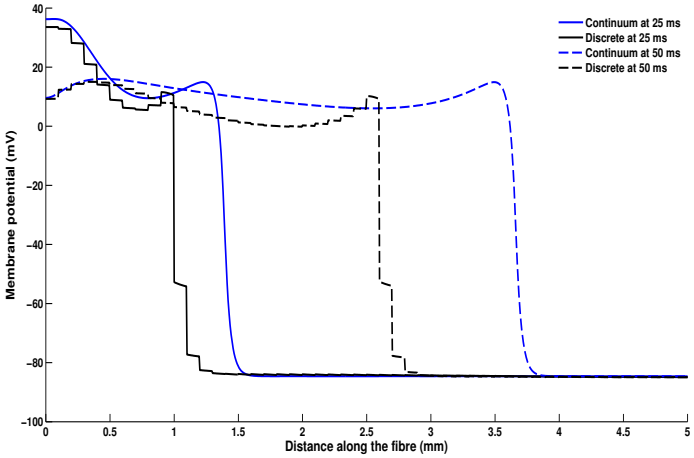

Figure 5.9: *A comparison of discrete and continuum models for a reduced value of gap junction conductivity ($\sigma_g = \sigma_i/1000$).*

and so the key assumption when deriving the continuum model (that we may ignore effects at cell-level and below) fails to hold. It is therefore the case that the bidomain equations, when derived using the inherent cell-level parameters of our system, may not be an accurate representation of the propagation of the action potential at this spatial scale if we include the effects of diseased gap junctions in the discrete model.

5.2.5 The Effect of Changing Upstroke Velocity

We have hypothesised that the steepness of the action potential upstroke reduces the length-scale of the solution and thus increases the parameter ϵ in our asymptotic expansion. This may affect the validity of the continuum approximation, and so we now investigate what effect changing the upstroke velocity has on the discrepancy between solutions of continuum and discrete models. To do this, we increase the sodium conductance g_{Na} of the Beeler-Reuter model used for the ionic current by a factor of ten, which has the effect of increasing the steepness of the action potential upstroke by around a factor of four (from 95 mV/ms to 362 mV/ms, which is still within the experimentally observed range [107, 162]).

We perform simulations using all other parameters from both 'Base' and 'Model 1' (see Table 5.1), and plot the results in Figure 5.10. We see that when gap junctions are not included, the discrete and continuum solutions match up almost identically for both values of g_{Na}

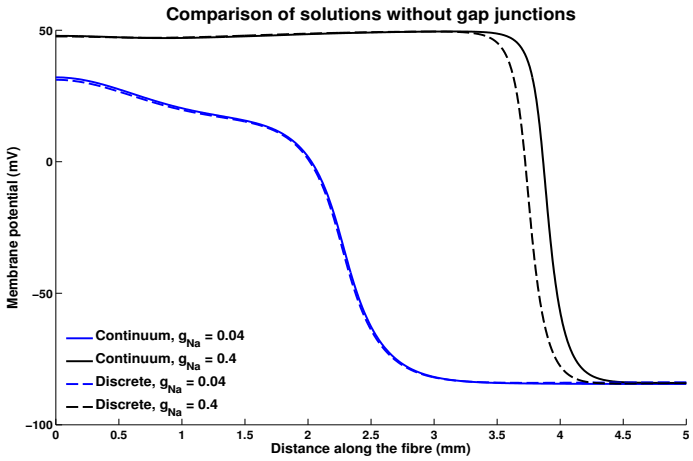

(a)

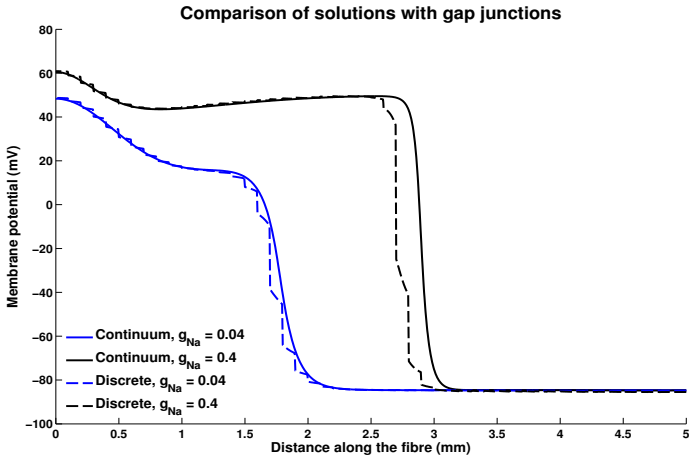

(b)

Figure 5.10: *Results of simulations for discrete and continuum models in which we have increased the sodium conductance g_{Na} by a factor of ten from the default value ($g_{Na} = 0.04$) used. Simulations were performed both without (plot (a)) and with (plot (b)) gap junctions.*

— this is expected as, for reasons outlined previously, a continuum model is appropriate and an accurate representation of the discrete system in the absence of gap junctions. However, when gap junctions are included ($\sigma_g = \sigma_i/100$, $\delta = 0.05$ as before) the discrepancy in conduction velocity observed under the normal sodium conductance value is slightly increased (from 3% to 6%) when we use the larger value for g_{Na}, which tells us that the effect of the upstroke velocity on the validity of the continuum model is not very significant compared to changes in gap junction conductivity.

5.3 How Changing the Discrete Geometry Affects Results of Simulations

In this section we consider the effect of changes in the discrete geometry on the results of both discrete and continuum simulations, and determine what factors affect the magnitude of the conduction velocity discrepancy between models. In Section 5.3.1 we change the length of the cells in our discrete geometry before considering a domain in which the geometry is non-periodic in Section 5.3.2.

5.3.1 The Effect of Changing Cell Length

We wish to see the effect that increasing the length of the cells in the underlying discrete geometry has on the results of discrete and continuum simulations, in order to model diseased conditions such as hypertrophy. Considering the definition of the ratio parameter ϵ, increasing cell length whilst keeping the solution lengthscale constant will increase ϵ, and thus a large enough cell length will invalidate the assumption that ϵ is small, provided that the solution lengthscale is not changed by modifying the geometry. We also note that increasing the cell length and correspondingly increasing the gap junction length will result in an identical continuum system, as the results of homogenisation are dependent on the relative length of the gap junction compared to the length of the cell. Therefore, if the discrete solution changes as we change cell length, a discrepancy will appear between

the results of continuum and discrete solutions and the continuum system will not give an accurate representation of the discrete case.

To this end we perform simulations using all other parameters from 'Model 1' in Table 5.1 and increase the cell length in increments from 50 μm to 300 μm, where 100 μm is the control value used in previous simulations. We keep gap junction length ratio δ constant at 0.05, so that the gap junction comprises 5% of the length of the whole cell unit. These upper and lower bounds are based on the experimental measurements of the physiological variation in mammalian myocyte length found in [130].

In Figure 5.11 we plot the results of the simulations outlined above at time points of 7.5 ms and 12.5 ms. We see that increasing cell length causes a drop in conduction velocity in the discrete case which is not accompanied by a drop in the continuum case, and in Table 5.2 we give the difference in conduction velocity between the continuum and discrete models for each value of cell length. Solutions using 50 μm cells match the continuum model well with a conduction velocity difference of 0.4% between the models. The conduction velocity discrepancy is moderate (3.1%) for cells of 100 μm but significant for lengths of 200 μm and above (ranging from 12.4%–24%). This is particularly noteworthy when considering cases such as cellular pathological hypertrophy [46], a condition known to be a precursor for heart failure [82] and one that is characterised by an increase in myocyte size. This result demonstrates that a continuum system is less accurate in predicting the conduction velocity of a discrete system for greater myocyte lengths.

Cell length (μm)	CV discrepancy (%)
50	0.4
100	3.1
150	7.1
200	12.4
250	17.3
300	24.0

Table 5.2: *The difference between conduction velocities (CV) of continuum and discrete models for varying cell length.*

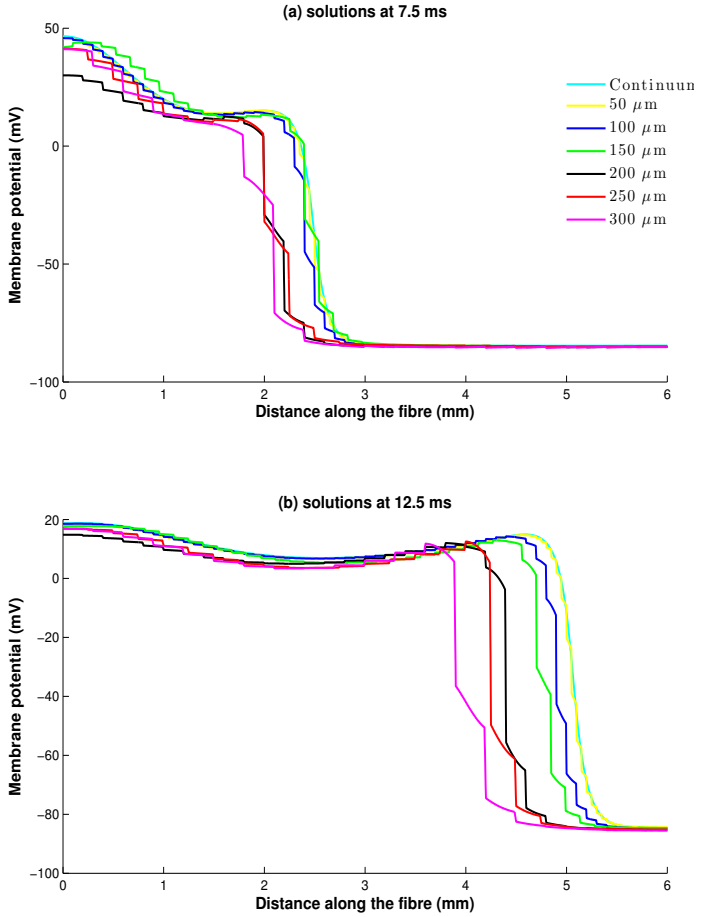

Figure 5.11: *Results of simulations for discrete and continuum models in which we have increased the cell length and kept the gap junction length δ constant.*

5.3.2 Using a Non-Periodic Discrete Lattice

In the derivation of the continuum model we assume that we have a periodic and repeatable subunit of tissue in the discrete case on which to homogenise. However, in reality cardiac cells will not be uniform. We wish to know if having small changes in the dimensions of the cells, and thus not quite a true periodic domain, will cause the results of simulations using discrete and continuum models to diverge. To test this, we perform a simulation in which we draw cell lengths from a uniform distribution covering the interval [50, 150] μm, and where gap junction length is fixed at 5 μm. Looking back at Section 5.3.1, we observed a difference of around 6% in discrete conduction velocity for cells of 50 μm compared to cells of 150 μm, which is a non-trivial but moderate change, and we now wish to see what the conduction velocity is for cells that vary between these two lengths. If it is not similar to that obtained using cells of length 100 μm, *i.e.* the mean length of the domain, then the variation of cell length has invalidated the assumption that we have a nearly periodic and repeating geometry.

As in previous simulations we use a domain size of 50 cells in the fibre direction, and the conductivity tensor used in the continuum model is derived by homogenising this 50-cell 'unit'. In Figure 5.12 we plot the results of simulations for both continuum and discrete models, as well as the results using a discrete model with a uniform cell length of 100 μm. We see that the non-uniform domain exhibits almost identical behaviour in terms of underlying conduction velocity as the uniform domain, with a difference of less than 0.5%. As such, we believe that a moderate variation in the length of cardiac cells is unlikely to affect conduction velocity.

5.4 Summary

In this chapter we have performed a detailed computational study comparing the results of discrete and continuum simulations when modelling no gap junctions, gap junctions at physiologically realistic coupling levels, and gap junctions with parameters representing

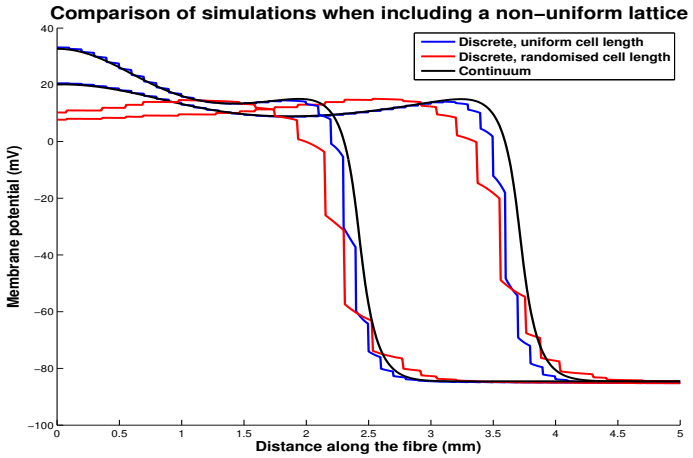

Figure 5.12: *Results of simulations in which we have used a non-periodic discrete lattice at times of 20 ms (left) and 25 ms (right).*

diseased states such as ischaemia, fibrillation and hypertrophy. We have also changed the discrete geometry both by increasing cell length and by randomly varying cell length, and again compared the results of discrete and continuum simulations.

In Section 5.2.2 we saw that when gap junctions are not included in a discrete model of tissue-level cardiac electrophysiology, the resulting continuum system gives almost identical solutions to the discrete problem both in terms of conduction velocity and the shape of the propagating wave.

However, we found in Section 5.2.3 that when gap junctions are included at physiologically healthy coupling levels, the continuum system is unable to predict exactly the effect that these junctions will have on action potential propagation. We observed a 3% difference in conduction velocities for gap junctions, and in addition saw that the continuum system does not allow for a 'stepped' action potential — the large jumps in potential across gap junctions seen in the discrete case were not exhibited in the continuum case.

When modelling diseased gap junctions, this small discrepancy in conduction velocity is exacerbated, as we saw in Section 5.2.4. In the case of a reduction in the conductivity of gap junctions we saw a 44% difference in conduction velocity. This tells us that for diseased tissue with reduced gap junction coupling strength, a continuum model is not appropriate to predict conduction velocity and will differ significantly from the discrete system from

which it is derived. When we increased the sodium conductance of the single-cell model used to reflect the steeper wave upstroke found in certain commonly-used cell models [107], we saw a small increase in the discrepancy between conduction velocities.

In Section 5.3 we discussed how changing the geometry of the discrete system under consideration affects the results of both discrete and continuum simulations. We observed that the moderate discrepancy between underlying conduction velocities of the two models seen when modelling myocytes of length 100 μm becomes much greater when myocyte length increases, with the difference between models increasing from 3.1% to 24% as the cell length was increased from 100 μm to 300 μm. This suggests that a continuum system is not appropriate for modelling tissue with elongated cells, for example in cases of cardiac hypertrophy. We also saw that using a non-periodic discrete lattice where cells vary in length uniformly over the range $[50, 150]$ μm did not significantly alter either the continuum or discrete solutions, suggesting that the assumption that our discrete domain consists of periodic units is valid when the cell geometry varies over this sort of physiological range.

Overall, we have demonstrated that the introduction of gap junctions has a marked effect on the ability of a continuum model to replicate the behaviour of the underlying discrete system. Most notably, modelling gap junctions with parameters representing common diseased states gives a significant difference in conduction velocity between models. We surmise that this is because the assumptions made in the derivation of the continuum model cease to hold. Specifically, the ratio parameter ϵ increases in the cases where we see a difference between model solutions, and as such the assumption that this parameter can be treated as negligible ceases to be true. As such, we believe that a discrete model is required to accurately model the propagation of an action potential in these cases.

The above paragraph tells us that the continuum model has been shown to provide a good representation of the underlying discrete case when modelling healthy tissue. We have seen how the microstructure, such as gap junctions, affects the homogenised conductivity tensors for rectangular cells in Chapter 4. We have also seen how this affects the results of discrete and continuum models in Chapter 5. As a next step, we consider cells with a more realistic geometry in Chapter 6. Due to the complexity of performing discrete simulations using these

geometries, we will focus on the calculation of the homogenised conductivity tensors in a manner that extends the work of Chapter 4. We will study how changes in the shape of the cell membrane affect conductivity, how replicating the brick-wall packing nature of cardiac cells affects the predicted continuum conductivity, and the effect of including off-fibre gap junctions on conductivity.

Chapter 6

How the Geometry of Cardiac Cells Affects the Homogenised Conductivity Tensors

Contents

In this chapter, we extend the work of Chapter 4 by considering the effect on the homogenised conductivity tensors of using a more realistic cell membrane shape, packing cells into a brick-wall structure, and including cell-to-cell connections in the off-fibre direction. As analytic results are not possible for a more general cell shape, we perform a computational study.

In Section 6.1 we parameterise a cardiac cell in two dimensions by cell height, cell membrane curvature, gap junction height, gap junction width, and gap junction conductivity. We investigate how changing each of these parameters in isolation affects both intracellular and extracellular homogenised conductivity tensors in Section 6.2.

Then, in Section 6.3 we modify the geometry to take account of the brick-wall structure of cardiac tissue described earlier in Section 2.3. We consider the combined effect of changing both cell height and the offset of one fibre with respect to another on the extracellular conductivity tensor.

Finally, in Section 6.4 we modify the cell geometry to include gap junctions connecting cells in the off-fibre direction. We look at the intracellular conductivity in both fibre and off-fibre directions, as well as the intracellular anisotropy ratio that is calculated from these two quantities, and determine how they are affected by changes in the width and conductivity of off-fibre gap junctions.

6.1 Creating a Parameterised Geometry Consisting of Cells with Curved Cell Membranes

In Chapter 4 we looked at the effect of gap junctions on the homogenised conductivity tensors using a rectangular geometry, and found that gap junctions had a significant effect on the tensors and the predicted conduction velocity, but also noted that this simple geometry was in essence replicating a resistor network and did not include some important properties of cardiac tissue.

Given that cardiac cells are not rectangular in shape, we now wish to use a more realistic cell shape in homogenised conductivity calculations to obtain more representative and physiologically accurate results. In general, however, a non-rectangular cell geometry in two or three spatial dimensions precludes the exact solution of the conductivity tensors from being calculated in the manner of Chapter 4. As such, we must numerically approximate the solutions to the equations governing the homogenised conductivity tensors (repeated at the start of Section 6.1.1) on a more general geometry. We do so using a finite element method (see Appendix A), and since the governing equations that must be solved are time-independent elliptic equations we are able to use an extremely fine spatial mesh (with around 100,000 triangles or elements per cell) without the solution method becoming computationally intractable.

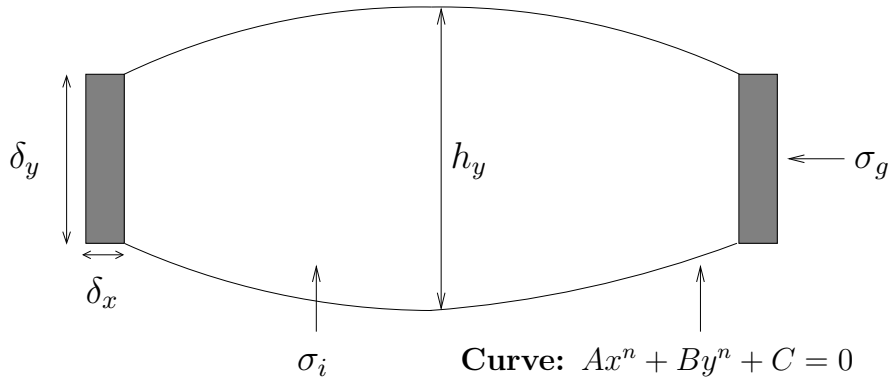

Figure 6.1: *A schematic of our parameterisation of the shape of a cardiac cell in two dimensions. This aims to provide a more realistic representation of the cell membrane. Example images upon which we based our cell can be found in [134].*

To provide this more realistic representation of cardiac cells in two dimensions, we consider cells with curved membranes as depicted in Figure 6.1. This has the effect of introducing two additional parameters into the geometry: the cell height h_y now differs from the gap junction height δ_y with both separately prescribed; and the curvature of the membrane is dependent on a parameter n, which is the exponent of the function that determines its shape. The cell membrane is curved so that it is widest in the middle of the cell, tapering to a narrower section at each end, where a gap junction is located. This geometry will be used to gain insight into how the shape of the cell membrane and the shape, size and conductivity of gap junctions affects both intracellular and extracellular homogenised conductivity tensors. In this parametric framework, the shape of the cell is represented by the following quantities:

- σ_i and σ_g, the conductivities (in mS/mm) of the cell and gap junctions respectively;
- δ_x, the length of the gap junctions (note that we now model a segment of gap junction at both ends of the cell as opposed to just one end, so that this quantity is analogous to half of the δ quantity used to represent gap junction length in previous chapters);
- δ_y, the height of the gap junctions;
- h_y, the maximum height of the cell; and
- n: the curvature parameter of the cell membrane. The membrane is given by the function $Ax^n + By^n + C = 0$, defined on each quarter of the cell. Here, A, B and C are scalars that vary depending on the quarter under consideration such that the four membrane sections are reflectively symmetric about the geometric centre of the cell.

In the list above, the quantities δ_x, δ_y and h_y do not have units as they represent size as a fraction of the whole cell unit, which is taken to be the unit square as previously explained in Chapter 4. The extracellular matrix is then defined as the remainder of the unit square that is not taken up by either the cell or the gap junctions, and has a scalar conductivity σ_e. As the functional representation of the cell membrane curvature may prove unintuitive when attempting to visualise the geometry, we have plotted the shape that the cell membrane takes for a range of values of n in Figure 6.2. It is worth noting that we will take positive integer values of n, and that increasing n has the qualitative effect of changing the cell

membrane shape in each quarter from a single straight line at $n = 1$ to a single curved line of increasing curvature, to (as $n \to \infty$) two intersecting straight lines that would make the intracellular space rectangular in shape.

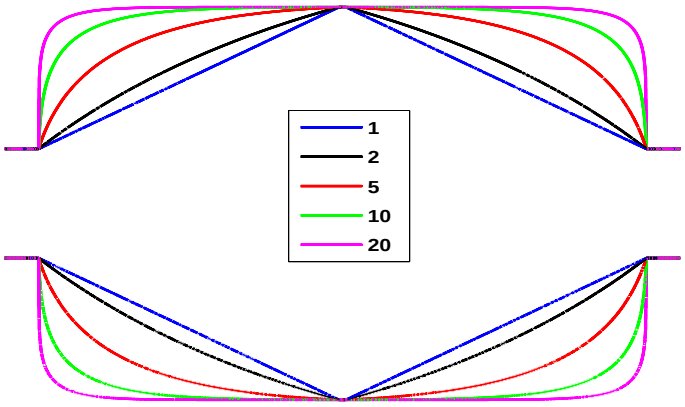

Figure 6.2: *A visualisation of the shape of the cell membrane for different values of the curvature parameter n. Here, we set gap junction height $\delta_y = 0.5$ to better see how the curvature shape changes.*

6.1.1 Outline of Calculations

As a reminder, the intracellular homogenised conductivity tensor Σ_i satisfies

$$\Sigma_i = \frac{1}{V_{\text{unit}}} \int_{\Omega_i} \sigma_i \left(I + \frac{\partial \mathbf{W}^i}{\partial \mathbf{z}} \right) \mathrm{d}V_{\mathbf{z}}, \tag{6.1}$$

where V_{unit} is the volume of our periodic subunit. The intracellular weight functions $\mathbf{W}^i$ satisfy

$$\nabla_{\mathbf{z}} \cdot (\sigma_i (I + \nabla_{\mathbf{z}} \mathbf{W}^i)) = 0, \qquad \mathbf{z} \in \Omega_i, \tag{6.2}$$

with boundary conditions

$$\mathbf{n} \cdot (I + \nabla_{\mathbf{z}} \mathbf{W}^i) = 0, \qquad \mathbf{z} \in \Gamma_m, \tag{6.3}$$

and are periodic in $\mathbf{z}$ with zero mean. Similarly the extracellular homogenised conductivity tensor Σ_e satisfies

$$\Sigma_e = \frac{1}{V_{\text{unit}}} \int_{\Omega_e} \sigma_e \left(I + \frac{\partial \mathbf{W}^e}{\partial \mathbf{z}} \right) \mathrm{d}V_{\mathbf{z}}, \tag{6.4}$$

and the extracellular weight functions $\mathbf{W}^e$ satisfy

$$\nabla_{\mathbf{z}} \cdot (\sigma_e (I + \nabla_{\mathbf{z}} W^e)) = 0, \qquad \mathbf{z} \in \Omega_e, \tag{6.5}$$

with boundary conditions

$$\mathbf{n} \cdot (I + \nabla_{\mathbf{z}} W^e) = 0, \qquad \mathbf{z} \in \Gamma_m. \tag{6.6}$$

We now solve the above equations that govern the homogenised conductivity tensors. To do this, we create a high-quality triangular mesh of the geometry under consideration using the 'Triangle' software [137] which results in a single cell being approximated by around 100,000 triangles, allowing us to both represent the geometry and to compute the numerical solution accurately. An example of such a mesh is given in Figure 6.3, in which the parameters used are the control parameters given in Table 6.1: $\delta_x = 0.05$, $\delta_y = 0.75$, $h_y = 0.9$, and $n = 5$. We then approximate the solution to the governing equation using a finite element method [120]. In order to ensure accuracy of the results generated, tolerances during both mesh creation and finite element solution are set such that upon mesh refinement, solutions

to the governing equations change by less than one part in a million.

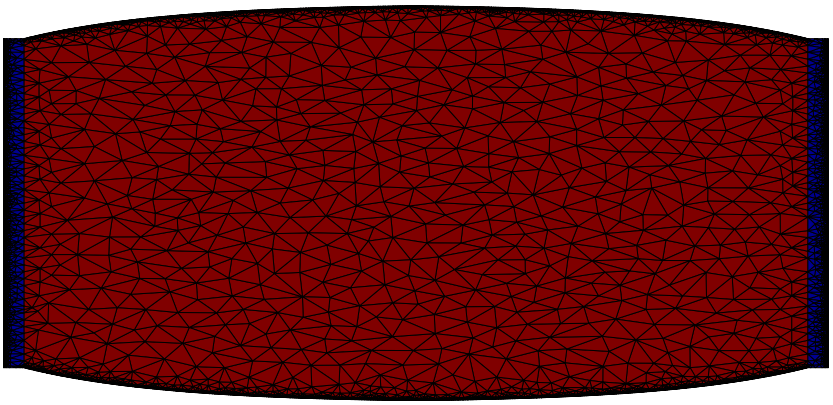

Figure 6.3: *An example of a mesh used for calculations. In this example the number of elements has been greatly reduced for the purposes of visualisation. The intracellular space is coloured red and the gap junction is coloured blue.*

We then calculate the intracellular and extracellular homogenised conductivity tensors and the surface-area-to-volume ratio using the values summarised in Table 6.1 for the six quantities σ_i, σ_g, δ_x, δ_y, h_y and n. For all but gap junction conductivity σ_g, the parameter values are varied linearly between the two values outlined in the table. Gap junction conductivity is varied logarithmically across three orders of magnitude, as this method provides a better spread of data points for considering changes in conductivity when σ_g is small.

For each set of calculations we will plot the two conductivity tensors used in the bidomain equations, Σ_i and Σ_e, as well as the percentage change in these values when compared to the control value. We will also plot the surface-area-to-volume ratio χ, as we wish to consider the effect that changing χ has on conductivity in combination with changes in the homogenised conductivity tensors. Including the effects of changes in χ gives rise to some interesting possibilities — for example, when changing a parameter has the effect of increasing both conductivity and surface-area-to-volume ratio, it is not clear how the ratio of these quantities will behave and thus how the overall conductivity will change.

On this geometry, cells are only connected in the fibre direction, and so the conductivity tensors will only have one nonzero entry corresponding to conduction in the fibre direction (as discussed in Section 4.3.2). Due to this we can also plot the relative conduction velocities

predicted by the conductivity tensors — as we are considering propagation in one spatial dimension, we can reduce the continuum system to a monodomain formulation, and so (see Section 3.2 for a specification of the monodomain equations) the fibre direction conduction velocity of the continuum system is proportional to

$$\sqrt{\frac{\Sigma_{i_{(1,1)}}\Sigma_{e_{(1,1)}}}{\chi(\Sigma_{i_{(1,1)}}+\Sigma_{e_{(1,1)}})}}, \tag{6.7}$$

as all other entries of Σ_i and Σ_e are zero.

Parameter values used in simulations						
Figure	σ_i (mS/mm)	σ_g (mS/mm)	δ_x	δ_y	h_y	n
6.6	0.25	0.0025	0.05	0.75	$0.75 \rightarrow 0.9975$	5
6.7	0.25	0.0025	0.05	0.75	0.9	$1 \rightarrow 20$
6.8	0.25	0.0025	0.05	$0.1 \rightarrow 0.9$	0.9	5
6.9	0.25	0.0025	$0.01 \rightarrow 0.1$	0.75	0.9	5
6.10	0.25	$0.25 \rightarrow 0.00025$	0.05	0.75	0.9	5
6.11	$0.1 \rightarrow 1$	0.0025	0.05	0.75	0.9	5

Table 6.1: *The various parameter sets used in calculations of the homogenised conductivity tensor for a domain consisting of discrete cells of the form outlined in Figure 6.1.*

6.1.2 Weight Functions

In Figure 6.4 and Figure 6.5 we show solutions to the equations governing the intracellular and extracellular weight functions for the cell given by the default parameter set specified in Section 6.1.1. From these, we can visualise how the weight functions have changed from the case where we calculated them for rectangular cells in Chapter 4.

We see in Figure 6.4 that the fibre direction intracellular weight function looks very similar to those seen in Section 4.3.5 for rectangular cells. It is piecewise linear in the cell and the gap junction, is constant in the off-fibre direction, and has sharp gradient changes at conductivity interfaces. The fibre direction extracellular weight function is quite different from the constant-gradient form that we found for rectangular cells, as shown in Figure 6.5. We see that the weight function varies smoothly across the length of the cell, from zero at

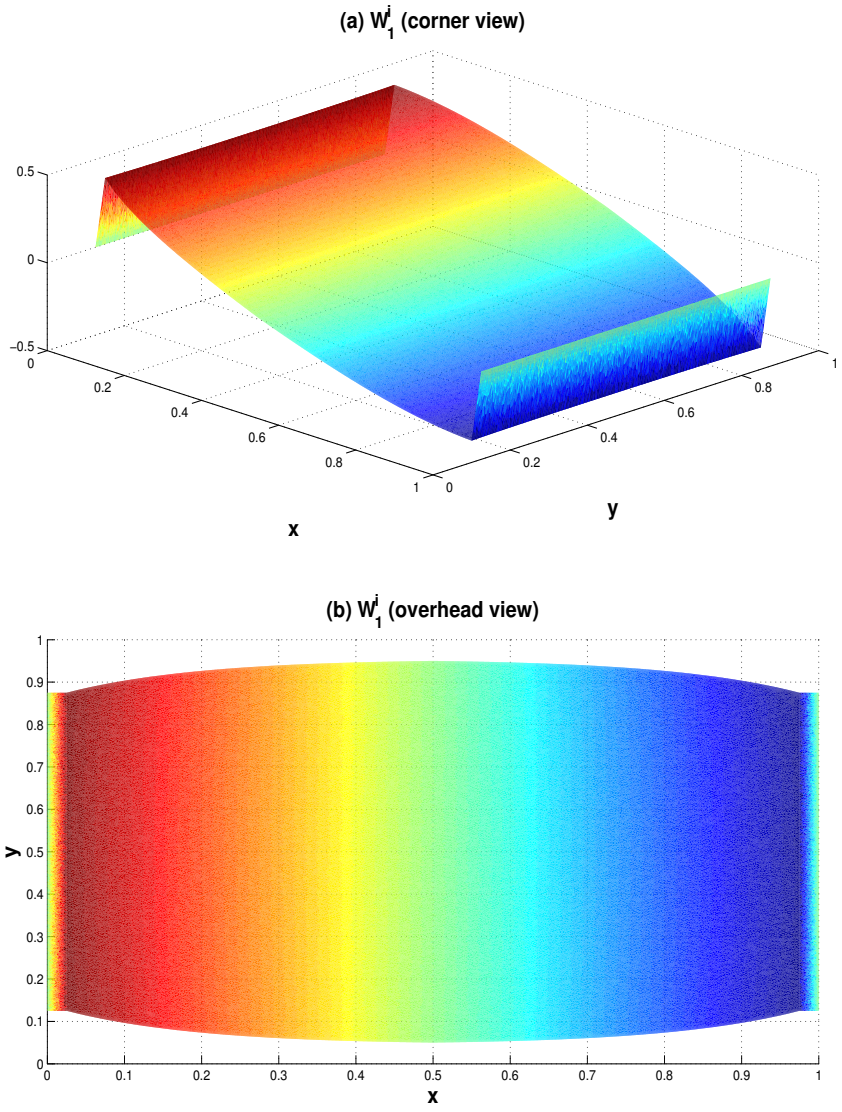

Figure 6.4: *Solutions to the governing equation* (6.2) *for the fibre-direction intracellular weight function using the default cell parameters outlined in Section 6.1.1. The two plots show the same results, viewed from different angles.*

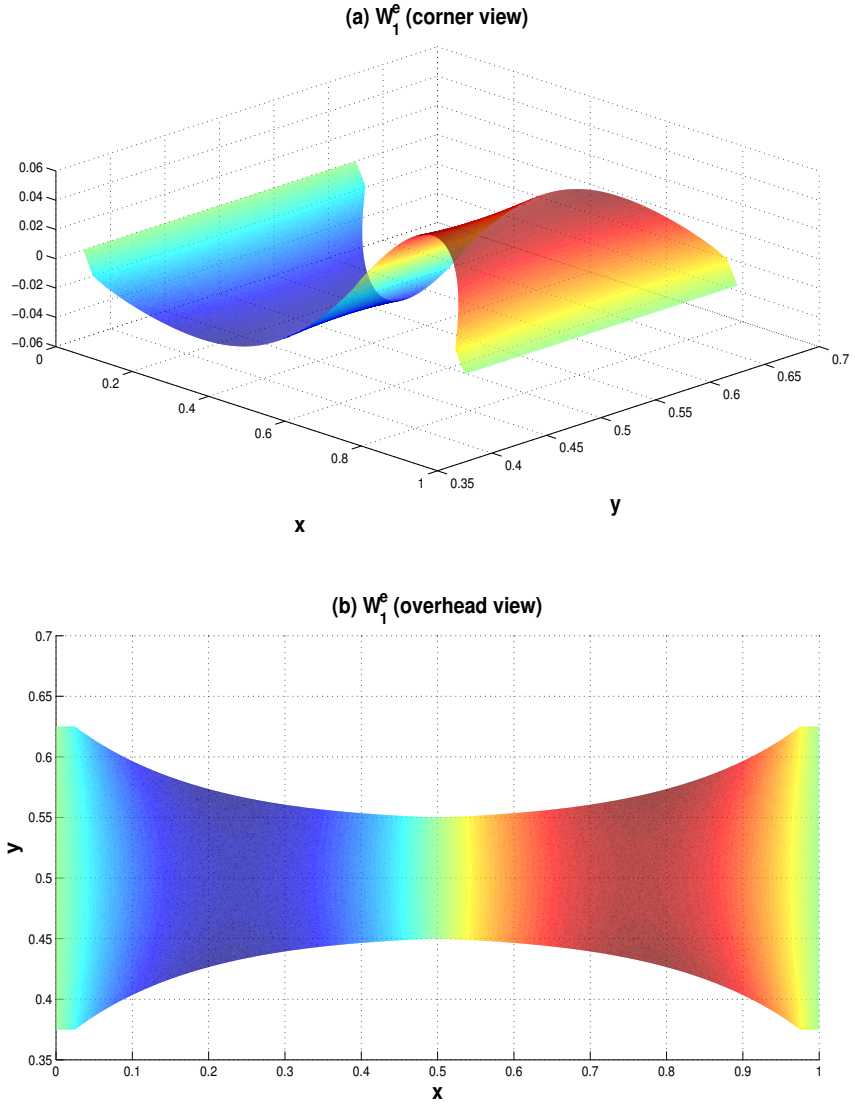

Figure 6.5: *Solutions to the governing equation* (6.5) *for the fibre direction extracellular weight function using the default cell parameters outlined in Section 6.1.1. The two plots show the same results, viewed from different angles.*

the cell ends to a negative value one quarter of the way down the cell, to zero again in the middle of the cell to a positive value three quarters of the way down the cell, and finally back to zero. The function is antisymmetric with respect to the middle of the cell, and as such any contribution to conductivity from one point is cancelled out by the matching point on the other half of the cell (due to the fact that the extracellular conductivity σ_e is a constant scalar). This means that the contribution to conductivity in this case is directly related to the area of the extracellular space.

6.2 Results of Calculations

In this section we perform simulations in which we vary a single parameter in our geometric framework in isolation. We then analyse the results to determine how each change affects the homogenised conductivity tensors, the surface-area-to-volume ratio, and the predicted conduction velocity.

In the following subsections we plot results of calculations of the homogenised conductivity tensors for the parameter values outlined in Table 6.1, and interpret the data provided by these calculations. Control values are taken to match those used in simulations in Chapter 5 where applicable, and for newly introduced parameters we choose control values to give an intracellular space whose volume fraction of the total volume matches that observed experimentally [14, 140]. As we are considering cells that are only connected in the fibre direction, all computed values represent the fibre direction (1,1) component of the conductivity tensors.

6.2.1 The Effect of Varying Cell Height, h_y

The first parameter we vary is the height of the cell h_y. We begin with an initial value of $h_y = 0.75$, which gives an identical geometry to the rectangles we considered in Chapter 4 and Chapter 5. We then increase the cell height up to a maximum value of 0.9975, as a value of 1 in this case would mean that cells would touch in the off-fibre direction and thus give cross-fibre coupling. This would force the extracellular conductivity to be zero in both

directions as discussed in Section 4.3.2, and so we take 0.9975 as a sensible upper bound.

In Figure 6.6 we plot results of the calculations, and see in plots (a) and (b) that increasing cell height from the initial value of 0.75 to the control value of 0.9 gives only a slight increase in intracellular conductivity of around 2%, but a much larger decrease in extracellular conductivity, which falls to less than 60% of its original value. This is because increasing cell height constricts the extracellular space at the centre of the cell in the fibre direction, making conduction difficult: in fact, the extracellular conductivity goes to zero as the cell height approaches 1. The intracellular conductivity does not increase concomitantly as there is still a gap junction of unchanging conductance through which the signal must propagate, which dominates the value of intracellular conductivity. To see this, we can interpret the cell and gap junction as resistors in series as we did in Section 4.4.1, and note that as the resistance of the second resistor (the intracellular space) decreases, the overall domain resistance is floored at that of the first resistor (the gap junction), and so domain conductance is capped at the inverse of this quantity.

We see in plot (d) of Figure 6.6 that conduction velocity changes are small when the cell height is not close to 1, with a decrease of 2% when we increase cell height from 0.75 to 0.9. When cell height is increased beyond the control value of 0.9 the conduction velocity starts to drop more significantly. This is slow at first but rapidly accelerates as the cell height approaches 1, as here the extracellular conductivity goes to zero and consequently so does conduction velocity. Throughout the range of cell height changes, we see negligible changes of around 0.1% in the surface-area-to-volume ratio χ, as shown in plot (c). These results tell us that changes in cell height can lead to large changes in conduction velocity when neighbouring cells are packed tightly together.

6.2.2 The Effect of Varying Cell Membrane Curvature, n

We now investigate varying the curvature of the cell membrane, parameterised by the exponent n in the function that determines its shape. We begin with an initial value of 1 that, although it represents an unrealistic cell shape, provides an extreme value when

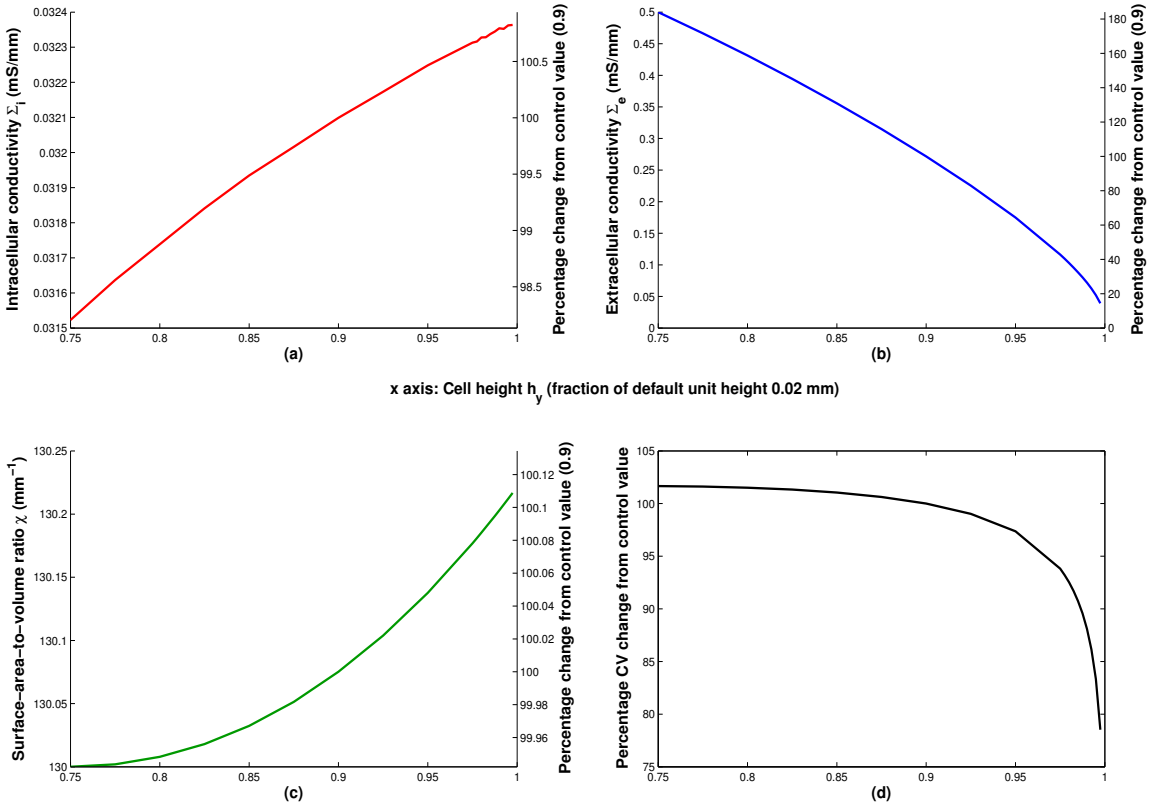

Figure 6.6: *Values of fibre direction conductivities (a,b), surface-area-to-volume ratio (c) and relative conduction velocity (d) as we change the height of the unit cell, h_y.*

considering a wide range of membrane curvatures. We increase n in whole units up to a maximum value of 20, and some of the resulting membrane shapes are plotted in Figure 6.2. In Figure 6.7 we plot the results of calculations, and see in plot (a) that changing curvature has a minimal impact on intracellular conductivity, and in fact for larger values of n the quantity is almost unchanging. Considering plot (b) we see that extracellular conductivity reduces more significantly as the curvature of the cell increases, with a drop of over 40% between the lower and upper bounds of n. We see from plot (c) that χ increases very slowly with curvature, and changes by less than 1% over the range considered.

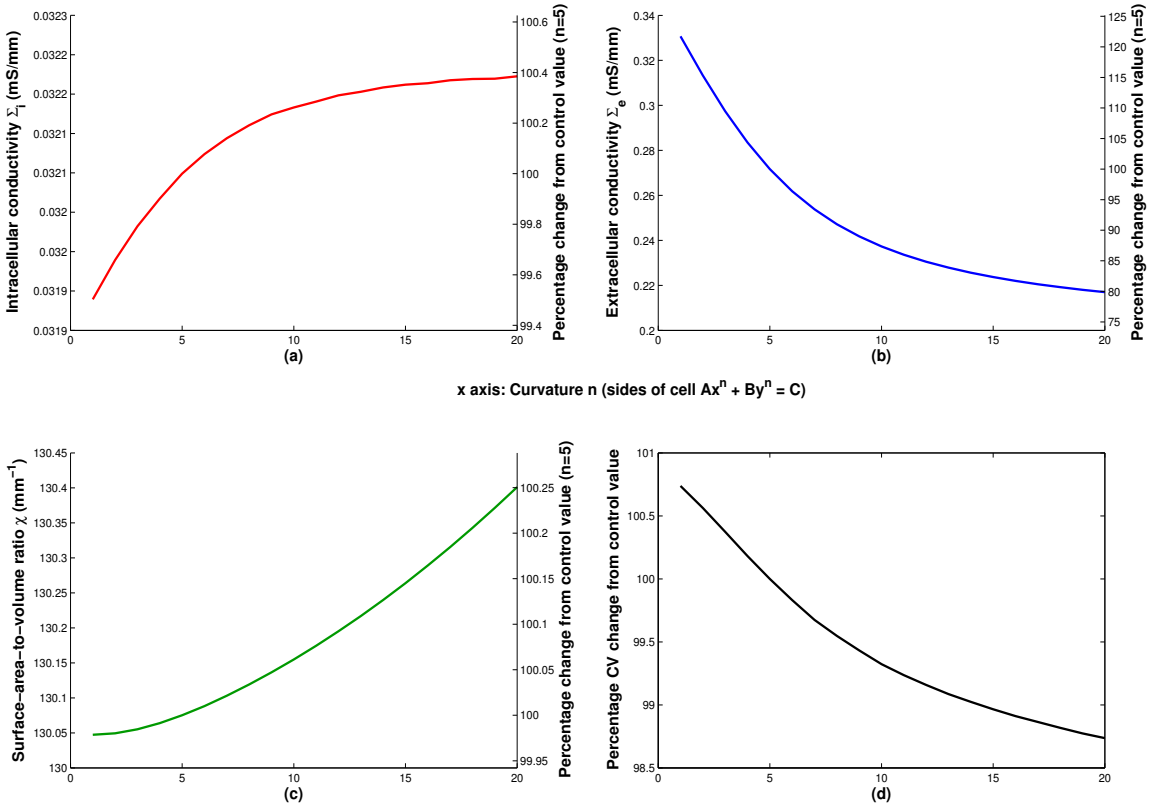

Figure 6.7: *Values of fibre direction conductivities (a,b), surface-area-to-volume ratio (c) and relative conduction velocity (d) as we change the curvature of the cell membrane n.*

Conduction velocity drops by a small amount, just over 2%, as we increase curvature, and this is shown in plot (d). This drop is expected as the decrease in Σ_e is much larger than the increase in Σ_i, and also because χ is increasing. However, the magnitude of the drop is small compared to both the decrease in Σ_e and the increase in χ, which suggests that the value of Σ_i dominates the value of conduction velocity in this case, and as explained in

Section 4.3.6 this is due to the relative sizes of the two tensors. Overall, that the change in conduction velocity is small suggests cell membrane curvature is not particularly important in determining conductivity.

6.2.3 The Effect of Varying Gap Junction Height, δ_y

Next, we vary the height of the gap junction δ_y. In this case the lower bound is 0.1, the upper bound is 0.9 and we perform calculations in steps of 0.1. In Figure 6.8 we plot the results of the calculations. We see in plot (a) that the intracellular conductivity increases rapidly as junction height increases, such that the final value is around six times the starting value, and in plot (b) that the extracellular conductivity decreases steadily with a final value of 55% of the starting value. The surface-area-to-volume ratio χ increases roughly linearly, with an overall change of 45%.

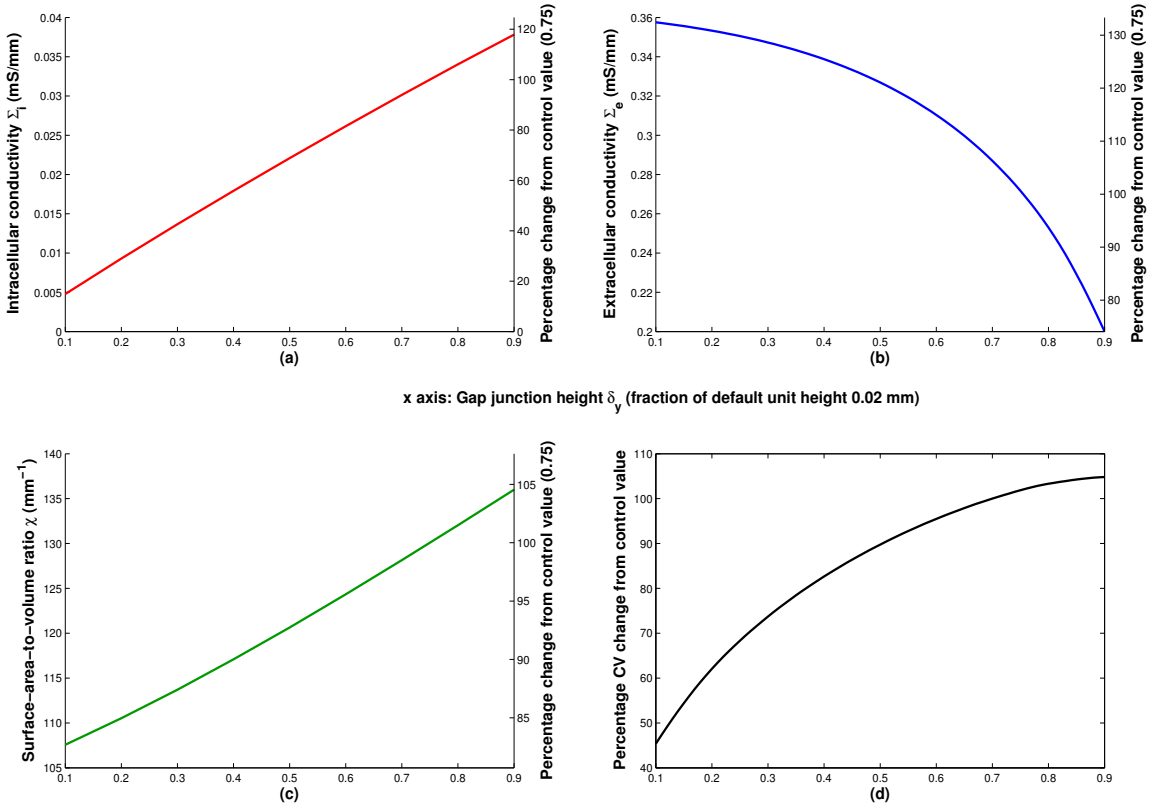

Figure 6.8: *Values of fibre direction conductivities (a,b), surface-area-to-volume ratio (c) and relative conduction velocity (d) as we change the height of the gap junctions δ_y.*

Given the rapid increase in intracellular conductivity, the conduction velocity increases

significantly as gap junction height increases, as demonstrated by plot (d). This change mirrors the increase in intracellular conductivity, as the conduction velocity increases to 230% of its starting value over the parameter range, and intracellular conductivity increases by a factor of around six. In an isolated framework where conduction velocity is proportional to the square root of intracellular conductivity, this sixfold change in Σ_i would give rise to a conduction velocity change by a factor of $\sqrt{6} = 2.44$, or to 244% of its starting value, which tells us that conduction velocity changes are almost solely due to intracellular conductivity changes. The results of this section tell us that gap junction height is an important factor in determining conduction velocity.

6.2.4 The Effect of Varying Gap Junction Length, δ_x

We now vary the length of the gap junctions, δ_x, between a lower bound of 0.005 and an upper bound of 0.1, so that the gap junction comprises between 0.5% and 10% of the length of the cell. As it has been observed experimentally that gap junctions can be anywhere up to 10% of the length of the cell [65], our selected parameter range covers physiologically realistic values.

In Figure 6.9 we plot results of the calculations. We see in plot (b) that the extracellular conductivity increases slightly and approximately linearly over the parameter range, finishing at 112% of the value at which it started. This is because we have a gap junction height of 0.75 and a cell height of 0.9, meaning that any increase in gap junction length will increase the extracellular fraction of the domain, because there is relatively more extracellular space surrounding the gap junction than the cytoplasm. To see this, consider elongating the gap junctions (coloured blue) in Figure 6.3 whilst simultaneously contracting the intracellular space (coloured red): the amount of space outside of the cell (*i.e.* the extracellular matrix) will increase and thus the overall extracellular conductivity will increase.

The intracellular conductivity drops dramatically over the range of values considered — by an order of magnitude between shortest and longest gap junctions, as seen in plot (a). This is because the gap junction conducts poorly when compared to the intracellular space so the

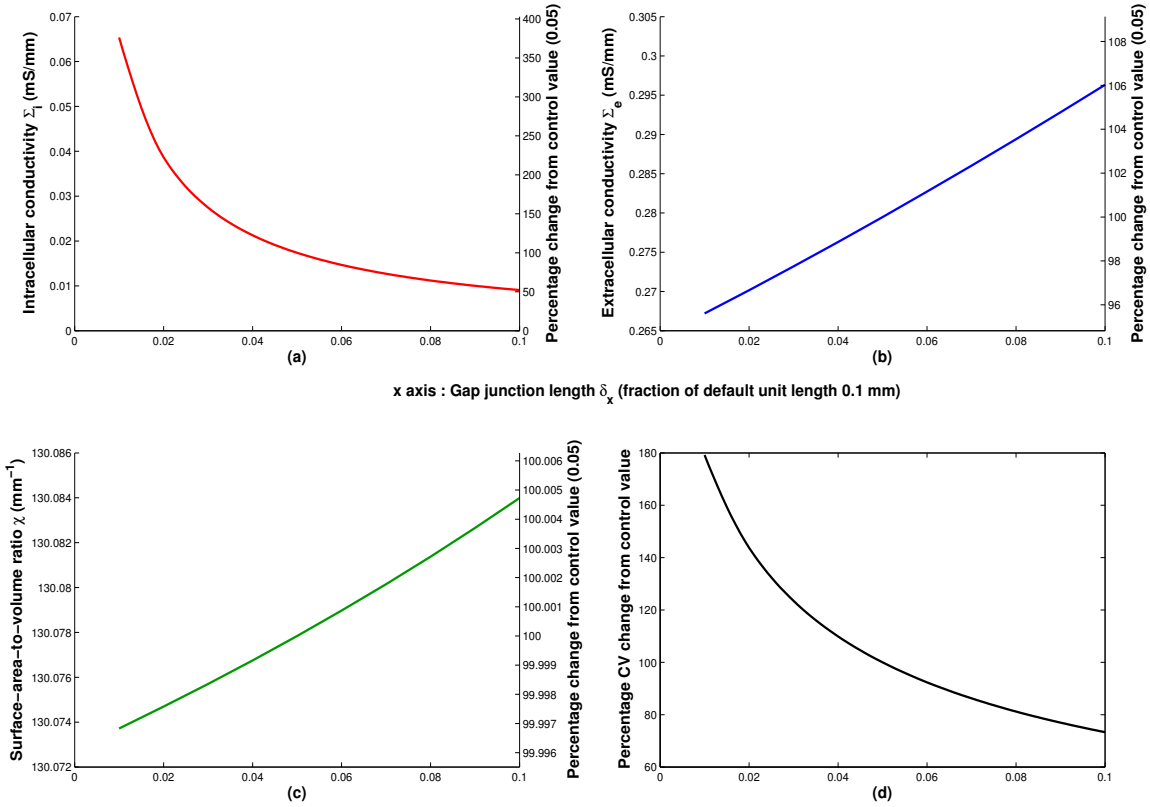

Figure 6.9: *Values of fibre direction conductivities (a,b), surface-area-to-volume ratio (c) and relative conduction velocity (d) as we change the length of the gap junctions* δ_x.

longer it is, the more of a barrier it presents to conduction. Surface-area-to-volume ratio χ increases negligibly as gap junction length increases, by 0.01% over the range of lengths considered.

Conduction velocity changes are dominated by the intracellular conductivity, as was the case when changing gap junction height. It drops over the range of gap junction lengths to 38% of its initial value, as seen in plot (d), with the level expected from intracellular conductivity changes alone being 36%. In this situation the majority of this change occurs when gap junction length is below the control value of 0.05 — when it is reduced to 0.01 the conduction velocity increases by 80% but when it is increased to 0.1 the conduction velocity only decreases by 25%.

It is worth noting that this last number roughly matches what we observed in Section 4.3.4 when increasing gap junction length from 0.05 to 0.1 for rectangular cells. In that situation, we saw a 20% change in conduction velocity. Overall, we observe that conduction velocity changes significantly when we vary gap junction length and so we must carefully take its effect into account when homogenising, and that the effect on conduction velocity of modelling changes in gap junction length is similar to that observed when using rectangular cells.

6.2.5 The Effect of Varying Gap Junction Conductivity, σ_g

Next we vary the conductivity of the gap junctions, σ_g, from a lower value of 0.00025 mS/mm to an upper value of 0.25 mS/mm. This upper value is the same used for the intracellular conductivity σ_i, and so essentially simulates a situation where the gap junctions are not present.

In Figure 6.10 we plot the results of calculations. As we are not changing the geometry of the domain between calculations, both Σ_e and χ are invariant, as seen from plot (b) and plot (c). The intracellular conductivity increases significantly over the range as shown in plot (a) — by over 70 times from the lowest to the highest values. This is expected, as taking a gap junction conductivity of zero gives zero intracellular conductivity, and so for

very small values of σ_g we have very small values of Σ_i.

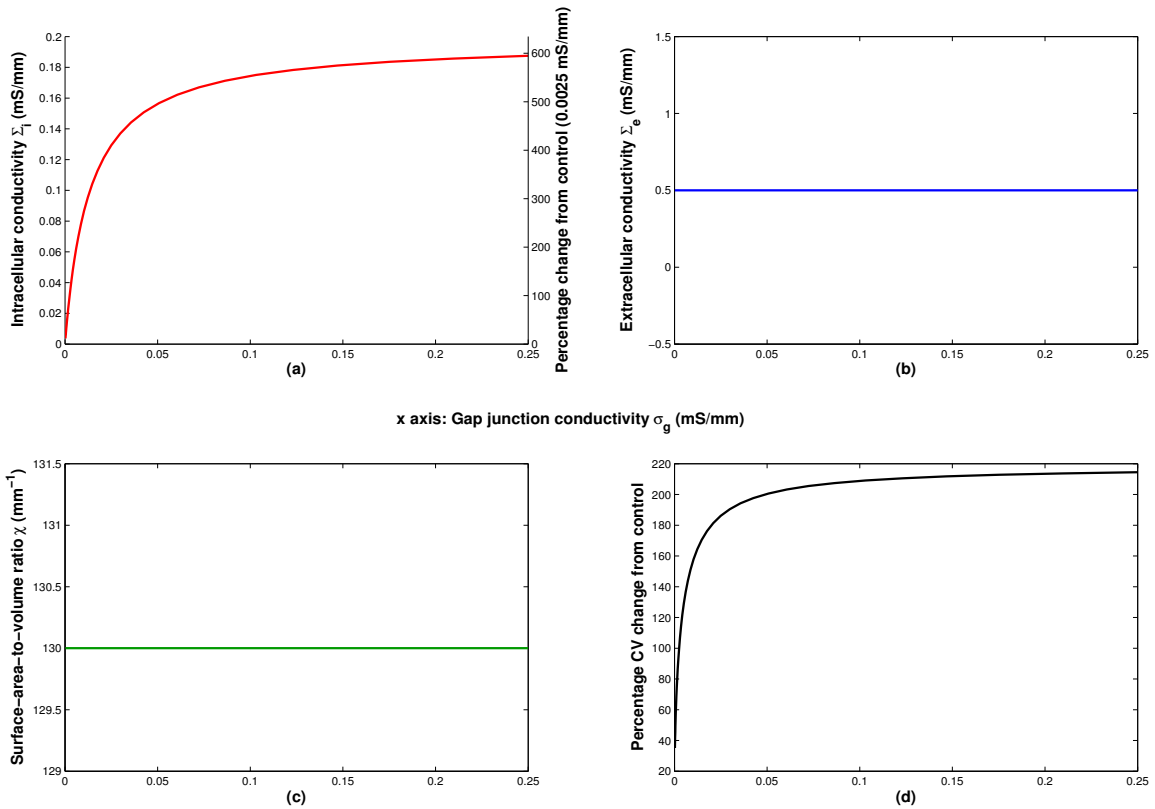

Figure 6.10: *Values of fibre direction conductivities (a,b), surface-area-to-volume ratio (c) and relative conduction velocity (d) as we change gap junction conductivity σ_g.*

Conduction velocity change is determined solely by changes to the value of the intracellular tensor as Σ_e and χ are both constant, and we see in plot (d) that increasing the gap junction conductivity by two orders of magnitude from the control value of 0.0025 mS/mm increases conduction velocity to nearly 220% of the control value, and reducing the gap junction conductivity by a single order of magnitude from the control value decreases conduction velocity to 30% of the control value.

We can compare this to the results of Section 4.3.4, in which we saw that changing the gap junction conductivity over three orders of magnitude changed conduction velocity by a factor of roughly six (see Table 4.3 where $\delta = 0.05$ and compare the value of 100 that we have when $\sigma_R = 1$ with the value of 16.3677 at $\sigma_R = 1000$). Now that we are considering curved cells, we have found that conduction velocity increases by a factor of around seven over the same range of σ_g values. This tells us that the effect of gap junction conductivity on

conduction velocity is slightly larger for curved cells than for rectangular cells, and overall is much larger than the effect of other parameters we have considered.

Finally, we can compare our results with the more specific case outlined in Section 4.3.4 in which we considered the effect of starting with physiologically healthy values for gap junction coupling and reducing gap junction conductivity by 50% in order to model the effect of diseases such as atrial fibrillation and ventricular hypertrophy where connexin expression levels are reduced. There, we saw a 25% reduction in conduction velocity. Here, we look at plot (d) of Figure 6.10 and find that when gap junction conductivity decreases from the control value of 0.0025 mS/mm to half that value, conduction velocity drops by 26%. This suggests that the effect of modelling diseases whose underlying pathophysiologies include a reduction in gap junction conductivity is similar when using a geometry consisting of cells with a curved membrane.

6.2.6 The Effect of Varying Scalar Intracellular Conductivity, $\boldsymbol{\sigma_i}$

Finally, we vary the scalar conductivity, σ_i, of the remainder of the intracellular space that is not part of a gap junction. As we found in Section 4.3.6, on a rectangular geometry the intracellular conductivity tensor is more sensitive to changes in gap junction conductivity than to changes in intracellular conductivity owing to the relative magnitudes of the two quantities. We wish to see if this remains true for our new geometry. In Figure 6.11 we plot the results of calculations in which we vary σ_i from 0.1 mS/mm to 1 mS/mm, and see that Σ_i changes relatively little for larger conductivity values (that is, when there is a greater discrepancy between the magnitudes of intracellular and gap junction conductivity). Overall, the conduction velocity changes by around 15% over the range of scalar conductivities compared to 700% for gap junction conductivity changes. This suggests that the intracellular homogenised conductivity tensor and the domain conduction velocity remain more sensitive to changes in gap junction conductivity than to changes in intracellular conductivity for cells with a curved membrane.

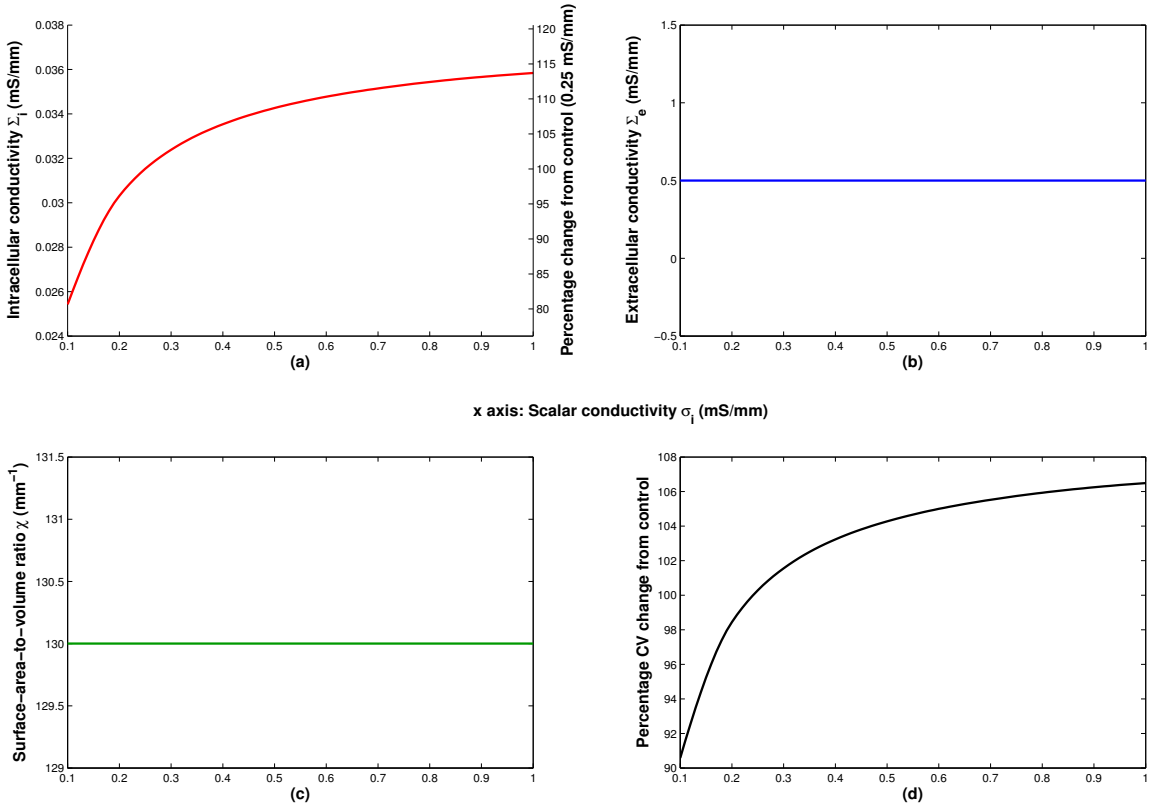

Figure 6.11: *Values of fibre direction conductivities (a,b), surface-area-to-volume ratio (c) and relative conduction velocity (d) as we change the intracellular conductivity σ_i of the discrete system.*

6.2.7 Conclusions

The six previous sections each discussed how changing one parameter in our discrete cell framework whilst keeping all others constant affected the intracellular and extracellular conductivity tensors, the surface-area-to-volume ratio, and the overall conduction velocity of the continuum system.

For the three sections in which gap junction parameters (length, height, and conductivity) were changed, we saw much larger changes in conduction velocity than in all other cases, suggesting that gap junction parameters remain equally as important to the result of homogenisation as we found in Chapters 4 and 5. We also found that conduction velocity changes were similar to those found in Chapter 4 when modelling diseased gap junctions with reduced conductivity.

For two of the sections in which gap junction parameters were kept constant (Section 6.2.1 in which cell height was varied and Section 6.2.2 in which we changed membrane curvature) we did not see such a strong dependence of conduction velocity on the parameters considered. In the case of changing curvature, we saw slight changes in the extracellular conductivity being reflected by slight changes in conduction velocity, suggesting that this parameter is not as important as others under consideration. In the case of changing cell height, we saw that the primary reason for changes in conduction velocity was the constriction of the extracellular space as the gap between successive cells in the off-fibre direction became smaller. This suggests that in cases where cells are tightly packed together, the precise nature of the extracellular space plays an important role in determining domain conduction velocity.

Overall, we observed that gap junctions have a much more significant effect on conduction velocity changes than cell shape. The one exception to this is when we model cells that are extremely tightly packed together, and we believe that the large conduction velocity changes here are due to a portion of the extracellular space being very narrow, restricting conduction. Moving forward, we wish to see if this narrow extracellular space is partly due to the horizontal alignment of cells used in our current geometry, as cardiac cells are not

perfectly aligned and instead form a brick-wall structure. To this end, we will investigate in Section 6.3 whether this rapid drop in conduction velocity, caused by the occlusion of the extracellular space around the widest point of the cell for tightly packed cells, is mitigated by modifying the discrete geometry to a brick-wall structure in which cell fibres are offset from one another.

6.3 Introducing a Geometry that Considers the Brick-Wall Structure of Cardiac Cells

In this section we study the effect of the brick-wall structure of cardiac cells on extracellular conductivity and conduction velocity. To do this we have extended our previous geometry to consist of two successive cells in the fibre direction and two further cells forming a second fibre running below the first, as shown in Figure 6.12. All four cells are taken to have identical parameters, and we have modified the definition of the periodic subunit on which to homogenise to be the parallelogram with vertices at the centres of the four cells. The second fibre of cells can be shifted along the fibre direction with respect to the first, so that the two lines are offset by a given amount. This is our 'offset' parameter, where a value of zero represents cells aligned vertically and a value of 0.5 represents the case where the second fibre is offset by half a cell length when compared to the first fibre. This is the maximum possible offset as a value of 1 represents the case where the bottom fibre is offset by a whole cell length compared to the top fibre, giving an identical geometry to that when the offset is zero.

We now calculate the homogenised conductivity tensors using this new geometric framework and consider the behaviour of the extracellular tensor (Σ_i and χ do not depend on the new offset parameter and so we can use the results from Section 6.2 to determine these) as we vary the offset between cell fibres, the height h_y of the cells, and the height δ_y of the gap junctions. We consider cell height in particular as we found in Section 6.1 that extracellular conductivity was significantly affected when the height of the cells approached the height of the periodic subunit, and wish to see if moving to a brick-wall structure affects this result.

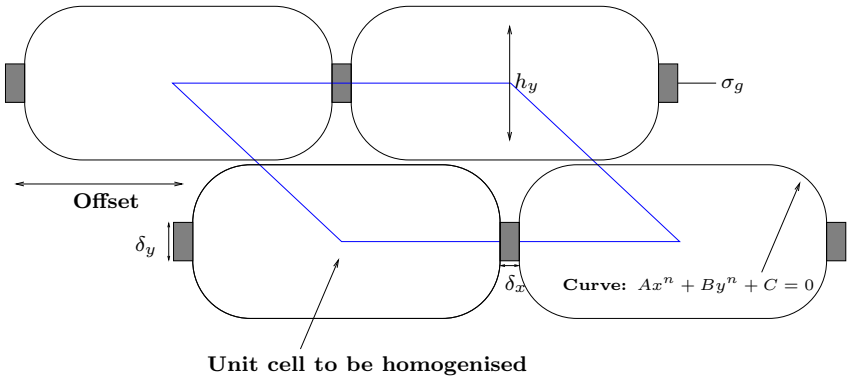

Figure 6.12: *A modification of our cell parameterisation (Figure 6.1) that takes into account the brick-wall packing of cells. The blue parallelogram represents the periodic subunit that we will homogenise to obtain the continuum conductivity tensors.*

6.3.1 The Effect of Cell Offset, Cell Height and Gap Junction Height

In order to study how a brick-wall geometry affects conduction velocity, we now calculate the extracellular tensor for a range of parameter values for gap junction height, cell height, and fibre offset. The behaviour of the intracellular tensor and the surface-area-to-volume ratio is the same as it was in Section 6.2 when we varied cell height and gap junction height, and both Σ_i and χ are constant when we vary offset. As such, we will only recalculate the extracellular tensor for the new geometry, and use the appropriate values of Σ_i and χ from Section 6.2 to write down conduction velocity changes for the domain. The parameter values used in calculations are outlined in Table 6.2, with all other parameter values set as those used as control values in Section 6.1.1.

Parameter values used in calculations			
Figure	δ_y	h_y	Offset
6.13	0.5	$0.58 \to 0.98$	$0 \to 0.5$
6.14	0.6	$0.66 \to 0.98$	$0 \to 0.5$
6.15	0.7	$0.74 \to 0.98$	$0 \to 0.5$
6.16	0.8	$0.82 \to 0.98$	$0 \to 0.5$
6.17	0.9	$0.90 \to 0.98$	$0 \to 0.5$

Table 6.2: *The various parameter sets used in calculations of the conductivity tensors for a brick-wall domain as shown in Figure 6.12. The 'Figure' column refers to the figure in which the results of the particular calculation set are plotted.*

In Figures 6.13–6.17 we plot the calculated conduction velocities for the parameter sets outlined in Table 6.2, with each figure showing the results for a fixed value of gap junction

height δ_y. We take as a reference value the conduction velocity calculated at maximum offset and cell height, and express other conduction velocities as a percentage of this reference. On each line in the figures, cell height is kept constant and the offset is varied from 0 to 0.5. The cell height varies between successive lines in each figure.

We find overall that conduction velocity changes are monotonic in the three parameters of interest — conduction velocity increases with increasing gap junction height, decreasing cell height and increasing offset. That conduction velocity increases with gap junction height follows the reasoning of Section 6.2.3, as whilst the extracellular tensor is decreasing steadily, the intracellular tensor is increasing much more rapidly. Considering cell height, a decrease will increase the domain fraction taken up by extracellular space, which has a higher scalar conductivity than the intracellular space, and as such conduction velocity increases.

The increase in conduction velocity as we increase cell offset is an interesting result. In this situation the intracellular conductivity is unchanged; the cells are not connected in the off-fibre direction and thus whether one fibre is offset from another does not affect the calculation result. In addition, the surface-area-to-volume ratio remains constant as the offset changes. *This means that any conduction velocity change is driven by a change in the shape of the extracellular space.*

From Figures 6.13–6.17 we see that any change in conduction velocity is very minor as we vary cell offset for small values of cell height — less than 0.1% between minimum and maximum offset values — but for large values of cell height the change is much greater. For instance, in the case where gap junction height is 0.5 and cell height is 0.98 (see the lowermost line of Figure 6.13), conduction velocity increases by 15% between minimum and maximum offset values. We also see that this change is smaller for greater gap junction heights: the lowermost line of Figure 6.17 shows us that varying offset only changes conduction velocity by 5% for a gap junction height of 0.9.

To investigate this further, in Figures 6.18 and 6.19 we plot relative changes in extracellular conductivity as we vary offset for the two examples above: the first in which gap junction height is 0.5 and cell height is 0.98; and the second where gap junction height is 0.9 and cell

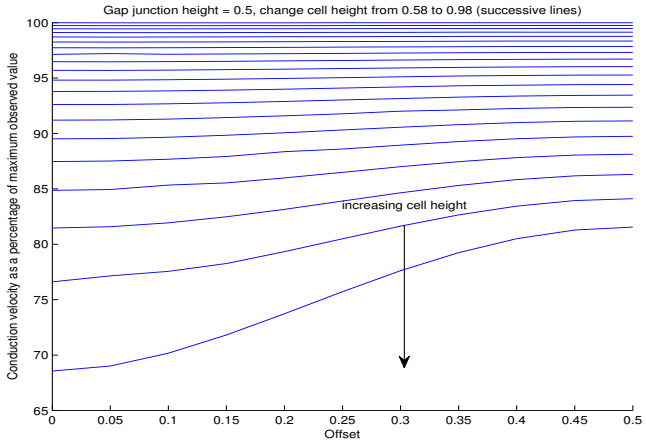

Figure 6.13: *The relative conduction velocity changes calculated as a result of varying cell height and offset between cell fibres for a gap junction height of 0.5.*

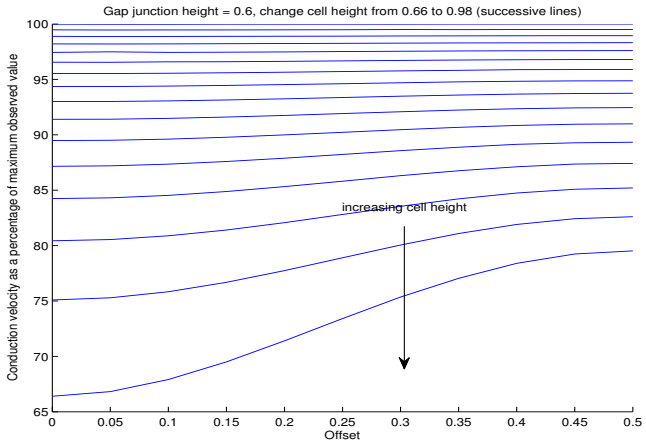

Figure 6.14: *The relative conduction velocity changes calculated as a result of varying cell height and offset between cell fibres for a gap junction height of 0.6.*

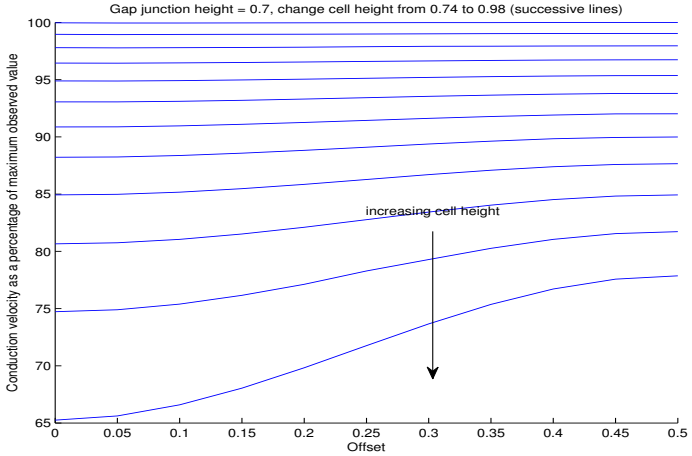

Figure 6.15: *The relative conduction velocity changes calculated as a result of varying cell height and offset between cell fibres for a gap junction height of 0.7.*

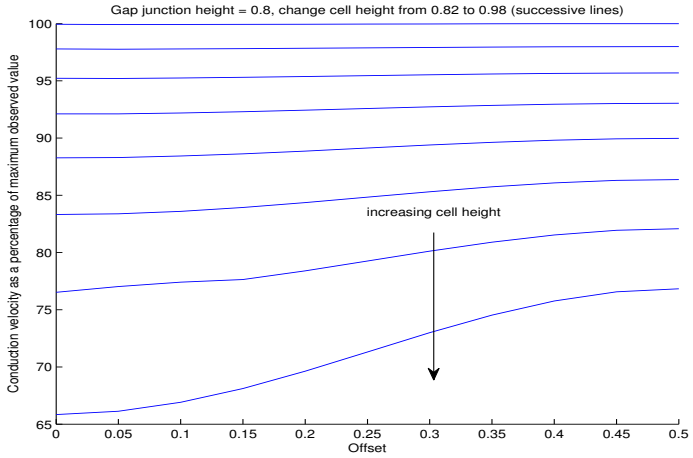

Figure 6.16: *The relative conduction velocity changes calculated as a result of varying cell height and offset between cell fibres for a gap junction height of 0.8.*

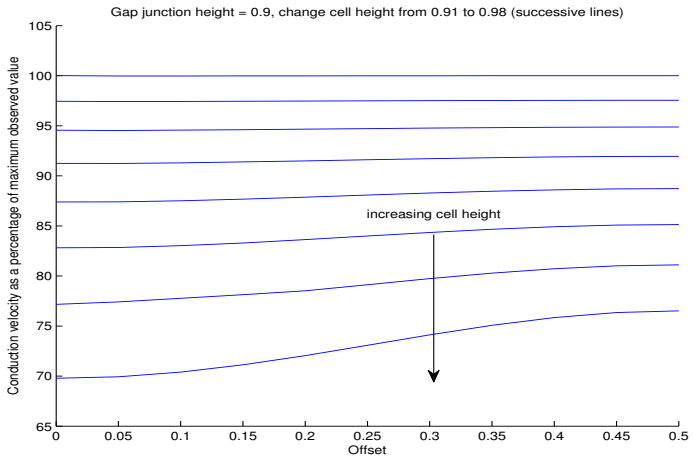

Figure 6.17: *The relative conduction velocity changes calculated as a result of varying cell height and offset between cell fibres for a gap junction height of 0.9.*

height is 0.98. We see that the extracellular conductivity increases by 25% when increasing offset for a gap junction height of 0.9, and by 85% when the gap junction height is 0.5. This may be because when we have small gap junction height and large cell height, the extracellular space is very wide at the gap junction and very narrow at the centre for aligned cells, but for offset cells the extracellular space is much more uniform.

These results demonstrate the magnitude of the effect of cell offset, *i.e.* the effect of the shape of the extracellular space, on conductivity. We have found that simply changing the offset of one fibre compared to another can cause a change of 85% in extracellular conductivity, with a concurrent 15% change in conduction velocity. Given the narrow and tortuous nature of the extracellular space in cardiac tissue [144, 167] this is a significant finding, as we deduce that for physiologically realistic tissue structures the offset of cell fibres has a large effect on extracellular conductivity and overall conduction velocity.

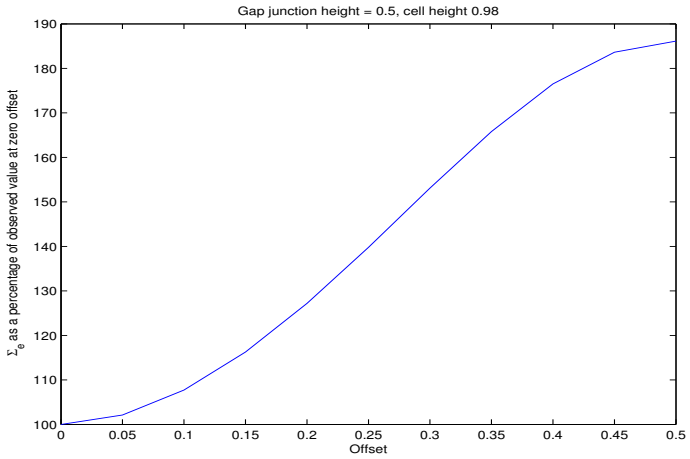

Figure 6.18: *The calculated extracellular conductivity in the fibre direction as a result of varying offset between cell fibres for a gap junction height of 0.5 and a cell height of 0.95.*

6.3.2 Weight Functions

In Figure 6.20 we plot the extracellular weight functions for the default parameter set used in Section 6.1.1 (that is, gap junction height 0.75 and cell height 0.9) for the case of maximum cell offset (0.5) in order to see how changing the cell offset affects the form of the

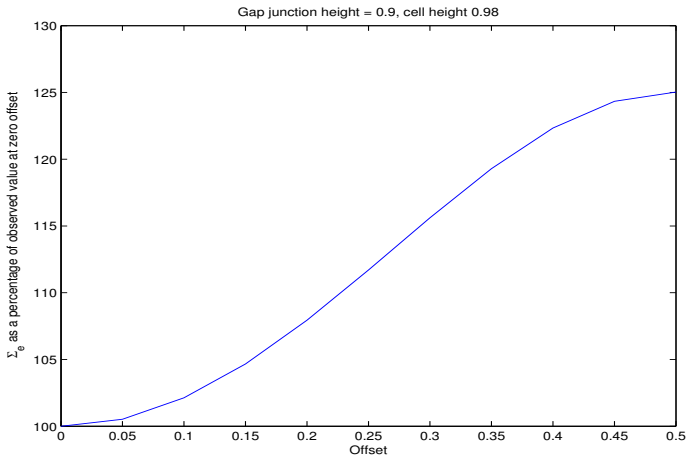

Figure 6.19: *The calculated extracellular conductivity in the fibre direction as a result of varying offset between cell fibres for a gap junction height of 0.9 and a cell height of 0.98.*

extracellular weight function.

As before, we see that the widening of the extracellular space at a gap junction causes the weight function to switch smoothly from a positive to a negative value. However, the fact that the two gap junctions (from the fibres above and below the extracellular portion) are not aligned means that this change occurs twice in separate locations, meaning that the weight function takes the form of a 'double twist' as the weight function increases and then decreases at the top of the intracellular space as it reaches the first gap junction, and increases and decreases again at the bottom of the cell as it passes the second gap junction.

6.3.3 Conclusions

In this section, we studied the effect of the brick-wall packing of cells on conduction velocity by introducing a geometry where successive cell fibres were offset from each other horizontally. We found that conduction velocity increased by up to 15% when fibres were offset from one another, and that this increase occurred when considering cells that are tightly packed together, *i.e.* for large values of cell height. This tells us that considering a geometry in which cells are aligned will give different results when calculating conduction velocity compared to a geometry in which cells are not aligned, and so we should take into account the brick-wall packing of cells when homogenising cardiac tissue.

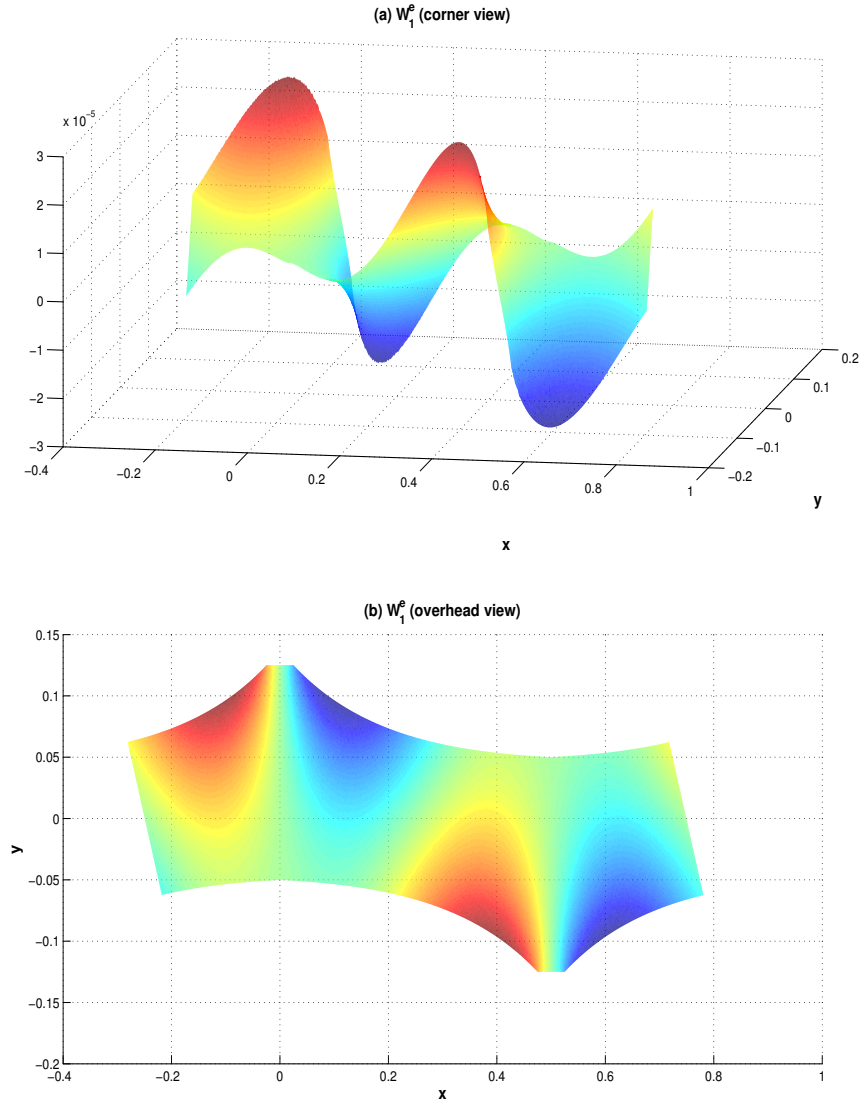

Figure 6.20: *Solutions to the governing equation* (6.5) *for the fibre direction extracellular weight function using the default cell parameters outlined in Section 6.1.1 and a cell offset of 0.5. The two plots show the same results, viewed from different angles.*

In all simulations to this point we have only considered propagation in the fibre direction. This is an unavoidable limitation of the method used as the intracellular and extracellular domains were only connected in the fibre direction, and so the homogenisation technique only gives nonzero conductivities in the fibre direction (see Section 4.3.2). We wish to understand how changes in cell geometry and gap junction properties affect conductivity in both directions, and so we will now connect fibres of cells via additional gap junctions.

6.4 The Effect of Off-Fibre Gap Junctions

In this section, we study the effect of introducing off-fibre gap junctions on fibre direction conductivity, off-fibre direction conductivity, and the anisotropy ratio of the intracellular space.

To do this we add small gap junctions to the geometry used in Section 6.3 which are oriented vertically and connect cells in the off-fibre direction, as shown in Figure 6.21. We introduce a new parameter σ_{g_y} that is the scalar conductivity of the off-fibre gap junctions, as these connections may have differing conductivity to fibre direction junctions [158]. This new geometry allows us to connect each cell to two cells in the neighbouring fibre, meaning that each cell is connected to six others when extending the periodic geometry to arbitrarily many fibres. As discussed previously in Section 2.3, this is close to what is observed experimentally [65].

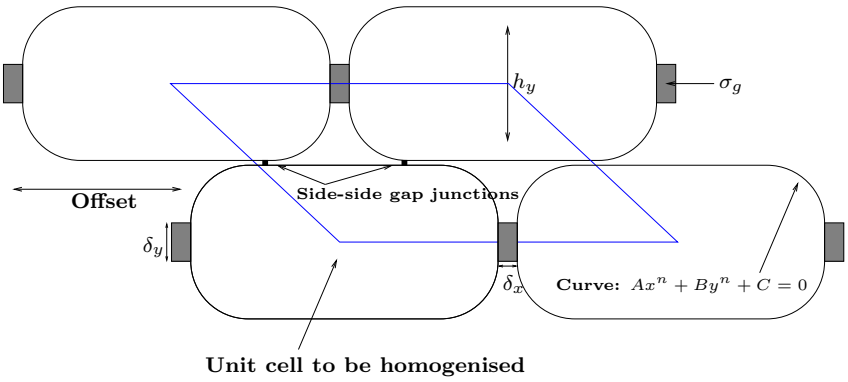

Figure 6.21: *A modification of the cell geometry in Figure 6.12 that takes into account off-fibre gap junctions. As in the previous section, the blue parallelogram represents the periodic subunit that we will homogenise to obtain the continuum conductivity tensors.*

On this geometry the extracellular space is disconnected, and so the extracellular conductivity is zero (see Section 4.3.2 for more details). As such, we are unable to write down the conduction velocity differences that correspond to the calculated changes in intracellular conductivity. However, as we will have nonzero conductivity in both directions in the intracellular space, we can calculate the intracellular anisotropy ratio (that is, the quotient of fibre direction conductivity and off-fibre direction conductivity) for the parameter set in question. It has been shown that changes in the anisotropy of cardiac tissue occur as part of ageing [143], with the anisotropy ratio decreasing as subjects get older, and that this changes the preferential direction of conduction block and re-entry from longitudinal to transverse [27, 77]. This tells us that the anisotropy of cardiac tissue is an important determinant of the propagation of an action potential, and as such we aim to provide insight as to how off-fibre gap junctions might affect the intracellular anisotropy ratio, given that they are known to play a large role from experimental observations [129].

In addition, we discussed in Section 2.3.1.2 how the proportion of gap junctions located at the cell ends versus located transversely is altered during disease — junctions can be lateralised during acute ischaemia, reduced more at transverse locations compared to the cell ends in healed infarct zones, or both are possibilities in atrial fibrillation. Now that we are modelling a cell with gap junctions in both directions, we can consider the effect of these changes on the intracellular anisotropy by changing off-fibre direction gap junction conductivity and width whilst keeping fibre direction gap junctions constant.

We proceed by calculating the intracellular homogenised conductivity tensor and anisotropy ratio in the following cases:

- we change the width of the off-fibre gap junctions from 0.001 to 0.025; and
- for each width, we change the conductivity of the side junctions σ_{g_y} from 0.00025 mS/mm to 0.25 mS/mm.

All other parameters are kept constant at the following control values:

- gap junction height $\delta_y = 0.75$;

- offset = 0.5;
- gap junction length $\delta_x = 0.05$;
- fibre direction gap junction conductivity $\sigma_g = 0.0025$ mS;
- cell height $h_y = 0.9$; and
- cell membrane curvature $n = 5$.

We begin by considering the individual diagonal components of the intracellular conductivity tensor $\Sigma_{i_{(1,1)}}$ and $\Sigma_{i_{(2,2)}}$, and see from Figure 6.22 that changes in off-fibre gap junction parameters have a surprisingly significant effect on the fibre direction conductivity. In the control situation where off-fibre gap junctions are not present, the intracellular fibre direction conductivity is 0.38 mS/mm, but for the largest values of off-fibre gap junction width and conductivity used, the intracellular conductivity in the fibre direction is 0.44 mS/mm, which is an increase of 16%. This tells us that adding transverse connections between fibres moderately improves conduction in the fibre direction, which is somewhat unintuitive as the two directions are orthogonal.

In Figure 6.23 we see that the intracellular off-fibre conductivity changes rapidly as we vary off-fibre gap junction parameters. Values run from zero (in the case where we have no off-fibre gap junctions) to as high as 0.3 mS/mm in the situation where we consider the largest values of conductivity and width, compared to the intracellular fibre direction conductivity of 0.44 mS/mm mentioned above. Whilst we expect this conductivity to increase sharply from zero as we add off-fibre gap junctions, that the off-fibre conductivity becomes almost as large as the fibre direction conductivity for certain parameter values is less expected. Physiologically, the intracellular anisotropy ratio should be somewhere in the region of 5–15 [126], and certainly not less than 2. This suggests that the higher values of gap junction conductivity and width that we used do not give realistic results.

We also know that as either gap junction width or conductivity goes to zero the intracellular anisotropy tends to infinity. Given this, we expect the anisotropy ratio of the geometry to be highly dependent on the width and conductivity of off-fibre gap junctions. As such, we

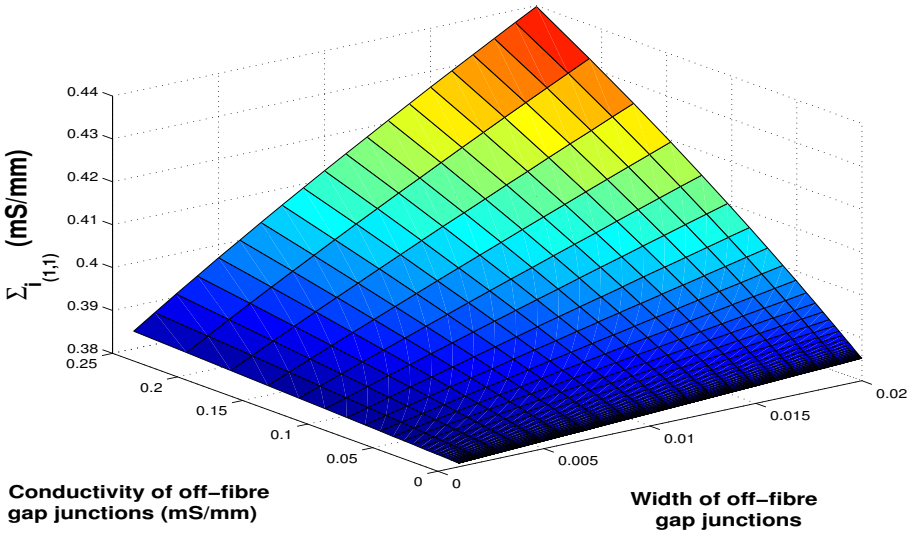

Figure 6.22: *The intracellular fibre direction conductivity as we vary the width and conductivity of off-fibre gap junctions.*

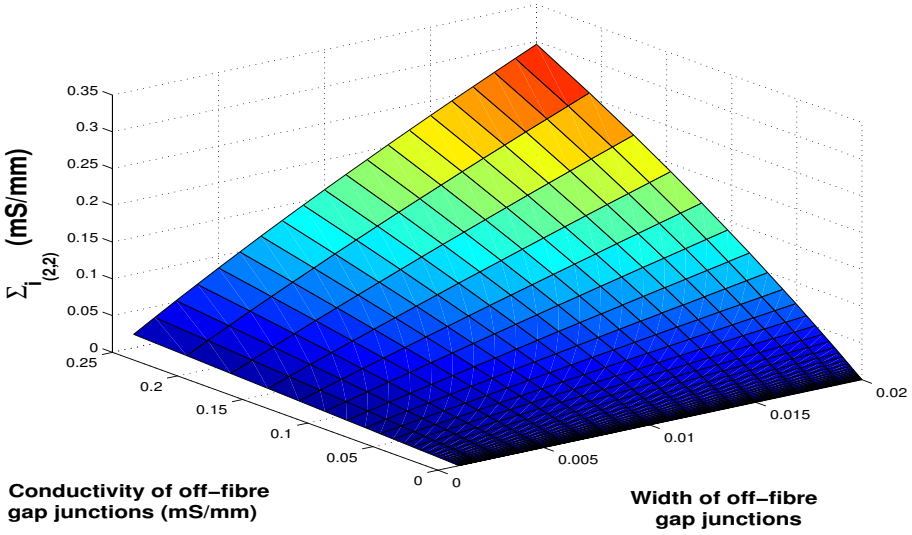

Figure 6.23: *The intracellular off-fibre direction conductivity as we vary the width and conductivity of off-fibre gap junctions.*

now plot the anisotropy ratio for each parameter set in Figure 6.24. We see the spike in the front corner where both width and conductivity of off-fibre gap junctions are close to zero, confirming that the anisotropy ratio tends to infinity in this case. Since this plot does not give us the resolution to analyse what is happening to the anisotropy ratio for other parameter values, we plot the calculated anisotropy ratio for a subset of parameter values in Figure 6.25, where off-fibre gap junction conductivity varies between 0.0025 mS/mm and 0.025 mS/mm (*i.e.* from 10% to 100% of the conductivity of the fibre direction gap junctions), and off-fibre gap junction width varies between 0.005 and 0.02.

We see that over this range, the anisotropy ratio varies from 1.5 in the case of highest off-fibre gap junction width and conductivity, to 17.5 in the case of lowest off-fibre gap junction width and conductivity. That the variations are still so large for a narrow parameter range demonstrates that the anisotropy ratio is extremely sensitive to the parameters we are varying, so we must accurately specify the off-fibre gap junction parameters to achieve a physiological value of intracellular anisotropy.

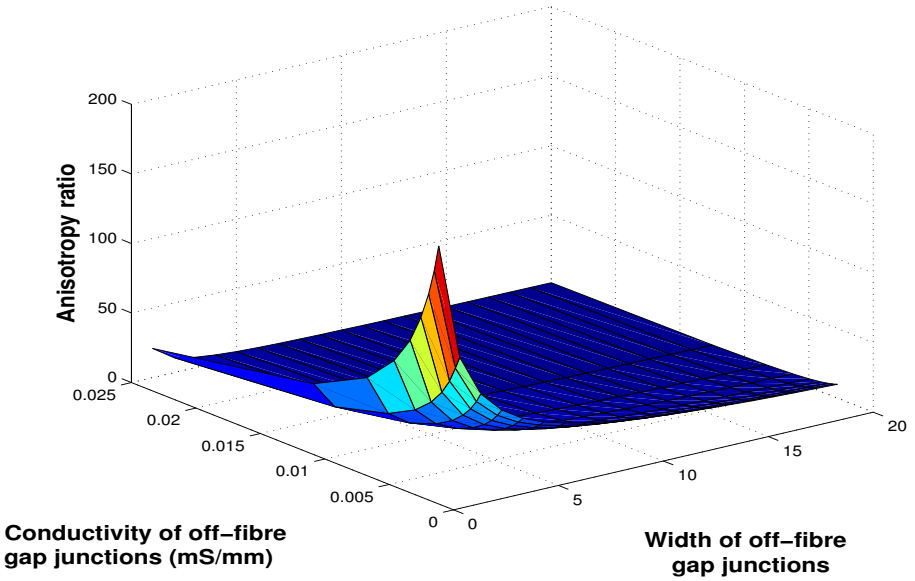

Figure 6.24: *The ratio of fibre direction to off-fibre direction intracellular conductivity as we vary the width and conductivity of the off-fibre gap junctions.*

We also notice that the anisotropy ratio is more sensitive to changes in conductivity than to changes in width of the off-fibre gap junctions. For example, the increase in anisotropy ratio over the range of gap junction width considered in Figure 6.25 ranges from 60% for

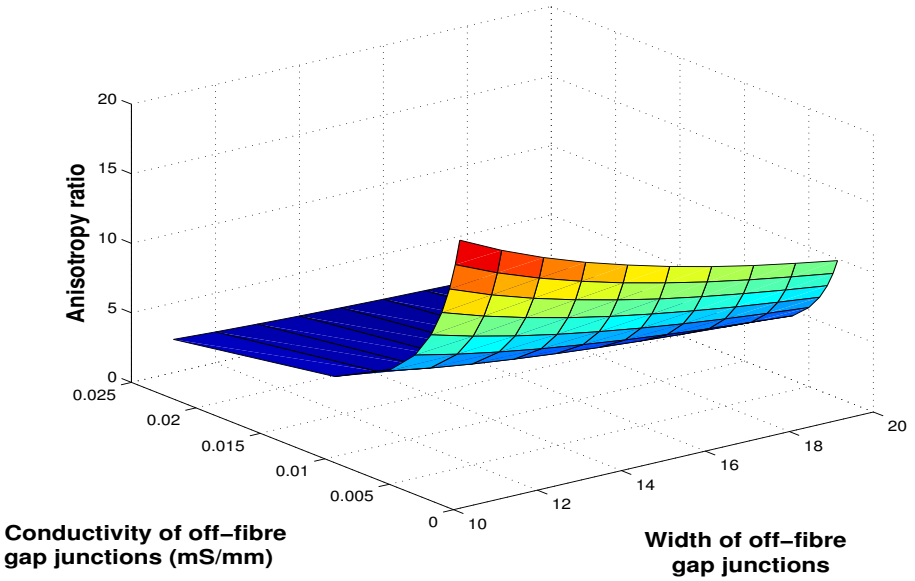

Figure 6.25: *The ratio of fibre direction to off-fibre direction intracellular conductivity as we vary the width and conductivity of the off-fibre gap junctions. Here, we only show a subset of the parameter sets calculated.*

the lowest value of gap junction conductivity to 80% for the highest value of gap junction conductivity. In contrast, the anisotropy ratio increases by between 566% and 640% when changing gap junction conductivity.

In terms of the changes in gap junction location that occur in disease, we find that when we model lateralisation of gap junctions by increasing the width or conductivity of the off-fibre gap junctions with respect to the fibre direction gap junctions, the intracellular anisotropy ratio decreases significantly. Conversely, when we model a situation when gap junctions are more preferentially located at cell ends, the intracellular anisotropy increases. These changes are certainly not negligible, and given the importance of the anisotropy ratio to conduction, we conclude that this remodelling of gap junctions in disease will have a large impact on conduction.

6.4.1 Weight Functions

We now plot example of the intracellular weight functions in both the fibre and off-fibre

direction for the case where off-fibre gap junction width is 0.02, and off-fibre gap junction conductivity is 0.0025 mS.

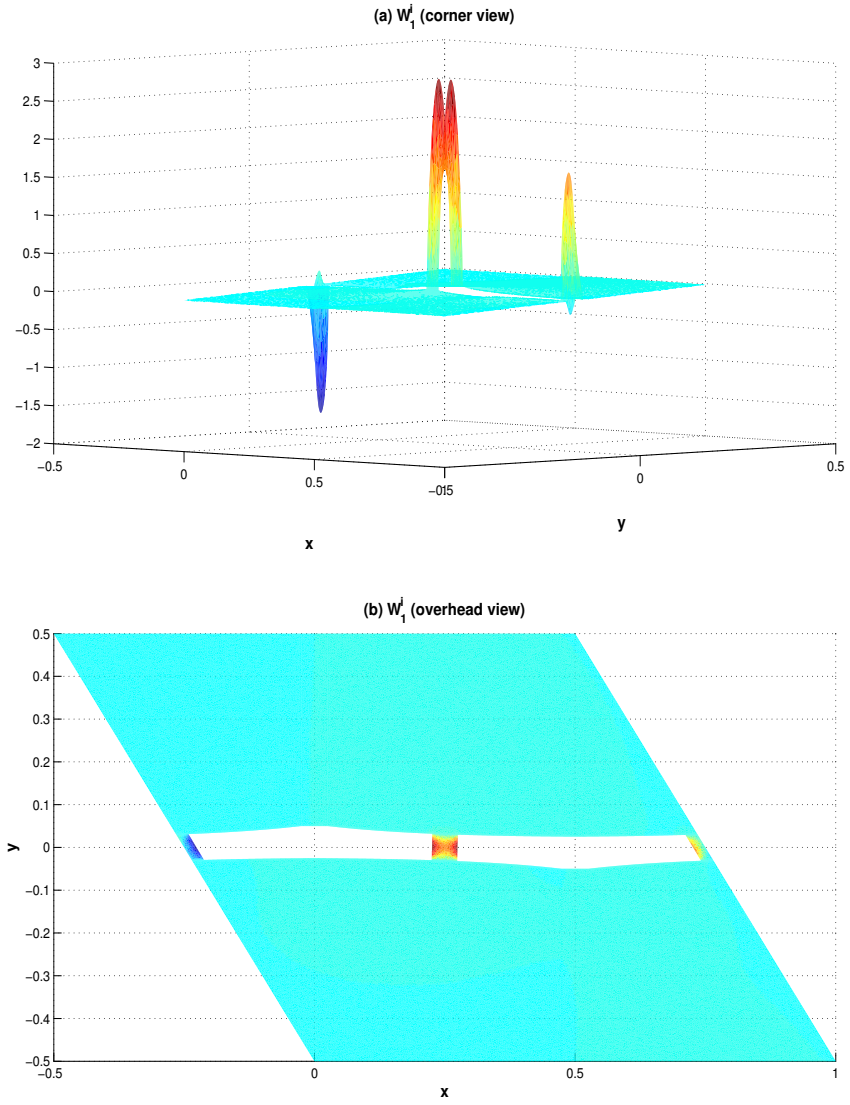

Figure 6.26: *Solutions to the governing equation* (6.2) *for the fibre direction intracellular weight function where off-fibre gap junction width in 0.02 and off-fibre gap junction conductivity is 0.0025 mS. The two plots show the same results, viewed from different angles.*

In Figure 6.26 we see that the intracellular weight function is very different from that in the absence of off-fibre gap junctions. The change in the weight function in the cell and in the fibre direction gap junctions is dwarfed by that in the off-fibre gap junctions, where we see a large positive spike in the weight function. This is of interest as it may explain (from a mathematical perspective) the source of the increased fibre direction conductivity when

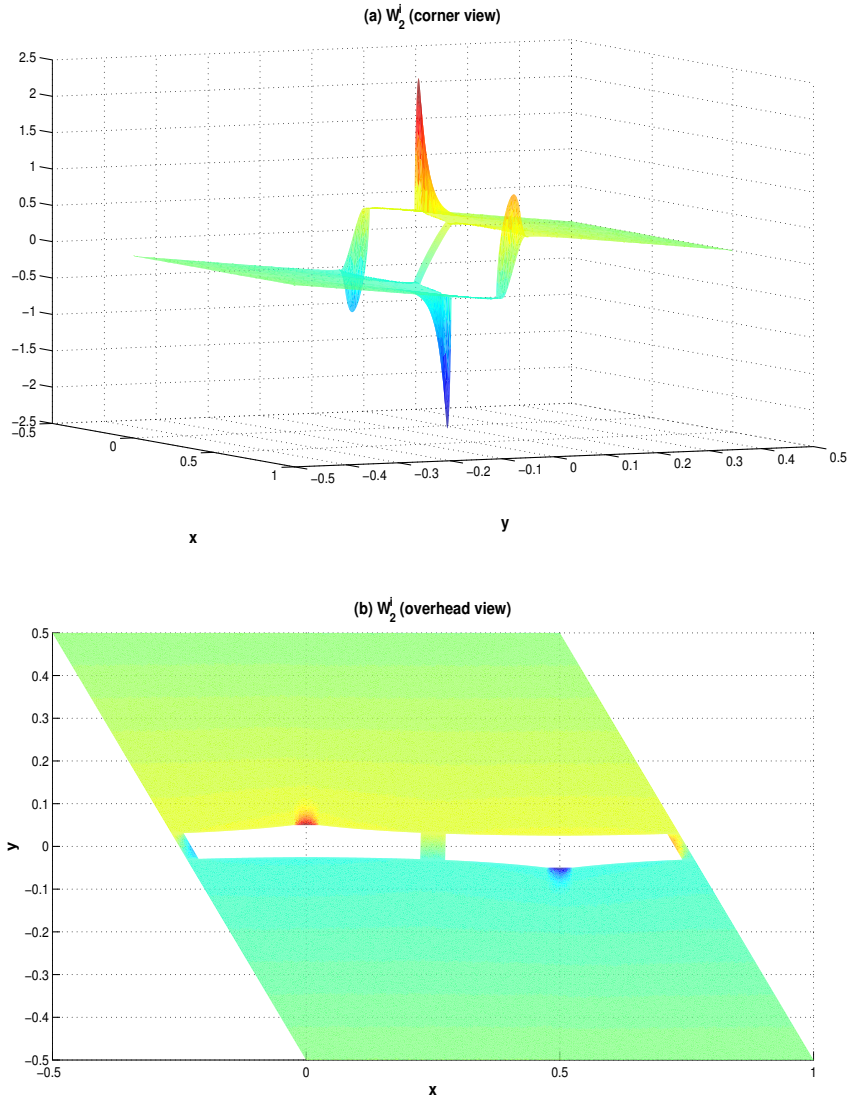

Figure 6.27: *Solutions to the governing equation* (6.2) *for the off-fibre direction intracellular weight function where off-fibre gap junction width in 0.02 and off-fibre gap junction conductivity is 0.0025 mS. The two plots show the same results, viewed from different angles.*

adding off-fibre gap junctions. In Figure 6.27 we similarly see that the off-fibre direction gap junctions dominate the form of the weight function, and in the same way the fibre direction gap junctions affected the fibre direction weight function in earlier discussions, we see here that the weight function changes gradient abruptly from negative in the cell to positive inside the gap junction.

6.4.2 Conclusions

In this section we investigated the effect of adding off-fibre gap junctions on intracellular conductivity and anisotropy. There was a noticeable increase in fibre direction conductivity when off-fibre gap junctions were included, which demonstrates that having successive fibres of cells electrically connected to one another is a source of increased intracellular fibre direction conductivity, despite the connections occurring perpendicular to the fibre.

In addition, we saw that the anisotropy ratio of the intracellular space is highly dependent on the width and conductivity of the off-fibre gap junctions, and that it is more sensitive to changes in gap junction conductivity than to width. Given that moderate changes in anisotropy have been shown to change the preferential direction of conduction block in tissue [77], we suspect that small changes in off-fibre gap junction properties could have a large effect on conduction. When simulating tissue in which gap junction remodelling has occurred, we found that the intracellular anisotropy ratio changed rapidly when the strength of gap junction coupling and size of gap junctions varied between fibre and off-fibre directions. Overall, these findings tell us that we must include off-fibre gap junctions when homogenising cardiac tissue.

6.5 Summary

In this chapter we considered the effect on the homogenised conductivity tensors and the predicted conduction velocity of introducing a curved cell membrane, a brick-wall cell packing, and off-fibre gap junctions.

In Section 6.2 we saw that gap junction parameters have a much larger effect than others for a geometry where the cell membrane is curved, that the cell membrane curvature itself is not that important in determining conduction properties, and that the effect of reducing gap junction conductivity is similar to that found in Chapter 4 when using rectangular cells. We also saw that cell height has a major effect on conduction velocity when cells are tightly packed together, and suggested that this could be due to the horizontal alignment of cells.

In Section 6.3 we considered a geometry in which successive fibres of cells were offset from one another. We found that the large change in conduction velocity when varying cell height found in Section 6.2 was slightly reduced when fibres were offset, showing that the brick-wall packing of cardiac cells should be modelled when homogenising cardiac tissue to avoid the conductivity being overly sensitive to the cell height. In addition, we saw that the conduction velocity of the domain increased when fibres were offset which suggests that this cell structure is beneficial with regard to propagation of an action potential.

Finally, in Section 6.4 we saw that adding off-fibre gap junctions increased both off-fibre and fibre direction conductivity in the intracellular space, which demonstrated that we should take into account electrical connection between fibres even when only considering propagation in the fibre direction, as their effect is non-negligible. We also saw that the anisotropy ratio of the intracellular space was highly dependent on the properties of the off-fibre gap junctions and thus to the effects of gap junction remodelling in diseased tissue, which also tells us that the width and conductivity of these connections could play a role in determining the preferential direction of action potential block.

The above findings are for two-dimensional geometries, and whilst we have been able to see the effect of both geometry and scalar conductivity changes on the homogenised conductivity tensors, cardiac tissue is, of course, a three-dimensional structure. In addition, the limitations of homogenising in two spatial dimensions means that the model either allows conduction through both spaces in only one direction (which leaves us able to calculate a monodomain conduction velocity, but unable to calculate anisotropy), or conduction throughout the intracellular space (and thus we can calculate the anisotropy ratio, but cannot find conduction velocity) but with no conduction in the extracellular space. As such, we

will now extend the geometry under consideration to three spatial dimensions in Chapter 7 and perform similar calculations in order to see if the results observed for two-dimensional geometries still hold true. In addition, we will explore how intracellular and extracellular anisotropy ratios and domain conduction velocity are affected when considering anisotropic cells that are fully connected in three dimensions.

Chapter 7

Comparing the Homogenised Conductivity Tensors Between a Two- and Three-Dimensional Schema

Contents

In this chapter, we move from two-dimensional geometries to a fully three-dimensional cell. We calculate homogenised conductivity tensors whilst varying model parameters, and compare the effect on conduction velocity with that calculated previously for a two-dimensional geometry in Chapter 6. In addition, in Chapter 6 we found limitations when looking at two-dimensional homogenisation, in that we could not obtain nonzero conductivities in both directions for both intracellular and extracellular spaces. Now that we are using a three-dimensional cell, we calculate homogenised conductivity tensors that are nonzero in all spatial directions, and write down the resulting anisotropy ratios to determine how they are affected by the geometry of the cell and gap junctions.

In Section 7.1 we present details of how we have constructed a three-dimensional parameterised representation of a cardiac cell in a manner that facilities a comparison with the results of the previous chapter, and in Section 7.1.1 we outline the parameter sets on which we will calculate a numerical solution to the equations governing the homogenised conductivity tensors.

Then, in Section 7.2 we discuss the results of homogenised conductivity calculations for isotropic cells as we vary cell membrane curvature, gap junction height, gap junction length, and gap junction conductivity. We focus on comparing the changes in conduction velocity due to varying each parameter with those changes calculated for two-dimensional cells in previous chapters.

Finally, in Section 7.3 we consider anisotropic cells, where the height and conductivity of gap junctions is different between the fibre direction and the two off-fibre directions. These geometric changes are equivalent to modelling realistically-shaped cells that are long and thin. We vary the amount by which these two quantities differ in order to model different cell aspect ratios and calculate both intracellular and extracellular anisotropy ratios as well as conductivity tensors and conduction velocity, comparing with the results obtained when

we investigated off-fibre gap junctions in two dimensions in Section 6.4.

7.1 Constructing a Parameterised Cell in Three Dimensions

In the previous three chapters we have studied the effect of gap junctions and cell geometry on discrete and continuum models, and on the resulting homogenised conductivity tensors used in the continuum model, using a two-dimensional geometry. We have found that gap junction parameters are important in determining conduction velocity and intracellular anisotropy, and that the brick-wall structure of cells makes a significant difference to the results of calculations. However, we have also seen that there are limitations to calculating homogenised conductivity tensors in two spatial dimensions. Most notably, we are unable to get nonzero entries along both principal axes for both intracellular and extracellular tensors: considering fibres of cells that are unconnected in the off-fibre direction gives nonzero values for both tensors in the fibre direction but zero conductivity in the off-fibre direction. Including connections between neighbouring fibres gives two nonzero entries for the intracellular tensor, but the extracellular space becomes enclosed and has zero conductivity in both directions. In particular, this means we cannot calculate both intracellular and extracellular anisotropy ratios, or both fibre direction and off-fibre direction conduction velocities, when using a two-dimensional cell.

In three dimensions we do not have such limitations, and so we move to considering a three-dimensional cellular geometry in this chapter, and begin by determining to what extent changing to three dimensions affects the results of the calculations performed in Chapter 6. We will do this first for isotropic cells in Section 7.2, changing one parameter in the schema in isolation, to compare with the results of Section 6.2. We will then consider anisotropic cells in which gap junction parameters are different between the fibre and off-fibre directions in Section 7.3, and determine how this affects the anisotropy ratio of both conductivity tensors — in Section 6.4 we saw that the intracellular anisotropy ratio was highly sensitive to changes in the ratio of gap junction height and conductivity between the fibre and off-fibre directions. Now that we are considering a three-dimensional geometry, we will determine

whether this result still holds true, and additionally we will calculate the extracellular anisotropy ratio, which we previously could not due to the limitations of homogenising in two dimensions mentioned in earlier in this section. This will allow us to see how unequal the anisotropy ratios of the two spaces are, as this property of cardiac tissue is an important factor in continuum modelling of action potential propagation [125, 127]. We also want to determine how the aspect ratio of cardiac cells — that is, they are typically much longer than they are wide or tall — affects both intracellular and extracellular anisotropy ratios as well as conduction velocity. These calculations are analogous to those performed in Section 6.4 for a two-dimensional cell.

To perform these comparisons and calculations, we extend our previous parameterisation of a cardiac cell discussed in Chapter 6 to a three-dimensional framework, keeping the same parameter scheme where applicable. Figure 7.1 shows a visualisation of our parameterised cardiac cell in three spatial dimensions. We have extended our two-dimensional unit (shown in Figure 6.1) by creating gap junctions, coloured green in Figure 7.1, at each of the six faces of the unit cube, each with a given length and height. The corresponding junctions at each end are identical, and the interface between them is assumed to be square (so that we indeed have one 'height' rather than two separate parameters). Each junction is connected to the remaining four (*i.e.* all except its opposite) by a curved surface, coloured red in Figure 7.1, analogous to that used in Chapter 6 which is of the form $Ax^n + By^n + D = 0$, $Ax^n + Bz^n + D = 0$, or $Ay^n + Bz^n + D = 0$, where in each case, one of x, y or z is constant, and A, B and D are different on each individual surface. The boundaries of these surfaces are then connected by another surface given by $Ax^n + By^n + Cz^n + D = 0$, coloured blue in Figure 7.1, where once more A, B, C and D are different on each individual surface such that the cell is reflectively and rotationally symmetric about its centre. We create the corresponding extracellular matrix by taking a unit cube and removing the intracellular portion described above, and assign scalar conductivities σ_i, σ_g and σ_e to the cell, gap junction, and extracellular matrix respectively. We then calculate the homogenised conductivity tensors Σ_i and Σ_e, the governing equations for which we will repeat for clarity in Section 7.1.1.

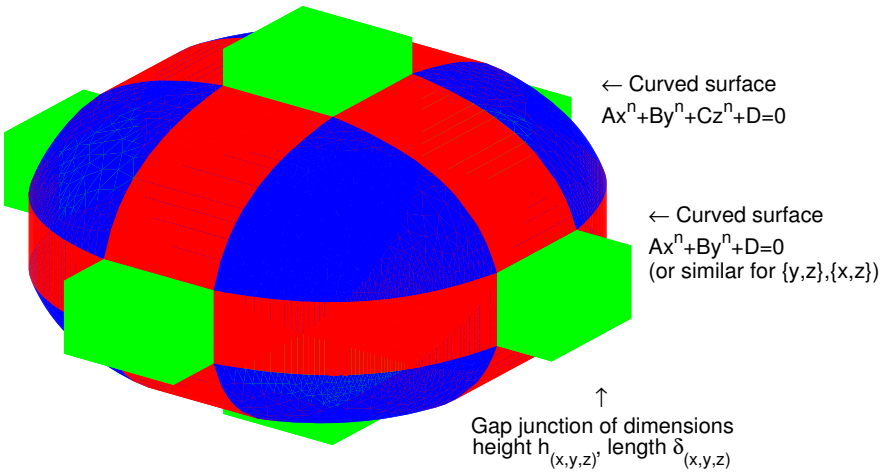

Figure 7.1: *Our parameterised cardiac cell in three dimensions. As previously, we have scalar conductivities σ_i in the intracellular space and σ_g in the gap junction, and can take the domain to be the unit cube due to the invariance of the homogenised conductivity tensors with respect to linear transformations.*

7.1.1 Outline of Calculations to Perform

As a reminder, the intracellular homogenised conductivity tensor Σ_i satisfies

$$\Sigma_i = \frac{1}{V_{\text{unit}}} \int_{\Omega_i} \sigma_i \left(I + \frac{\partial \mathbf{W}^i}{\partial \mathbf{z}} \right) \mathrm{d}V_{\mathbf{z}}, \tag{7.1}$$

where V_{unit} is the volume of our periodic subunit. The intracellular weight functions $\mathbf{W}^i$ satisfy

$$\nabla_{\mathbf{z}} \cdot (\sigma_i (I + \nabla_{\mathbf{z}} \mathbf{W}^i)) = 0, \qquad \mathbf{z} \in \Omega_i, \tag{7.2}$$

with boundary conditions

$$\mathbf{n} \cdot (I + \nabla_{\mathbf{z}} \mathbf{W}^i) = 0, \qquad \mathbf{z} \in \Gamma_m, \tag{7.3}$$

and are periodic in $\mathbf{z}$ with zero mean. Similarly the extracellular homogenised conductivity tensor Σ_e satisfies

$$\Sigma_e = \frac{1}{V_{\text{unit}}} \int_{\Omega_e} \sigma_e \left(I + \frac{\partial \mathbf{W}^e}{\partial \mathbf{z}} \right) \mathrm{d}V_{\mathbf{z}}, \tag{7.4}$$

and the extracellular weight functions $\mathbf{W}^e$ satisfy

$$\nabla_{\mathbf{z}} \cdot (\sigma_e (I + \nabla_{\mathbf{z}} W^e)) = 0, \qquad \mathbf{z} \in \Omega_e, \tag{7.5}$$

with boundary conditions

$$\mathbf{n} \cdot (I + \nabla_{\mathbf{z}} W^e) = 0, \qquad \mathbf{z} \in \Gamma_m. \tag{7.6}$$

We calculate both intracellular and extracellular conductivity tensors by solving Equation (7.1) and Equation (7.4) using the isotropic cell shown in Figure 7.1. The cell is represented by a tetrahedral mesh, created using the 'Tetgen' software package [139], where each cell is composed of around one million elements — this level of detail allows us to compute the numerical solution to the governing equations extremely accurately. For this, we use a finite element method (see Appendix A), and as in the previous chapter we ensure that tolerances are set such that upon refinement of the mesh, the solution changes by less than one part in a million.

We will begin using an isotropic cell in which the gap junction parameters are the same in all three directions, and perform calculations where we vary:

- n, the curvature of the cell membrane;
- σ_g, the conductivity of the gap junctions;
- δ, the length of the gap junctions; and
- h, the height of the gap junctions.

Having done this, we want to see how these numbers compare to the two-dimensional case. We will then modify the geometry such that the cell is anisotropic and vary:

- the height of the gap junctions between fibre and off-fibre directions (h_{fibre} and $h_{\text{off-fibre}}$); and
- the conductivity of the gap junctions between fibre and off-fibre directions ($\sigma_{g_{\text{fibre}}}$ and $\sigma_{g_{\text{off-fibre}}}$).

7.2 Isotropic Cell Results

In this section, we calculate the homogenised conductivity tensors for an isotropic version of the cell shown in Figure 7.1, *i.e.* where the gap junctions are the same size in all three directions. We change one parameter in the geometry in isolation and determine the effect that it has on the conductivity tensors, surface-area-to-volume ratio, and the predicted conduction velocity when using a monodomain reduction. We then use these results to compare with those obtained in Section 6.2, and ask to what extent using a three-dimensional cell changes the behaviour of the system when cell and gap junction parameters are varied.

In all calculations we use the following default parameter values, where heights and lengths are once more expressed as fractions of the unit on which we are homogenising:

- curvature $n = 5$;
- gap junction length $\delta = 0.05$;
- cell height $= 0.9$ (note that here cell height is always equal to $1 - 2\delta$);
- gap junction height $h = 0.5$; and
- gap junction conductivity $\sigma_g = 0.0025$ mS/mm.

We then vary one parameter in isolation over the following ranges:

- curvature $n = 1$–10;
- gap junction length $\delta = 0.01$–0.1;
- gap junction height $h = 0.1$–0.8; and
- gap junction conductivity $\sigma_g = 0.00025$–0.25 mS/mm.

In the following sections we plot the results of the calculations described earlier. In each case, we plot the same quantities that we displayed in the figures within Section 6.2: the two conductivity tensors Σ_i and Σ_e; the percentage change in these values when compared to the default values; the surface-area-to-volume ratio χ; and the percentage change in predicted conduction velocity obtained using a monodomain formulation (as detailed in

Section 3.2). As the cell is isotropic, the conductivity tensors will be scalar multiples of the identity matrix and so we will take these scalars as the intracellular and extracellular conductivity values.

7.2.1 The Effect of Changing Cell Membrane Curvature, n

First, we vary the cell membrane curvature, changing the parameter n from 1 to 10 in integer increments, and plot the results in Figure 7.2. In plot (b) we see that extracellular conductivity decreases approximately linearly as we increase curvature. At the starting value of 1 the conductivity is 115% of that at the control value, and at the highest value of 10 the conductivity is 85% of that at the control value.

Over the same range the intracellular conductivity decreases by 10%, as seen in plot (a). Almost all of this decrease occurs when n is increasing from 5 to 10, and conductivity actually increases slightly (by less than 1%) as n increases from 1 to 5. In the two-dimensional case (Figure 6.7) the intracellular conductivity changed by a much smaller amount (and in fact it increased, but only by less than 1% over the range of membrane curvatures considered), while the extracellular conductivity decreases from 120% to 80% of the control value, which are similar values to what we have observed in three dimensions.

Considering conduction velocity, we see in plot (d) that conduction velocity decreases by 8.5% over the range of curvature values used compared to 2% in the two-dimensional case. This is both because of the decrease in intracellular conductivity in three dimensions, and because of the greater increase in χ in the three-dimensional case: as can be seen from plot (c), the surface-area-to-volume ratio increases by 6% compared to less than 1% in two dimensions. This tells us that membrane curvature has more of an effect on conduction velocity in a three-dimensional geometry than in two dimensions.

7.2.2 The Effect of Changing Gap Junction Height, h

Next, we vary the height of the gap junctions from 0.1 to 0.8, with the results shown in Figure 7.3. In plot (a) we see that increasing gap junction height significantly increases the

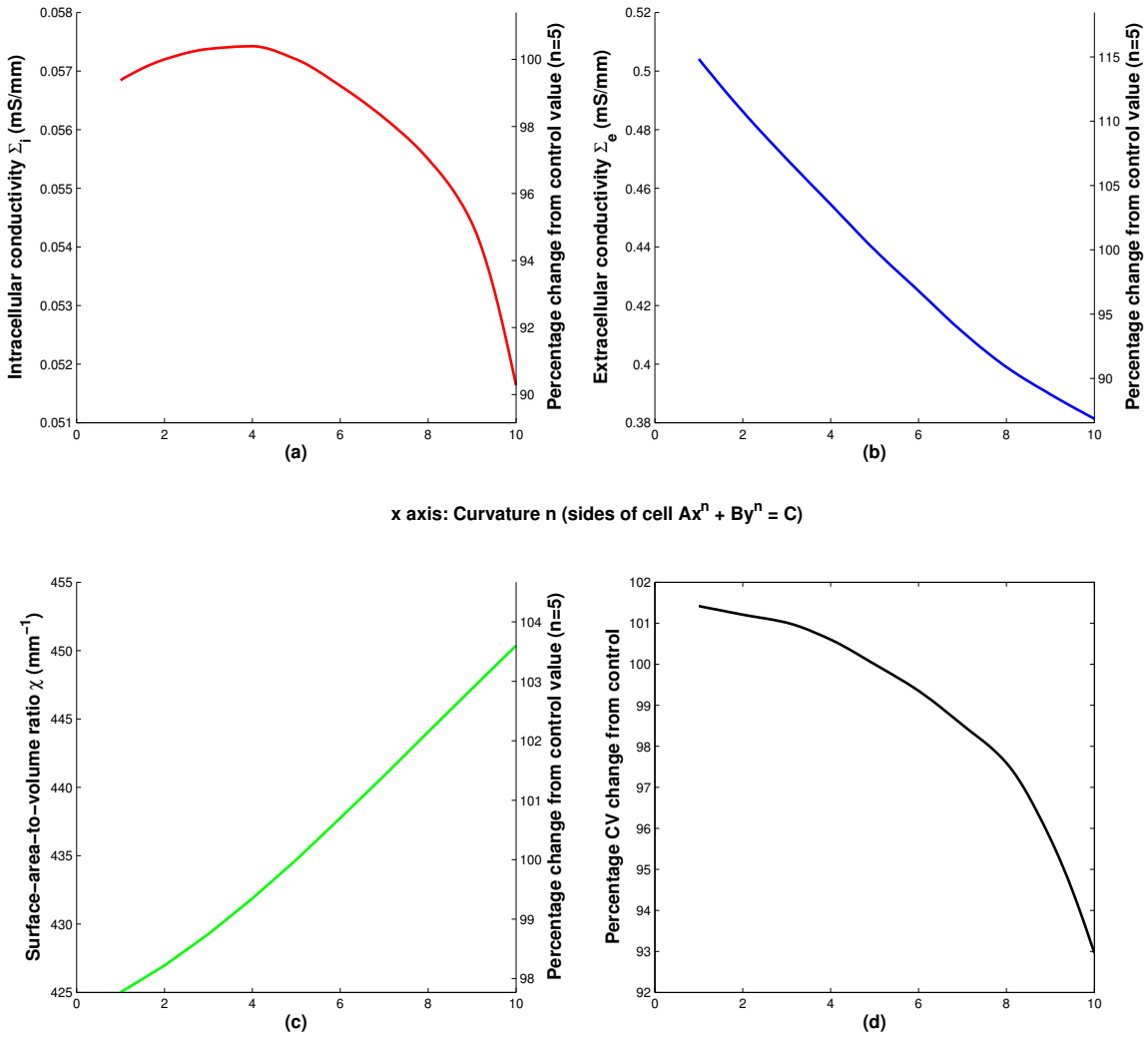

Figure 7.2: *The results of calculations using an isotropic cell as we vary the cell membrane curvature n.*

intracellular conductivity, with values increasing from just 6% of the control value of 0.5 when considering the lowest value of gap junction height, to 250% when considering the highest value of gap junction height. We expect this behaviour at the low end because the intracellular conductivity will be zero when the gap junction height is zero, however in the two-dimensional case (see Figure 6.8) the respective percentage changes were much smaller (from 20% to 120%), which suggests that the intracellular conductivity drops faster as gap junction height decreases (and rises faster as it increases) in a three-dimensional geometric framework. The extracellular conductivity decreases fairly significantly over the range, from 220% of the control value to 25% of the control value, as shown in plot (b) of Figure 7.3, which is more than we saw in two dimensions (where the conductivity decreased from 130% down to 75%).

The overall effect on conduction velocity can be seen in plot (d), and is noteworthy. When increasing gap junction height from 0.1 to 0.5, conduction velocity more than triples. However, when increasing gap junction height from 0.5 to 0.8, conduction velocity actually decreases to 85% of the starting value. In the two-dimensional case, conduction velocity uniformly increased with gap junction height, and values changed from 45% to 105% of the control value.

We believe the overall magnitude of the increase in conduction velocity for the three-dimensional case is partly due to the increase in intracellular conductivity already discussed, and partly due to the more rapid change in surface-area-to-volume ratio over the specified parameter range, which increased by around 25% in the two-dimensional case, but increases by 100% in the three-dimensional case, with the majority of the increase in three dimensions occurring as gap junction height increases from the lowest value to the control value.

However, the subsequent decrease in conduction velocity for larger gap junction heights is down to the change in the relative sizes of the intracellular and extracellular tensors. Referring back to Section 4.3.6, we know that the conduction velocity is more sensitive to changes in the intracellular tensor when it is small compared to the extracellular tensor. When gap junction height is 0.1, the intracellular tensor is over an order of magnitude smaller than the extracellular tensor, and so the conduction velocity increases due to the increase in in-

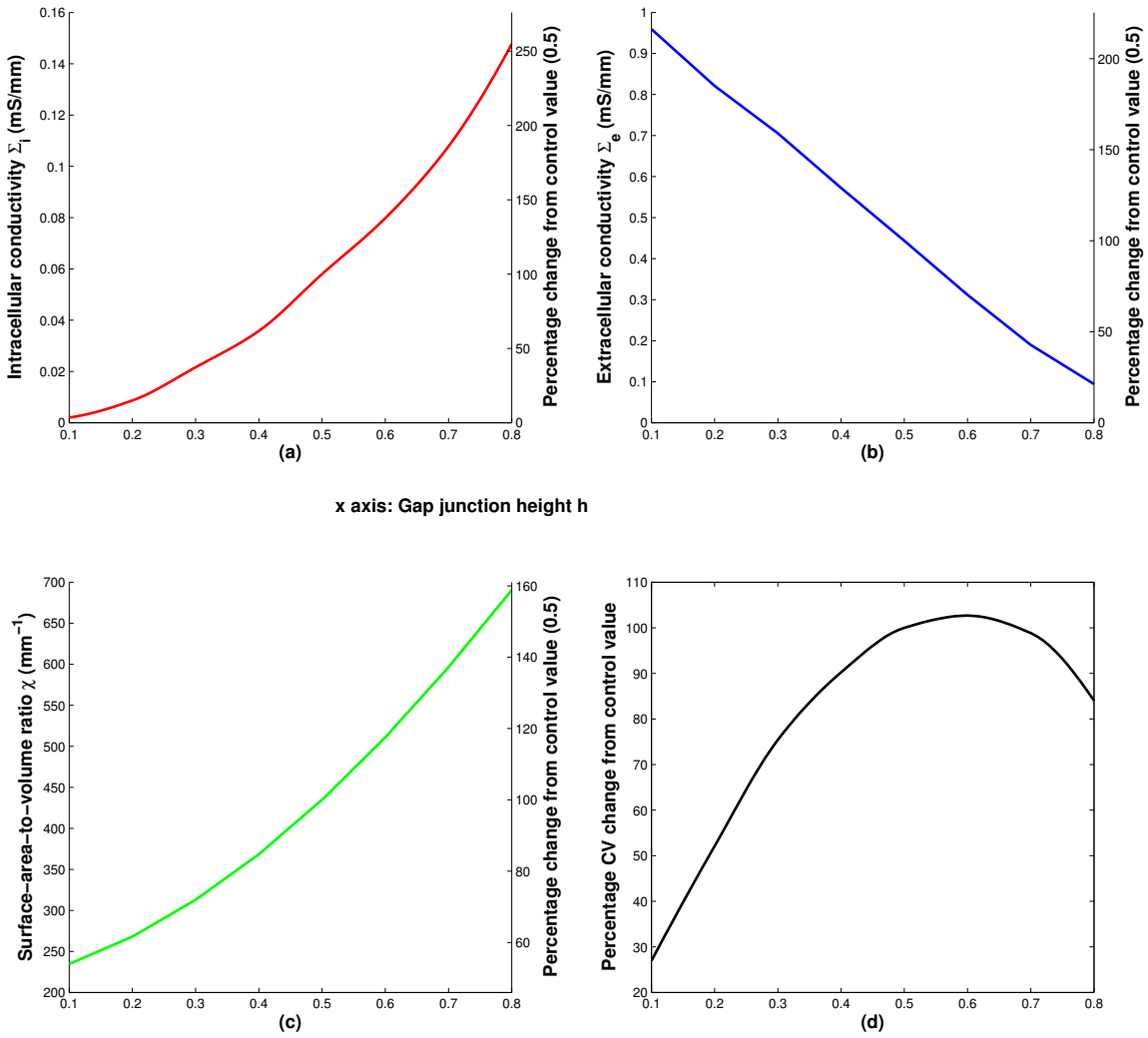

Figure 7.3: *The results of calculations using an isotropic cell as we vary the gap junction height h.*

tracellular conductivity. However, when gap junction height is 0.8, the intracellular tensor is almost an order of magnitude bigger than the extracellular tensor as the intracellular conductivity is rapidly increasing while the extracellular conductivity is decreasing, and so the conduction velocity is more sensitive to changes in the extracellular tensor. This drops as we increase gap junction height, and so the conduction velocity decreases.

Overall, this tells us that conduction velocity changes are very different when we vary gap junction height depending on the dimensionality of the geometry, and therefore we must take this into account when homogenising cardiac tissue.

7.2.3 The Effect of Changing Gap Junction Length, δ

We now vary gap junction length from 0.01 to 0.1 and plot the results in Figure 7.4. In plot (d) we see that the conduction velocity decreases over the parameter range, from 160% to 75% of the control value. The change in χ is small, as shown in plot (c), and we see from plots (a) and (b) that the intracellular conductivity decreases significantly, from 400% to 50% of the control value, whilst the extracellular conductivity increases moderately, from 70% to 130% of the control value.

Comparing this with the results when using a two-dimensional geometry (see Figure 6.9) we see that conduction velocity changes are similar as we vary gap junction length — in the two-dimensional case, conduction velocity decreased from 180% to 75% of the control value as δ increased, compared to a decrease from 160% to 75% in the three-dimensional case. Changes in the intracellular conductivity, extracellular conductivity and surface-area-to-volume ratio were also comparable to those in two dimensions.

This tells us that the effect of gap junction length on conduction velocity is similar in both two- and three-dimensional frameworks, and in particular that increasing gap junction length from 0.05 to 0.1 reduced conduction velocity by 25%, which matches the values found both in Section 4.3.4 and Section 6.2.4.

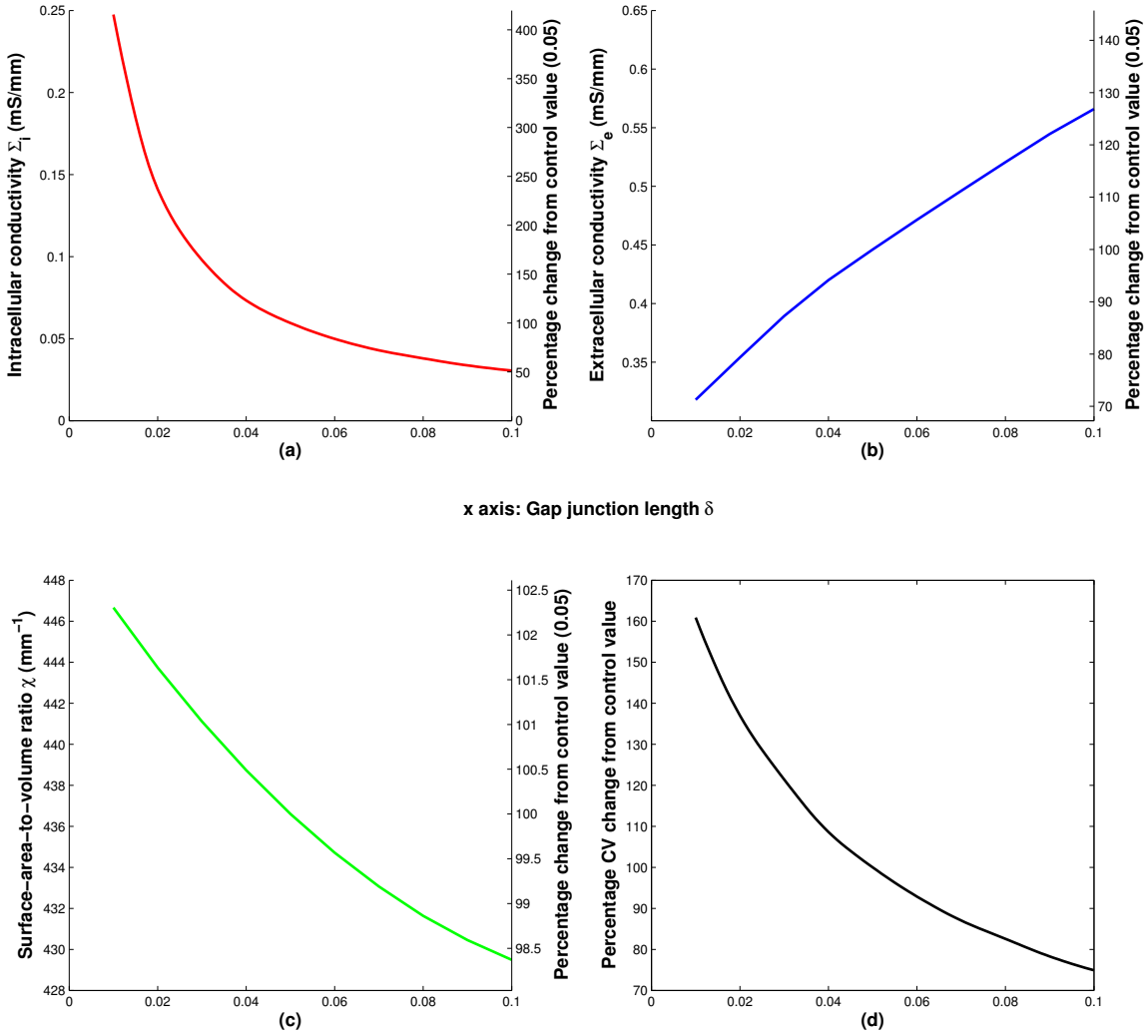

Figure 7.4: *The results of calculations using an isotropic cell as we vary the gap junction length δ.*

7.2.4 The Effect of Changing Gap Junction Conductivity, σ_g

Finally we vary gap junction conductivity, which we do logarithmically between 0.00025 mS/mm and 0.25 mS/mm in the same manner as Section 6.2.5. We plot the results in Figure 7.5 and see in plots (b) and (c) that as gap junction conductivity does not affect the geometry of the cell, it does not impact either Σ_e or χ, and so changes in conduction velocity are solely due to changes in the intracellular conductivity.

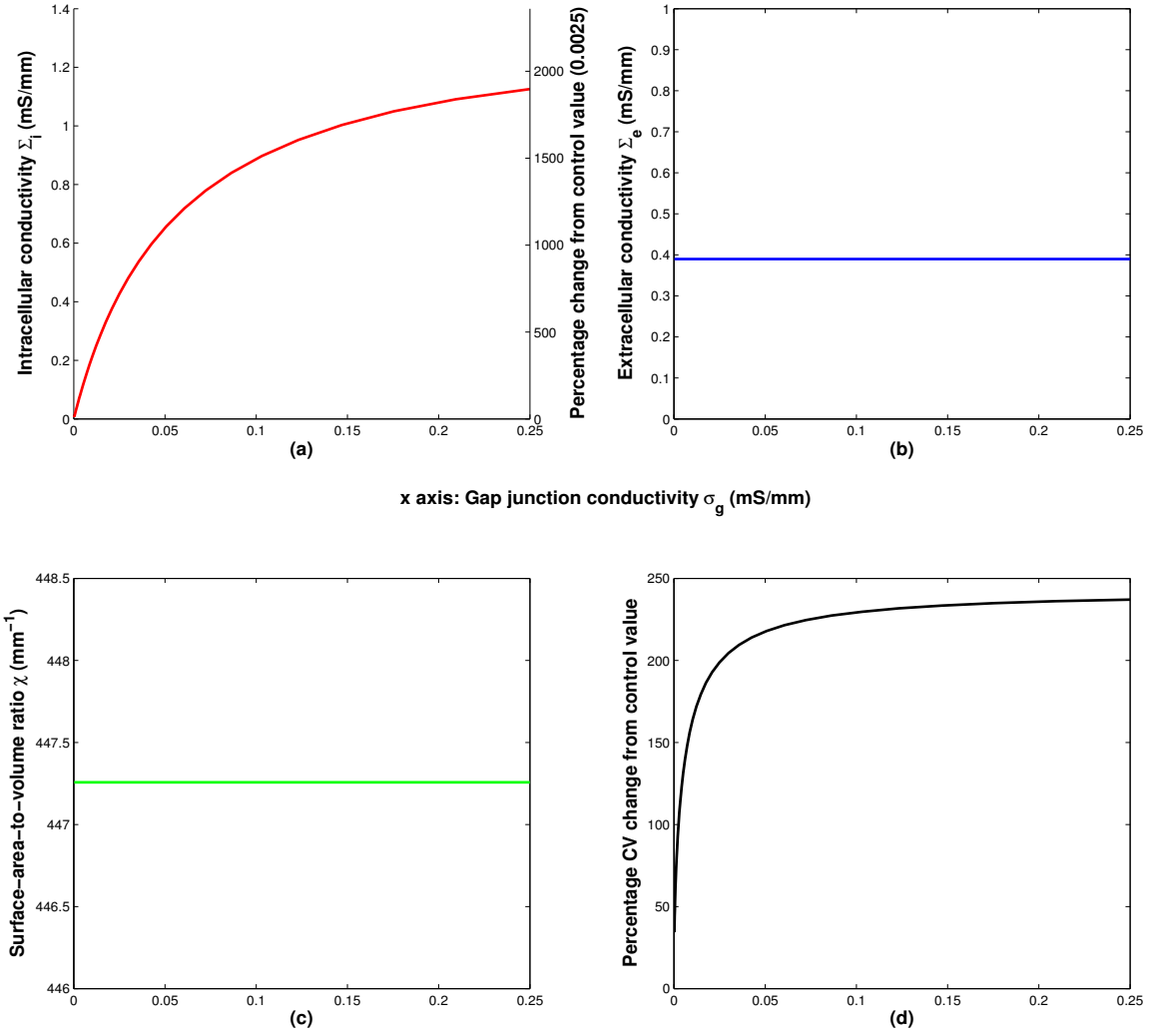

Figure 7.5: *The results of calculations using an isotropic cell as we vary gap junction conductivity σ_g.*

Turning to the results of intracellular conductivity calculations, we see in plot (a) that Σ_i increases nearly 20-fold from the control value of $\sigma_g = 0.0025$ mS/mm to the highest value of 0.25 mS/mm, and decreases to 10% of the control value when we decrease σ_g to

the lowest calculated value of 0.00025 mS/mm. This has the effect of increasing conduction velocity from 32% of the control value of the lowest value of σ_g to almost 240% of the control value at the highest value of σ_g, as can be seen in plot (d). In the two-dimensional case, shown in Figure 6.10, conduction velocity increased from 30% to 220% of the control value, which suggests that increasing gap junction conductivity has a similar effect on conduction velocity on a three-dimensional geometry as for a two-dimensional geometry.

We also note that in the specific case where σ_g is reduced by 50% of the control value, conduction velocity decreases by 25%. We discussed in Section 6.2.5 that this case models diseased conditions in which connexin levels are reduced below their normal values, and we have now found that this has the same effect on conduction velocity whether we consider a two-dimensional rectangular cell, a two-dimensional cell with a curved cell membrane, or a three-dimensional cell.

7.2.5 Conclusions

In this section we calculated intracellular and extracellular homogenised conductivity tensors for an isotropic three-dimensional cell as we varied cell and gap junction parameters. We wrote down the predicted change in conduction velocity of a monodomain formulation of the continuum model, and compared these changes with those in Chapter 6 for two-dimensional cells.

We found that the effect of modelling diseased gap junctions with reduced conductivity was similar between two- and three-dimensional simulations. We also found that certain parameters, most notably gap junction height, had a much larger effect on conduction velocity in three dimensions. From this we concluded that we should take care when homogenising on a domain of different dimensionality from that on which we conduct simulations — for example, if we are modelling a monolayer of cardiac cells, this would normally be described as a two-dimensional continuum simulation, and we would expect to use homogenised conductivity tensors that are nonzero in both intracellular and extracellular spaces and in both fibre and off-fibre directions. We have already seen that we cannot achieve this by homogenising a

two-dimensional discrete cell, so we must use a three-dimensional cell. However, the results of this section and of Section 6.2 tell us that the effect on the continuum conductivities (and the predicted conduction velocity) of varying the discrete geometry does not match when we move to a three-dimensional cell. In this case, the inferences drawn would be inaccurate, and the resulting two-dimensional continuum model would have a conduction velocity that does not adapt in the manner expected to changes in the underlying discrete geometry.

7.3 Anisotropic Cell Results

We now consider a cell with a more realistic aspect ratio — that is, one which is much longer than it is tall. In our homogenised conductivity tensor calculations in previous chapters, we considered two-dimensional cells connected only in the fibre direction. This meant that we were unable to see the effect that the natural shape of cardiac cells has on the anisotropy of the tissue. We finished this work in Section 6.4 by starting to consider off-fibre gap junctions and the resulting intracellular anisotropy, but owing to the limitations of homogenising in two dimensions we were unable to get extracellular anisotropy values. It is only now that we have a three-dimensional cell that we can see what effect the long, thin nature of cardiac cells has on the homogenised conductivity tensors.

In addition, now that we are considering a more realistic cell in which we have nonzero conductivities in all three directions and a geometry that permits both spaces to be anisotropic, we wish to determine the effect of varying those parameters that were previously outlined as having a large effect on conduction velocity when in a diseased state. Referring back to Chapter 5, gap junction conductivity and cell length had a major role in determining conductivity, and in Chapter 6 it was gap junction conductivity and gap junction length (which, as we were homogenising on the unit square and as the homogenised conductivity tensors are invariant to stretch, is equivalent to looking at changing cell length and keeping a constant gap junction length). We have also explained earlier in this chapter how modelling long, thin cells is equivalent to having smaller gap junctions in the off-fibre directions than in the fibre direction, and this is another component of cellular anisotropy that we

wish to consider.

To model this anisotropy, we stretch the cell shown in Figure 7.1 so that it is of length L, width W and height H, and allow the gap junction dimensions to vary so that they are different in each direction. We then assume that the two off-fibre directions are isotropic, *i.e.* that the cells are transversely isotropic, which is equivalent to setting H=W and making the two off-fibre direction gap junctions have identical dimensions. As a result, this change in cell geometry can be parameterised in the manner caricatured for a two-dimensional cell in Figure 7.6 by length L, height H, gap junction heights GJH_x and GJH_y, and gap junction lengths GJL_x and GJL_y.

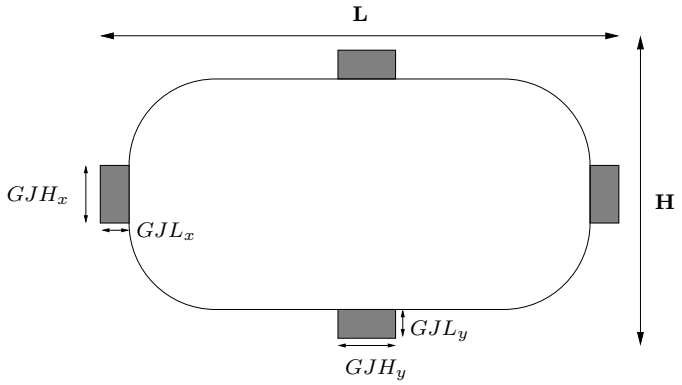

Figure 7.6: *A two-dimensional representation of a three-dimensional cell that is anisotropic.*

We can then use the fact that the homogenised conductivity tensors are invariant to linear stretch (see Appendix C.3) to transform the cell back to the unit cube. We do this by setting $\hat{x} = \frac{\mathrm{H}}{\mathrm{L}}x$, where x represents the fibre direction. This has the effect of setting $\widehat{GJL_x} = \frac{\mathrm{H}}{\mathrm{L}}GJL_x$ and $\widehat{GJH_y} = \frac{\mathrm{H}}{\mathrm{L}}GJH_y$. In other words, we simply have a version of the cell in Figure 7.1 where the gap junction sizes are different between fibre and off-fibre directions, which means that to see how cell geometry affects the anisotropy ratio, we can vary the properties of the off-fibre direction gap junctions with respect to the fibre direction gap junctions. Given this, we want to continue with the theme of studying those diseased states that were found to have a large impact on both homogenised conductivity tensor calculations and on the results of discrete and continuum simulations across the previous three chapters.

The first of these was gap junction conductivity, for which we saw large changes to conduction velocity and intracellular anisotropy in Section 6.4 when we changed off-fibre gap junction conductivity whilst keeping fibre direction conductivity constant. This modelled diseases where we have a change in the distribution or expression of gap junctions between cell ends and transverse locations, such as in ischaemic tissue or in a healed infarct zone — we described in Section 2.3.1.2 how these changes in gap junctions affect propagation. Specifically, we saw that the anisotropy of the intracellular space was modified, leading to an increased susceptibility to re-entrant arrhythmias (when side-to-side junction coupling strength is reduced) or to a slowing of propagation (when gap junctions are lateralised).

The second was myocyte length, an increase in which caused the result of discrete and continuum simulations to diverge and caused a significant change in the conductivities of the system when modelling diseases such as hypertrophy in Chapters 4 and 5. As described in this chapter, we can model an elongated myocyte using our geometric framework by reducing gap junction height in the off-fibre directions when compared to an isotropic cell.

As such, we now calculate the homogenised conductivity tensors for the cell shown in Figure 7.1 where we use the same default parameters as in Section 7.2 and vary model parameters as follows:

- we change the ratio between fibre direction and off-fibre direction gap junction height so that the fibre direction gap junction height ranges from 1 to 10 times that of the off-fibre direction gap junctions; and
- we change the gap junction conductivity of the off-fibre direction gap junctions between 0.0025 mS/mm and 0.025 mS/mm, that is from 10% to 100% of the conductivity of the fibre direction gap junction.

We have chosen to vary the parameters as specified in order to perform a direct comparison with Section 6.4 in which we found that the intracellular anisotropy ratio was highly sensitive to changes in gap junction parameters. Physiologically, changing gap junction conductivity in the off-fibre direction models the case where connexin expression is non-uniformly changed between the two directions in disease, and changing gap junction height simulates the

situation either where the number of gap junctions is varied, or where the aspect ratio of the cell is changed.

Using the results of the calculations outlined, we write down intracellular and extracellular anisotropy ratios along with the quotient of these two values, in order to see whether we have unequal anisotropy ratios between intracellular and extracellular domains. We also calculate the theoretical fibre direction conduction velocity under the monodomain assumption.

7.3.1 The Intracellular Anisotropy Ratio

In Figure 7.7 we plot the intracellular anisotropy ratio of the conductivity tensors calculated for the range of gap junction height and conductivity ratios specified in Section 7.3. In the geometry under consideration, the two off-fibre directions are isotropic, and so the intracellular anisotropy ratio (denoted AR_i) is equal to

$$\mathrm{AR}_i = \frac{\Sigma_{i_{(1,1)}}}{\Sigma_{i_{(2,2)}}} \equiv \frac{\Sigma_{i_{(1,1)}}}{\Sigma_{i_{(3,3)}}}. \tag{7.7}$$

We see from the results that the intracellular anisotropy ratio is moderately sensitive to changes in the ratio of gap junction height. If we fix off-fibre gap junction conductivity at the lowest value used and vary gap junction height ratio, the anisotropy ratio changes from 6.1 to 9.1 as the gap junction height ratio varies from 1 to 10, which is an increase of 50%. Similarly if we fix off-fibre gap junction conductivity at the highest value used then the anisotropy ratio changes from 1 to 1.6; a 60% increase.

We can look at these changes in gap junction height from the perspective of changing the aspect ratio of the cell, where decreasing gap junction height in the off-fibre direction, and thus increasing the ratio between fibre and off-fibre direction gap junction heights, means that we are modelling a longer, thinner cell. In this case, the intracellular anisotropy increases as outlined in the previous paragraph, which tells us that as we might expect, a cell that is much longer than it is wide will have a greater intracellular anisotropy. However, the magnitude of the numbers hint that this discrepancy in gap junction height and the

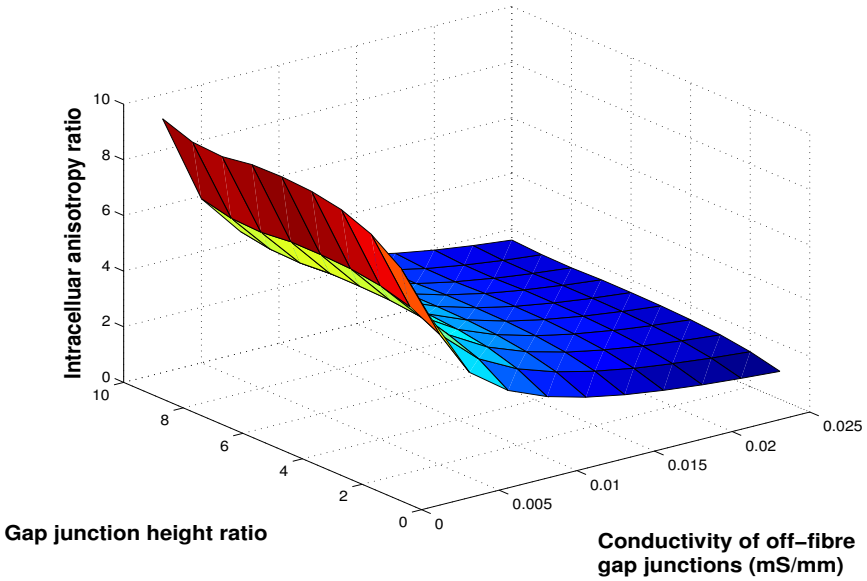

Figure 7.7: *The intracellular anisotropy ratio as we vary gap junction conductivity in the off-fibre direction and gap junction height ratio between the fibre direction and off-fibre directions.*

associated change in aspect ratio does not fully account for the experimentally observed values of intracellular anisotropy ratio. If we assumed that the off-fibre gap junction conductivity was equal to that of the fibre direction gap junction conductivity, and that the cell was almost ten times as long as it is wide, then our results give the anisotropy ratio as 1.6, which is significantly lower than physiologically normal values. From this we conclude that the conductivity or proportional size of the off-fibre gap junctions must be set at a lower value than that of the fibre direction gap junctions in order to produce realistic anisotropy ratios.

Next, we observe that the anisotropy ratio is much more sensitive to changes in the ratio of gap junction conductivity than to changes in gap junction height. For the lowest considered value of gap junction height ratio, the anisotropy ratio changes from 1 to 6.1 over the range of σ_g values considered, which is an increase of 510%. When we fix gap junction height ratio at the highest value and change σ_g, the anisotropy ratio increases from 1.6 to 9.1, and this is a 450% change. These results are similar to those in Section 6.4 obtained when we considered a subset of the overall results in that section that corresponded to the more physiologically realistic values of intracellular anisotropy. There, we found increases

of 560% and 640% when changing gap junction conductivity for high and low gap junction widths respectively, compared to 450% and 510% here. The increases in anisotropy ratio for varying gap junction size are also similar (60% and 80% in Section 6.4 compared to 50% and 60% in this section).

However, in this section we are considering a wider range of gap junction height changes than in the previous chapter, where the gap junction height ratio changed by a factor of two from smallest to largest in the subset of results that we considered in Figure 6.25. If we similarly restrict our attention to this sort of parameter range by varying gap junction height ratio from 5 to 10, we find that the increase in anisotropy is at maximum 25% for any fixed value of σ_g.

Overall, we have found that the effect of changing gap junction height and conductivity is slightly smaller for a three-dimensional geometry when compared to the results using a two-dimensional geometry, and that changing the cell aspect ratio alone does not give a physiologically realistic intracellular anisotropy ratio. The findings suggest that the observation made in the previous chapter still holds: the intracellular anisotropy ratio is very sensitive to changes in gap junction parameters, in particular conductivity, and as such we must specify these parameters accurately to get a physiologically realistic anisotropy.

7.3.2 The Extracellular Anisotropy Ratio

We now consider the extracellular anisotropy ratio, which we were not able to calculate in two dimensions as the extracellular space was not connected in both fibre and off-fibre directions. We note that only variation in gap junction height ratio will affect this quantity, as changes in gap junction conductivity do not affect the extracellular space. As in the previous section, the two off-fibre directions are isotropic and so the anisotropy ratio is defined as

$$\mathrm{AR}_e = \frac{\Sigma_{e_{(1,1)}}}{\Sigma_{e_{(2,2)}}} \equiv \frac{\Sigma_{e_{(1,1)}}}{\Sigma_{e_{(3,3)}}}. \tag{7.8}$$

We plot this extracellular anisotropy ratio against gap junction height ratio in Figure 7.8, and see it changes very little from the control value of 1 (when fibre and off-fibre direction gap junctions have the same heights and so the whole cell is isotropic), with an increase of 7% over the range of gap junction height ratios considered. This suggests that the extracellular anisotropy ratio is not sensitive to changes in gap junction size, or changes in the aspect ratio of the cell.

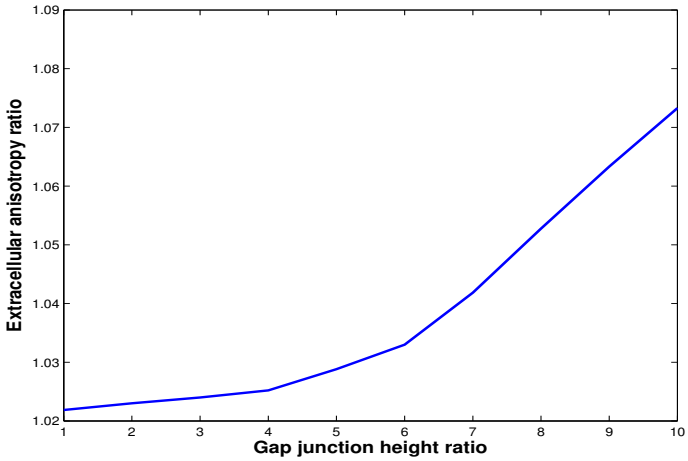

Figure 7.8: *The extracellular anisotropy ratio as we vary gap junction height ratio between the fibre direction and off-fibre directions.*

Given that a typical value for extracellular anisotropy is 5:2 [126], the result also tells us that our current extracellular geometry is not providing us with realistic values for the anisotropy ratio — simply modelling the extracellular space as long and thin does not meaningfully change the conductivity properties. Due to this we suggest that there are other factors which we are not considering that affect extracellular conductivity, and determining these would be a valuable step forward when modelling discrete cardiac tissue.

7.3.3 Comparing Intracellular and Extracellular Anisotropy Ratios

Considering a three-dimensional cell allows us to compare the anisotropy ratios between the intracellular and extracellular spaces. The phenomenon of unequal anisotropy ratios [125] in cardiac tissue is known to be fundamental to certain features of cardiac electrophysiology such as defibrillation [127, 128]. To see how gap junction parameters affect this, we plot

the quotient of the two anisotropy ratios, given by AR_i/AR_e, in Figure 7.9 for the same parameter set considered in the previous two sections. As expected, the plot looks very similar to that of the intracellular anisotropy ratio alone. This is because the extracellular anisotropy ratio changes very little as we vary gap junction parameters and the intracellular anisotropy ratio is highly sensitive to changes in gap junction parameters, as discussed in Section 7.3.1.

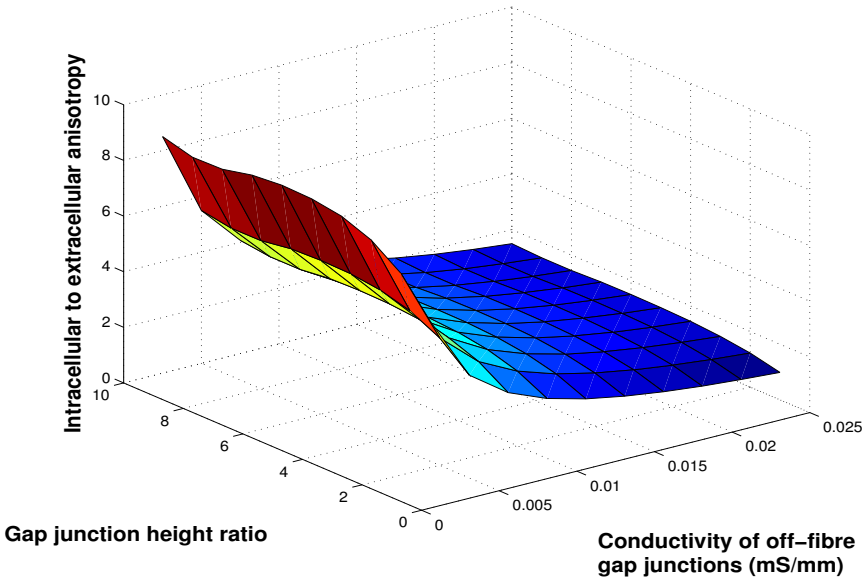

Figure 7.9: *The intracellular to extracellular anisotropy in the fibre direction as we vary gap junction conductivity in the off-fibre direction and gap junction height ratio between the fibre direction and off-fibre directions.*

This reinforces the importance of accurately specifying gap junction parameters when calculating conduction velocity and anisotropy in a three-dimensional model of cardiac tissue, especially in diseased conditions where gap junction parameters are altered: the intracellular anisotropy ratio is sensitive to changes in these parameters, so in turn the unequal anisotropy of the tissue depends heavily on gap junctions, and we know that the condition of unequal anisotropy has a large impact on action potential propagation.

Additionally, we discussed in Section 2.3.1 how certain common diseases such as ischaemia, atrial fibrillation, and hypertrophy, can cause changes in the structure and function of gap junctions, and outlined the effect that these changes have on propagation in living tissue. The finding in this section adds to the potential mechanisms by which gap junction

changes can affect propagation, in that we have calculated that a 50% reduction in gap junction conductivity can increase the intracellular anisotropy ratio by 25% (in the case where conductivity decreases from 0.005 mS/mm to 0.0025 ms/mm in Figure 7.9). This in turn changes the magnitude of the unequal anisotropy ratio condition by around 25%, which may have an effect on the propagation of action potentials.

7.3.4 Conductivity and Conduction Velocity Changes

We saw in Section 6.4 that increasing the size and conductivity of off-fibre gap junctions also increased fibre direction intracellular conductivity, which was a slightly unexpected result, and therefore we wish to see if this still holds true in three spatial dimensions. In addition, we now have nonzero conductivity in the extracellular space, so we can calculate the individual components of conduction velocity using a monodomain formulation and see how they are affected by gap junction changes. As the cells we are considering are aligned, Σ_i and Σ_e are diagonal, which means we can decompose the conduction velocity vector so that the quantity

$$\sqrt{\frac{\Sigma_{i_{(j,j)}}\Sigma_{e_{(j,j)}}}{\chi(\Sigma_{i_{(j,j)}}+\Sigma_{e_{(j,j)}})}}, \qquad j=1,2,3,$$

is the predicted conduction velocity in the j-th direction of a monodomain system. In Figure 7.10 we plot the fibre direction and off-fibre direction intracellular conductivity changes as we vary gap junction width and conductivity ratios, and also plot changes in the extracellular tensor and the surface-area-to-volume ratio against gap junction width ratio (these two quantities do not depend on gap junction conductivity). We then plot the fibre direction and off-fibre direction conduction velocities in Figure 7.11, where once more the two off-fibre directions are isotropic and so conduction velocity is identical in both directions.

We notice from plot (a) of Figure 7.10 that fibre direction intracellular conductivity changes negligibly as we vary off-fibre gap junction conductivity. This is in sharp contrast to the results found in Section 6.4 for two-dimensional cells, where increasing both conductivity

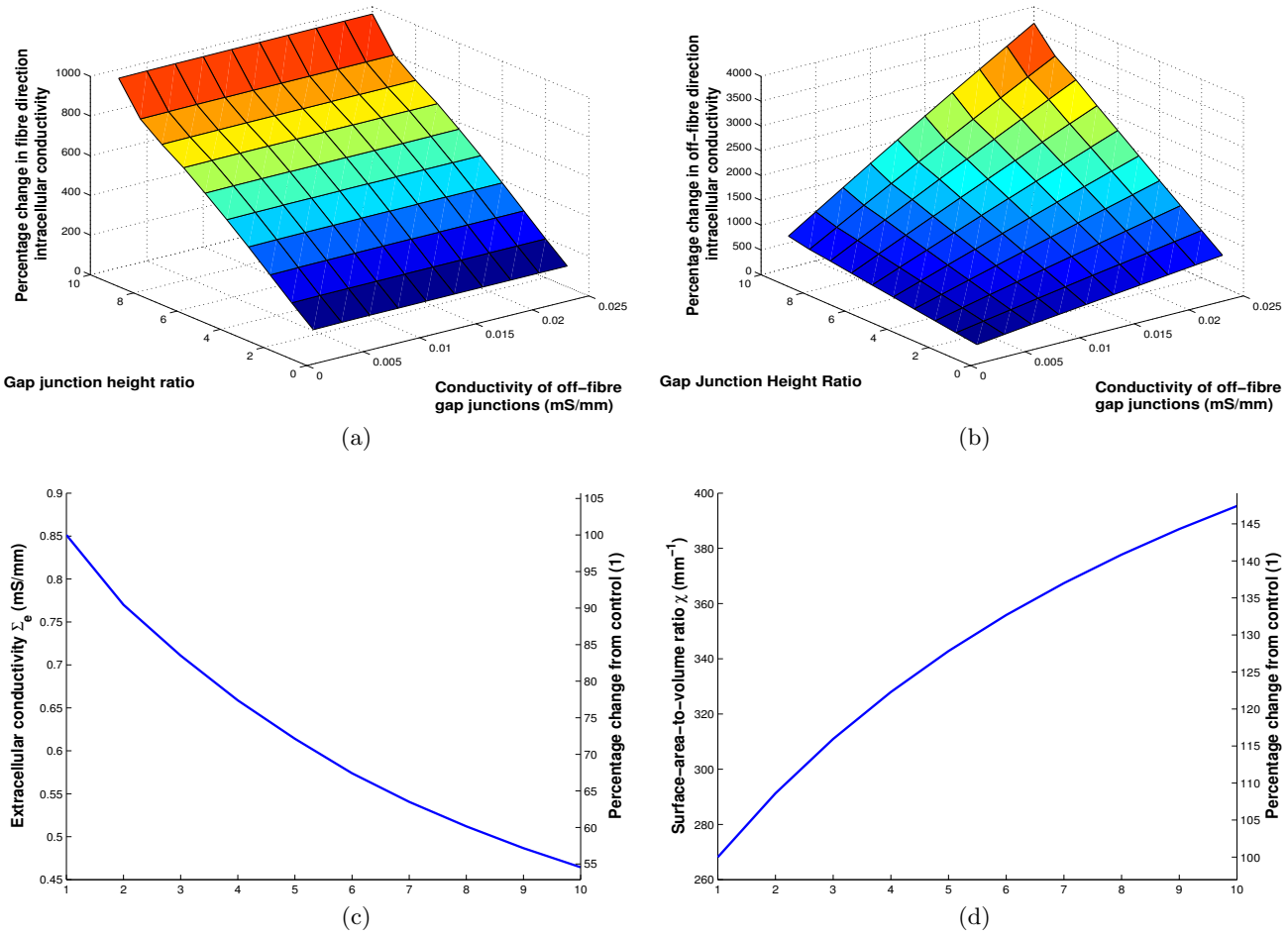

Figure 7.10: *Changes in fibre direction and off-fibre direction intracellular conductivity (a,b) for varying gap junction height and conductivity ratios; and changes in fibre direction extracellular conductivity and surface-area-to-volume ratio (c,d) as we vary gap junction height ratio.*

and width of the off-fibre gap junctions increased fibre direction intracellular conductivity. This difference in behaviour may be because we are considering aligned cells in this section, compared to the brick-wall structure used in the previous chapter. In that situation, the off-fibre gap junctions connected a given cell to two others in each adjacent fibre: one that was further down the fibre, and one that was less far down the fibre when compared to the given cell. As such, the off-fibre gap junctions may have created a pathway for enhanced conduction to occur, one that is in the fibre direction but that switches between fibres. In the three-dimensional case where cells are aligned with one another, off-fibre gap junctions connect cells to neighbouring cells that are at the same point along the fibre, and so do not create this pathway.

The remainder of the plots in Figure 7.10 show results that are more what we expect, in that they tie in more closely with the previous chapter. The off-fibre direction conductivity is once again highly sensitive to off-fibre gap junction parameters (plot (b)): the extracellular conductivity decreases by 45% as we increase gap junction height ratio, and this is because the fibre direction gap junctions are growing in size which reduces the extracellular volume fraction. This is similar to what we observed in Section 6.2.3 ,where we saw an almost identical change in extracellular conductivity when modifying fibre direction gap junction height. We also see in plot (d) that the surface-area-to-volume ratio increases moderately — as we increase gap junction height ratio, gap junction surface area also increases.

Given the moderate change in extracellular conductivity compared to the much greater changes in intracellular conductivity, combined with the fact that the extracellular conductivity and surface-area-to-volume ratio do not depend on gap junction conductivity, we see in Figure 7.11 that conduction velocity changes take a similar form to intracellular conductivity changes in both the fibre direction (plot (a)) and the off-fibre direction (plot (b)). That is, fibre direction conduction velocity increases significantly with gap junction height ratio, rising to 240% of its starting value, and stays almost constant as gap junction conductivity ratio changes. Off-fibre direction conduction velocity increases rapidly as we increase both gap junction height and conductivity ratio, to almost 500% of its starting value.

Tying this in with the gap junction remodelling seen in various common clinical conditions that we outlined in Section 2.3.1.2, we find that the fibre direction conduction velocity of a three-dimensional system is likely to be sensitive to those conditions that result in a change between fibre direction and off-fibre direction gap junction conductivities — for example, when connexin expression is reduced non-uniformly in a healed infarct zone. In this situation, our results predict that the onset of this condition will significantly affect the conduction of an action potential down a fibre of cells. Considering propagation in the off-fibre direction, we observe that the conduction velocity changes rapidly when varying either gap junction conductivity or width, and so when considering any condition in which gap junction remodelling occurs, transverse propagation will be altered. In combination, we will see situations where conduction speed changes very differently between the two directions, which will modify the anisotropy and may cause issues such as conduction block or re-entry (see Section 2.3.2 for more details).

7.4 Summary

In this chapter, we considered the effect of introducing a three-dimensional geometry on homogenisation of cardiac tissue. We calculated the homogenised conductivity tensors and associated fibre direction conduction velocity for a range of cell membrane curvatures, gap junction heights, gap junction lengths and gap junction conductivities, using both isotropic and anisotropic cells.

We then compared the results for isotropic cells with those obtained in Section 6.2 using a two-dimensional geometry. Most notably, we found that conduction velocity behaved very differently when changing gap junction height. In two dimensions, conduction velocity increased uniformly for increasing gap junction height. This was driven by an increase in intracellular conductivity, and whilst extracellular conductivity steadily decreased, it was large compared to the intracellular conductivity and so it had less of an impact on conduction velocity. In three dimensions, conduction velocity started to increase for increasing gap junction height but then began to decrease for sufficiently large values of gap junction height.

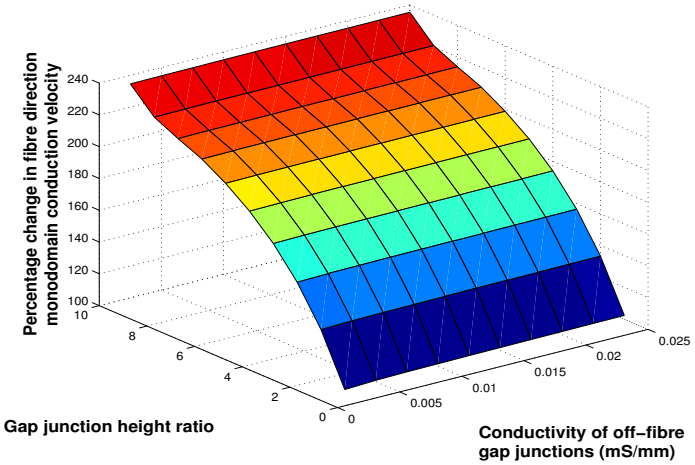

(a)

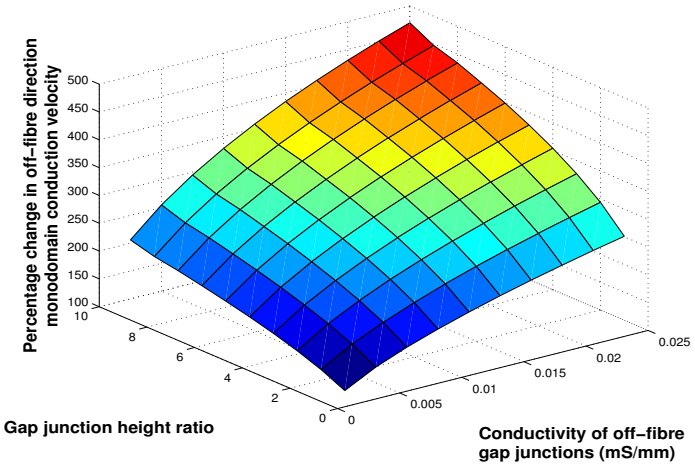

(b)

Figure 7.11: *The relative monodomain conduction velocity changes in the fibre direction (a) and off-fibre directions (b) as we vary gap junction height and conductivity ratios.*

This was because the extracellular tensor became much smaller than the intracellular tensor and so it had a much larger effect on conduction velocity. As the extracellular conductivity was decreasing with increasing gap junction height, conduction velocity decreased.

We determined that this discrepancy in behaviour would have a knock-on effect when performing continuum simulations on a geometry of different dimensionality to that on which we calculated the homogenised conductivity tensors — the changes in conductivity and predicted conduction velocity obtained by homogenising a three-dimensional cell may not be an accurate representation of the changes expected in a two-dimensional model.

When we considered anisotropic cells in Section 7.3, we saw that the intracellular anisotropy ratio behaved similarly to the way it did in two dimensions, in that it was highly sensitive to changes in gap junction parameters. We saw that changing gap junction height to model long, thin cells does not in itself give a physiologically normal intracellular anisotropy ratio, and that we must also model the off-fibre gap junctions as having reduced conductivity in relation to the fibre direction gap junction to obtain a realistic value.

We also found that the extracellular anisotropy ratio did not change appreciably when varying gap junction parameters. Additionally, the values obtained were not physiologically typical, suggesting that simply changing the aspect ratio of the cell does not account for the experimentally observed extracellular anisotropy.

As the extracellular anisotropy ratio was insensitive to these changes but the intracellular anisotropy ratio was much more sensitive, the factor by which the anisotropy ratios were unequal was greatly affected by gap junction parameters. As the phenomenon of unequal anisotropy ratios is known to be important for propagation of action potentials, this tells us that we need to accurately specify gap junction parameters in order to get physiologically realistic conductivity tensors, and that changes in gap junction parameters that occur in disease may have a large effect on the nature of the unequal anisotropy ratio and thus on propagation. Furthermore, we found that conduction velocity changes significantly when we change these gap junction parameters, which tells us that in those clinical conditions where gap junction remodelling occurs such as ischaemia or fibrillation, conduction is likely

to be impacted significantly.

Chapter 8

Conclusions and Future Work

Contents

The use of mathematical models to describe the behaviour of electrical activity in the heart is becoming more prevalent and important within the physiological and life sciences. A significant component of these models is the spread of an electrical signal through cardiac tissue. This propagation is determined by the structure of the tissue, and by cell-to-cell connections in the form of gap junctions that permit the signal to travel. There have been experimental and theoretical studies to determine the impact of gap junctions and tissue structure on impulse propagation in discrete tissue, and other work that outlines the changes in gap junction properties in diseased tissue. Concurrently, tissue-level systems are being used to model diseased states and predict the outcome of physiological changes on conduction. They often use a continuum approximation where macroscale parameters, most notably the homogenised conductivity tensors, are derived from the underlying microscale properties.

This thesis aims to provide a link between the threads outlined above. There is, or should be, a desire to model the changes in gap junction function or tissue structure that have been

observed in common diseased conditions, and to do this at the tissue level using a continuum system. To do this, we must ask various questions: is the derivation of the continuum model still valid when we include gap junctions with properties representing either healthy or diseased tissue, and what factors affect this validity? What is the theoretical effect on the continuum system of certain gap junction and tissue structure changes? What is the effect of the underlying discrete framework on the theoretical change in the continuum system? For example, how does changing this framework from a single strand of cells with propagation in one direction to a three-dimensional connected group of cells affect the properties of the continuum system? We have contributed to the field by attempting to answer these questions.

In the upcoming sections, we first summarise the findings of our research in Section 8.1. We then present a graphical summary of some of the major results concerning the effect of microstructure changes on conduction velocity in Section 8.2, before outlining a set of possible future work strands that build on this thesis in Section 8.3.

8.1 Summary of Findings

We considered the effect of gap junctions on the homogenised conductivity tensors in Chapter 4 by adapting both a discrete model, and a continuum system rigorously derived from the discrete model, to include gap junctions as distinct physical entities. We derived analytic forms of the homogenised conductivity tensors, both with and without gap junctions, for a two-dimensional rectangular cell geometry. From there we determined that the conduction velocity obtained by performing continuum simulations closely matched the theoretical predictions from the calculated homogenised conductivity tensors, which led us to assume throughout the thesis that this theoretical value is an accurate representation of the continuum conduction velocity. We then used this to calculate the expected change in conduction velocity when modifying gap junction parameters on our simplified geometry, finding that the contribution of including gap junctions at healthy coupling levels was to reduce conduction velocity by over 50%, and that reducing coupling levels to model a diseased state

further reduced conduction velocity by 20%.

We presented an analysis of the validity of the assumptions underpinning the creation of the continuum model in Chapter 5. The research demonstrated that modelling gap junctions at physiologically normal coupling levels gave a slight change in underlying conduction velocity between the discrete and continuum systems, which suggests that the continuum system provides a reasonable representation of the discrete model in this case. However, when modelling gap junctions with reduced coupling strength (as is observed in many common clinical conditions such as ischaemia and fibrillation), this change increased markedly such that the continuum conduction velocity was up to 44% higher than that of the discrete model. This means that when considering the effect on cardiac propagation of a disease in which gap junction strength is significantly reduced, a continuum system is likely to be inaccurate. We also discovered that the discrepancy between models increased for greater cell lengths, so that when looking at conditions in which myocyte length increases (*e.g.* hypertrophy), a continuum approximation again may give inaccurate results.

In Chapters 6 and 7 we extended the work of Chapter 4 and performed a comprehensive study to determine how changes in microstructure affect the homogenised conductivity tensors for both two- and three-dimensional geometries. In two dimensions, we discovered that gap junction parameters had a much larger effect on conductivity than other parameters (such as cell membrane curvature), and so must be carefully specified when creating a continuum model. We also found that the effect on conduction velocity of modelling diseased gap junctions with reduced conductivity was similar to that calculated using a simplified geometry in Chapter 4, which tells us that our work provides a reliable theoretical figure for the effect of diseased gap junctions on the conduction velocity of a continuum system. In addition, we demonstrated that both a brick-wall packing of cells and off-fibre connection between cells increased conductivity, and that the intracellular anisotropy ratio was highly sensitive to changes in off-fibre gap junction properties.

We then compared the results between two- and three-dimensional geometries, finding that the effect of changing gap junction parameters was different in each case, most prominently when changing gap junction height. As such, we concluded it may not be sufficient

to calculate homogenised conductivity using a three-dimensional cell and use it to study propagation in two dimensions (for example, when modelling a monolayer of cells with a two-dimensional continuum system), as the effect of changes to the underlying discrete system could be incorrectly reflected in the continuum model. We also found that conduction velocity changed rapidly when simulating the effects of gap junction remodelling, telling us that propagation is likely to be substantially affected in those conditions where remodelling is seen (such as post-infarct, in acute ischaemia or during atrial fibrillation). Finally, we found throughout the thesis that modelling gap junctions with reduced conductivity (as seen in many common diseases such as ischaemia and infarction) led to a similar decrease in conduction velocity whether using a simplified two-dimensional cell, a more complex two-dimensional cell, or a fully three-dimensional geometry.

We also observed that there are limitations to homogenising in two dimensions — one cannot obtain two homogenised conductivity tensors that are each nonzero in both fibre- and off-fibre direction. As a result, we were unable to calculate both intracellular and extracellular anisotropy ratios, and thus when using a three-dimensional cell we modelled anisotropic cells in order to calculate these quantities. We found that the anisotropy ratios behaved very differently between intracellular and extracellular spaces, with the intracellular anisotropy ratio much more sensitivity to changes in cell and gap junction parameters. This had a substantial effect on the phenomenon of unequal anisotropy ratio that is known to be a factor in determining action potential propagation.

8.2 Graphical Comparison of Geometric Schemes

In order to provide an intuitive understanding of the results of Chapters 4, 6, and 7, this section brings together similar calculations from the three chapters so that the effect of changing a certain physical quantity in each of the underlying discrete geometries can be easily compared. This will enable us to reach a simple conclusion that relates a physical or physiological change in the microstructure of cardiac tissue to the most appropriate

geometric framework for modelling said phenomenon.

We first show the effect of changing gap junction conductivity, σ_g, on the predicted conduction velocity of the continuum system for the two-dimensional rectangular cells of Section 4.3, the two-dimensional curved cells of Section 6.2, and the three-dimensional isotropic cells of Section 7.2. We do this because we found that conduction velocity is significantly impacted by a change in gap junction conductivity, and also because reduced gap junction conductivity is a pathophysiology prevalent in many common cardiac diseases such as ischaemia and infarction.

The results, plotted in Figure 8.1, show us that the effect of changing gap junction conductivity is identical between two-dimensional rectangles and two-dimensional curved cells, and this is because we modelled the gap junction as a rectangle in both cases. We also see that the effect of increasing gap junction conductivity above physiologically normal values is larger in three dimensions than in two dimensions. We focus on the effect of reducing gap junction conductivity in Figure 8.2, and in agreement with that discussed previously from a numerical standpoint, we see here that the effect of reducing gap junction conductivity is very similar in both two and three dimensions. We therefore suggest that a simple geometric framework suffices to accurately capture the effects of those diseases characterised by a reduction in gap junction conductivity.

Next, we show how changing gap junction height, δ_y, of the two-dimensional curved cells of Section 6.2, the two-dimensional brick-wall cells of Section 6.3, and the three-dimensional isotropic cells of Section 7.2, affects conduction velocity. We see from Figure 8.3 that the effect is very different for each of the three geometries, and that a reduction in gap junction height causes conduction velocity to drop much faster when modelling three-dimensional cells compared to two-dimensional cells. More notably, when we increase gap junction height the conduction velocity increases when using two-dimensional cells, but decreases for three-dimensional cells. For cases where gap junction height is altered, it seems that a two-dimensional geometric framework is unable to replicate the true effect on conduction

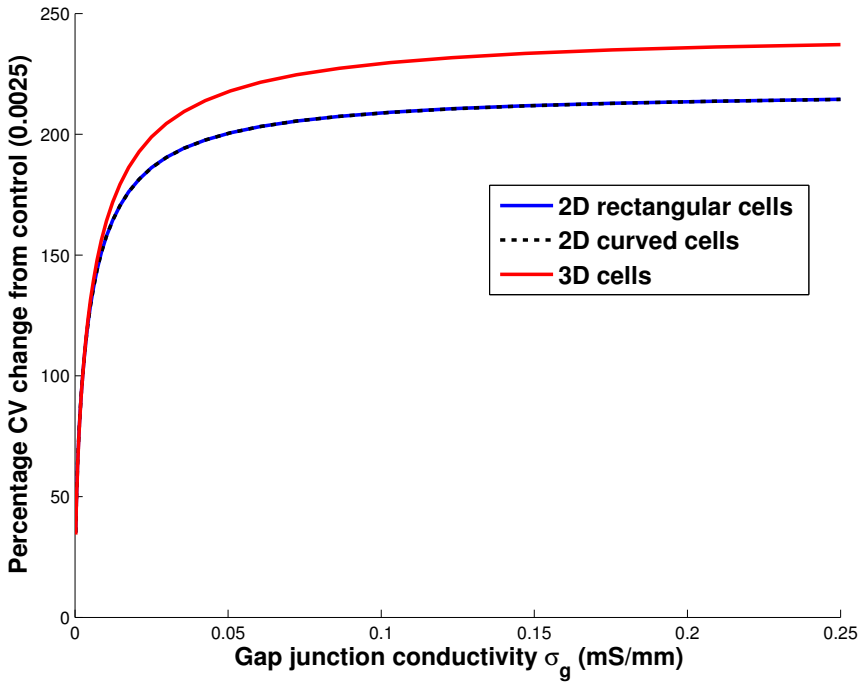

Figure 8.1: *A comparison of the effect of changing gap junction conductivity σ_g in different geometric schemes. The solid blue line and dotted black line lie exactly on top of each other.*

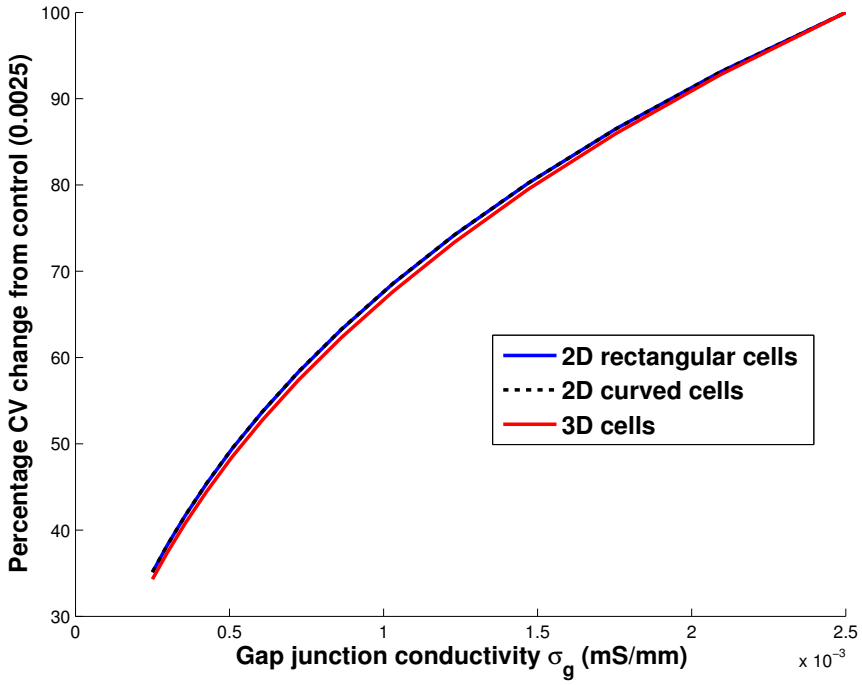

Figure 8.2: *A comparison of the effect of changing gap junction conductivity σ_g in different geometric schemes, focusing on reducing gap junction conductivity below physiologically normal values.*

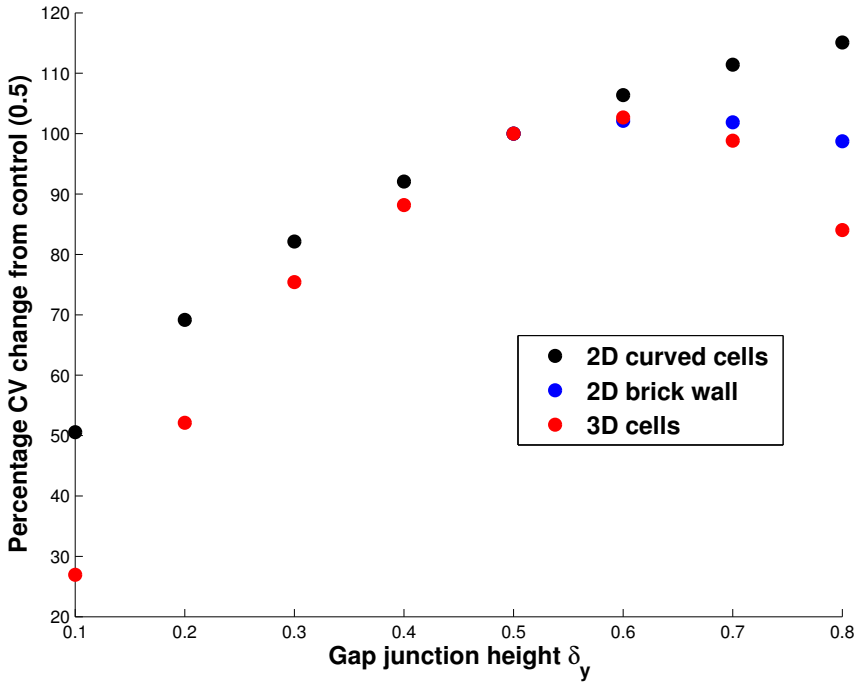

Figure 8.3: *A comparison of the effect of changing gap junction height δ_y in different geometric schemes.*

velocity in three dimensions, and so a three-dimensional geometry should be used.

We then see in Figure 8.4 that changing gap junction length, δ_x, has a similar effect for two-dimensional rectangular cells, two-dimensional curved cells, and three-dimensional cells. This suggests that a simple geometry is able to accurately model the effect of changing gap junction length on the predicted conduction velocity of the continuum system.

Lastly, we show the effect of changing cell height, h_y, between the two-dimensional curved cells of Section 6.2 and the two-dimensional brick-wall cells of Section 6.3. We do this as we found from calculations that the shape of the extracellular space had a large impact on conduction velocity, and that this was manifested when moving from an aligned cell structure to a brick-wall structure. We see this confirmed visually in Figure 8.5 — changes in cell height has a much more moderate effect for an aligned geometry than it does for a brick-wall geometry. We can therefore say that to model cells of varying height, a simple aligned geometry does not correctly capture the expected changes in conduction velocity,

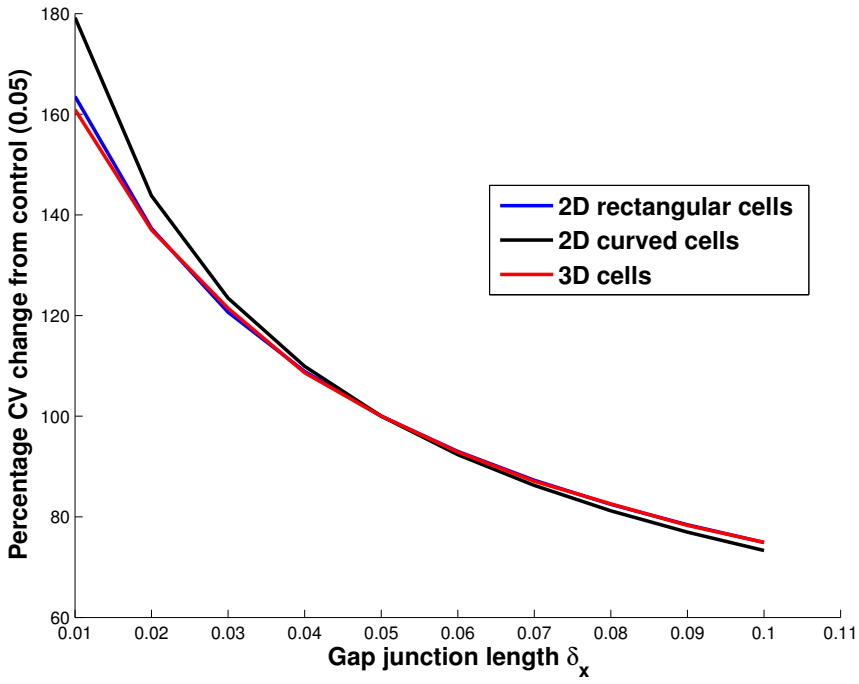

Figure 8.4: *A comparison of the effect of changing gap junction length δ_x in different geometric schemes.*

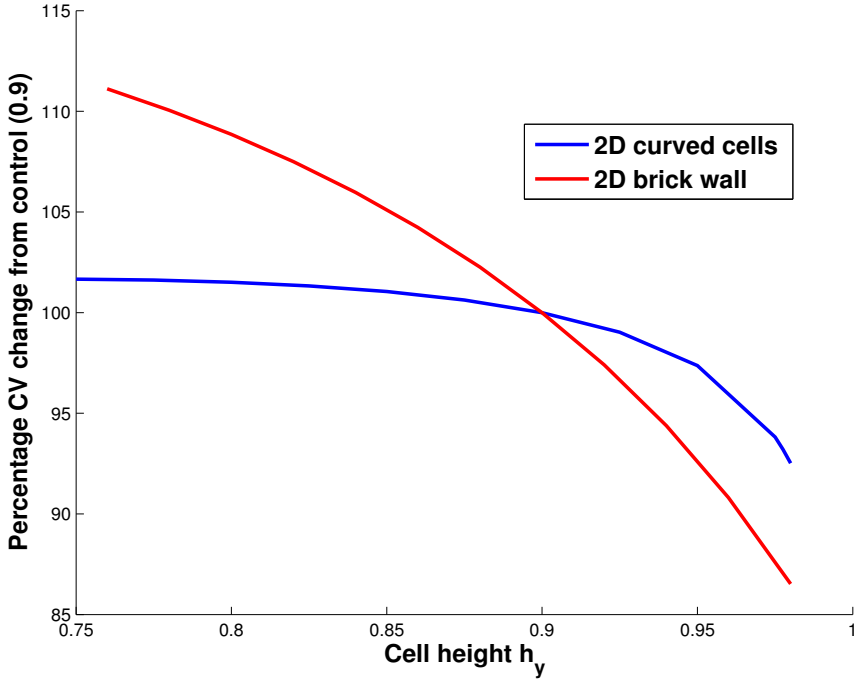

Figure 8.5: *A comparison of the effect of cell height h_y in different geometric schemes.*

and so a brick-wall structure should be used.

Having given an intuitive, visual representation of some of the major results of this thesis, accompanied by some basic recommendations as to the most appropriate geometry for modelling various physiological changes in cardiac cell structure, we now discuss ways in which the work of this thesis might be augmented.

8.3 Future Work

Looking forwards, our research can be extended in a number of directions. The majority of homogenised conductivity calculations were performed on a two-dimensional geometry, and it would be valuable to replicate more of these using a three-dimensional system. Specifically, the three-dimensional framework used in this thesis considers cells that are uniformly arranged. Extending this geometry to incorporate the brick-wall packing of cells would give further insight. The results of this thesis for two-dimensional cells could be used as a reference point for conductivity changes, and a thorough comparison could be performed. Additionally, it would be valuable to discover a potential explanation for the observed extracellular anisotropy ratios, as those obtained in our simulations did not match physiologically normal values.

Furthermore, we used a simple representation of cell geometry and gap junction structure when determining the validity of the continuum assumption in Chapter 5. As computing power increases, it will become feasible to perform a similar comparison between discrete and continuum simulations in which we use a highly detailed discrete cell representation, similar to those detailed in Chapter 6 and Chapter 7. This would provide the ability to determine whether the deductions in this thesis regarding the validity of the continuum approximation still hold for more complex and realistic cell geometries in either two or three dimensions.

Lastly, there is a small body of work that considers a hybrid approach to modelling tissue-level cardiac electrophysiology in which discrete and continuum systems are used in conjunction. The recent work of Hand and Griffith [48, 49] presented a one-dimensional model

in which a discrete system was used around the propagating wavefront and a continuum system was used elsewhere, which gave a system whose solutions closely matched those obtained using a fully discrete system. The authors mentioned the desire to extend this to a three-dimensional system, and we believe that the geometries considered in this thesis would provide a natural set of stepping stones for doing this. For example, one might begin by using the two-dimensional rectangular cells used for simulations in Chapter 4 to create a hybrid system in which propagation only occurs in one direction, which would provide a way to check the results against those of [48]. This could then be extended to the more realistically shaped two-dimensional cells considered in Chapter 6 and finally to the three-dimensional cells in Chapter 7. In addition, the homogenisation results presented here could be used to ensure accuracy of the continuum part of the hybrid system by providing the rigorously calculated homogenised conductivity tensors that take cellular microstructure into account.

However, the computational tractability of such a system must still be carefully considered given the level of detail required to model discrete cells, especially in three spatial dimensions, and as such we now outline a series of rough calculations that aim to estimate the computational requirements of a hybrid system based on the work in this thesis. The hybrid system proposed by Hand *et al.* uses a discrete model during the upstroke of the action potential, and a continuum model elsewhere. We have seen in Chapter 3 that a typical lengthscale of the upstroke is ten cells. If we were to consider one fibre of cells with a single wave propagating through it, then at any one time only ten cells will be described by the discrete model. Using the estimations in Appendix B of typical simulation running times on a desktop computer, and assuming that we were able to access a powerful computing resource ten times greater than a desktop, we would be able to perform the simulations in this thesis in around a minute for two-dimensional rectangular cells, in six minutes for two-dimensional curved cells, and in around ten hours for three-dimensional cells. However, if we consider a bundle of one hundred fibres and use three-dimensional cells, the computations will take several months even for a single second of electrical activity. Given this, the geometric setup of the three-dimensional cells used in this thesis should be optimised

for speed of simulation before attempting to use them in a hybrid system, and performance should be considered as a priority throughout the rest of the system — for example, by attempting to parallelise certain costly parts of the solution process.

Appendix A

The Finite Element Method

In this appendix, we will first give an overview of the finite element method for a generalised problem, before providing details of how to adapt the method to approximate the solution to the continuum model (given by the bidomain equations), and the discrete model used in this thesis. We will also outline more practical aspects of the implementation at each stage.

A.1 An Overview of the Finite Element Method

The finite element method is a technique for computing a numerical solution to a set of differential equations. The idea is to partition the domain of solution into small regions, called elements, and then approximate the solution on each of these elements using a low order polynomial function. To illustrate the method using a simple example, let us consider Poisson's equation with mixed boundary conditions in the two-dimensional region Ω, whose solution satisfies

$$\nabla^2 u = -f(x,y), \qquad (x,y) \in \Omega, \tag{A.1}$$

$$u = u^*(x,y) \qquad \text{on } \partial\Omega_D, \tag{A.2}$$

$$\nabla u \cdot \mathbf{n} = g(x,y) \qquad \text{on } \partial\Omega_N, \tag{A.3}$$

where $\partial\Omega_D$ and $\partial\Omega_N$ partition the boundary of Ω into two non-intersecting sets. We multiply Equation (A.1) through by a continuous *test function*, w, which is zero on $\partial\Omega_D$ and whose derivative is continuous except at finitely many points, and integrate over the whole domain and use the divergence theorem to give

$$\begin{aligned} 0 &= -\int_\Omega (\nabla^2 u) w \, \mathrm{d}V + \int_\Omega f w \, \mathrm{d}V, \\ &= \int_\Omega \nabla u \cdot \nabla w \, \mathrm{d}V - \int_{\partial\Omega} w \nabla u \cdot \mathbf{n} \, \mathrm{d}S + \int_\Omega f w \, \mathrm{d}V, \\ &= \int_\Omega \nabla u \cdot \nabla w \, \mathrm{d}V - \int_{\partial\Omega_D} w \nabla u \cdot \mathbf{n} \, \mathrm{d}S - \int_{\partial\Omega_N} w \nabla u \cdot \mathbf{n} \, \mathrm{d}S + \int_\Omega f w \, \mathrm{d}V. \end{aligned}$$

Using the boundary condition $\nabla u \cdot \mathbf{n} = g(x, y)$ on $\partial\Omega_N$ and the fact that $w = 0$ on $\partial\Omega_D$, we obtain the *weak form* of the Poisson equation:

Find u satisfying $u = u^*$ on $\partial\Omega_D$ and

$$\int_\Omega \nabla u \cdot \nabla w \, \mathrm{d}V - \int_{\partial\Omega_N} g w \, \mathrm{d}S + \int_\Omega f w \, \mathrm{d}V = 0, \qquad \forall w. \tag{A.4}$$

To discretise the weak form, we first discretise the geometry, replacing Ω with a computational mesh made up of triangular elements. Assume that there are N nodes in total in the mesh. We next choose a set of N basis functions ψ_j, $j = 1, 2, \ldots, N$, that are piecewise linear (linear in each element) and satisfy

$$\psi_j(\mathbf{x}_i) = \begin{cases} 1 & \text{if } i = j, \\ 0 & \text{if } i \neq j, \end{cases}$$

where the nodes are denoted by $\mathbf{x}_i$, $i = 1, 2, \ldots, N$. We write the finite element solution as

$$U = \sum_{j=1}^{N} U_j \psi_j,$$

where U_j will be the approximation of $u(\mathbf{x}_j)$. The finite element equations are obtained by restricting our test functions w to be such basis functions that also satisfy $w = 0$ on $\partial\Omega_D$

so that Equation (A.4) becomes

$$\int_\Omega \sum_{j=1}^{N} U_j \nabla\psi_j \cdot \nabla\psi_i \, \mathrm{d}V = \int_{\partial\Omega_N} g\psi_i \, \mathrm{d}S - \int_\Omega f\psi_i \, \mathrm{d}V, \qquad i = 1, \ldots, N. \tag{A.5}$$

We may write Equation (A.5) as

$$\sum_{j=1}^{N} K_{ij} U_j = b_i, \qquad i = 1, \ldots, N,$$

where K is the *stiffness matrix* with entries given by

$$K_{ij} = \int_\Omega \nabla\psi_j \cdot \nabla\psi_i \, \mathrm{d}V, \qquad i = 1, \ldots, N, \tag{A.6}$$

and

$$b_i = \int_{\partial\Omega_N} g\psi_i \, \mathrm{d}S - \int_\Omega f\psi_i \, \mathrm{d}V, \qquad i = 1, \ldots, N. \tag{A.7}$$

To apply the Dirichlet boundary condition to a given node, we simply zero the corresponding row of K and set its diagonal entry to be one, and set the corresponding entry of $\mathbf{b}$ to be equal to the boundary condition value, *i.e.* $u^*(\mathbf{x}_k)$ where k is a node with a Dirichlet boundary condition. We compute the stiffness matrix by assembly, meaning that we break the integral down into a sum of integrals over each individual element, before looping over all elements calculating the elemental contribution to the matrix.

Having outlined an overview of the finite element method from a mathematical perspective, we next give details about the practical implementation of the method for the generic Poisson problem considered in this section.

A.1.1 Practical aspects

In a two-dimensional framework, the domain is partitioned into triangular elements. The numbering of the nodes and elements is arbitrary, but we must know two properties of them — for each node, we must know its x- and y- positions, and for each element, we must know the three nodes that comprise its vertices. An important point is that on each element the vertices should be ordered in a consistent manner, and we choose to do so in a right-handed fashion (*i.e.* in the anti-clockwise direction). For example, consider the most basic case as shown in Figure A.1.

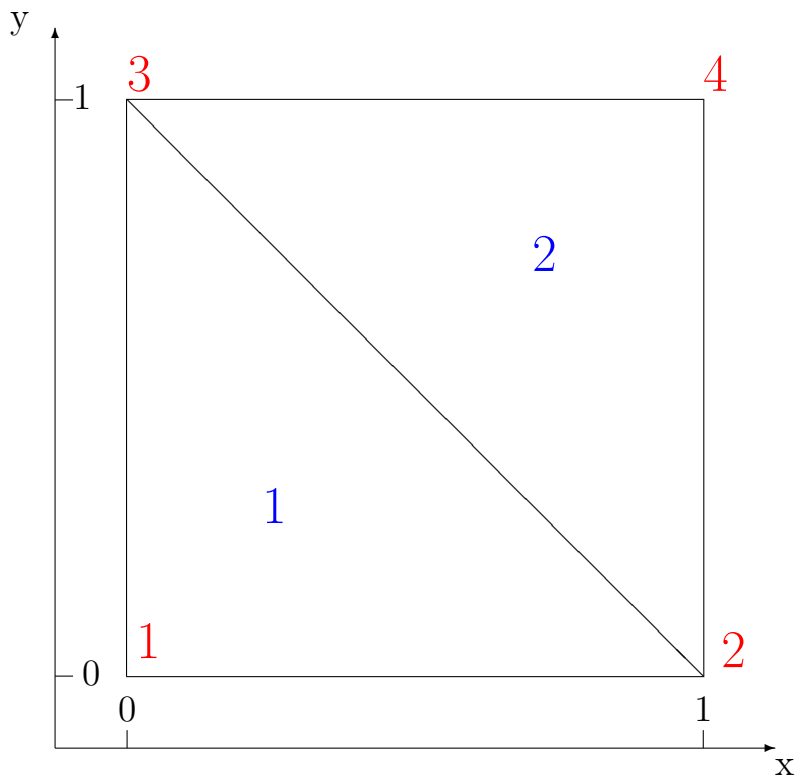

Figure A.1: *An example of a partitioned domain, the square* $[0,1] \times [0,1]$. *Node numberings are in red, and elements in blue.*

From this, we can write down a node position matrix

$$\text{nodes} = \begin{pmatrix} 0 & 0 \\ 1 & 0 \\ 0 & 1 \\ 1 & 1 \end{pmatrix}, \tag{A.8}$$

where the $(i, 1)$ entry contains the x-position of node i, and the $(i, 2)$ entry contains its y-position. We can also construct a connectivity matrix

$$\text{connectivity} = \begin{pmatrix} 1 & 2 & 3 \\ 4 & 3 & 2 \end{pmatrix}, \tag{A.9}$$

where the i-th row contains the node indices of element i.

We are now in a position to compute the entries of the matrix K (Equation (A.6)) and the vector $\mathbf{b}$ (Equation (A.7)) on each individual element. These contributions will then be summed over all elements to get the full form of the matrix. To use our previous example of a square cut along its diagonal into two triangular elements, the contribution from the second element will be added to the 4^{th}, 3^{rd}, and 2^{nd} rows of the global matrix and vector.

We then consider the triangle whose vertices lie at $(0, 0)$, $(1, 0)$ and $(0, 1)$, which is known as the *canonical triangle*, and choose basis functions, which are defined on the canonical triangle and are linear on each element, to be of the form

$$\begin{aligned} \psi_1(s, t) &= 1 - s - t, \\ \psi_2(s, t) &= s, \\ \psi_3(s, t) &= t. \end{aligned}$$

For any other triangle with vertices at (x_1, y_1), (x_2, y_2) and (x_3, y_3), the mapping to the canonical triangle is given by

$$x = x_1(1 - s - t) + x_2 s + x_3 t,$$
$$y = y_1(1 - s - t) + y_2 s + y_3 t.$$

The determinant of the Jacobian of this coordinate transformation is

$$\det(J) = (x_2 - x_1)(y_3 - y_1) - (x_3 - x_1)(y_2 - y_1),$$

and using the chain rule, partial derivatives become

$$\frac{\partial}{\partial x} = \frac{1}{\det(J)} \left((y_3 - y_1) \frac{\partial}{\partial s} + (y_2 - y_1) \frac{\partial}{\partial t} \right),$$
$$\frac{\partial}{\partial y} = \frac{1}{\det(J)} \left((x_1 - x_3) \frac{\partial}{\partial s} + (x_2 - x_1) \frac{\partial}{\partial t} \right).$$

For the simple form of the matrix K that we have here (Equation (A.6)) we may now calculate its entries, as we are integrating a constant over a known area.

However, for a more general form, or indeed for the entries of the vector $\mathbf{b}$, we must integrate numerically. We do this using Gaussian quadrature, for which the rule in two dimensions is

$$\int_0^1 \int_0^1 f(x, y) \, \mathrm{d}x \, \mathrm{d}y \approx \sum_{p,q=1}^{M} w_p w_q f(x_p, y_q), \tag{A.10}$$

where w_p and w_q are the weights, x_p and y_q are the quadrature points, and M is the number of quadrature points used in each coordinate direction. This method can yield exact results for polynomials of up to order $2M-1$, and as such two points in each direction are sufficient for linear basis functions. In this case the weights are both equal to 0.5, and the points are given by the tensor product of

$$\left[\frac{1}{2} \left(1 - \frac{1}{\sqrt{3}} \right), \frac{1}{2} \left(1 + \frac{1}{\sqrt{3}} \right) \right],$$

with itself. However, we want to integrate over the canonical triangle. To map the unit square onto the canonical triangle, where (s,t) are coordinates in the triangle and (x,y) are coordinates in the square, we set

$$s = x(1-y),$$
$$t = y.$$

Note that the determinant of the Jacobian of this mapping is simply $(1-y)$, and so we now have

$$\int\int_{\triangle} f(s,t)\ \mathrm{d}s\ \mathrm{d}t \approx \sum_{p,q=1}^{2} \frac{1}{4} f(x_p, y_q)(1-y_q).$$

After looping over all elements to assemble the matrix equation ($K\mathbf{u} = b$) we then solve the system using the PETSc package [3] to obtain an estimate for the value of u at each node.

In this section we have given on overview of the theoretical and practical aspects of the finite element method as applied to a general Poisson problem in two dimensions. We will now demonstrate how to implement the method for the continuum problem considered in this thesis (the bidomain equations).

A.2 The Finite Element Approximation to the Bidomain Equations

As a reminder, the bidomain equations are given by

$$\chi c_m \frac{\partial V}{\partial t} = \nabla_{\mathbf{x}} \cdot (\Sigma_i \nabla_{\mathbf{x}} (V + \phi_e)) - \chi I_{ion},$$
$$\nabla_{\mathbf{x}} \cdot ((\Sigma_i + \Sigma_e)\nabla_{\mathbf{x}} \phi_e + \Sigma_i \nabla_{\mathbf{x}} V) = 0,$$

with boundary conditions

$$-\Sigma_i \nabla(V + \phi_e) \cdot \mathbf{n} = 0,$$
$$\Sigma_e \nabla \phi_e \cdot \mathbf{n} = 0.$$

We apply the finite element method to this system using a semi-implicit time discretisation in which terms involving the spatial derivatives are discretised implicitly and the term involving the ionic current flux is discretised explicitly (as the ordinary differential equations governing the ionic concentrations can be highly nonlinear). At a given timestep $n+1$, we thus solve

$$\chi c_m \frac{V^{n+1} - V^n}{\Delta t} = \nabla_{\mathbf{x}} \cdot (\Sigma_i \nabla_{\mathbf{x}} (V^{n+1} + \phi_e^{n+1})) - \chi I_{ion}^n,$$
$$\nabla_{\mathbf{x}} \cdot ((\Sigma_i + \Sigma_e) \nabla_{\mathbf{x}} \phi_e^{n+1} + \Sigma_i \nabla_{\mathbf{x}} V^{n+1}) = 0.$$

We then choose a set of basis functions $\psi_k, k = 1 \ldots N$, and set $V^n = \sum_{k=1}^N V_k^n \psi_k$ and $\phi_e^n = \sum_{k=1}^N \Phi_k^n \psi_k$. The stiffness matrix K is now dependent on the conductivities Σ_i and Σ_e, and therefore we define the matrix $K[\Sigma]$ by

$$(K[\Sigma])_{jk} = \int_\Omega \nabla \psi_j \cdot (\Sigma \nabla \psi_k) \, \mathrm{d}^2\mathbf{x}.$$

We also notice that the time contribution will be related to the *mass matrix* M, whose entries are

$$M_{jk} = \int_\Omega \psi_j \psi_k \, \mathrm{d}\mathbf{x}. \tag{A.13}$$

We can then present our finite element system in block form, so that we are solving the matrix-vector equation

$$\begin{pmatrix} \frac{\chi c_m}{\Delta t} M + K[\Sigma_i] & K[\Sigma_i] \\ K[\Sigma_i] & K[\Sigma_i + \Sigma_e] \end{pmatrix} \begin{pmatrix} \mathbf{V}^{n+1} \\ \boldsymbol{\phi}_e^{n+1} \end{pmatrix} = \begin{pmatrix} \frac{\chi c_m}{\Delta t} M \mathbf{V}^n + \mathbf{b} \\ 0 \end{pmatrix}, \tag{A.14}$$

where

$$b_j = -\int_\Omega \chi I_{ion}^n \psi_j \, \mathrm{d}\mathbf{x}.$$

A.2.1 Implementation

We now give details of the implementation of the finite element method to solve the bidomain equations on a two-dimensional rectangular geometry, and begin by setting up the spatial mesh. On this simple geometry we can use a uniform triangular mesh, that is, a direct extension of that shown in Figure A.1 in which we scale the size of the triangles equally in both x- and y- directions. We can reduce this size arbitrarily, but must bear in mind that halving the edge size of the triangles will lead to four times the number of elements, and thus we would expect any simulation to take substantially longer. The amount of additional time taken will depend on the properties of the linear solver used, which in our case is the PETSc [3] implementation of the generalized minimal residual method, preconditioned using incomplete LU factorisation. Additionally, the accuracy gained by reducing our element size ceases to have a meaningful effect on results after a point. The accuracy and speed of computations will be discussed in more detail in Appendix B, and so here we will just point out that our elements will be scaled versions of those in Figure A.1.

We must now set up the system given by Equation (A.14). Assuming that we have already used the underlying discrete geometry to find the homogenised conductivity tensors Σ_i and Σ_e and the surface-area-to-volume ratio χ, we can calculate the stiffness matrices $K[\Sigma_i]$ and $K[\Sigma_e]$ and mass matrix M for each element, and add these contributions to the left-hand matrix. We also note that these matrices does not depend on time (assuming that our chosen timestep Δt remains constant), and as much must only be computed once upon initiation.

The right-hand vector will depend on time due to changes in the ionic concentrations and in transmembrane potential, and therefore we must recalculate it at each timestep. We can calculate the term given by $\frac{\chi c_m}{\Delta t} M \mathbf{V}^n$ easily, as we already know $\mathbf{V}_n$. We now have to calculate the contribution of the source term to $\mathbf{b}$. We know that we may do this using Gaussian quadrature on the unit square, but we only know the value of I_{ion}^n at our nodes, and thus at the corners of the unit square, but not at the interior Gauss points. We will therefore use a bilinear interpolation method to approximate these values, in which a function f defined at the corners of the unit square has a value at an interior point (x, y) of

$$f(x, y) \approx f(0, 0)(1 - x)(1 - y) + f(1, 0)x(1 - y) + f(1, 1)(1 - x)y + f(1, 1)xy.$$

Considering the transformation from the canonical triangle to the square, we have that $f(0, 0) = f(\text{node}_1)$, $f(1, 0) = f(\text{node}_2)$, $f(0, 1) = f(\text{node}_3) = f(1, 1)$. At each timestep, we therefore construct the vector $\mathbf{b}$ by:

- solving the equations for the gating variables in our chosen ionic current model (those for the Beeler-Reuter model are given in [5]) using an implicit Euler method to obtain values at each node;
- using these values along with the solution for V at the previous timestep to find the value of the source function at each node;
- performing Gaussian quadrature to numerically integrate the integrand of the vector $\mathbf{b}$ on each element; and
- summing the contributions of each element to construct the final version of $\mathbf{b}$ on each node;

We can now solve the equation system at any given timestep $n + 1$. For the first timestep, we input the specified initial values of V, ϕ_e, m, h and n at each node — natural conditions are for the transmembrane potential to be equal to the equilibrium potential of the system (so that $V = V_{eq}$ and $\phi_e = 0$), with appropriate values for the gating variables m, h and n given in [5].

In this section we have shown how the finite element method can be applied to the bidomain equations. We will now give details of how to use the method to approximate the solution to the equations governing the discrete model used in this thesis.

A.3 The Finite Element Approximation to the Discrete Equation System

In this section, we show how the finite element method can be applied to the discrete equation system used in this thesis on a two-dimensional rectangular geometry where no gap junctions are modelled. As σ_i and σ_e are constant scalars, we will be solving

$$\nabla^2 \phi_i = 0, \qquad \mathbf{x} \in \Omega_i,$$

in the intracellular space, subject to

$$-\sigma_i \nabla \phi_i \cdot \mathbf{n} = I_m(\mathbf{x}), \qquad \mathbf{x} \in \partial\Omega_m,$$

and correspondingly in the extracellular space we will be solving

$$\nabla^2 \phi_e = 0, \qquad \mathbf{x} \in \Omega_e,$$

subject to

$$\sigma_e \nabla \phi_e \cdot \mathbf{n} = I_m(\mathbf{x}), \qquad \mathbf{x} \in \partial\Omega_m,$$

with the coupling term

$$V = \phi_i - \phi_e, \qquad \mathbf{x} \in \partial\Omega_m,$$

defined on the cell membrane. The transmembrane current is given by

$$I_m = c_m \frac{\partial V}{\partial t} + I_{ion},$$

and so if we know ϕ_i and ϕ_e at a given timestep, we may calculate V and thus I_{ion} and I_m. The finite element system analogous to Equation (A.14) for the discrete case is

$$\begin{pmatrix} K^i + \frac{c_m}{\Delta t} M & -\frac{c_m}{\Delta t} M \\ -\frac{c_m}{\Delta t} M & K^e + \frac{c_m}{\Delta t} M \end{pmatrix} \begin{pmatrix} \boldsymbol{\phi}_i^{n+1} \\ \boldsymbol{\phi}_e^{n+1} \end{pmatrix} = \begin{pmatrix} -(\mathbf{d}_1 + \mathbf{d}_2) \\ \mathbf{d}_1 + \mathbf{d}_2 \end{pmatrix}. \tag{A.15}$$

The vectors $\mathbf{d}_1, \mathbf{d}_2$ are given by

$$\mathbf{d}_1 = -\frac{c_m}{\Delta t} M_1 (\boldsymbol{\phi}_i^n - \boldsymbol{\phi}_e^n), \qquad \mathbf{d}_2 = \int_{\partial\Omega_m} I_{ion} \psi_j \, \mathrm{d}S,$$

and the mass matrix M has entries

$$M_{jk} = \int_{\partial\Omega_m} \psi_j \psi_k \, \mathrm{d}S,$$

for nodes j and k that lie on $\partial\Omega_m$, and zero entries for all other nodes in the domain of definition of the matrix. The stiffness matrices K^i and K^e are given by

$$K^i_{jk} = \int_{\Omega_i} \sigma_i \nabla\psi_j \cdot \nabla\psi_k \, \mathrm{d}V, \qquad k = 1, \ldots, N_1, \tag{A.16}$$

$$K^e_{jk} = \int_{\Omega_e} \sigma_e \nabla\psi_j \cdot \nabla\psi_k \, \mathrm{d}V, \qquad k = 1, \ldots, N_2, \tag{A.17}$$

where N_1 and N_2 represent the size of the discretisations of the intracellular and extracellular spaces respectively.

A.3.1 Implementation

As with the continuum case, we begin by setting up the spatial mesh. We must now ensure that each element is either wholly cell or extracellular matrix, so that it is isotropic. This can be achieved using a uniform triangular mesh, so long as the mesh size is a factor of both the cell height, h_1, and the extracellular height, $h - h_1$.

The left-hand matrix is again time-independent and once more we calculate the stiffness matrices on an element-wise basis, summing the contribution from each element. The mass matrix acts only on the boundary nodes, and so here the elements are line segments, not triangles. The reference line is now $[0, 1]$, and we take basis functions on this to be

$$\psi_1(s) = 1 - s,$$
$$\psi_2(s) = s.$$

For any given line with vertices at (x_1, y_1) and (x_2, y_2), the mapping to the reference line is given by

$$x = x_1(1 - s) + x_2 s,$$
$$y = y_1(1 - s) + y_2 s.$$

The determinant of the Jacobian of this transformation is simply the length of the original line, which is

$$\det(J) = \sqrt{(x_2 - x_1)^2 + (y_2 - y_1)^2}.$$

We can now use the one-dimensional version of the Gaussian quadrature formula, Equation (A.10), which gives

$$\oint_{\mathrm{C}} f(s)\ \mathrm{d}s\ \mathrm{d}t \approx \sum_{p=1}^{2} \frac{1}{2} f(x_p) \times \det(J),$$

where again the points x_p are given by

$$\left[\frac{1}{2}\left(1-\frac{1}{\sqrt{3}}\right), \frac{1}{2}\left(1+\frac{1}{\sqrt{3}}\right)\right],$$

and we use linear interpolation to find the value at the Gauss points of these functions defined only on the nodes by writing

$$f(x) \approx f(0)(1-x) + f(1)x.$$

From this information, we may calculate the mass matrix M. As we know ϕ_i and ϕ_e at timestep n, we can calculate V on the boundary nodes and thus I_{ion} at each node, which allows us the calculate the vectors $\mathbf{d}_1$ and $\mathbf{d}_2$. Therefore, once we pick initial values of ϕ_i at each intracellular node, ϕ_e at each extracellular node, and the gating variables at each boundary node, we can solve the equation system at any future time point.

Appendix B

Accuracy and Speed of Computations

This appendix gives details of the computational approaches used in this thesis and of the convergence of the finite element method both for the simulations performed in Chapter 5, and for the homogenised conductivity tensor calculations in Chapter 6 and Chapter 7.

B.1 Computational Approaches Used in this Thesis

In this section, we give a short overview of the approaches used to perform the computations in this thesis.

B.1.1 Programming Details

All computations were performed on the machine detailed in Table B.1. In all cases, the mesh used to discretise the domain of the problem was created as a preprocessing step.

For two-dimensional simulations the domain was decomposed into a Delaunay triangulation using the 'Triangle' software package [137], where we additionally specified that any triangle in the mesh must contain no angle smaller than 30 degrees, and that no single triangle may

comprise more than 0.1% of the total domain area. The first stipulation ensures the overall quality of the mesh, while the second reduces the error introduced by the finite element approximation. It is worth noting that the second stipulation was modified in Section B.2 when determining the accuracy and convergence of our numerical methods, and provides a simple way to alter the size of the elements of the discretisation.

For three-dimensional simulations, we formed a Delaunay tetrahedralisation of the domain using the 'Tetgen' software package [137]. Analogously to the two-dimensional mesh, we ensured that a high-quality mesh was created by specifying a maximum radius-to-edge ratio of 1.5 for any given tetrahedron, and controlled the error introduced by the finite element method by capping the volume of a single tetrahedron at 0.001% of that of the total domain volume. Once again, this second constraint was altered as part of the convergence analysis in Section B.2.

Machine Details	
Machine and OS	Apple iMac running OS X Yosemite
Processor	2.9 GHz Intel Core i5
Memory	8GB 1600 MHz DDR3
Graphics	NVIDIA GeForce GT 650M 512 MB

Table B.1: *Details of the machine on which all computations in this thesis were run.*

Following creation of the mesh, the details of the finite element system to be solved were set up using the `C++` programming language, and the resulting matrix-vector system was solved using the PETSc package [3]. In the next section we will give details of typical run times of the programs created for the simulations detailed in Chapter 5.

B.1.2 Typical Run Times

In Table B.2 we show typical run times for the simulations performed in Chapter 5. The simulations performed in Chapter 5 considered simple geometries, which means that a relatively small number of elements was required in the discrete case to construct a high-quality mesh where the solution converged appropriately. As such, we see from Table B.2 that the continuum system is only seven times quicker to solve using than the discrete system

for a domain consisting of 100 cells. Over 50,000 timesteps, the continuum simulation took around eight minutes to solve compared to 45 minutes for the discrete case, both of which are relatively fast considering the modest computing power used (desktop computer, single-threaded program).

Typical Run Times		
Cells simulated	100	
Domain size	5 mm by 0.04 mm	
Timesteps run	50000	
	Continuum	**Discrete**
Total nodes	3012	32036
Total elements	4000	64000
Time taken (sec)	461	2687

Table B.2: *Typical run times for the simulations performed in Chapter 5.*

We can attempt to extrapolate these figures out to get some sense of the computational requirements for more complex two- and three-dimensional geometries. For rectangular cells, we see that the continuum model used 40 elements per cell and the discrete model used 640 elements per cell. However, for the complex curved cells considered in Chapter 7 we found that we required at least 10,000 elements per cell to accurately calculate the weight functions, if not more. Even in a best-case scenario the discrete system would therefore take ten times longer to solve than for rectangular cells (that is, roughly half a day), and even longer if being conservative (several days might be required). Given the tiny size of tissue considered, the approach seems prohibitive if using current desktop computational power. Moving to a three-dimensional framework adds another two orders of magnitude to the number of elements required, and thus to the expected solution time, suggesting that a full three-dimensional discrete system cannot feasibly be solved for any meaningful size of tissue.

B.2 Convergence of Computations

In this section we outline the convergence properties of the computations performed in this thesis. We first see how the conduction velocity calculated from simulations in Chapter 5

changes as we modify both the space- and timestep used, and then see how the homogenised conductivity tensors computed in Chapter 6 and Chapter 7 are affected by the number of elements used in the cell. We also pay specific attention to those geometries with sharp corners where corner singularities might be introduced, and see how the conductivity tensors converge in these cases.

B.2.1 Convergence of Simulations

In this section we show how the results of our simulations depend on the mesh parameters, namely the spacestep and timestep, and how we use this information to choose appropriate values for these parameters for each of the discrete and continuum systems. The simulations are those discussed in Section 5.2.1, with conduction velocity measured in the same fashion.

In each table that follows, we show how the percentage conduction velocity changes when either increasing the number of elements per cell, or decreasing the timestep used. We use as an acceptance criteria a conduction velocity changes of less than 0.1% when changing the space- or timestep. It is also worth noting that in the discrete case, conduction velocity is only measurable on nodes that lie on the cell membrane, and thus the resulting conduction velocities have a minimum resolution proportional to the timestep considered divided by the distance between nodes on the cell membrane.

In Table B.3 we show how the conduction velocity of the continuum system converges as we quadruple the number of elements that correspond to the area taken up by a single discrete cell in the continuum domain. We see that the conduction velocity changes by 0.23% when increasing the number of element from 10 to 40, by 0.078% when further increasing the number to 160, and by less than is discernible when the number of elements per cell is 640. This led us to use 40 elements per cell in all continuum simulations in Chapter 5.

In Table B.4 we show how the conduction velocity of the discrete system converges as we quadruple the number of elements that comprise a single cell in our domain. In order to achieve the change in the number of elements we simply halved the distance between successive nodes on the cell membrane, which when extrapolated to two spatial dimensions

Continuum Model Spacestep Convergence		
Elements per cell	CV (mm/ms)	% CV change
10	0.1282	N/A
40	0.1279	0.23
160	0.1278	0.078
640	0.1278	<0.01

Table B.3: *A table showing the convergence of the conduction velocity (CV) of the continuum model as we quadruple the number of elements in the area corresponding to a single cell.*

caused the overall number of elements to quadruple.

One thing to note is that given this protocol, the conduction velocity is only resolved to within 0.01 mm/ms when considering 160 elements per cell, and to within 0.005 mm/ms when using 640 elements per cell. Thus, whilst the fact that conduction velocity changes by 0.8% when increasing the number of elements per cell from 160 to 640 and not at all when increasing the number of element per cell above 640, this is because the 0.8% change is the smallest discernible change, and not because the convergence 'jumps' from 0.8% to zero.

As might be expected from Table B.4, we chose to use 640 elements per cell in all discrete simulations in Chapter 5. Finally, in Tables B.5 and B.6 we see that 0.01 ms is an appropriate timestep for both continuum and discrete models

Discrete Model Spacestep Convergence		
Elements per cell	CV (mm/ms)	% CV change
160	0.1250	N/A
640	0.1240	0.81
2560	0.1240	<0.01
10240	0.1240	<0.01

Table B.4: *A table showing the convergence of the conduction velocity of the discrete model as we quadruple the number of elements in single cell.*

Continuum Mode Timestep Convergence		
Timestep (ms)	CV (mm/ms)	% CV change
0.1	0.1366	N/A
0.01	0.1279	6.8
0.001	0.1278	0.078

Table B.5: *A table showing the convergence of the conduction velocity of the continuum model as we increase the number of timesteps by a factor of ten.*

Discrete Model Timestep Convergence		
Timestep (ms)	CV (mm/ms)	% CV change
0.1	0.1265	N/A
0.01	0.1240	2.02
0.001	0.1240	<0.01

Table B.6: *A table showing the convergence of the conduction velocity of the discrete model as we increase the number of timesteps by a factor of ten.*

B.2.2 Convergence of Homogenised Conductivity Tensor Calculations

In this section, we show how the values calculated for the homogenised conductivity tensors in Chapter 6 and Chapter 7 converge as we increase the number of elements in a single cell. As described in Section B.1.1, we are able to control this number by imposing a maximum area constraint on each triangle of the cell. We set the acceptance threshold of the convergence to be 10^{-6}, and if the normalised change in the result is greater than this figure, the mesh is deemed to have insufficient quality and is refined.

In Figure B.1 we show the results of a convergence analysis whereby we successively doubled the number of triangles per cell from 6,250 to 400,000 on two representative geometries. The first is that generated by using the 'default' parameters in Chapter 6, that is, the cell in Figure 6.3. The second is on a set of parameters that create much sharper 'corners' at points in the cell, as in these cases we expect convergence to be slower, and the cell is that shown with a curvature of 20 in Figure 6.2.

We see from Figure B.1 that the cell with default parameters reaches acceptance relatively quickly, requiring 25,000 triangles per cell, whereas the cell with sharper corners requires over 100,000 triangles per cell to reach the acceptance threshold. This demonstrates that we must ensure that the quality of the mesh is appropriate for the specific geometry we are considering, and that given the homogenised conductivity tensors satisfy a time-invariant problem that is fast to solve, we should be very conservative with our choice of mesh quality and use a large number of triangles.

In Figure B.2 we perform the same analysis for the three-dimensional cells of Chapter 7, again looking at both the default parameters and at the parameter set most likely to induce

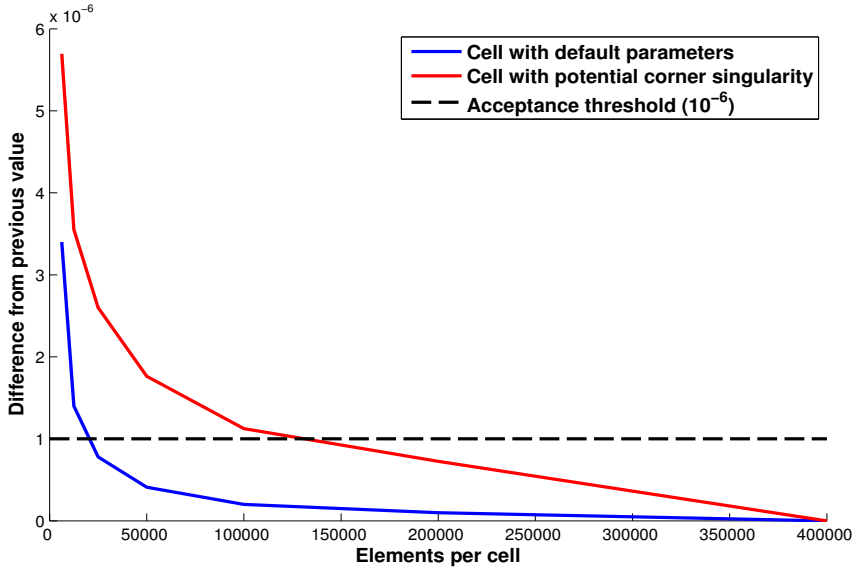

Figure B.1: *A figure showing the convergence of the approximation of the solution to the equations governing the homogenised conductivity tensors for the two-dimensional curved cells considered in Chapter 6. We provide examples both for the default parameters and for the parameter set that is most likely to introduce a corner singularity.*

a corner singularity. We successively double the number of tetrahedra per cell from 100,000 to 12,800,000, and see that the default parameter set passes our acceptance test when using 1,600,000 tetrahedra and the 'corner case' cell passes with 3,200,000 tetrahedra. In this case the convergence in the second case is much closer to that of the default parameter set than in two dimensions, which suggests that moving to three dimensions might 'smooth' the cell membrane shape and introduce less of a potential corner singularity.

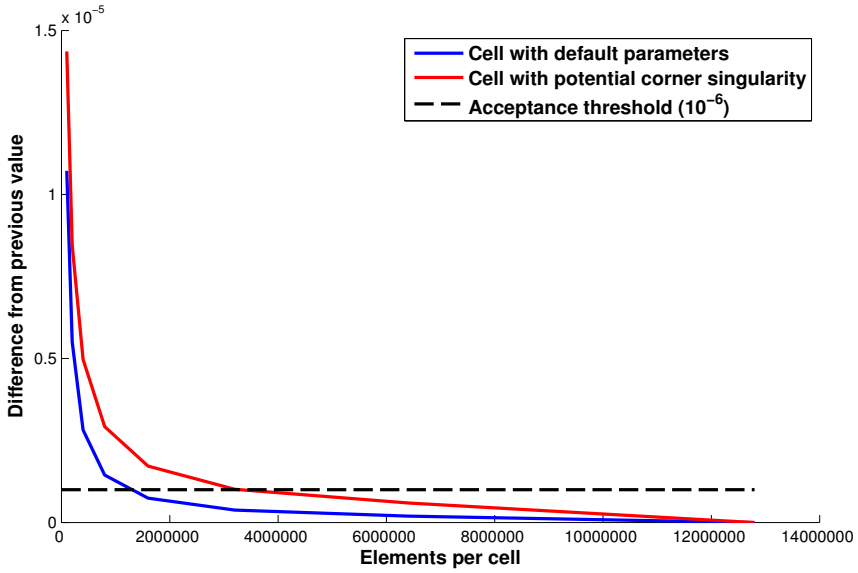

Figure B.2: *A figure showing the convergence of the approximation of the solution to the equations governing the homogenised conductivity tensors for the three-dimensional cells considered in Chapter 7. We provide examples both for the default parameters and for the parameter set that is most likely to introduce a corner singularity.*

Appendix C

Proofs

C.1 Proof of the Symmetry of the Homogenised Conductivity Tensors

We will show that the intracellular conductivity tensor given in Equation (4.17) is symmetric by demonstrating that $\Sigma_{i_{(1,2)}} = \Sigma_{i_{(2,1)}}$, with the symmetry of the other components following in an analogous manner. The extracellular conductivity tensor given in Equation (4.20) can then be shown to be symmetric using the same logic. The intracellular conductivity is defined as

$$\Sigma_i = \frac{1}{V_{\text{unit}}} \int_{\Omega_i} \sigma_i \left(I + \frac{\partial W^i}{\partial \mathbf{z}} \right) \, \mathrm{d}V_{\mathbf{z}}. \tag{C.1}$$

As the identity matrix is symmetric, we need to show that $\int \sigma_i \frac{\partial W^i}{\partial \mathbf{z}} \, \mathrm{d}V_{\mathbf{z}}$ is symmetric. Using integration by parts we have

$$\iiint \sigma_i \left(\frac{\partial W_1^i}{\partial z_2} - \frac{\partial W_2^i}{\partial z_1} \right) \, \mathrm{d}V_{\mathbf{z}} = \iiint \left[\frac{\partial (\sigma_i W_1^i)}{\partial z_2} - \frac{\partial (\sigma_i W_2^i)}{\partial z_1} - \frac{\partial \sigma_i}{\partial z_2} W_1^i + \frac{\partial \sigma_i}{\partial z_2} W_2^i \right] \, \mathrm{d}V_{\mathbf{z}}, \tag{C.2}$$

where $\sigma_i = \sigma_i(\mathbf{z})$ and, for discontinuous σ_i, the derivative is taken to be the weak derivative.

Using Equation (4.13) this becomes

$$\iiint \left[\nabla_{\mathbf{z}} \cdot (-\sigma_i W_2^i, \sigma_i W_1^i, 0) + \nabla_{\mathbf{z}} \cdot (\sigma_i \nabla_{\mathbf{z}} W_2^i) W_1^i - \nabla_{\mathbf{z}} \cdot (\sigma_i \nabla_{\mathbf{z}} W_1^i) W_2^i\right] \, \mathrm{d}V_{\mathbf{z}}, \tag{C.3}$$

which upon rearrangement can be expressed as

$$\iiint \nabla_{\mathbf{z}} \cdot \left[(-\sigma_i W_2^i, \sigma_i W_1^i, 0) + \sigma_i W_1^i \nabla_{\mathbf{z}} W_2^i - \sigma_i W_2^i \nabla_{\mathbf{z}} W_1^i\right] \, \mathrm{d}V_{\mathbf{z}}. \tag{C.4}$$

Applying the divergence theorem then gives

$$\iint \left[\sigma_i(-W_2^i n_1 + W_1^i n_2) + \sigma_i W_1^i (\nabla_{\mathbf{z}} W_2^i) \cdot \mathbf{n} - \sigma_i W_2^i (\nabla_{\mathbf{z}} W_1^i) \cdot \mathbf{n}\right] \, \mathrm{d}S_{\mathbf{z}}, \tag{C.5}$$

and by grouping terms we see that this may be written

$$\iint \left[\sigma_i W_1^i (n_2 + (\nabla_{\mathbf{z}} W_2^i) \cdot \mathbf{n}) - \sigma_i W_2^i (n_1 + (\nabla_{\mathbf{z}} W_1^i) \cdot \mathbf{n})\right] \, \mathrm{d}S_{\mathbf{z}}. \tag{C.6}$$

We see from Equation (4.14) that this quantity is zero, so that $\iiint \sigma_i \frac{\partial W_1^i}{\partial z_2} \, \mathrm{d}V_{\mathbf{z}} = \iiint \sigma_i \frac{\partial W_2^i}{\partial z_1} \, \mathrm{d}V_{\mathbf{z}}$ as required and hence $\Sigma_{i_{(1,2)}} = \Sigma_{i_{(2,1)}}$.

C.2 The Off-Fibre Direction Diagonal Entries of the Homogenised Conductivity Tensors are Zero

The governing equations for the intracellular weight functions W_j^i, $j = 1, 2, 3$, are given in Equation (4.13), and the boundary conditions are given in Equation (4.14). The only other restrictions on W_j are that they are periodic in z_j with zero mean. The general solution to the governing equations and boundary conditions are

$$W_j^i = -z_j + C_j, \tag{C.7}$$

where C_j, $j = 1, 2, 3$, are arbitrary constants that are chosen such that W_j^i has zero mean. We now consider the domain on which the weight functions are defined, here denoted by Ω. If Ω does not touch the boundary of the periodic subunit at $z_j = 0$ and $z_j = 1$ then the function W_j^i given in Equation (C.7) is periodic in z_j and thus satisfies all conditions. Considering the definition of the homogenised conductivity tensor, Equation (4.17), we see that

$$I_{(j,j)} + \frac{\partial W_j^i}{\partial z_j} = 0,$$

and so

$$\Sigma_{i_{(j,j)}} = 0.$$

This also holds for the extracellular conductivity tensors, as long as the domain Ω does not touch the boundary of the periodic subunit. That is, for either the intracellular or the extracellular space, there is zero conductivity along any direction in which the domain does not touch the boundary of the periodic subunit.

C.3 The Invariance of the Homogenised Conductivity Tensors with Respect to the Dimensions of the Unit Cell

We now demonstrate that the absolute dimensions of the unit cell do not affect the conductivity calculation, and so the dimensions of a cell may be defined in relative form. This means that we may take the periodic subunit to be the box $[0, 1]^n$, where n is the dimensionality of the solution geometry. To show this, we stretch the domain under consideration by a (scalar) factor of λ in the x-direction and introduce a new co-ordinate $\widehat{x} = \lambda x$, with all other quantities in this new framework denoted with a $\widehat{(hat)}$. The only entry of the homogenised conductivity tensor that could be affected by this change is $\Sigma_{i_{(1,1)}}$ as the off-fibre diagonal entries are zero.

The weight function $\widehat{W_1^i} = \lambda W_1^i$ satisfies the differential equation (4.13) and the boundary condition in Equation (4.14) for the new co-ordinate system, thus it is the unique solution (up to a constant), which gives us that $\frac{\partial \widehat{W^i}}{\partial \hat{x}_i} = \frac{\partial W^i}{\partial x_i}$. The integrand of Equation (4.17) is thus unchanged by the co-ordinate transformation, and so

$$\begin{aligned}
\widehat{\Sigma_i}_{(1,1)} &= \frac{1}{\widehat{V}_{\text{unit}}} \int_{\Omega_i} \sigma_i \left(1 + \frac{\partial \widehat{W_1^i}}{\partial \hat{x}_1}\right) \mathrm{d}\hat{x}_1, \\
&= \frac{1}{\widehat{V}_{\text{unit}}} \int_{\Omega_i} \lambda\sigma_i \left(1 + \frac{\partial W_1^i}{\partial x_1}\right) \mathrm{d}x_1, \\
&= \frac{1}{\lambda V_{\text{unit}}} \int_{\Omega_i} \lambda\sigma_i \left(1 + \frac{\partial W_1^i}{\partial x_1}\right) \mathrm{d}x_1, \\
&= \Sigma_{i_{(1,1)}}.
\end{aligned}$$

Thus, the element of the homogenised conductivity tensor corresponding to the direction in which the co-ordinate transformation was applied is unchanged. By similar logic, any linear transformation to the co-ordinate system does not affect the homogenised conductivity tensor.

References

[1] B. Alberts, A. Johnson, J. Lewis, M. Raff, K. Roberts, and P. Walter. *Molecular Biology of the Cell*. Garland Science, fifth edition, November 2007.

[2] R. R. Aliev and A. V. Panfilov. A simple two-variable model of cardiac excitation. *Chaos, Solitons & Fractals*, **7**(3):293–301, March 1996.

[3] S. Balay, M. F. Adams, J. Brown, P. Brune, K. Buschelman, V. Eijkhout, W. D. Gropp, D. Kaushik, M. G. Knepley, L. C. McInnes, K. Rupp, B. F. Smith, and H. Zhang. PETSc Users Manual. Technical Report ANL-95/11 - Revision 3.4, Argonne National Laboratory, 2013.

[4] J. R. Baum, B. Long, C. Cabo, and H. S. Duffy. Myofibroblasts cause heterogeneous Cx43 reduction and are unlikely to be coupled to myocytes in the healing canine infarct. *American Journal of Physiology — Heart and Circulatory Physiology*, **302**(3):H790–H800, February 2012.

[5] G. W. Beeler and H. Reuter. Reconstruction of the action potential of ventricular myocardial fibres. *The Journal of Physiology*, **268**(1):177–210, June 1977.

[6] A. Bensoussan, J. L. Lions, and G. Papanicolaou. *Asymptotic Analysis for Periodic Structures (Chelsea Publications)*. American Mathematical Society, 10 2011.

[7] M. R. Boyett, H. Honjo, and I. Kodama. The sinoatrial node, a heterogeneous pacemaker structure. *Cardiovascular Research*, **47**(4):658–687, September 2000.

[8] P. Brugada and J. Brugada. Right bundle branch block, persistent ST segment elevation and sudden cardiac death: a distinct clinical and electrocardiographic syndrome. A multicenter report. *Journal of the American College of Cardiology*, **20**(6):1391–1396, November 1992.

[9] A. Bueno-Orovio, E. M. Cherry, and F. H. Fenton. Minimal model for human ventricular action potentials in tissue. *Journal of Theoretical Biology*, **253**(3):544–560, August 2008.

[10] R. A. Chapman and C. H. Fry. An analysis of the cable properties of frog ventricular myocardium. *The Journal of Physiology*, **283**(1):263–282, October 1978.

[11] E. M. Cherry, F. Xie, Z. Feliciano, and A. Garfinkel. Computer Modeling of Atrial Fibrillation. *Cardiac Electrophysiology Review*, **5**(2-3):271–276, 2001.

[12] J. Clark and R. Plonsey. A mathematical evaluation of the core conductor model. *Biophysical Journal*, **6**(1):95–112, January 1966.

[13] R. B. Clark, R. A. Bouchard, E. Salinas-Stefanon, J. Sanchez-Chapula, and W. R. Giles. Heterogeneity of action potential waveforms and potassium currents in rat ventricle. *Cardiovascular Research*, **27**(10):1795–1799, October 1993.

[14] L. Clerc. Directional differences of impulse spread in trabecular muscle from mammalian heart. *The Journal of Physiology*, **255**(2):335–346, February 1976.

[15] K. S. Cole. Rectification and Inductance in the Squid Giant Axon. *The Journal of General Physiology*, **25**(1):29–51, September 1941.

[16] K. S. Cole and R. F. Baker. Longitudinal Impedance of the Squid Giant Axon. *The Journal of General Physiology*, **24**(6):771–788, July 1941.

[17] K. S. Cole and R. F. Baker. Transverse Impedance of the Squid Giant Axon During Current Flow. *The Journal of General Physiology*, **24**(4):535–549, March 1941.

[18] K. S. Cole and H. J. Curtis. Electric Impedance of the Squid Giant Axon During Activity. *The Journal of General Physiology*, **22**(5):649–670, May 1939.

[19] K. S. Cole and H. J. Curtis. Membrane Potential of the Squid Giant Axon During Current Flow. *The Journal of General Physiology*, **24**(4):551–563, March 1941.

[20] K. S. Cole and A. L. Hodgkin. Membrane and Protoplasm Resistance in the Squid Giant Axon. *The Journal of General Physiology*, **22**(5):671–687, May 1939.

[21] C. M. M. Costa and R. Weber Dos Santos. Limitations of the homogenized cardiac Monodomain model for the case of low gap junctional coupling. *Conference proceedings: ... Annual International Conference of the IEEE Engineering in Medicine and Biology Society. IEEE Engineering in Medicine and Biology Society*, **2010**:228–231, 2010.

[22] M. Courtemanche, R. J. Ramirez, and S. Nattel. Ionic mechanisms underlying human atrial action potential properties: insights from a mathematical model. *The American Journal of Physiology*, **275**(1 Pt 2):H301–H321, July 1998.

[23] H. J. Curtis and K. S. Cole. Transverse Electric Impedance of the Squid Giant Axon. *The Journal of General Physiology*, **21**(6):757–765, July 1938.

[24] P. Daleau and J. Délèze. Conduction block in Purkinje fibers by homogeneous versus localized decrease of the gap junction conductance. *Canadian Journal of Physiology and Pharmacology*, **76**(6):630–641, June 1998.

[25] J. M. de Bakker, F. J. van Capelle, M. J. Janse, A. A. Wilde, R. Coronel, A. E. Becker, K. P. Dingemans, N. M. van Hemel, and R. N. Hauer. Reentry as a cause of ventricular tachycardia in patients with chronic ischemic heart disease: electrophysiologic and anatomic correlation. *Circulation*, **77**(3):589–606, March 1988.

[26] J. M. de Bakker and H. M. van Rijen. Continuous and discontinuous propagation in heart muscle. *Journal of Cardiovascular Electrophysiology*, **17**(5):567–573, May 2006.

[27] C. de Diego, F. Chen, Y. Xie, R. K. Pai, L. Slavin, J. Parker, S. T. Lamp, Z. Qu, J. N. Weiss, and M. Valderrábano. Anisotropic conduction block and

reentry in neonatal rat ventricular myocyte monolayers. *American Journal of Physiology — Heart and Circulatory Physiology*, **300**(1):H271–H278, January 2011.

[28] A. Defauw, I. V. Kazbanov, H. Dierckx, P. Dawyndt, and A. V. Panfilov. Action potential duration heterogeneity of cardiac tissue can be evaluated from cell properties using Gaussian Green's function approach. *PloS one*, **8**(11), 2013.

[29] M. Delmar, D. C. Michaels, T. Johnson, and J. Jalife. Effects of increasing intercellular resistance on transverse and longitudinal propagation in sheep epicardial muscle. *Circulation Research*, **60**(5):780–785, May 1987.

[30] S. Dhein. *Cardiac Gap Junctions: Physiology, Regulation, Pathophysiology and Pharmacology*, **1**. S Karger Pub, first edition, 1998.

[31] P. J. Diaz, Y. Rudy, and R. Plonsey. Intercalated discs as a cause for discontinuous propagation in cardiac muscle: A theoretical simulation. *Annals of Biomedical Engineering*, **11**(3):177–189, May 1983.

[32] S. Dutta, M. J. Bishop, P. Pathmanathan, P. Lee, P. Kohl, T. A. Quinn, and B. Rodriguez. Interpreting Optical Mapping Recordings in the Ischemic Heart: A Combined Experimental and Computational Investigation. In D. Metaxas and L. Axel, editors, *Functional Imaging and Modeling of the Heart*, **6666** of *Lecture Notes in Computer Science*, chapter 3, pages 20–27. Springer Berlin Heidelberg, Berlin, Heidelberg, 2011.

[33] J. R. Egan, T. L. Butler, C. G. Au, Y. M. M. Tan, K. N. North, and D. S. Winlaw. Myocardial water handling and the role of aquaporins. *Biochimica et Biophysica Acta*, **1758**(8):1043–1052, August 2006.

[34] B. Engquist and P. E. Souganidis. Asymptotic and numerical homogenization. *Acta Numerica*, **17**:147–190, May 2008.

[35] V. G. Fast and A. G. Kléber. Microscopic conduction in cultured strands of neonatal rat heart cells measured with voltage-sensitive dyes. *Circulation Research*, **73**(5):914–925, November 1993.

[36] V. G. Fast and A. G. Kléber. Anisotropic conduction in monolayers of neonatal rat heart cells cultured on collagen substrate. *Circulation Research*, **75**(3):591–595, September 1994.

[37] R. Fitzhugh. Impulses and Physiological States in Theoretical Models of Nerve Membrane. *Biophysical Journal*, **1**(6):445–466, July 1961.

[38] M. R. Franz, K. Bargheer, W. Rafflenbeul, A. Haverich, and P. R. Lichtlen. Monophasic action potential mapping in human subjects with normal electrocardiograms: direct evidence for the genesis of the T wave. *Circulation*, **75**(2):379–386, February 1987.

[39] P. C. Franzone and L. Guerri. Spreading of excitation in 3-D models of the anisotropic cardiac tissue. I. Validation of the eikonal model. *Mathematical Biosciences*, **113**(2):145–209, February 1993.

[40] P. C. Franzone, L. Guerri, and S. Rovida. Wavefront propagation in an activation model of the anisotropic cardiac tissue: asymptotic analysis and numerical simulations. *Journal of Mathematical Biology*, **28**(2):121–176, 1990.

[41] P. C. Franzone, L. Guerri, and S. Tentoni. Mathematical modeling of the excitation process in myocardial tissue: influence of fiber rotation on wavefront propagation and potential field. *Mathematical Biosciences*, **101**(2):155–235, October 1990.

[42] A. M. Gerdes, S. E. Kellerman, J. A. Moore, K. E. Muffly, L. C. Clark, P. Y. Reaves, K. B. Malec, P. P. McKeown, and D. D. Schocken. Structural remodeling of cardiac myocytes in patients with ischemic cardiomyopathy. *Circulation*, **86**(2):426–430, August 1992.

[43] H. A. Ghaly, P. M. Boyle, E. J. Vigmond, Y. Shimoni, and A. Nygren. Simulations of reduced conduction reserve in the diabetic rat heart: response to uncoupling and reduced excitability. *Annals of Biomedical Engineering*, **38**(4):1415–1425, April 2010.

[44] D. E. Goldman. Potential, Impedance and Rectification in Membranes. *The Journal of General Physiology*, **27**(1):37–60, September 1943.

[45] C. Gutierrez and D. G. Blanchard. Atrial fibrillation: diagnosis and treatment. *American Family Physician*, **83**(1):61–68, January 2011.

[46] D. E. Gutstein, G. E. Morley, D. Vaidya, F. Liu, F. L. Chen, H. Stuhlmann, and G. I. Fishman. Heterogeneous expression of Gap junction channels in the heart leads to conduction defects and ventricular dysfunction. *Circulation*, **104**(10):1194–1199, September 2001.

[47] J. E. Hall. *Guyton and Hall Textbook of Medical Physiology*. Saunders, 12th edition, June 2010.

[48] P. E. Hand and B. E. Griffith. Adaptive multiscale model for simulating cardiac conduction. *Proceedings of the National Academy of Sciences*, **107**(33):14603–14608, August 2010.

[49] P. E. Hand and B. E. Griffith. Empirical Study of an Adaptive Multiscale Model for Simulating Cardiac Conduction. *Bulletin of Mathematical Biology*, **73**(12):3071–3089, December 2011.

[50] P. E. Hand, B. E. Griffith, and C. S. Peskin. Deriving Macroscopic Myocardial Conductivities by Homogenization of Microscopic Models. *Bulletin of Mathematical Biology*, **71**(7):1707–1726, October 2009.

[51] P. E. Hand and C. S. Peskin. Homogenization of an Electrophysiological Model for a Strand of Cardiac Myocytes with Gap-Junctional and Electric-Field Coupling. *Bulletin of Mathematical Biology*, **72**(6):1408–1424, August 2010.

[52] D. Harrild and C. Henriquez. A computer model of normal conduction in the human atria. *Circulation Research*, **87**(7):25–36, September 2000.

[53] A. L. Harris and D. Locke, editors. *Connexins*. Humana Press, Totowa, NJ, 2009.

[54] D. C. Hellam and J. W. Studt. A core-conductor model of the cardiac Purkinje fibre based on structural analysis. *The Journal of Physiology*, **243**(3):637–660, December 1974.

[55] C. S. Henriquez and R. Plonsey. Effect of resistive discontinuities on waveshape and velocity in a single cardiac fibre. *Medical and Biological Engineering and Computing*, **25**(4):428–438, July 1987.

[56] C. S. Henriquez and R. Plonsey. Simulation of propagation along a cylindrical bundle of cardiac tissue–I: Mathematical formulation. *IEEE Transactions on Biomedical Engineering*, **37**(9):850–860, September 1990.

[57] C. S. Henriquez and R. Plonsey. Simulation of propagation along a cylindrical bundle of cardiac tissue–II: Results of simulation. *IEEE Transactions on Biomedical Engineering*, **37**(9):861–875, September 1990.

[58] C. S. Henriquez, N. Trayanova, and R. Plonsey. Potential and current distributions in a cylindrical bundle of cardiac tissue. *Biophysical Journal*, **53**(6):907–918, June 1988.

[59] A. L. Hodgkin and A. F. Huxley. A quantitative description of membrane current and its application to conduction and excitation in nerve. *The Journal of Physiology*, **117**(4):500–544, August 1952.

[60] A. L. Hodgkin and A. F. Huxley. Currents carried by sodium and potassium ions through the membrane of the giant axon of Loligo. *The Journal of Physiology*, **116**(4):449–472, April 1952.

[61] A. L. Hodgkin and A. F. Huxley. The components of membrane conductance in the giant axon of Loligo. *The Journal of Physiology*, **116**(4):473–496, April 1952.

[62] A. L. Hodgkin and A. F. Huxley. The dual effect of membrane potential on sodium conductance in the giant axon of Loligo. *The Journal of Physiology*, **116**(4):497–506, April 1952.

[63] A. L. Hodgkin, A. F. Huxley, and B. Katz. Measurement of current-voltage relations in the membrane of the giant axon of Loligo. *The Journal of Physiology*, **116**(4):424–448, April 1952.

[64] A. L. Hodgkin and W. A. H. Rushton. The Electrical Constants of a Crustacean Nerve Fibre. *Proceedings of the Royal Society of London. Series B - Biological Sciences*, **133**(873):444–479, December 1946.

[65] R. H. Hoyt, M. L. Cohen, and J. E. Saffitz. Distribution and three-dimensional structure of intercellular junctions in canine myocardium. *Circulation Research*, **64**(3):563–574, March 1989.

[66] M. L. L. Hubbard and C. S. Henriquez. Microscopic variations in interstitial and intracellular structure modulate the distribution of conduction delays and block in cardiac tissue with sourceload mismatch. *Europace*, **14**(suppl 5):v3–v9, November 2012.

[67] M. L. L. Hubbard, W. Ying, and C. S. Henriquez. Effect of gap junction distribution on impulse propagation in a monolayer of myocytes: a model study. *Europace :*

European pacing, arrhythmias, and cardiac electrophysiology : Journal of the working groups on cardiac pacing, arrhythmias, and cardiac cellular electrophysiology of the European Society of Cardiology, **9 Suppl 6**, November 2007.

[68] V. Jacquemet, L. Kappenberger, and C. S. Henriquez. Modeling Atrial Arrhythmias: Impact on Clinical Diagnosis and Therapies. *IEEE Reviews in Biomedical Engineering*, **1**:94–114, 2008.

[69] S. K. Jain, R. B. Schuessler, and J. E. Saffitz. Mechanisms of delayed electrical uncoupling induced by ischemic preconditioning. *Circulation Research*, **92**(10):1138–1144, May 2003.

[70] H. J. Jongsma and R. Wilders. Gap Junctions in Cardiovascular Disease. *Circulation Research*, **86**(12):1193–1197, June 2000.

[71] J. P. Keener. An eikonal-curvature equation for action potential propagation in myocardium. *Journal of Mathematical Biology*, **29**(7):629–651, 1991.

[72] J. P. Keener and A. V. Panfilov. A biophysical model for defibrillation of cardiac tissue. *Biophysical Journal*, **71**(3):1335–1345, September 1996.

[73] J. P. Keener. The effects of discrete gap junction coupling on propagation in myocardium. *Journal of Theoretical Biology*, **148**(1):49–82, January 1991.

[74] J. P. Keener. Direct Activation and Defibrillation of Cardiac Tissue. *Journal of Theoretical Biology*, **178**(3):313–324, February 1996.

[75] J. P. Keener and J. Sneyd. *Mathematical Physiology*. Springer, corrected edition, May 2001.

[76] R. E. Klabunde. *Cardiovascular Physiology Concepts*. Lippincott Williams & Wilkins, July 2004.

[77] T. Koura, M. Hara, S. Takeuchi, K. Ota, Y. Okada, S. Miyoshi, A. Watanabe, K. Shiraiwa, H. Mitamura, I. Kodama, and S. Ogawa. Anisotropic Conduction Properties in Canine Atria Analyzed by High-Resolution Optical Mapping. *Circulation*, **105**(17):2092–2098, April 2002.

[78] W. Krassowska, T. C. Pilkington, and R. E. Ideker. Periodic conductivity as a mechanism for cardiac stimulation and defibrillation. *IEEE Transactions on Biomedical Engineering*, **34**(7):555–560, July 1987.

[79] W. Krassowska, T. C. Pilkington, and R. E. Ideker. Potential distribution in three-dimensional periodic myocardium–Part I: Solution with two-scale asymptotic analysis. *IEEE Transactions on Biomedical Engineering*, **37**(3):252–266, March 1990.

[80] W. Krassowska. Field stimulation of cardiac fibers with random spatial structure. *IEEE Transactions on Biomedical Engineering*, **50**(1):33–40, January 2003.

[81] W. Krassowska, T. C. Pilkington, and R. E. Ideker. The Closed Form Solution to the Periodic Core-Conductor Model Using Asymptotic Analysis. *IEEE Transactions on Biomedical Engineering*, **x34**(7):519–531, July 1987.

[82] D. Levy, R. J. Garrison, D. D. Savage, W. B. Kannel, and W. P. Castelli. Prognostic implications of echocardiographically determined left ventricular mass in

the Framingham Heart Study. *The New England Journal of Medicine*, **322**(22):1561–1566, May 1990.

[83] J. Lin and J. P. Keener. Ephaptic coupling in cardiac myocytes. *IEEE Transactions on Biomedical Engineering*, **60**(2):576–582, February 2013.

[84] R. Luengo-Fernández, J. Leal, A. Gray, S. Petersen, and M. Rayner. Cost of cardiovascular diseases in the United Kingdom. *Heart*, **92**(10):1384–1389, October 2006.

[85] R. A. Luke and J. E. Saffitz. Remodeling of ventricular conduction pathways in healed canine infarct border zones. *The Journal of Clinical Investigation*, **87**(5):1594–1602, May 1991.

[86] C. H. Luo and Y. Rudy. A model of the ventricular cardiac action potential. Depolarization, repolarization, and their interaction. *Circulation Research*, **68**(6):1501–1526, June 1991.

[87] C. H. Luo and Y. Rudy. A dynamic model of the cardiac ventricular action potential. I. Simulations of ionic currents and concentration changes. *Circulation Research*, **74**(6):1071–1096, June 1994.

[88] G. Marmont. Studies on the axon membrane; a new method. *Journal of Cellular Physiology*, **34**(3):351–382, December 1949.

[89] R. E. McAllister, D. Noble, and R. W. Tsien. Reconstruction of the electrical activity of cardiac Purkinje fibres. *The Journal of Physiology*, **251**(1):1–59, September 1975.

[90] M. L. McCain, T. Desplantez, N. A. Geisse, B. Rothen-Rutishauser, H. Oberer, K. K. Parker, and A. G. Kleber. Cell-to-cell coupling in engineered pairs of rat ventricular cardiomyocytes: relation between Cx43 immunofluorescence and intercellular electrical conductance. *American Journal of Physiology — Heart and Circulatory Physiology*, **302**(2):H443–H450, January 2012.

[91] H. McIntyre and C. H. Fry. Abnormal action potential conduction in isolated human hypertrophied left ventricular myocardium. *Journal of Cardiovascular Electrophysiology*, **8**(8):887–894, August 1997.

[92] L. H. Michael, R. M. Lewis, T. A. Brandon, and M. L. Entman. Cardiac lymph flow in conscious dogs. *The American Journal of Physiology*, **237**(3):H311–H317, September 1979.

[93] G. R. Mirams, C. J. Arthurs, M. O. Bernabeu, R. Bordas, J. Cooper, A. Corrias, Y. Davit, S.-J. Dunn, A. G. Fletcher, D. G. Harvey, M. E. Marsh, J. M. Osborne, P. Pathmanathan, J. Pitt-Francis, J. Southern, N. Zemzemi, and D. J. Gavaghan. Chaste: An Open Source C++ Library for Computational Physiology and Biology. *PLoS Computational Biology*, **9**(3), March 2013.

[94] G. R. Mirams, Y. Cui, A. Sher, M. Fink, J. Cooper, B. M. Heath, N. C. McMahon, D. J. Gavaghan, and D. Noble. Simulation of multiple ion channel block provides improved early prediction of compounds' clinical torsadogenic risk. *Cardiovascular Research*, **91**(1):53–61, July 2011.

[95] G. R. Mirams, M. R. Davies, Y. Cui, P. Kohl, and D. Noble. Application of cardiac electrophysiology simulations to pro-arrhythmic safety testing. *British Journal of Pharmacology*, **167**(5):932–945, November 2012.

[96] J. D. Moreno and C. E. Clancy. Using computational modeling to predict arrhythmogenesis and antiarrhythmic therapy. *Drug Discovery Today: Disease Models*, **6**(3):71–84, 2009.

[97] J. D. Moreno, Z. I. Zhu, P.-C. Yang, J. R. Bankston, M.-T. Jeng, C. Kang, L. Wang, J. D. Bayer, D. J. Christini, N. A. Trayanova, C. M. Ripplinger, R. S. Kass, and C. E. Clancy. A Computational Model to Predict the Effects of Class I Anti-Arrhythmic Drugs on Ventricular Rhythms. *Science Translational Medicine*, **3**(98):98ra83, August 2011.

[98] G. E. Morley, D. Vaidya, F. H. Samie, C. Lo, M. Delmar, and J. Jalife. Characterization of conduction in the ventricles of normal and heterozygous Cx43 knockout mice using optical mapping. *Journal of Cardiovascular Electrophysiology*, **10**(10):1361–1375, October 1999.

[99] P. J. Murray, C. M. Edwards, M. J. Tindall, and P. K. Maini. From a discrete to a continuum model of cell dynamics in one dimension. *Physical Review E: Statistical, Nonlinear, and Soft Matter Physics*, **80**(3), 2009.

[100] J. Nagumo, S. Arimoto, and S. Yoshizawa. An Active Pulse Transmission Line Simulating Nerve Axon. *Proceedings of the IRE*, **50**(10):2061–2070, October 1962.

[101] S. Nattel, A. Maguy, S. Le Bouter, and Y.-H. H. Yeh. Arrhythmogenic ion-channel remodeling in the heart: heart failure, myocardial infarction, and atrial fibrillation. *Physiological Reviews*, **87**(2):425–456, April 2007.

[102] J. C. Neu and W. Krassowska. Homogenization of syncytial tissues. *Critical Reviews in Biomedical Engineering*, **21**(2):137–199, 1993.

[103] S. A. Niederer, M. Fink, D. Noble, and N. P. Smith. A meta-analysis of cardiac electrophysiology computational models. *Experimental Physiology*, **94**(5):486–495, May 2009.

[104] D. Noble. A modification of the Hodgkin-Huxley equations applicable to Purkinje fibre action and pacemaker potentials. *The Journal of Physiology*, **160**(2):317–352, February 1962.

[105] A. V. Panfilov, R. H. Keldermann, and M. P. Nash. Drift and breakup of spiral waves in reaction-diffusion-mechanics systems. *Proceedings of the National Academy of Sciences of the United States of America*, **104**(19):7922–7926, May 2007.

[106] P. Pathmanathan, M. O. Bernabeu, R. Bordas, J. Cooper, A. Garny, J. M. Pitt-Francis, J. P. Whiteley, and D. J. Gavaghan. A numerical guide to the solution of the bidomain equations of cardiac electrophysiology. *Progress in Biophysics and Molecular Biology*, **102**(2-3):136–155, June 2010.

[107] P. Pathmanathan, G. R. Mirams, J. Southern, and J. P. Whiteley. The significant effect of the choice of ionic current integration method in cardiac electrophysiological simulations. *International Journal for Numerical Methods in Biomedical Engineering*, **27**(11):1751–1770, November 2011.

[108] C. R. Paul. *Fundamentals of Electric Circuit Analysis*. John Wiley & Sons Inc, January 2004.

[109] C. Peracchia. *Gap Junctions: Molecular Basis of Cell Communication in Health and Disease*. Academic Press, first edition, December 1999.

[110] J. B. Picone, N. Sperelakis, and J. E. Mann. Expanded model of the electric field hypothesis for propagation in cardiac muscle. *Mathematical and Computer Modelling*, **15**(8):17–35, January 1991.

[111] J. Pitt-Francis, M. O. Bernabeu, J. Cooper, A. Garny, L. Momtahan, J. Osborne, P. Pathmanathan, B. Rodriguez, J. P. Whiteley, and D. J. Gavaghan. Chaste: using agile programming techniques to develop computational biology software. *Philosophical Transactions of the Royal Society A: Mathematical, Physical and Engineering Sciences*, **366**(1878):3111–3136, September 2008.

[112] J. Pitt-Francis, P. Pathmanathan, M. O. Bernabeu, R. Bordas, J. Cooper, A. G. Fletcher, G. R. Mirams, P. Murray, J. M. Osborne, A. Walter, S. J. Chapman, A. Garny, I. M. M. van Leeuwen, P. K. Maini, B. Rodríguez, S. L. Waters, J. P. Whiteley, H. M. Byrne, and D. J. Gavaghan. Chaste: A test-driven approach to software development for biological modelling. *Computer Physics Communications*, **180**(12):2452–2471, December 2009.

[113] G. Plank, L. J. Leon, S. Kimber, and E. J. Vigmond. Defibrillation depends on conductivity fluctuations and the degree of disorganization in reentry patterns. *Journal of Cardiovascular Electrophysiology*, **16**(2):205–216, February 2005.

[114] R. Plonsey and R. C. Barr. Current flow patterns in two-dimensional anisotropic bisyncytia with normal and extreme conductivities. *Biophysical Journal*, **45**(3):557–571, March 1984.

[115] R. Plonsey and R. C. Barr. Effect of microscopic and macroscopic discontinuities on the response of cardiac tissue to defibrillating (stimulating) currents. *Medical and Biological Engineering and Computing*, **24**(2):130–136, March 1986.

[116] R. Plonsey and R. C. Barr. Inclusion of junction elements in a linear cardiac model through secondary sources: Application to defibrillation. *Medical and Biological Engineering and Computing*, **24**(2):137–144, March 1986.

[117] H. Poincaré. *Les Méthodes Nouvelles De La Mécanique Céleste: Solutions Périodiques. Non-Existence Des Intégrales Uniformes. Solutions Asymptotique (French Edition)*. Nabu Press, February 2010.

[118] M. Potse, B. Dubé, J. Richer, A. Vinet, and R. M. Gulrajani. A comparison of monodomain and bidomain reaction-diffusion models for action potential propagation in the human heart. *IEEE Transactions on Biomedical Engineering*, **53**(12):2425–2435, December 2006.

[119] A. Pumir and V. I. Krinsky. Two biophysical mechanisms of defibrillation of cardiac tissue. *Journal of Theoretical Biology*, **185**(2):189–199, March 1997.

[120] J. N. Reddy. *Introduction to the Finite Element Method*. McGraw-Hill Science/Engineering/Math, second edition, January 1993.

[121] G. Richardson and S. J. Chapman. Derivation of the Bidomain Equations for a Beating Heart with a General Microstructure. *SIAM Journal on Applied Mathematics*, **71**(3):657–675, 2011.

[122] S. Rohr, J. P. Kucera, and A. G. Kléber. Slow conduction in cardiac tissue, I: effects of a reduction of excitability versus a reduction of electrical coupling on microconduction. *Circulation Research*, **83**(8):781–794, October 1998.

[123] S. Rohr. Role of gap junctions in the propagation of the cardiac action potential. *Cardiovascular Research*, **62**(2):309–322, May 2004.

[124] M. Roseau. *Asymptotic Wave Theory (Mathematics & Mechanics)*. Elsevier Science Publishing Co Inc.,U.S., first edition, 12 1975.

[125] B. J. Roth. How the anisotropy of the intracellular and extracellular conductivities influences stimulation of cardiac muscle. *Journal of Mathematical Biology*, **30**(6):633–646, June 1992.

[126] B. J. Roth. Electrical conductivity values used with the bidomain model of cardiac tissue. *IEEE Transactions on Biomedical Engineering*, **44**(4):326–328, April 1997.

[127] B. J. Roth. How to explain why 'unequal anisotropy ratios' is important using pictures but no mathematics. *Conference proceedings: ... Annual International Conference of the IEEE Engineering in Medicine and Biology Society. IEEE Engineering in Medicine and Biology Society.*, **1**:580–583, 2006.

[128] B. J. Roth and D. Langrill Beaudoin. Approximate analytical solutions of the Bidomain equations for electrical stimulation of cardiac tissue with curving fibers. *Physical Review E: Statistical, Nonlinear, and Soft Matter Physics*, **67**(5), May 2003.

[129] J. E. Saffitz, L. M. Davis, B. J. Darrow, H. L. Kanter, J. G. Laing, and E. C. Beyer. The molecular basis of anisotropy: role of gap junctions. *Journal of Cardiovascular Electrophysiology*, **6**(6):498–510, June 1995.

[130] H. Satoh, L. M. Delbridge, L. A. Blatter, and D. M. Bers. Surface:volume relationship in cardiac myocytes studied with confocal microscopy and membrane capacitance measurements: species-dependence and developmental effects. *Biophysical Journal*, **70**(3):1494–1504, March 1996.

[131] M. Schroeder. The eikonal equation. *The Mathematical Intelligencer*, **5**(1):36–37, March 1983.

[132] T. Seidel, A. Salameh, and S. Dhein. A simulation study of cellular hypertrophy and connexin lateralization in cardiac tissue. *Biophysical Journal*, **99**(9):2821–2830, November 2010.

[133] N. G. Sepulveda, B. J. Roth, and J. P. Wikswo. Current injection into a two-dimensional anisotropic bidomain. *Biophysical Journal*, **55**(5):987–999, May 1989.

[134] N. J. Severs, A. F. Bruce, E. Dupont, and S. Rothery. Remodelling of gap junctions and connexin expression in diseased myocardium. *Cardiovascular research*, **80**(1):9–19, October 2008.

[135] N. J. Severs, E. Dupont, N. Thomas, R. Kaba, S. Rothery, R. Jain, K. Sharpey, and C. H. Fry. Alterations in cardiac connexin expression in cardiomyopathies. *Advances in Cardiology*, **42**:228–242, 2006.

[136] R. M. Shaw and Y. Rudy. Ionic Mechanisms of Propagation in Cardiac Tissue : Roles of the Sodium and L-type Calcium Currents During Reduced Excitability and Decreased Gap Junction Coupling. *Circulation Research*, **81**(5):727–741, November 1997.

[137] J. Shewchuk. Triangle: Engineering a 2D quality mesh generator and Delaunay triangulator. In M. C. Lin and D. Manocha, editors, *Applied Computational Geometry Towards Geometric Engineering*, **1148** of *Lecture Notes in Computer Science*, chapter 23, pages 203–222. Springer-Verlag, Berlin/Heidelberg, 1996.

[138] R. Shipley and S. J. Chapman. Multiscale Modelling of Fluid and Drug Transport in Vascular Tumours. *Bulletin of Mathematical Biology*, **72**(6):1464–1491, August 2010.

[139] H. Si. *TetGen A Quality Tetrahedral Mesh Generator and Three-Dimensional Delaunay Triangulator*. 2006.

[140] J. R. Sommer. Implications of structure and geometry on cardiac electrical activity. *Annals of Biomedical Engineering*, **11**(3–4):149–157, 1983.

[141] M. S. Spach, W. T. Miller, D. B. Geselowitz, R. C. Barr, J. M. Kootsey, and E. A. Johnson. The discontinuous nature of propagation in normal canine cardiac muscle. Evidence for recurrent discontinuities of intracellular resistance that affect the membrane currents. *Circulation Research*, **48**(1):39–54, January 1981.

[142] M. S. Spach and J. F. Heidlage. The Stochastic Nature of Cardiac Propagation at a Microscopic Level. *Circulation Research*, **76**(3):366–380, March 1995.

[143] M. S. Spach, J. F. Heidlage, P. C. Dolber, and R. C. Barr. Electrophysiological Effects of Remodeling Cardiac Gap Junctions and Cell Size. *Circulation Research*, **86**(3):302–311, February 2000.

[144] N. Sperelakis and K. McConnell. Electric field interactions between closely abutting excitable cells. *IEEE Engineering in Medicine and Biology Magazine*, **21**(1):77–89, January 2002.

[145] K. H. W. J. ten Tusscher, A. Mourad, M. P. Nash, R. H. Clayton, C. P. Bradley, D. J. Paterson, R. Hren, M. Hayward, A. V. Panfilov, and P. Taggart. Organization of ventricular fibrillation in the human heart: experiments and models. *Experimental Physiology*, **94**(5):553–562, May 2009.

[146] K. H. W. J. ten Tusscher, D. Noble, P. J. Noble, and A. V. Panfilov. A model for human ventricular tissue. *American Journal of Physiology — Heart and Circulatory Physiology*, **286**(4):H1573–H1589, April 2004.

[147] K. H. W. J. ten Tusscher and A. V. Panfilov. Alternans and spiral breakup in a human ventricular tissue model. *American Journal of Physiology — Heart and Circulatory Physiology*, **291**(3):H1088–H1100, September 2006.

[148] S. P. Thomas, J. P. Kucera, L. Bircher-Lehmann, Y. Rudy, J. E. Saffitz, and A. G. Kléber. Impulse propagation in synthetic strands of neonatal cardiac myocytes with genetically reduced levels of connexin43. *Circulation Research*, **92**(11):1209–1216, June 2003.

[149] N. Trayanova. Discrete versus syncytial tissue behavior in a model of cardiac stimulation. I. Mathematical formulation. *IEEE Transactions on Biomedical Engineering*, **43**(12):1129–1140, December 1996.

[150] N. Trayanova and T. C. Pilkington. The use of spectral methods in bidomain studies. *Critical Reviews in Biomedical Engineering*, **20**(3-4):255–277, 1992.

[151] N. Trayanova and T. C. Pilkington. A bidomain model with periodic intracellular junctions: a one-dimensional analysis. *IEEE Transactions on Biomedical Engineering*, **40**(5):424–433, May 1993.

[152] N. Trayanova. An approximate solution to the periodic bidomain equations in one dimension. *Mathematical Biosciences*, **120**(2):189–210, April 1994.

[153] N. Trayanova. Defibrillation of the heart: insights into mechanisms from modelling studies. *Experimental Physiology*, **91**(2):323–337, March 2006.

[154] N. Trayanova. Whole-Heart Modeling. *Circulation Research*, **108**(1):113–128, January 2011.

[155] L. Tung. *A bi-domain model for describing ischemic myocardial D-C potentials*. PhD thesis, MIT, Cambridge, MA, 1978.

[156] V. L. Van Breemen. Intercalated discs in heart muscle studied with the electron microscope. *The Anatomical Record*, **117**(1):49–63, 1953.

[157] N. Vandersickel, I. V. Kazbanov, A. Nuitermans, L. D. Weise, R. Pandit, and A. V. Panfilov. A study of early afterdepolarizations in a model for human ventricular tissue. *PloS one*, **9**(1), 2014.

[158] R. D. Veenstra. *Ion permeation through connexin gap junction channels: effects on conductance and selectivity*, **49**, pages 95–129. Elsevier, 1999.

[159] S. Viskin and B. Belhassen. Idiopathic ventricular fibrillation. *American Heart Journal*, **120**(3):661–671, September 1990.

[160] S. Weidmann. Effect of current flow on the membrane potential of cardiac muscle. *The Journal of Physiology*, **115**(2):227–236, October 1951.

[161] S. Weidmann. The diffusion of radiopotassium across intercalated disks of mammalian cardiac muscle. *The Journal of Physiology*, **187**(2):323–42+, 1966.

[162] S. Weidmann. The effect of the cardiac membrane potential on the rapid availability of the sodium-carrying system. *The Journal of Physiology*, **127**(1):213–224, January 1955.

[163] L. D. Weise, M. P. Nash, and A. V. Panfilov. A discrete model to study reaction-diffusion-mechanics systems. *PloS one*, **6**(7), 2011.

[164] J. P. Whiteley. An Efficient Numerical Technique for the Solution of the Monodomain and Bidomain Equations. *IEEE Transactions on Biomedical Engineering*, **53**(11):2139–2147, November 2006.

[165] J. P. Whiteley. An efficient technique for the numerical solution of the bidomain equations. *Annals of Biomedical Engineering*, **36**(8):1398–1408, August 2008.

[166] J.-A. Yao, D. E. Gutstein, F. Liu, G. I. Fishman, and A. L. Wit. Cell Coupling Between Ventricular Myocyte Pairs From Connexin43-Deficient Murine Hearts. *Circulation Research*, **93**(8):736–743, October 2003.

[167] M. Yeager. Structure of Cardiac Gap Junction Intercellular Channels. *Journal of Structural Biology*, **121**(2):231–245, January 1998.

[168] M. Zoni-Berisso, F. Lercari, T. Carazza, and S. Domenicucci. Epidemiology of atrial fibrillation: European perspective. *Clinical Epidemiology*, **6**:213–220, 2014.